PAUL SCHERRER INSTITUT

PSI Proceedings 98-01
August 1998
ISSN 1019-6447

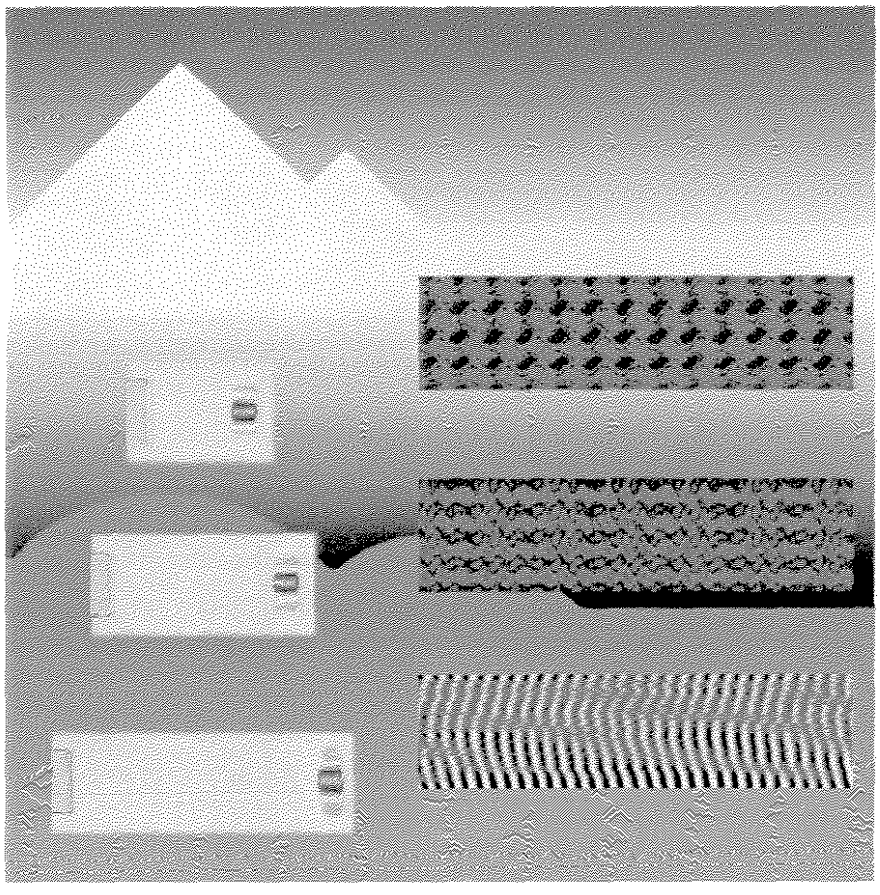

Proceeding

Selected Papers of the First International Symposium on Ultrasonic Doppler Methods in Fluid Mechanics and Fluid Engineering

Villigen PSI, Switzerland
September 09–11, 1996

PAUL SCHERRER INSTITUT

PSI Proceedings 98-01
August 1998

1st ISUD

Selected Papers of the First International Symposium on Ultrasonic Doppler Methods in Fluid Mechanics and Fluid Engineering

held at Paul Scherrer Institut

September 9 - 11, 1996

Editors

Y. Takeda
J.-F. Ravoux

Paul Scherrer Institut, CH-5232 Villigen PSI

Contents

Preface

The First International Symposium on Ultrasonic Doppler Method for Fluid Mechanics and Fluid Engineering (1. ISUD) was held at PSI for 9.-11. September 1996. Its scope and aims are quoted below from its announcement. Total 60 scientists and engineers gathered to discuss this new measuring method, and there were 20 presentations and 3 plenary lectures. Lectures were given by Prof. Busse of Uni. Bayreuth, Prof. Ertl of Uni. Erlangen and Prof. Kirby of Uni. Colorado.

The scientific committee selected 8 presentations for publication, which are bound in this volume. These papers were further reviewed and 5 papers were accepted for publication in the journal of 'Experiments in Fluids'. This indicates that investigations presented in the symposium has highly scientific contents and we are pleased to find that their work are well evaluated.

I am grateful for all participants and all members of the scientific committee who worked for a good start of this symposium. I believe that the symposium tradition of bringing up their scientific work and of publication in the highly respectful journal must be a good one for the USD community and would induce more users to gather.

At last but not least, we thank companies, Met-Flow SA in Lausanne and Asahi Thermal and Fluid System in Nagoya, for their financial support to the symposium.

Yasushi Takeda

Scope

The ultrasonic Doppler method for velocity profile measurement has now become established and accepted in the fields of general fluid mechanics and fluid engineering. It is attracting increasing interest from physicists and fluid engineers for its use as a research tool. The time is now appropriate for a first international symposium on this method. The purpose of the symposium is the exchange of information on applications of the ultrasonic Doppler method to a variety of flow configurations and liquids including industrial measurements.

It is the aim of the symposium to bring together researchers from all over the world to discuss the results of their applications of the ultrasonic Doppler method to fluid mechanics research and fluid engineering. Papers will be presented at the symposium that deal with the technique itself, with its applications and with future developments. The main aim is, however, to present the latest fluid mechanics results that are based on the ultrasonic Doppler technique.

Ultrasonic Doppler Method for velocity profile measurement in Fluid Dynamics and Fluid Engineering

Y. Takeda

Paul Scherrer Institute, CH-5232 Villigen PSI, Switzerland

1. Introduction

An Ultrasound Doppler Velocity Profile method (UVP method) has been developed for fluid mechanical measurements in physics and engineering. The principle of the method is straightforward; echography and Doppler effect. This method was originally developed in medical engineering to measure blood flow. However, due to various constraints arising from its direct application to the human body, the measurement method never realized its full potential. We subsequently extended this method to non-medical flow measurements and developed specific application systems. Although the initial motivation was to find a new flow measurement method for liquid metal flows, the method itself was found to be quite useful to flow measurements in general and additionally through years of use has gradually become accepted as a tool to study the physics and engineering of fluid flow. In the sections to follow we will describe the measurement method and review the applications to date.

The working principle of the method is described in detail in Takeda (1995). It uses pulsed ultrasonic Doppler effect together with the echography relationship. An ultrasound pulse is emitted from a transducer into liquid, and the same transducer receives the echoes, which originate from tiny particles suspended in the fluid. The position information is given by the time duration between the pulse emission and the instant of echo reception, thus recording the position from where the echo is reflected. The velocity information is derived from the instantaneous Doppler shift frequency at that instant. The velocity profile is formed by processing the echo signal such that the instantaneous frequency is estimated at each instant. The system to realize such signal processing requires intricate analogue and digital electronics but most of the principal elements and algorithms can be found in Atkinson & Woodcook (1982). The system parameters such as basic frequency, maximum velocity, maximum measuring length and so on can be designed such that for many applications in ordinary fluids measurement requirements and conditions are fulfilled. The typical parameter values available at present can also be found by Met-Flow (1998).

In contrast to other measurement methods, this technique has the following three major advantages:

(1) It obtains a spatio-temporal information about the flow field.

(2) It is applicable to opaque liquids.

(3) It is a line measurement and thus a flow mapping is practicable.

Each of these advantages will be further explained below. We should emphasize that this measurement method is not a pointwise measurement but a linewise measurement. Thus a velocity profile consisting of a multiple number of data points, say 128, is realized and not incrementally scanned from the first through the last data

point in the field. This is quite important contrast to the conventional methods, which calls upon the user to re-think the way the data is interpreted. Moreover the means by which data sets are manipulated and analyzed are inherently different. Thus the advantageous features are :

(1) Spatio-temporal information : The velocity field described in an Eulerian frame is a function of both space and time. In conventional measurement techniques, except for PIV (particle image velocimetry) and other image recording schemes, we can obtain the velocity field at one instant or velocity values at one spatial point as a time series. Due to the inherent constraints of such velocimetry, there has been a clear need to develop a measurement technique by which one can obtain velocity fields as a function of time. The UVP, though obtaining data along its beam line, can give such information. A spatio-temporal velocity information is important in physics study such as flow instability, where the spatio-temporal nature of the flow field is essential.

(2) Until recently it was practically impossible to make velocity measurement of opaque fluids. Flow visualization techniques by optical means are obviously impossible and other measurements such as pressure or torque measurements do not give spatially local information. In addition many of these fluids show non-Newtonian behavior and are highly viscous so that immersing any velocity sensing probe disturbs the flow field. By employing the UVP method and non-invasively, it is possible to measure flow field in opaque, non-Newtonian viscous liquids as if it were an ordinary liquid. It is potentially possible to explore areas in rheology, process related flow engineering and liquid metal systems.

(3) In order to validate computational codes, it is desirable to experimentally measure the same velocity field as that calculated. Usually from numerical codes, velocity fields are generated in vector form, from which various related flow quantities such as flow rate are computed. A subset of these results are often compared with experiments in order to validate the codes. This is, however, merely an implicit and insufficient validation procedure since the integration often smears out fine structure existing in the flow. With the UVP used, for the purpose of flow mapping the obtained flow fields can be directly compared with numerical results. The comparison is possible not only concerning the flow pattern but also quantitatively. The speed as well as other physical quantities which are derived from the velocity field, such as stream function or vorticity, can be compared.

In the following sections, investigations employing the UVP method are described from the perspective of the above described features. Some of these works are included in the present issue of the journal. In addition, as the development was largely conducted at PSI, it includes many of reports of myself. The reports which deal with the development and the use are not included.

2. Spatio-temporal velocity field

In the first example of the application of UVP method, we reported an investigation on flow in a gap between two concentric cylinders, the so-called Taylor-Couette system (Takeda et al. 1990). The axial velocity component was obtained as a function of axial position and time, $V_z(z,t)$, in order to investigate the transient behavior of Taylor vortices formation upon a sudden start of the inner cylinder. They observed an

evolution of the wave-length of the Taylor vortices and found that the Taylor vortices is really formed in a gap due to a centrifugal instability and not generated by the end wall. He further extended his investigation of this system to azimuthal modulating waves (Takeda et al. 1993) and weakly turbulent flow (Takeda et al. 1994).

The spatio-temporal behavior of flow in the wake of cylinder (Peschard et al. 1996) and also the multiple wake behind a row of cylinders (Le Gal et al. 1996) (both are for parallel plates configuration) have been investigated at Marseille (IRPHE). In the single wake experiment, they identified several fundamental spatial modes from the spatio-temporal velocity distribution. Comparison with numerical calculation verified this experimental result. In the multiple wake experiment, they obtained a transverse velocity distribution and analyzed using a bi-orthogonal decomposition to investigate the collective behavior of such wakes.

A similar investigation has been undertaken by Gifu University where researchers studied flow in the wake behind a torus ring aligned perpendicular and/or oblique to the flow direction (Inoue et al. 1996). Upon scrutinizing the temporal nature by analyzing the power spectrum the data revealed counterrotating vortex rings that are alternately shed from the torus. The structure for the oblique arrangement was characterized by a transverse change in the power spectrum.

Flow on a rotating disc has also been investigated by researchers at Marseille (Schouveiler et al. 1996). When the Reynolds number for this system is defined in terms of the radial position, a range of phenomena for Reynolds numbers ranging from zero to a large number but finite in number can appear simultaneously, and under these circumstances the spatio-temporal observation of the flow field is essential. They found a system of circular and spiral waves, which interact non-linearly, and drive the transition to turbulence. They also determined the flow regimes of various complex wave modes.

In more industrially relevant configuration, flow in a Czochralski (Cz) crystal puller has been investigated (Tokuhiro & Takeda, 1993, Azuma et al. 1997). In a Cz crystal puller the flow, especially near the seed crystal, is critical for producing a silicon crystal of large diameter and with low impurity content. The flow shows quite a complex flow behavior due to not only rotational boundary condition of the seed crystal but as natural convection driven by the heating for melting silicon within the crucible and solidification at crystal. Tokuhiro and Takeda (1993) investigated the transient and spatio-temporal nature of a flow in a simulated Cz-model induced by simple rotation of the seed crystal and determined the critical Reynolds number for breaking of the axisymmetric flow. Azuma et al. (1997) extended this work to a system with natural convection heating of silicon oil. By changing the Reynolds number at a fixed Raleigh number, they observed a steady, oscillatory quasi-periodic flow and turbulence. The associated flow transition was studied by 2D Fourier spectral analysis and a correlation function from which one concluded that the transition occurs via spatio-temporal intermittency.

3. Flow measurement in opaque liquids

The initial motivation of the author to develop a method was to study liquid metal flow. The first test medium was mercury (Takeda 1990). The ultrasonic transducer was immersed directly into mercury and the flow in a T-branch of a pipe was

measured to confirm the method. Flow measurement in mercury has recently been extended to study flow in the accelerator target geometry (Takeda & Kikura 1998). The container is made of stainless steel and the transducer is placed externally to the container wall. This is possible thanks to a transmission property of ultrasonic beam for a combination of mercury and stainless steel. They made a flow mapping of the mercury flow.

A group at the Swiss Federal Institute of Technology in Zurich is working on the application to flow of food materials, Uriev et al. (1998). The food materials are usually opaque and non-Newtonian so that to date there was no good way to investigate flow behavior in pipes or other containers. Uriev and co-workers have succeeded in measuring velocity profile of chocolate flow from which a flow rate was estimated. They evaluate such velocity profiles together with pressure difference to obtain various parameters such as shear rate and viscosity, both of which can be used as parameters in process control.

Sawada et al. (1996) have been investigating flow of magnetic fluids. The magnetic fluid is composed of tiny magnetic particles of diameter having the range of 5 to 15 nm suspended in water or oil. They are mostly black liquid and no optical method can be used. This kind of liquids has characteristics that its apparent viscosity changes by the external magnetic field and thus its flow behavior is sensitive to it. Although it has potential for various industrial applications, its use was very limited due to its difficulty to study the flow behavior. They studied a sloshing flow. A rectangular container filled with a magnetic liquid (free surface) is set on a oscillating bench. A transducer is set outside the container and moves together. A permanent magnet is used to apply a magnetic field. They studied an effect of the intensity of magnetic field on flow by time-averaged velocity distributions and power spectrum. A spatial distribution of peak intensities in power spectra for resonant frequency and its higher harmonics agrees well with theoretical prediction. They also found the harmonic components are suppressed by the magnetic field.

Finally in measurement of sodium flow in fast reactor development an effort has been made to measure Na flow in a pipe. The Japanese institute for FBR research and development, PNC, has developed a high temperature transducer which can be used up to 350°C and applied to a flow in a circular pipe [17]. Because of the high temperature and equally reactive environment, the set-up of transducer is constrained and less flexible than in ordinary fluid applications such that multiple reflections from surrounding walls appear to distort the recorded profiles. With careful analysis of each profile, a time-averaged velocity distribution was obtained which shows reasonable agreement with results from numerical calculations.

4. Flow mapping

In fact, a flow mapping is quite often an integral task in the industrial design of cooling channels and shrouds. The complex flow regions and paths in thermal hydraulics in nuclear reactor is also one of the areas of continuing interest.

Several types of flow have been mapped; these being in a square cavity attached to a parallel channel (Takeda et al. 1991) and a circular jet emanating into a tank of the same liquid (Takeda et al. 1995).

An extensive study was made by Wachter et al. (1996) for a flow in a stirrer of waste water tank. The measured field is 40x40x50 cm^3 with a rotating stirrer located centrally at the bottom. Using a traversing mechanism for a single transducer, they measured velocity profiles at 8x8x9 positions; that is a total of 576 velocity profiles. Data analysis was subsequently made such that two dimensional (x,y) velocity vector fields were computed at 9 different heights. This data set is displayed using various formats such as vector fields, relative velocity fields, turbulent velocity fields, and local energy dissipation contours. The results show that full flow mapping enables us to evaluate the flow phenomena using various physical quantities derived from the vector velocity field; that is, quantities such as the stream function distribution and vorticity distribution. A similar study has been made for water flow in a parallel channel flow (Kikura & Takeda 1998).

A group at PSI is also investigating flow of mercury in a stainless steel container (Takeda & Kikura 1998). The investigation is on flow pattern in a hemispherical end region of a double coaxial tube type target container for a spallation neutron source. The axisymmetric 2D flow is being studied in terms of a flow map and in comparison to results from numerical computation. Additionally, it is partly for geometrical optimization of the target design parameters and moreover to validate the computer code, especially as applied to liquid metal flow.

In the field of hydraulics, DeCesare & Boillat (1997) at Ecole Polytechnique Federale de Lausanne have used flow mapping in order to investigate flow with sedimentation. They investigated flow using a model flume and also behind a dam (Beyer-Portner et al. 1998). A flow map was obtained at various times after starting the flow, especially at along the bottom region near the flow bed. These results were compared with numerical computations.

5 Other applications

The UVP method is being used in various other configurations where, mostly, the size of the fluid body of interest is relatively large, typically larger than 1 m. Such large dimension are often encountered in nuclear engineering, civil engineering (Deininger et al. 1996), chemical engineering, environmental sciences such as in oceanic and geophysical flows, where even a time-averaged velocity profile is often difficult to obtain.

Thermal striping, a phenomenon which appears in the fast breeder thermal hydraulics is an issue concerning thermal fatigue of components due to poor thermal mixing of coolant. The phenomenon to date has been investigated mainly using temperature information, but Tokuhiro (1997) are studying its hydrodynamic features in a water based experiment. A hot-cold-hot, three jet configuration simulates flow out of the core with UVP, PIV and temperature recording the spatio-temporal nature of the thermal-hydraulics.

In the area of experimental gas-liquid flows the UVP method can be applied to a moving interface such as bubbles and free surfaces. Aritomi et al. (1996) have been investigating a water-air bubbly two phase flow. At present the application is limited to a bubbly flow with low void fraction, since the ultrasonic beam is totally reflected or deflected by large bubbles in certain flow regimes and at large void fraction multiple scattering amongst the bubbles introduces error into the position information

such that the profile is deformed. The purpose of Aritomi's investigation is to apply the method to obtain a void fraction by analyzing the shape of each velocity profile, detecting the position of the bubble (which appears as a sharp change of the velocity on the velocity profile) and noting the rate of such appearance. In order to validate UVP measurements a comparison with visual observation recorded as a video movie has been conducted and showed a good agreement.

Another group at EPFL, Rolland (1994, 1997) has developed their own system using acoustic waves and applied this method to open channel turbulent flows (Lhermitte & Lemmin 1994). They obtained mean vertical water velocity distributions and several turbulent characteristics.

Finally, Nakamura et al. (1996) made simultaneous measurements of velocity profile and interfacial profile in a horizontal duct containing free surface wavy flow. The position of the free surface appears on the velocity profile as a sudden and discontinuous change of the velocity values. A time change of the water level was compared with results from a level detector probe and showed good agreement. The velocity profile in the liquid also showed agreement with results taken by Particle Tracking Velocimetry.

6 ISUD and USDJ Symposium

The First International Symposium on Ultrasonic Doppler method for fluid mechanics and fluid engineering (1. ISUD) was held September 1996 at PSI (Takeda 1996). The main objective of the symposium was to introduce the applications to various flow configurations and to promote this method for a wider variety of flow investigations. The emphasis of the meeting was made on the physical understanding of the data obtained by this method so that plenary talks were given on the physics to be made based on the experimental spatio-temporal data as well as on the mathematical methods to display and analyze such data. Approximately 60 participants gathered, discussed their own applications and exchanged information and experience.

In 1997 a Seminar on flow measurements using Ultrasonic Doppler method (USDJ 97) was held in Yokohama, Japan (Sawada et al. 1998). At the seminar a dozen or so papers oriented toward the industrial applications were presented.

Acknowledgment

The author is grateful to many investigators who have employed the UVP method in their investigations, especially Dr. G. King and Dr. A. Tokuhiro for their constant and encouraging support for many cases in my activity and for making this review.

References

Aritomi, M; Zhou, S; Nakajima, M; Takeda, Y; Mori, M; Yoshioka, Y; (1996) Measurement system of bubbly flow using ultrasonic velocity profile monitor and video data processing unit, J. Nucl. Eci. Technol, 33: 915-923.

Atkinson, P; Woodcook, JP; (1982) Doppler ultrasound and its use in clinical measurement, Academic Press, Inc.

Azuma, H; (1997) Flow instabilities in a simulated Czochralski crystal puller, A seminar on Flow Measurements using Ultrasound Doppler Methods; USDJ '97, November 10-11, 1997, Proceedings, PSI-Proc. 98-01

Beyer-Portner NA; DeCesare, G; Schleiss, A; Boillat, JL; (1998) Erosion and sedimentation in mountainous environment - physical and numerical modeling, Proceedings of Humid Tropics '98, Pangkor Island, Malaysia, November 1998.

DeCesare G; Boillat JL; (1997) Turbidity current monitoring in a physical model flume using ultrasonic Doppler method, ERCOFTAC 1997, Annual Report, February 1998.

Deininger, A; Gurthert FW; Widerer, PA; (1996) The influence of Currents on circular secondary clarifier performance and design, 18th IAWQ Biennial Conference on Water Quality, Conference Prepring Book 3, Singapore

Inoue, Y; Yamashita, S; Kumada, M; (1996) An experimental study on a wake of a torus using UVP monitor, Exp. in Fluids, this issue.

Kamosida, H; Hayashi, K; Komatuzaki, K; Takeda, Y; (1995) Measurement of velocity profile in Sodium using ultrasonic velocity monitor, Annual Meeting of Atomic Energy Society of Japan, 17-20 October, 1995

Kikura H; Takeda, Y; (1998) Flow Mapping using Ultrasonic Doppler Method, 1998 ASME Fluid Engineering Division Summer Meeting, Washington DC, June

Nakamura H; (1996) Simultaneous Measurement of Liquid Velocity and Interface Profiles of Horizontal Duct Wavy Flow by Ultrasonic Velocity Profile Meter, to be published.

Le Gal, P; Pescherd, I; Chauve, MP; Takeda, Y; (1996) Collective behavior of wakes downstream a row of cylinders, Phys. Fluids, 8: 2097 - 2106

Lhermitte, R; Lemmin, U; (1996) Open-channel Flow and Turbulent Measurement by High-Resolution Doppler Sonar, J. Atmos. & Oceanic Technol. 11, 1296 - 1308

Met-Flow S.A., Lausanne, (1998) visit http://www.met-flow.ch

Peschard, I; Ravoux, JF; Le Gal, P; Takeda, Y; Chauve, MP; (1996) On the spatio-temporal structure of the cylinder wake, Exp. in Fluids, this issue.

Rolland, T; (1994) Development d'une instrumentation Doppler ultrasonore: application aux ecoulements turbulents en hydraulique. These EPFL No.1281, Lausanne.

Rolland, T; Lemmin, U; A two-component acoustic velocity profile for use in turbulent open-channel flow, J. Hydraulic Res., 35, 545 - 561.

Sawada, T; Kikura, H; Tanahashi; (1996) Kinematic characteristics of magnetic fluid sloshing in a rectangular container subject to non-uniform magnetic field, Exp. in Fluids, this issue.

Sawada, T; Tkuhiro A; Aritomi, M; (1998) A seminar on Flow Measurements using Ultrasound Doppler Methods; USDJ '97, November 10-11, 1997, Bulletin of the Research Reactor Laboratory for Nuclear Reactors, Special issue No.2, Tokyo Institute of Technology.

Schouveiler, L; Takeda, Y; Le Gal, P; Chauve, MP; (1996) Spiral and circular waves in the flow between a rotating and a stationary disk, Exp. in Fluids, this issue.

Takeda, Y; (1990) Development of ultrasound velocity profile monitor, Nucl. Eng. & Design, 126: 277

Takeda, Y; Kobashi, K; Fischer, WE; (1990) Observation of the transient behavior of Taylor vortex flow between rotating concentric cylinders after sudden start, Exp. in Fluids, 9: 317-319

Takeda, Y; Samec, K; Kobayashi, K; (1991) Experimental measurements of 2D velocity vector field using ultrasonic velocity profile monitor (UVP), ASME FED-Vol.128: p47.

Takeda Y; Fischer, WE; Sakakibara, J; Ohmura, K; (1993) Experimental observation of the quasiperiodic modes in a rotating Couette system, Phys. Rev. E, 47: 4130

Takeda, Y; Fischer, WE; Sakakibara, J; (1994) Decomposition of the modulated waves in a rotating Couette system, Science, 263: 502 - 505

Takeda, Y; (1995) Velocity profile measurement by ultrasonic Doppler method, Exp. Therm. & Fluid Sci., 10: 444-453

Takeda, Y; (1995) Instantaneous Velocity Profile Measurement by Ultrasonic Doppler Method, JSME International Journal **B**, 38: 8-16

Takeda, Y; (1996) 1st International Symposium on Ultrasonic Doppler Methods for Fluid Mechanics and Fluid Engineering, September 9-11, 1996, Paul Scherrer Institute, Switzerland.

Takeda, Y; Kikura, H; (1998) Measurement of mercury flow by ultrasonic Doppler Method, ASME Fluid Engineering Division Summer meeting, Forum 'Measurements in Opaque Fluids', Washington DC, June 1998

Tokuhiro, A; Takeda, Y; (1993) Measurement of flow phenomena using the ultrasonic velocity profile method in a simulated Czochralski crystal puller, J. Crystal Growth, 130: 421 - 432

Tokuhiro, (1997) An experimental investigation on thermal striping. Mixing of a vertical non-buoyant jet with two adjacent buyonat jets as measured by ultrasound Doppler velocimetry, submitted to Nucl. Eng. Design.

Uriev, B; Koller, S; Windhab, E; Baltes, H; Brand, O; (1998) Foodstuff Rheology Microsensor, Proc. MINAST conference, Second Annual Convention, p.102, 29. April, 1998, Bern

Wachter, P; (1996) Application of the Ultrasound Velocity Measuring Technique to Stirred Vessel Flows with Multi Elements Stirrers, to be published.

Spiral and circular waves in the flow between a rotating and a stationary disk

L. Schouveiler, P. Le Gal, M. P. Chauve

Institut de Recherche sur les Phénomènes Hors Equilibre
U.M.R 138 CNRS - Universités Aix-Marseille I & II
12, Avenue du Général Leclerc, 13003 Marseille, France

Y. Takeda

Laboratory for Spallation Neutron Source
Paul Scherrer Institute
CH-5232 Villigen PSI, Switzerland

ABSTRACT

Circular and spiral waves are observed in the flow between a rotating and a stationary disk. These waves are generated by instabilities of the stationary disk boundary layer. This experimental work is then devoted to their study by means of flow visualisations and measurements of the associated velocity fields. In particular, instantaneous velocity profiles are measured by ultrasonic Doppler anemometry. The spatio-temporal characteristics of the waves are studied with the help of Fourier transforms of these velocity signals.

List of symbols

A_c, A_s	amplitudes of respectively the circular and the spiral waves
f_c, f_s	frequencies of respectively the circular and the spiral waves
h	axial distance between the two disks
N	rotation frequency of the rotating disk
P1, P2	UDA probe positions
R	radius of the disks
$Re_R = \Omega R^2/\nu$	Reynolds number
t	time
$v_\xi(\xi,t)$, $\langle v_\xi(\xi)\rangle$	instantaneous and mean profiles of the velocity projection on the ξ axis
$v_r(r,t)$, $\langle v_r(r)\rangle$	instantaneous and mean profiles of the radial velocity
(r,θ,z)	cylindrical coordinate system
ε	orientation angle of the spiral waves
$\gamma = h/R$	aspect ratio
$\Omega = 2\pi N$	angular velocity of the rotating disk
ξ	coordinate along the ultrasonic beam axis

1
Introduction

In a previous exprimental study (Schouveiler *et al.* 1996), we showed that the flow between a rotating and a stationary coaxial parallel disk in a fixed casing, exhibits different instabilities according to the value of the distance between the two disks and to the angular velocity of the rotating disk. Some aspects of such instabilities have already been reported in the earlier experimental works of San'kov and Smirnov (1984), Itoh (1988) and Sirivat (1991).

In this paper, we describe the flow regimes which appear when the distance between the two disks is much larger than the thickness of the two disk boundary layers and for moderate Reynolds numbers. In this case, we observe two coexisting traveling waves that appear near the stationary disk. As expected, the flow pattern resulting from the interaction of these systems becomes more and more complex when the Reynolds number is increased. First, visualizations of the flow patterns are realized. Then, an ultrasonic Doppler anemometer is used to quantify the spatio-temporal behavior of the flow. This new type of anemometer permits to measure instantaneous velocity profiles and a spectral analysis of the obtained space-time velocity signals are realized with the help of the Fourier transform.

2
Experimental details

2.1
Experimental apparatus and procedure

The experimental setup is schematically shown in Fig. 1. It consists of a stainless steel horizontal rotating disk, of radius $R = 140$ mm , driven at a variable speed by an electrical motor. The rotation frequency N is measured with an optical encoder. This disk is set in a vertical cylindrical housing with a sliding fit so that there is no radial gap between the vertical cylindrical wall and the edge of the disk. The top of the housing, constituting the stationary disk, is made of Plexiglas to permit flow visualization. The system is completely filled with tap water at ambient temperature. The height of the rotating disk inside the housing is adjustable in such a way that the axial distance h between the two parallel disks can be continuously varied from 1 to 20 mm.

A cylindrical coordinate system (r, θ, z) is defined with the z axis coinciding with the axis of rotation and with its origin located at the center of the stationary disk. The control

parameters of this flow are the aspect ratio $\gamma = h/R$ and the Reynolds number $Re_R = \Omega R^2/\nu$, where $\Omega = 2\pi N$ is the angular velocity of the rotating disk and ν the kinematic viscosity of water.

In the present study, the distance h is fixed to 16 mm ($\gamma = 11.43 \times 10^{-2}$) and N is first increased from 0.1 to 0.6 Hz (or rotation per second) by steps of 0.02 Hz, then decreased back in the same manner. Thus the Reynolds number Re_R is varied in the range 12.3×10^3 to 73.9×10^3.

2.2

Experimental techniques

The patterns of the different flow regimes are visualized by adding a small amount of flake particles to the working fluid. These particles have a high reflective index and they tend to align themselves along stream surfaces, thus becoming visible under appropriate lighting conditions (for further details on this visualization technique, see Savas(1985)). The flow patterns are filmed, through the stationary disk, with a video camera located above the stationary disk on the rotation axis (Fig. 1).

The velocity field has been measured with an Ultrasonic Doppler Anemometer (UDA). This device, working with a pulsed ultrasonic emission, allows the measurement of instantaneous profiles of the velocity component projected onto the ultrasound beam direction. The working fluid is seeded with nylon spherical microparticles having a diameter of 80 µm and a density of 1.02 g/cm^3. This apparatus, working alternately in emitter and receiver, detects the Doppler frequency shift of the ultrasound beam which is reflected by these particles in suspension in the flow. Thus, instantaneous velocity profiles can be recorded as a function of time. In our case, the space resolution of this method is 0.74 mm along the ultrasonic beam and 2.5 mm or 5 mm in the transversal direction. The profile acquisition frequency is either 9.35 Hz or 7.39 Hz. For more details on the UDA method, see Takeda *et al.* (1993).

In order to measure different components of the velocity field, the UDA piezoelectric probe has been placed along two typical axis ; P1 for radial profiles and P2 for axial profiles. These two positions (P1 and P2) of the UDA probe are given in Fig. 2. In position P1, the UDA probe and then the ultrasonic beam are parallel to a radius of the disks at a distance of 7 mm from the stationary disk. In this case, we measure, with the 2.5 mm transversal resolution, instantaneous radial velocity profiles along a radius : $v_r(r,t)$. For position P2, the probe is placed in a azimuthal plane defined by a constant radius r, and makes an angle of 20°

versus the vertical axis. This angle has been chosen large enough to minimize the echo due to the rotating disk and small enough to minimize the reflections on the different interfaces. For P2, we define a local coordinate ξ (Fig. 2) along the ultrasonic beam with its origin on the stationary disk. ξ is scaled by $h/\cos 20°$ so that it is equal to 1 on the rotating disk. In this case, the measured profiles $v_\xi(\xi,t)$ of the velocity projection onto the ξ axis reveal the axial structure of the flow.

3
Results

3.1
Basic flow

The characteristic features of these types of rotating flows can be found in the extensive review of Zandbergen and Dijkstra (1987). For the values of γ and Re_R used in the present investigation and outside the boundary layer of the vertical housing, the stationary axisymmetrical basic flow is of Batchelor type. We recall that this flow consists of two boundary layers, one on each disk, separated by an inviscid rotating core where the tangential component of the velocity is constant and the radial component is zero. The main features of this Batchelor flow are recovered on the temporal mean profiles $\langle v_\xi(\xi) \rangle$ which will be presented later in Fig. 5.a and 6.a.

3.2
Visualization

The primary instability of the Batchelor basic flow occurs in the boundary layer of the stationary disk which is more unstable than the rotating one, in accordance with the experimental and numerical studies of Itoh (1988, 1991). When N is close to 0.1 Hz (for $\gamma = 11.43 \times 10^{-2}$) this instability gives rise to the formation of traveling circular vortices (Fig. 3). These vortices are formed near the periphery of the disk and move towards the center. Such traveling circular structures have also been reported, in similar experiments, by Itoh (1988), more recently by Gauthier and Rabaud (1996), and in the numerical simulations of Cousin-Rittemard (1996). They have also been observed by Savas (1983, 1987) in an experimental study of the transient regimes of the boundary layer over a stationary disk in a

rotating fluid (Bödewadt layer). As they travel towards the center, we observe pairings of vortices in such a way that the frequency corresponding to this circular wave system varies along a radius. Similar observations of frequency variation have also been made in the numerical studies of Cousin-Rittemard (1996) and of Lopez (1996) for transient Bödewadt layer flows. This point will be quantitatively investigated by the measurements presented in § 3.3.

As the angular velocity Ω is increased, a second system of waves, constituted by 16 spiral vortices, appears in the peripheral area together with the circular ones (Fig. 4). These spirals possess an angle $\varepsilon \approx 25°$, where ε is defined, in accordance with the terminology of Sirivat (1991), as the angle between the vortex axis and the azimuthal direction, positively counted in the rotation sense of the disk. They are non stationary and, contrary to the circular waves, travel outwards. This kind of traveling spiral waves is only reported in the experimental study of Itoh (1988).

3.3

Anemometry

In this part, we present the results of the UDA measurements realized for an experimental series when Re_R is increased. The raw velocity fluctuation data, obtained by subtraction of the temporal mean profile from the instantaneous profiles, and/or the filtered velocity fluctuation data, obtained by using frequency windows in order to eliminate the experimental noise, are displayed. The values of these spatiotemporal velocity signals and of the corresponding temporal power spectra are coded with gray levels in the space-time plane, respectively in the space-frequency plane.

For flow parameter values for which the two wave systems coexist (see e.g. Fig. 4), UDA measurements with the P2 probe position have been realized at two different radii $r = 70$ and 120 mm in order to determine the axial structure of the flow disturbed respectively by the circular vortex system (central area) and by the spiral vortex system (peripheral area). At these radii and for $Re_R = 23.4 \times 10^3$ (N = 0.19 Hz), the temporal mean profiles $\langle v_\xi(\xi) \rangle$ are displayed in Fig. 5.a and 6.a. We recall that the ξ coordinate is equal to 0 on the stationary disk and to 1 on the rotating one. The axial component of the velocity being small in comparison with the tangential one, the features of the tangential velocity of the Batchelor flow are clearly recovered on these mean profiles. Thus, we can distinguish two boundary

layers (one on each disk) separated by a central core in which the gradient, versus ξ, of the velocity is nearly zero. For the same parameter values, Fig. 5.b and Fig. 6.b present the filtered signals of the velocity fluctuations $v_\xi(\xi,t)-\langle v_\xi(\xi)\rangle$ respectively in the circular waves ($r = 70$ mm) and in the spiral waves ($r = 120$ mm). Although the fluctuation amplitude is quite small, the periodic passages of the circular and spiral vortices are revealed by the gray encoding of the measurements. In both cases, these vortical structures located close to the stationary disk appear periodically in time (for $\xi < 0.5$) as alternate dark and light zones. The temporal power spectra of these fluctuations show one frequency peak called f_c for the circular waves and f_s for the spiral waves. The amplitude distributions along ξ of these temporal Fourier modes of frequencies f_c and f_s, referred as $A_c(\xi)$ and $A_s(\xi)$, are displayed in Fig. 5.c and 6.c. Both curves show clearly that the circular and spiral modes are located near the stationary disk. The distribution $A_s(\xi)$ (Fig. 6.c) presents one maximum at $\xi \approx 0.2$, contrary to $A_c(\xi)$ (Fig. 5.c) which vanishes at $\xi \approx 0.25$ which separates two maxima. Accordingly, we can see on the velocity fluctuation signals of Fig. 5.b, a layer around $\xi = 0.25$ where the fluctuations are nearly zero and which divides the perturbated area in two zones of same frequency f_c but with a phase difference close to π. Thus, the circular waves appear to be formed by a pair of vortical structures superposed on top on each other. Some visualizations of the flow in a radial plane realized by laser tomography (not presented here) confirm the existence of this double layer structure.

The raw and filtered velocity fluctuations of the radial velocity $v_r(r,t)-\langle v_r(r)\rangle$ in the external half of the flow ($r > 75$ mm) are displayed for two different Re_R in Fig. 7 and 8. These measurements are obtained with the P1 probe position. In Fig. 9, we present the temporal mean profile of radial velocity $\langle v_r(r)\rangle$ corresponding to the signal of Fig. 7 ($Re_R = 17.2\times10^3$). This mean profile shows the existence of a recirculation eddy at the periphery of the disk, near the stationary vertical side wall. This stationary recirculation eddy extends up to the point where the change of sign of the radial velocity occurs, here at around 135 mm. Such a recirculation has also been detected by Oliveira *et al.* (1982) in the case of an open rotating system. Vizualisations by laser tomography in a radial plane has confirmed the existence of this recirculation zone which radial extension decreases with Re_R.

On Fig. 7, the velocity fluctuation signal shows the circular vortices for $Re_R = 17.2 \times 10^3$ (N = 0.14 Hz). These vortices appear near the periphery ($r \approx 135$ mm) travel towards the center with a decreasing phase velocity. For the considered case of Fig. 7, this traveling velocity evolves from 10 mm/s near the periphery to 4 mm/s at a radius of 80 mm. Then, we can see periodic pairings of two vortices on three which occur at a radius r of around 95 mm. Therefore, at this radius we see the disappearing of one vortex on three. At a smaller radius, $r < 75$ mm (outside the measure area), secondary pairings that merge vortices two by two this time, have been observed by flow visualization. These pairings appear as space-time dislocations of the flow patterns as it can be verified on Fig. 7 at a radius $r \approx 95$ mm. On the corresponding power spectrum (Fig. 10) the dominating frequency f_c associated with these traveling cirular waves is, for $r > 95$ mm, equal to 0.42 Hz. This value is exactly three times the rotation frequency N of the disk. Then, for $r < 95$ mm, f_c is equal to twice the rotation frequency N. For radii less than 85 mm, the level of noise in the signal is too important to distinguish the frequency peaks which lead to secondary pairings and finally to $f_c = N$.

The velocity fluctuation signal of Fig. 8 shows, for $Re_R = 34.5 \times 10^3$ (N = 0.28 Hz), the coexistence of the two wave systems : the circular waves for $r < 105$ mm and the spiral ones for $r > 105$ mm. The opposite slopes of the traces of these two wave systems confirm the opposite sign of their radial phase velocity. Due to the frequency difference between the two wave systems, periodic dislocations occur at a radius around 105 mm, as it can be observed for t between 20 s and 30 s. The corresponding power spectrum is presented in Fig. 11. Now, the circular waves appear for a smaller radius than previously (Fig. 7), and at a frequency $f_c = 0.56$ Hz $= 2N$. We distinguish in the peripheral area ($r > 105$ mm) a peak at $f_s = 0.59$ Hz, clearly different and slightly higher than the frequency $f_c = 2N$ and corresponding to the traveling spiral vortices. The evolution with the rotation frequency N of dominating frequency f_s in the external area, associated with these spiral vortices, is displayed in Fig. 12. By comparing these evolutions for experimental series with increasing (O) and decreasing (+) N, we can see a significant difference at the same N. Thus, this diagram shows obviously a hysteresis in the spiral wave mode. We observe also frequency jumps, at N between 0.28 and 0.30 Hz for increasing N or between 0.31 and 0.29 Hz and between 0.23 and 0.21 Hz for decreasing N. These jumps separate N ranges where f_s evolves quasi-linearly

with N and which could correspond to changes of the number of spiral vortices on the disk circumference.

When the rotation frequency is further increased, we observe at the periphery of the disk, the appearance of new frequency peaks, as it can be seen in Fig. 13 for $Re_R = 39.4 \times 10^3$ (N = 0.32 Hz). Then, at higher Reynolds numbers, the number of peaks in the power spectra continues to increase, and the whole flow becomes more and more complex up to its turbulent state.

4

Conclusion

This experimental study shows that the flow between a rotating and a stationary disk shrouded by a stationary cylindrical housing is, at least in the central part, of Batchelor type in the sense that it consists of two boundary layers, one on each disk, separated by a core in which the azimuthal velocity is constant. At the periphery of the disks, we observe also the presence of a recirculation eddy. This circular roll may play a role in the destabilization of the whole flow. For the aspect ratio value considered here, the primary instability occurs near the stationary disk. It gives rise to the formation of a traveling vortex system constituted by double layer circular structures. The frequency f_c associated with this system is locked on the rotation frequency N of the rotating disk. In fact, it evolves from 3N at the periphery, to 2N for intermediate radii and finally to N near the center of the disk. These changes in frequency occur via pairings of vortices. It is noteworthy that such a frequency variation, with the same frequency ratios (1, 2/3 and 1/3), has also been observed in the numerical simulations of Cousin-Rittemard (1996), for axisymmetrical instability modes traveling in a toric cavity. When the Reynolds number is increased, a secondary instability occurs in the form of a traveling spiral vortex system located near the stationary disk. We show that the selection of the mode associated with these traveling spiral vortices is subject to a significant hysteresis. Moreover, jumps are observed in the evolution with the rotation frequency N of the corresponding frequency f_s. These frequency jumps could result from discrete changes of the number of spirals present on the disk, due to an Eckhaus instability.

References

Cousin-Rittemard N (1996) Contribution à l'étude des instabilités des écoulements axisymétriques en cavité inter-disques de type rotor-stator. Thèse de Doctorat, Université Paris VI

Gauthier G; Rabaud M (1996) Pivate communication

Itoh M (1988) Instability and transition of the flow around a rotating disk in a casing. Toyota Report 36: 28-36 (in Japanese)

Itoh M (1991) On the instability of flow between coaxial rotating disks. ASME Boundary Layer Stability and Transition to Turbulence, FED 114: 83-89

Lopez JM (1996) Flow between a stationary and a rotating disk shrouded by a co-rotating cylinder. Phys Fluids 8 (11): 2605-2613

Oliveira L; Bousgarbiès JL; Pécheux J (1982) Etude expérimentale de l'écoulement entre un disque fixe et un disque tournant. C R Acad Sc Paris 294 Série II: 1163-1165 (in French)

Savas Ö (1983) Circular waves on a stationary disk in a rotating flow. Phys Fluids 26: 3445-3448

Savas Ö (1985) On flow visualization using reflective flakes. J Fluid Mech 152: 235-248

Savas Ö (1987) Stability of Bödewadt flow. J Fluid Mech 183: 77-94

San'kov PI; Smirnov EM (1984) Bifurcation and transition to turbulence in the gap between rotating and stationary parallel disks. Fluid Dyn 19 (5): 695-702 (Original article in Russian (1984) Izv Akad Nauk SSSR, Mekh Zhidk Gaza 5: 28-36)

Schouveiler L; Le Gal P; Chauve MP; Takeda Y (1996) Experimental study of the stability of the flow between a rotating and a stationary disk. In : Advances in Turbulence VI. Gavrilakis S et al. (eds.): 385-388, Kluwer Academic Publishers

Sirivat A (1991) Stability experiment of flow between a stationary and a rotating disk. Phys Fluids A 3 (11): 2664-2671

Takeda Y; Fisher WE; Sakakibara J; Ohmura K (1993) Experimental observation of the quasiperiodic modes in a rotating Couette system. Phys Rev E 47: 4130

Zandbergen PJ; Dijkstra D (1987) Von Kármán swirling flows. Ann Rev Fluid Mech 19: 465-491

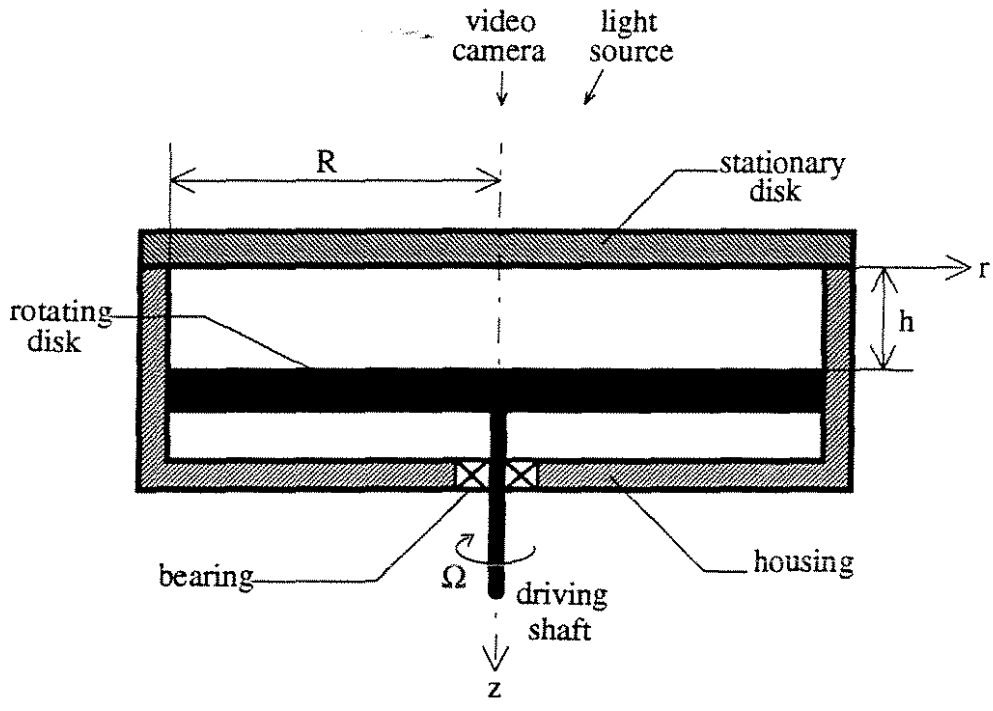

Fig. 1. Experimental apparatus

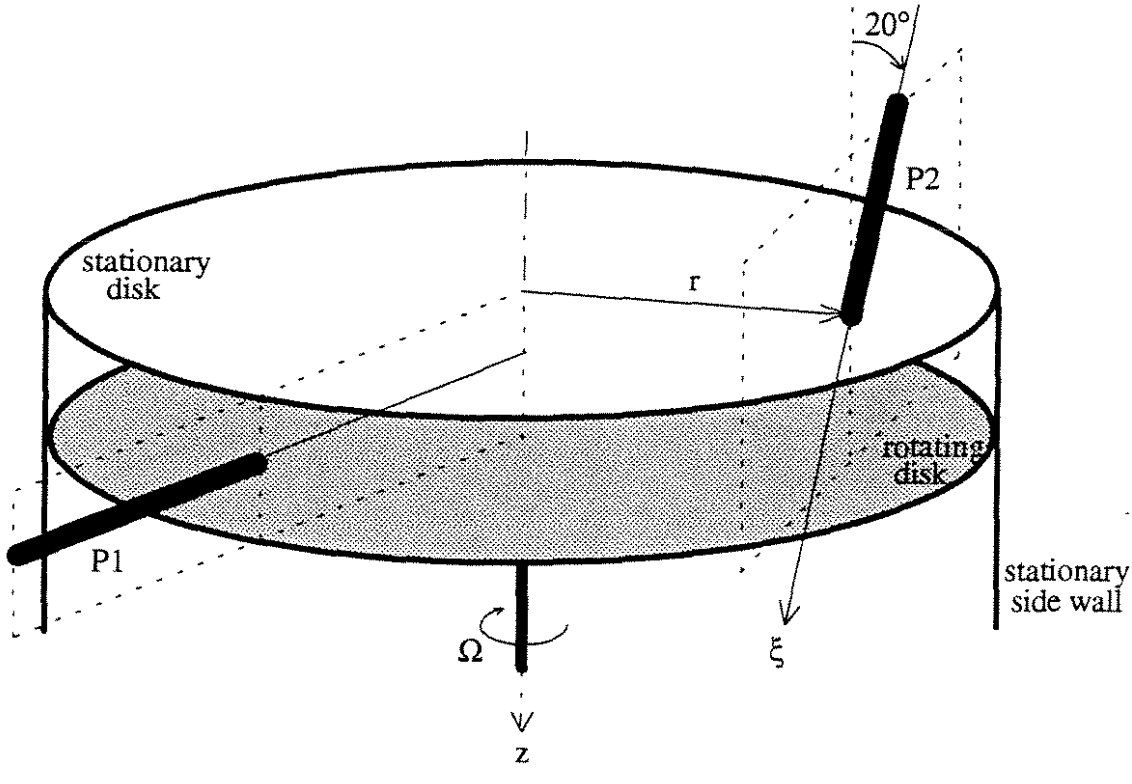

Fig. 2. UDA probe positions

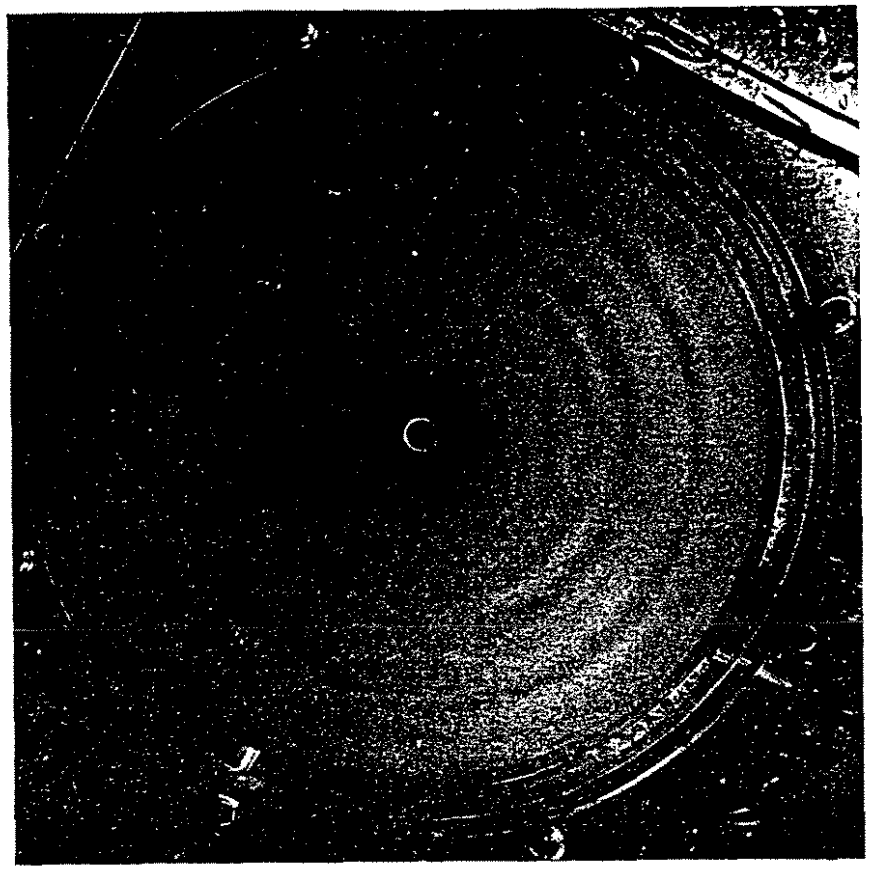

Fig. 3. Flow visualization : $\gamma = 11.43 \times 10^{-2}$, $Re_R = 16 \times 10^3$, $N = 0.13$ Hz. Clockwise rotation.

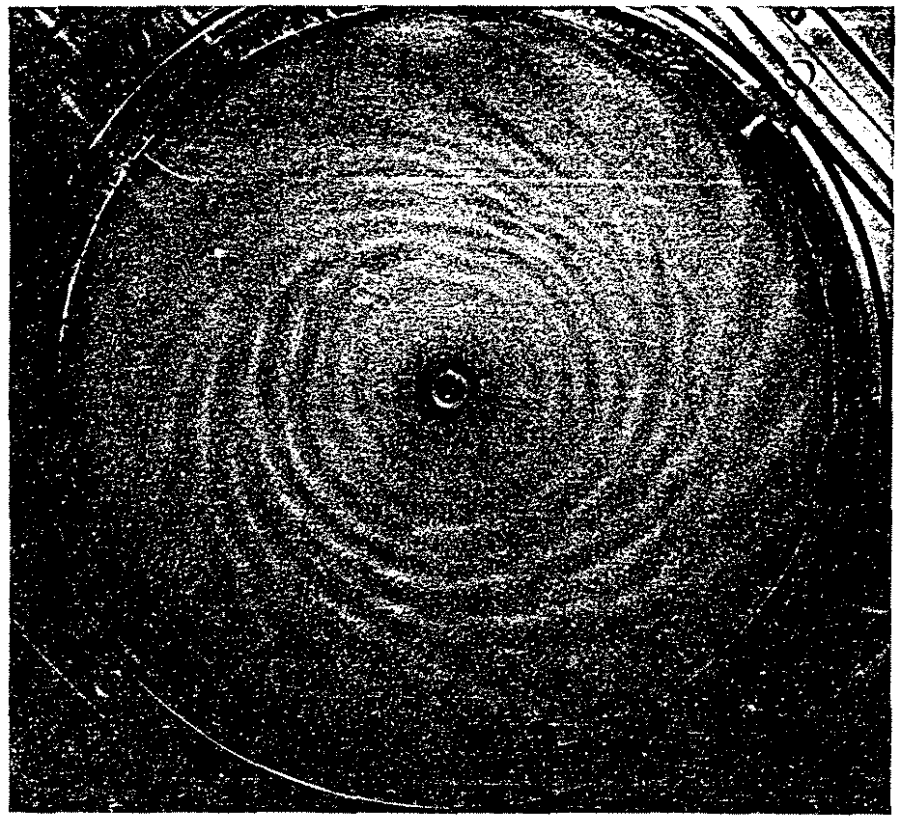

Fig. 4. Flow visualization : $\gamma = 11.43 \times 10^{-2}$, $Re_R = 28.3 \times 10^3$, $N = 0.23$ Hz. Clockwise rotation.

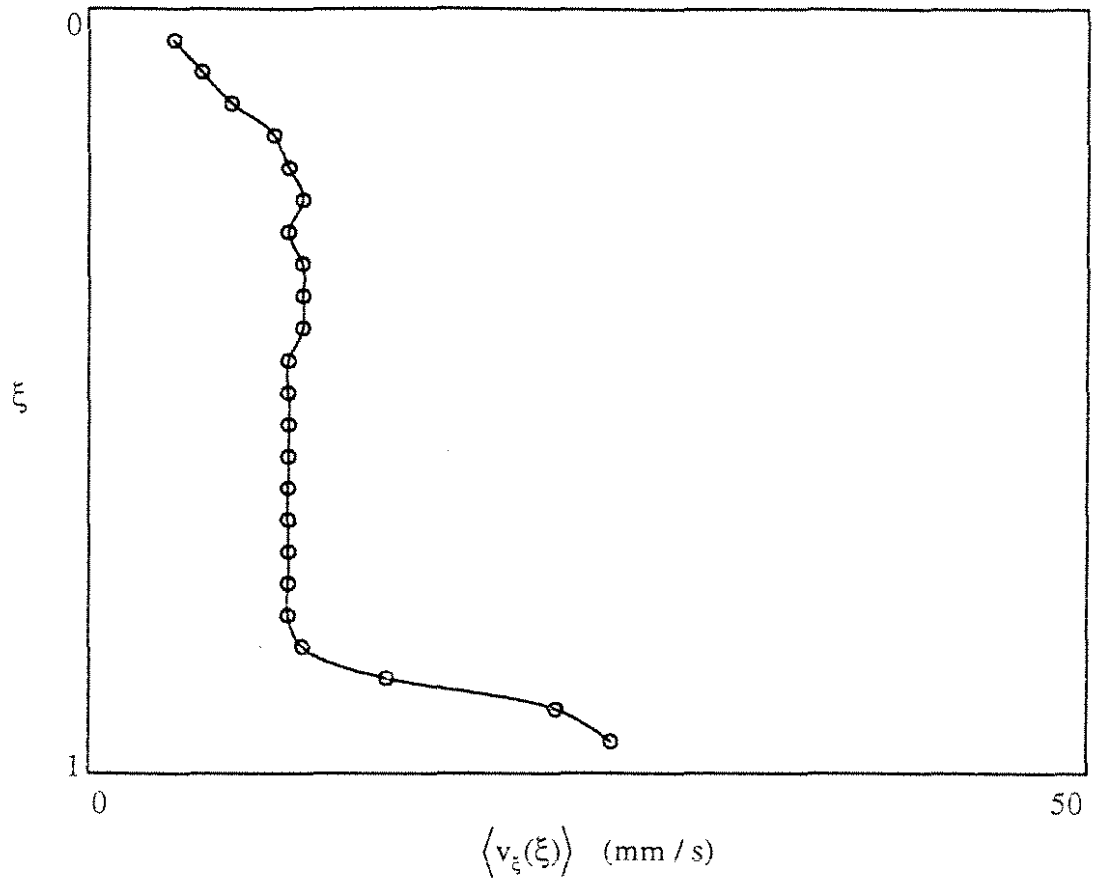

Fig. 5. $\gamma = 11.43 \times 10^{-2}$, $Re_R = 23.4 \times 10^3$, N = 0.19 Hz, r/R = 0.5. a. Temporal mean profile : $\langle v_\xi(\xi) \rangle$.

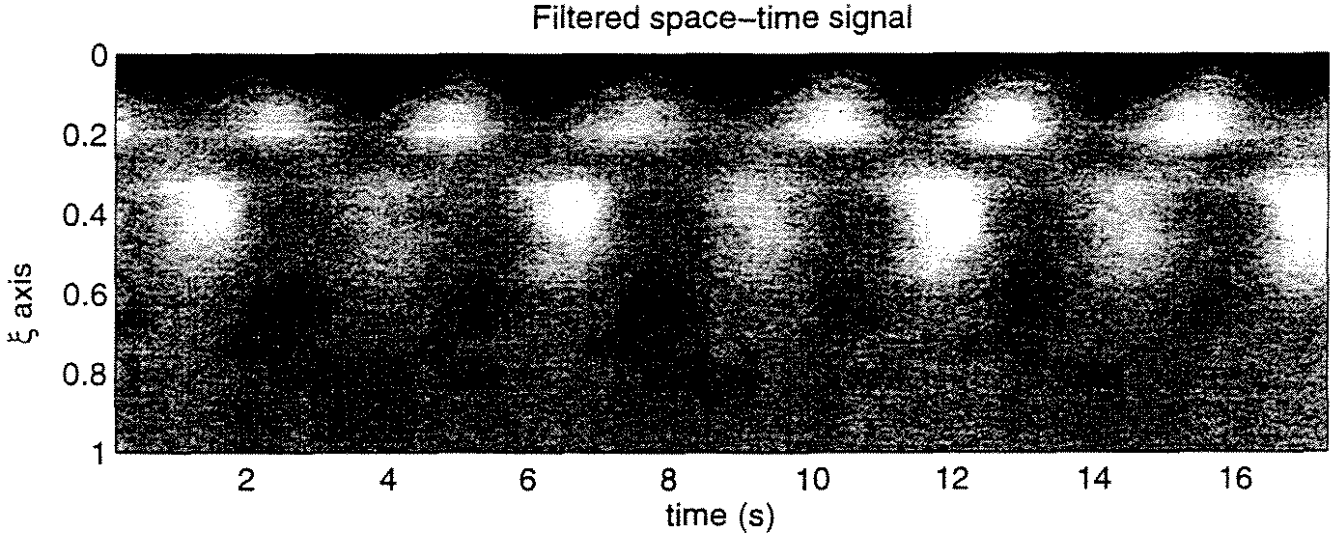

Fig. 5. $\gamma = 11.43 \times 10^{-2}$, $Re_R = 23.4 \times 10^3$, N = 0.19 Hz, r/R = 0.5. b. Filtered signal : $v_\xi(\xi, t) - \langle v_\xi(\xi) \rangle$.

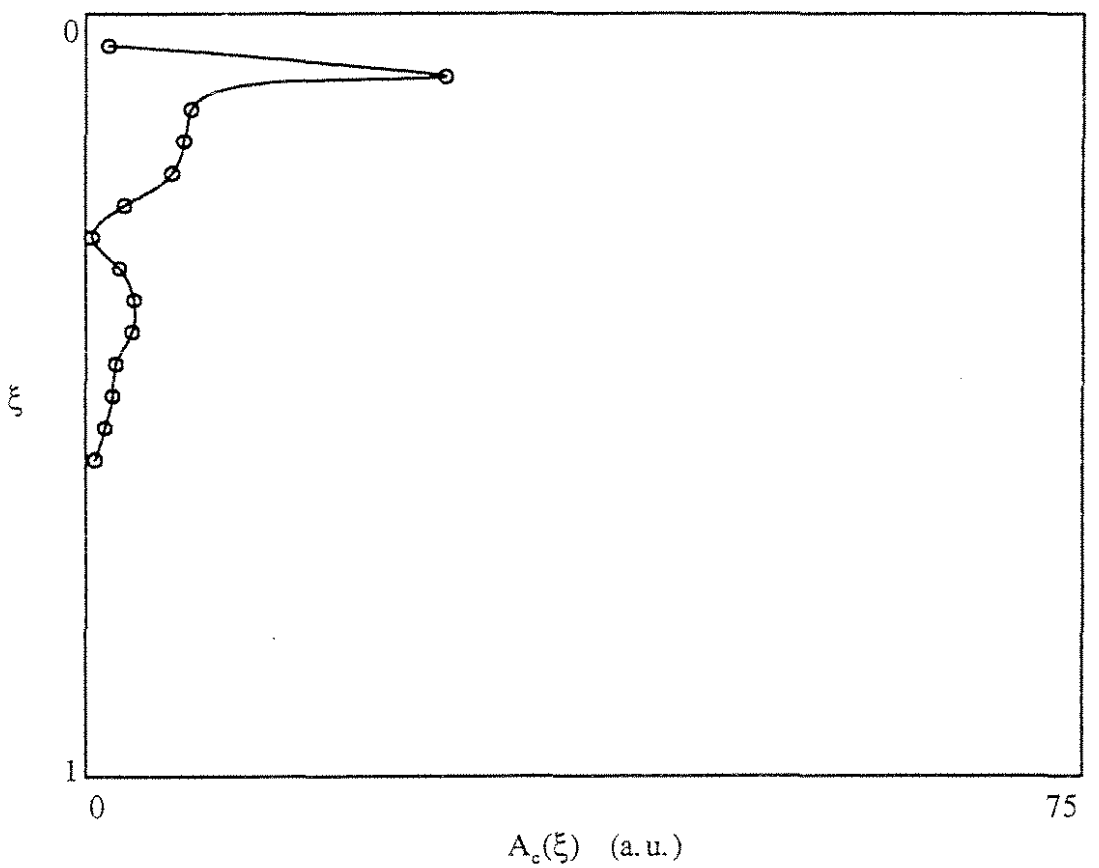

Fig. 5. $\gamma = 11.43 \times 10^{-2}$, $Re_R = 23.4 \times 10^3$, $N = 0.19$ Hz, $r/R = 0.5$. c. Amplitude $A_c(\xi)$ of the f_c Fourier mode.

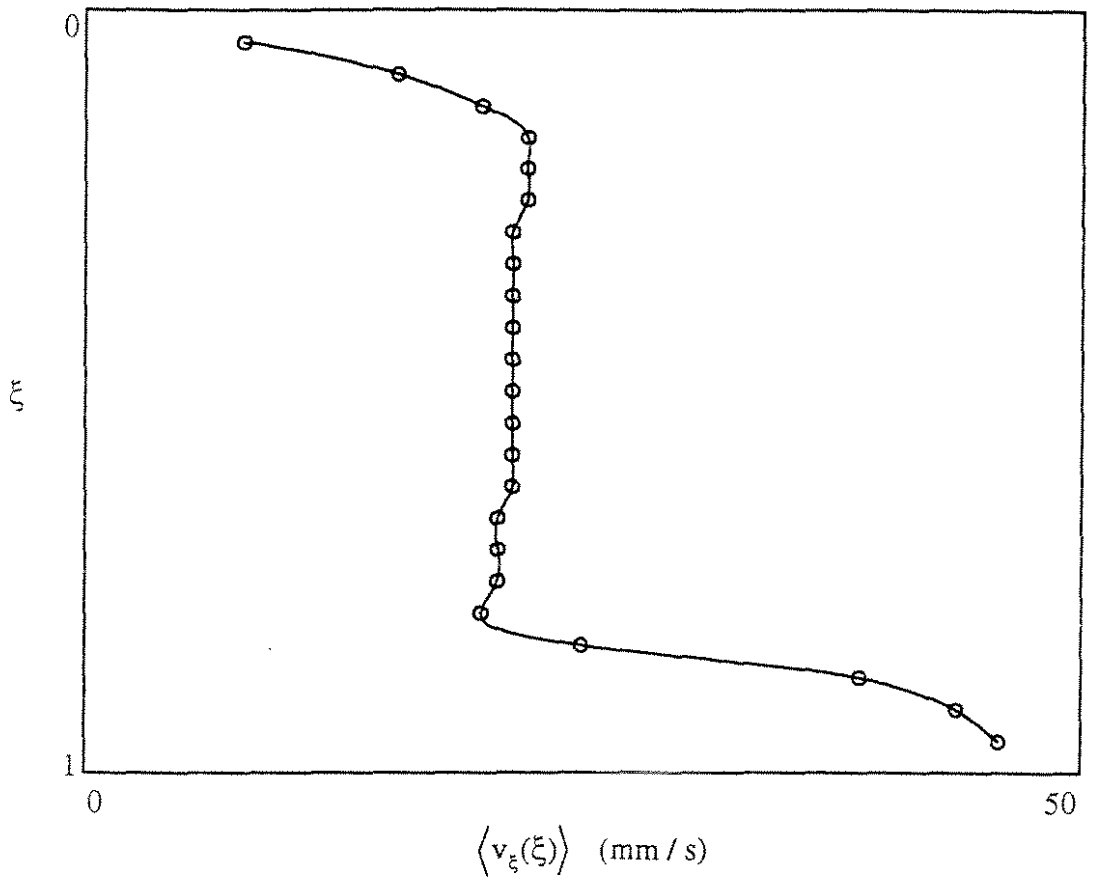

Fig. 6. $\gamma = 11.43 \times 10^{-2}$, $Re_R = 23.4 \times 10^3$, N = 0.19 Hz, r/R = 0.86.

a. Temporal mean profile : $\langle v_\xi(\xi) \rangle$.

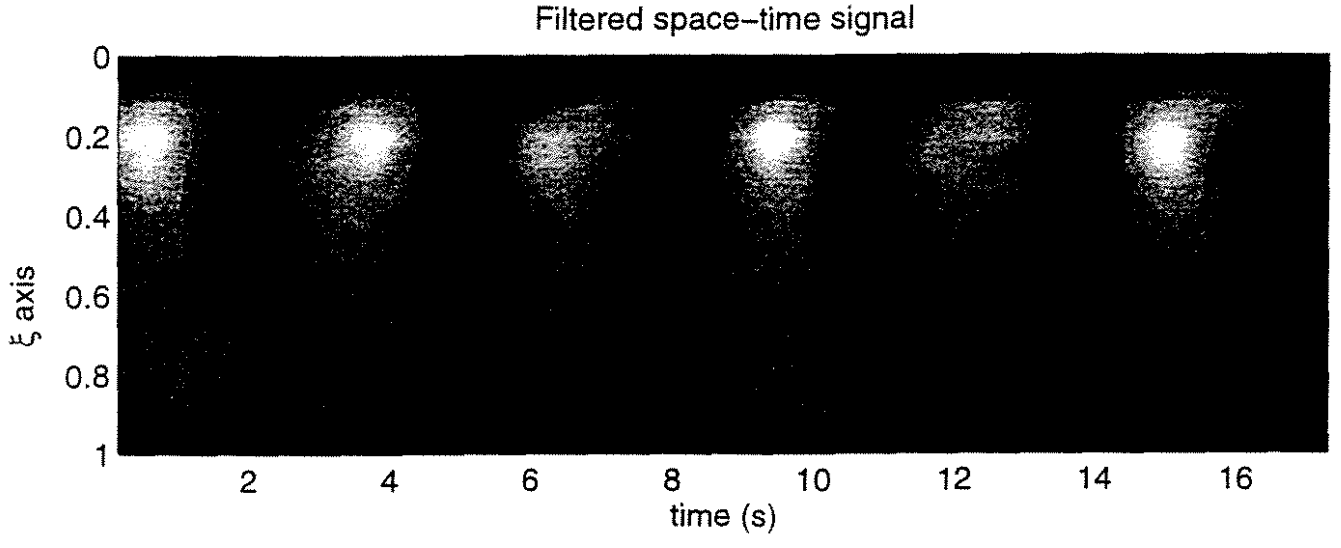

Fig. 6. $\gamma = 11.43 \times 10^{-2}$, $Re_R = 23.4 \times 10^3$, N = 0.19 Hz, r/R = 0.86.

b. Filtered signal : $v_\xi(\xi, t) - \langle v_\xi(\xi) \rangle$.

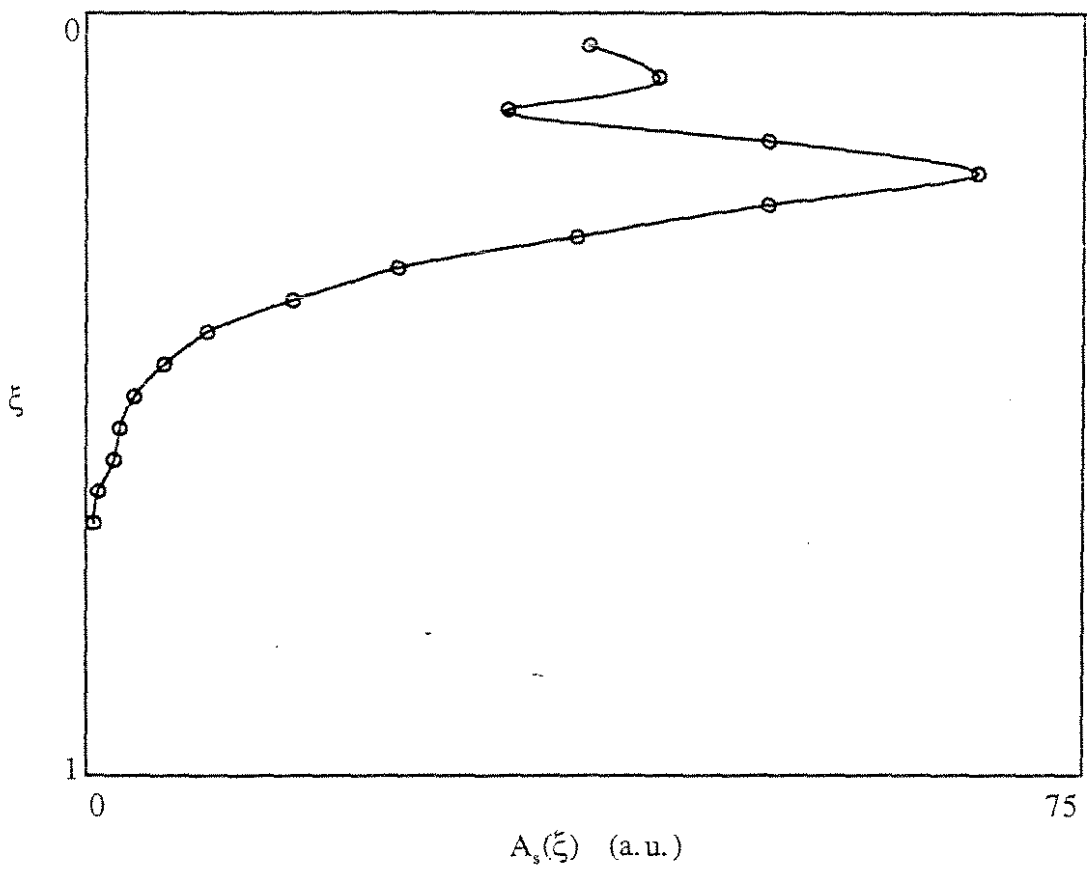

Fig. 6. $\gamma = 11.43 \times 10^{-2}$, $Re_R = 23.4 \times 10^3$, $N = 0.19$ Hz, $r/R = 0.86$.

c. Amplitude $A_s(\xi)$ of the f_s Fourier mode.

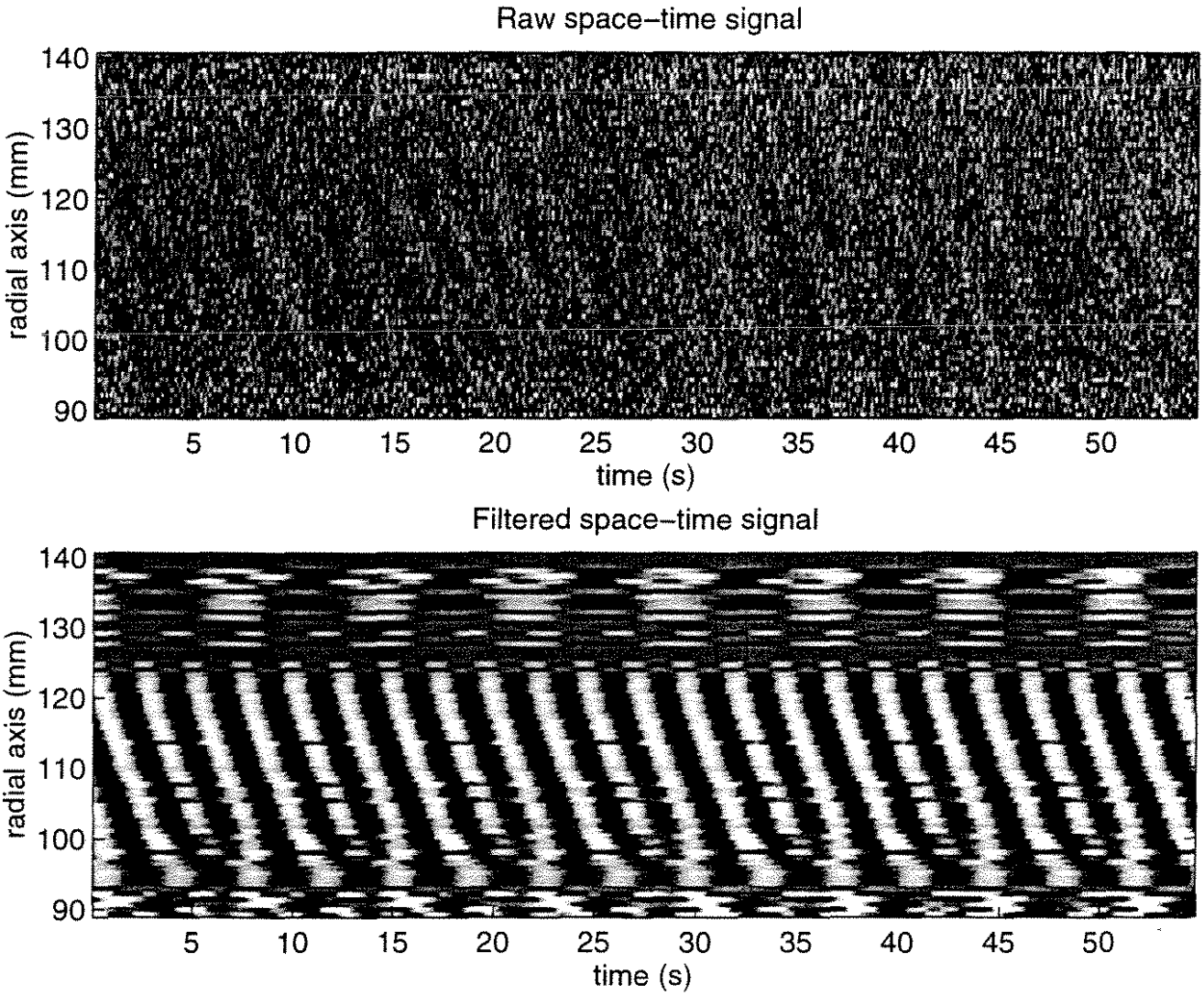

Fig. 7. $v_r(r,t) - \langle v_r(r) \rangle$ for $\gamma = 11.43 \times 10^{-2}$, $Re_R = 17.2 \times 10^3$, $N = 0.14$ Hz. Top : Raw signal, Bottom : Filtered signal.

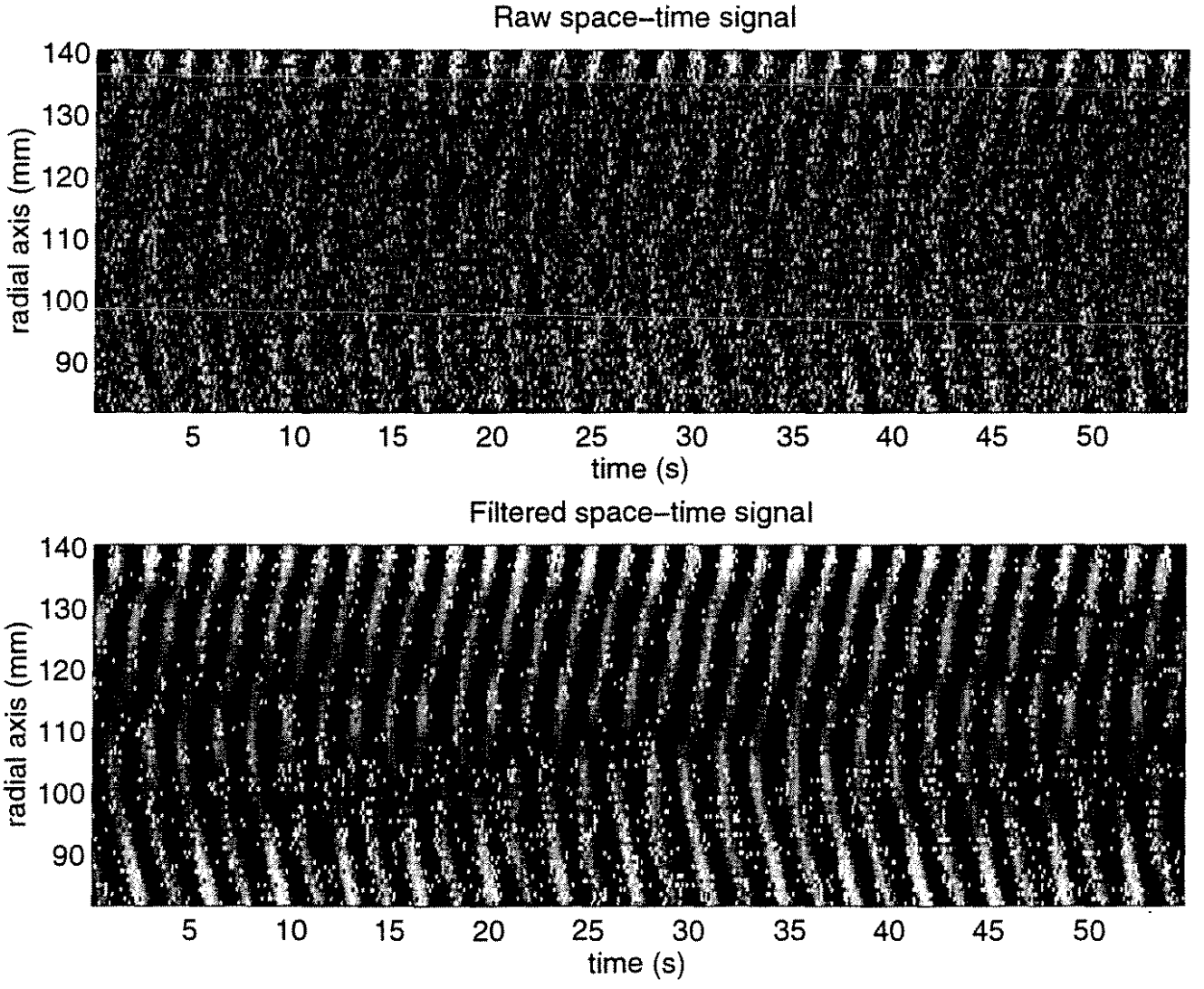

Fig. 8. $v_r(r,t) - \langle v_r(r) \rangle$ for $\gamma = 11.43 \times 10^{-2}$, $Re_R = 34.5 \times 10^3$, $N = 0.28$ Hz. Top : Raw signal, Bottom : Filtered signal.

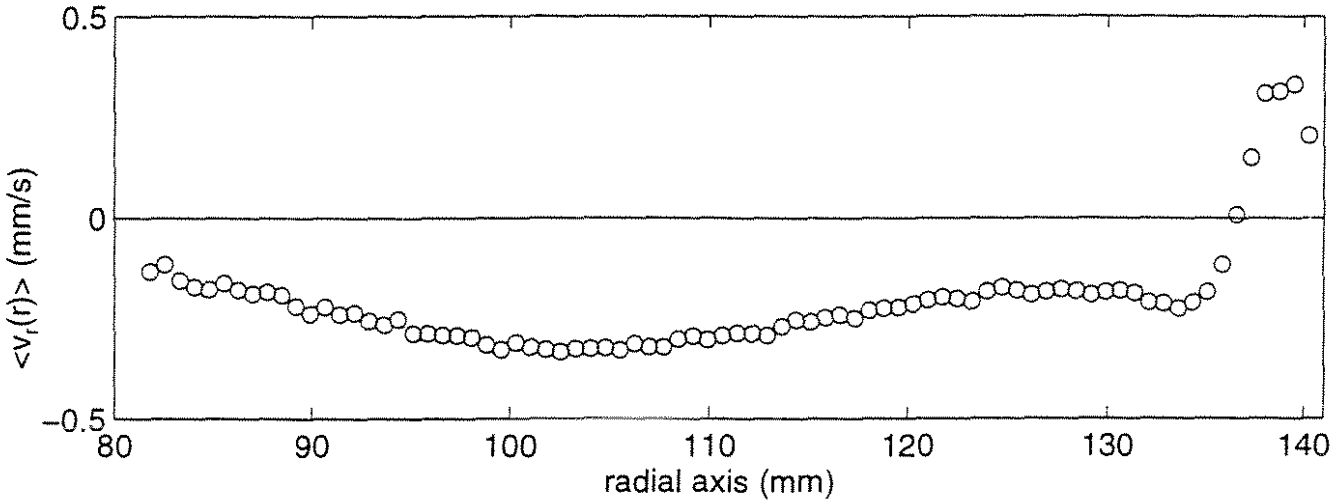

Fig. 9. Temporal mean profile $\langle v_r(r) \rangle$ for $\gamma = 11.43 \times 10^{-2}$ and $Re_R = 17.2 \times 10^3$, $N = 0.14$ Hz.

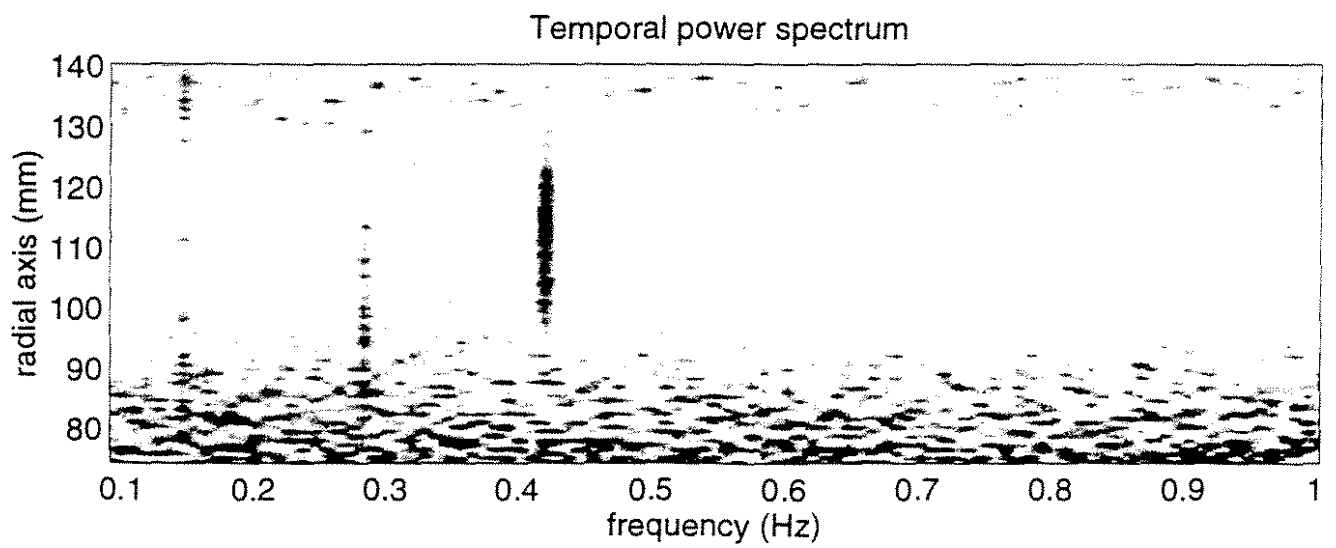

Fig. 10. Temporal power spectrum of $v_r(r,t)$ for $\gamma = 11.43 \times 10^{-2}$ and $Re_R = 17.2 \times 10^3$, $N = 0.14$ Hz.

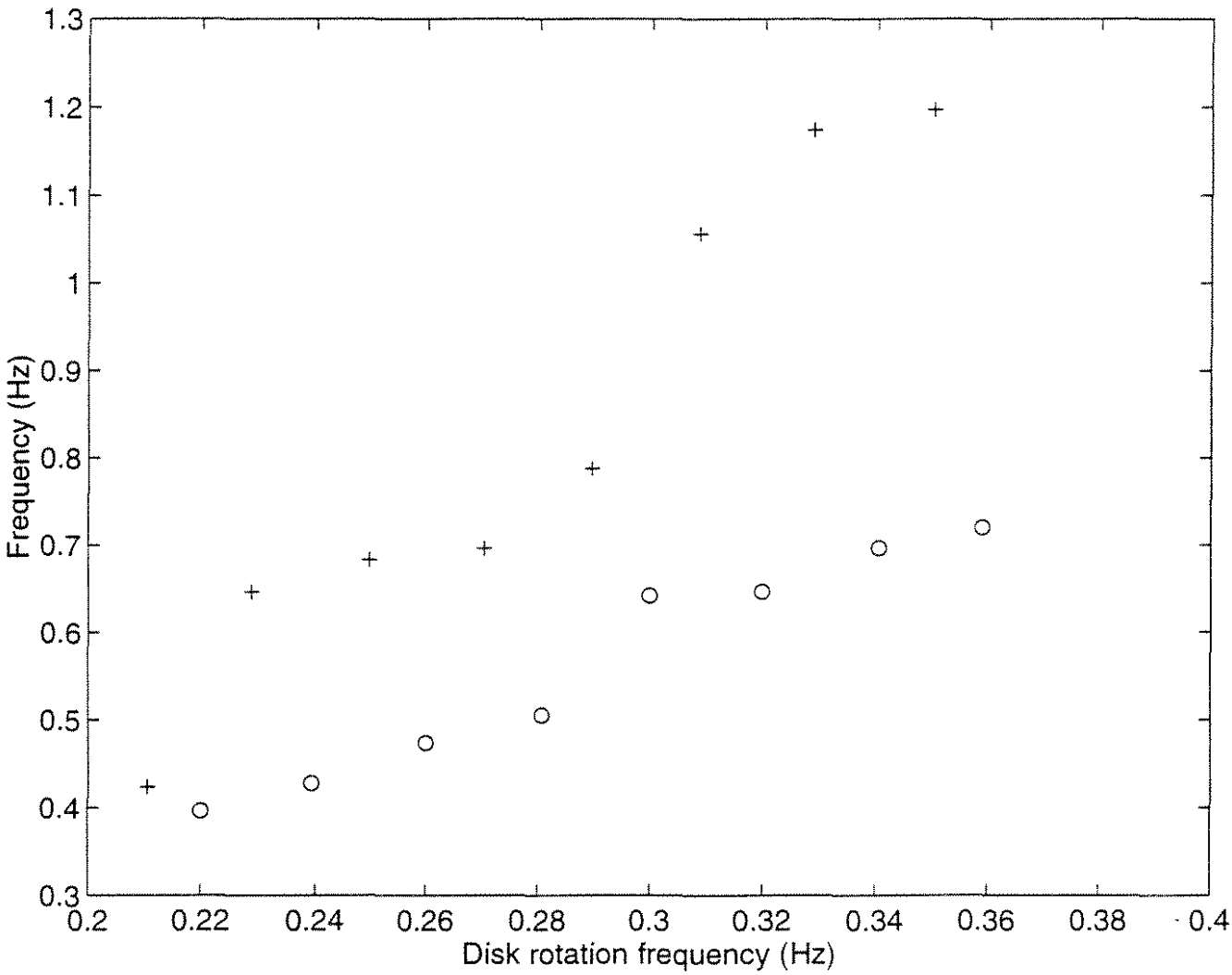

Fig. 12. Evolution of f_s with N : O. increasing, +. decreasing. $\gamma = 11.43 \times 10^{-2}$.

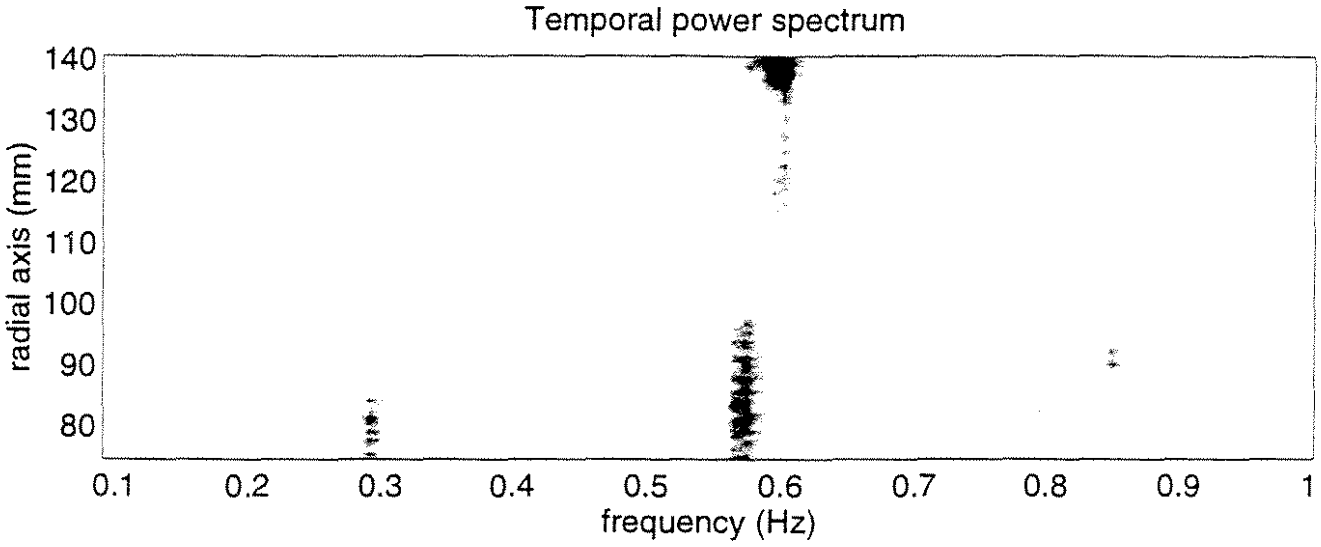

Fig. 11. Temporal power spectrum of $v_r(r,t)$ for $\gamma = 11.43\times10^{-2}$ and $Re_R = 34.5\times10^3$, $N = 0.28$ Hz.

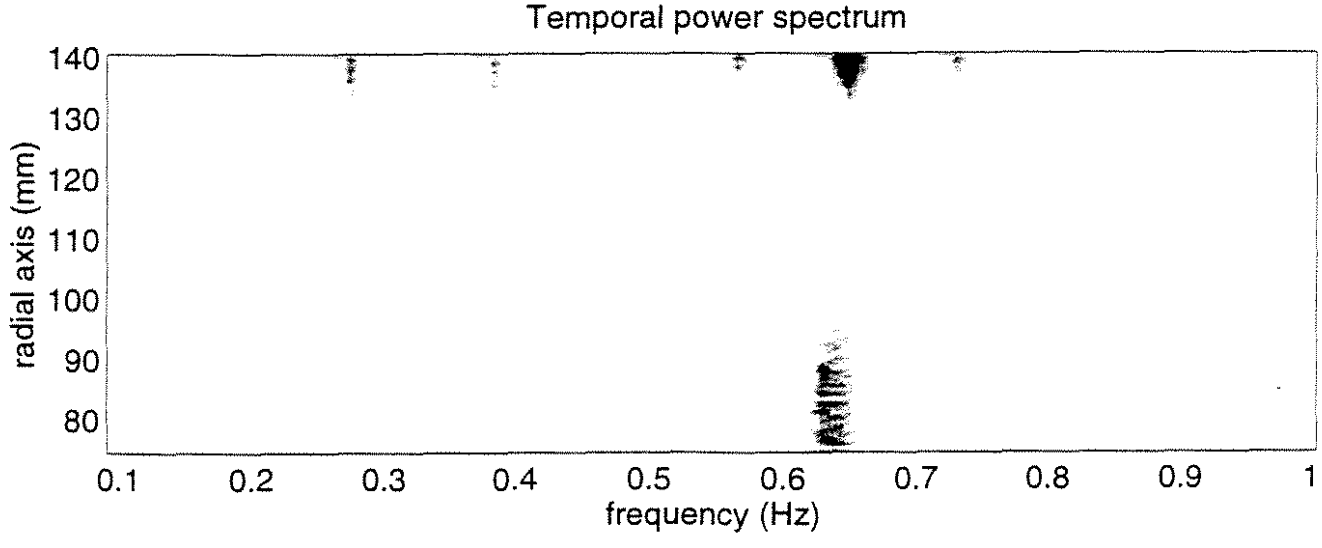

Fig. 13. Temporal power spectrum of $v_r(r,t)$ for $\gamma = 11.43\times10^{-2}$ and $Re_R = 39.4\times10^3$, $N = 0.32$ Hz.

Application of the ultrasound velocity measuring technique to stirred vessel flows

P. Wächter, W. Steidl, M. Höfken, F. Durst

performed at the

Institute of Fluid Mechanics of the Friedrich-Alexander-University Erlangen-Nuremberg

P. Wächter, W. Steidl[1], F. Durst

Lehrstuhl für Strömungsmechanik, Friedrich-Alexander-Universtät Erlangen-Nürnberg

Cauerstraße 4, D-91058 Erlangen, Germany

Correspondence to: P. Wächter

[1] *Present address*: Invent Umwelt- und Verfahrenstechnik GmbH & Co. KG,

Am Weichselgarten 7, D-91058 Erlangen, Germany

M. Höfken

Invent Umwelt- und Verfahrenstechnik GmbH & Co. KG,

Am Weichselgarten 7, D-91058 Erlangen, Germany

Abstract This publication presents results of local velocity measurements in a stirred vessel obtained by means of ultrasound Doppler anemometry. The flow in a rectangular tank, equipped with a hyperboloid stirrer, was investigated with respect to the mean flow field, the

mean turbulence properties and the avarage characteristic length scales of turbulence. The ultrasound Doppler anemometry was utilized to demonstrate its applicability to stirred vessel flows. The employment of this technique in the present work demonstrates its ease of use. Since the measurements result in velocity profiles rather than point measurements, the relevant velocity information could be obtained in short times.

Symbols

c	Sound velocity	m/s
C	Constant value in equation (9)	-
d_R	Stirrer diameter	m
f_0	Basic frequency of the UVP-monitor	s^{-1}
f_d	Doppler frequency	s^{-1}
f_{prf}	Pulse repetition frequency	s^{-1}
L	Ultrasound beam length	m
L	Macro value of turbulent flow	m
L_I	Integral length value in stirred systems	m
n	Revolutions per second	s^{-1}
N	Number of measuring points	-
Ne	Newton number	-
P	Power input of the stirrer	J/s
Re	Reynolds number	-
t_I	Integral time value	-
Tu	Degree of turbulence	-
U	Mean velocity	m/s
U_{Tip}	Circumferential velocity of the stirrer	m/s
u'	Rms-value of turbulent velocity fluctuations	m/s
V	Volume	m^3
z	Size of confidence interval	-
ε	Statistical error	-
ε_{ges}	Total specific power intake	m^2/s^3
ε_{loc}	Local energy dissipation	m^2/s^3
η	Kolmogorov microscale	m

λ	Taylor microscale	m
ν	Kinematic viscosity	m^2/s
ρ	Fluid density	kg/m^3
σ_x^2	Standard deviation	-
Λ	Macroscale of turbulence in stirred systems	m
Ω	Sampling rate	s^{-1}

1

Introduction

Stirred flow reactors are widely employed in process engineering with applications ranging from maintaining suspensions, production of emulsions through to improvements of mixing and enhancement of heat transfer. Convential design methods for stirred flow reactors employ integral information such as input energy, mixing time, etc. and scale-up rules to predict the performance of large stirrers from small scale experiments. It is only recently that advancements in numerical techniques and the increase in available computer power permit numerical predictions of stirred vessel flows. Such computer codes solve the time averaged Navier-Stokes equations (Reynolds equations), extended by turbulence models to close the resulting set of partial differential equations. The solutions of these equations provide local information on time averaged mean flow and turbulence properties. In the case of predictions of stirred vessel flows, local turbulence information results (see e.g. Kresta and Wood (1992), Yianneskis et. al. (1987, 1993, 1994), Höfken (1994)), which can extend empirical correlations of stirred vessel flows, e.g. as provided by Nicolaus (1961). However, the turbulence models employed for numerically predicting the flow, contain model assumptions, which need to be experimentally verified in stirred vessel flows.

To investigate the velocity field of stirred vessel flows, a multi-purpose mixer test facility has been designed, manufactured and put into service at *LSTM*-Erlangen. It is equipped with

an ultrasound Doppler anemometer and features also a flow visualisation facility employing the laser light sheet technique. The test rig can be used to experimentally study various stirrers in detail and to carry out flowvelocity measurements to obtain a database for the validation of numerical simulations. It is demonstrated in this paper that the ultrasound Doppler technique is suitable for obtaining detailed and comprehensive experimental velocity profile data in stirred vessel flows.

The ultrasound Doppler technique, as it stands today, can not compete with laser Doppler anemometery with respect to the spatial resolution of the measurements, but the technique shows a variety of other advantages that makes it interesting to stirred vessel flows. No optical access to the measuring volume is necessary and so the probe can be set outside an optically non-transparent wall. It also can be applied to opaque fluid flows. Furthermore, the employment in tanks of an industrial scale is possible because the available ultrasound probes are water resistant and can be immersed in most measuring fluids. An ultrasound Doppler anemometer can also obtain a complete velocity profile over the penetration length of the ultrasound beam which helps to reduce the measurement time.

The present paper is written to document the authors' investigation of stirred vessel flows with the METFLOW S.A. UVP-Monitor, a commercially available ultrasound Doppler velocimeter. In chapter 2 the test facility, the water tank and the stirrer that were used are explained. Chapter 3 deals with some basic information about ultrasound Doppler anemometry, the accuracy of the measurements, and the evaluation of the data by special software. The results of the investigations, i.e. the flow field and the turbulent properties, are shown in Chapter 4. This paper will close with some conclusions derived from the presented results.

2

Test facility and stirrer

In recent years laser Doppler anemometry has proven to be the most precise and reliable measuring technique for highly turbulent flows which occur in stirred vessels, more accurate than other techniques such as Pitot probes and hot wire anemometers. But a standard LDA system results only in flow information at a single measuring point, i.e. time traces of a local velocity. This is disadvantageous where velocity information is needed in the entire flow field. For this purpose, the LDA-measuring volume needs to be traversed and the resultant flow field information is provided by a sequence of point measurements. This is time consuming. It is therefore desirable to use techniques that provide "profile information", rather than "point information" of the velocity field. The ultrasound Doppler velocimeter is a technique of this kind, providing in a short time the entire velocity profile along the ultrasound beam. Hence, the application of this technique to stirred vessel flows should result in shorter measuring times, but might result in velocity information of less temporal and spatial resolution.

To demonstrate the applicability of the ultrasound Doppler technique in stirred vessel flow and quantify its resolution, the present study was performed. A multi-functional test rig for stirred vessel flow investigations was set up at *LSTM*-Erlangen and equipped with laser light sheet optics to permit flow visualization of the overall flow field in the rectangular water tank. A sketch of the test facility is given in Figure 1, showing the main components of the tank, the light sheet glass fibre optics and the Ultrasound Velocity Profile (UVP) Monitor X-1.

2.1

The water tank

The internal dimensions of the experimental vessel were 1,750 mm x 400 mm x 550 mm. The Plexiglas vessel had a wall thickness of 25 mm. It was seperated into two sections by a dividing wall, which could be set to any desired position, so that practically any rectangular vessel geometry could be achieved. The tank was constructed in such a way to have the opportunity of studying different tank geometries, as they are used in waste water treatment plants, but at a model scale. With this test rig it is possible to determine the necessary rotational speed of stirrers to fulfil a desired mixing task, e.g. to keep particles homogeneously suspended. Furthermore, it is possible to determine the number of stirrers which should be employed in a longitudinal tank with respect to the investment and the running costs. In the present investigation a square vessel of dimensions (T x T x H) 400 mm x 400 mm x 500 mm was chosen.

On one longitudinal and one lateral side of the vessel, aluminium rails were mounted above and below, that allowed the mounting of brackets to hold the UVP transducer and to traverse it to every required position.

The x, y and z components of the velocity vectors were determined in nine horizontal measurement planes of 8 x 8 measuring points. The locations of the individual measuring points can be seen from Figure 2 below. The coordinates of the measuring points on each axis were set as follows in Table 1.

The front left-hand corner of the experimental vessel was chosen as the coordinate origin. The x-axis ran along the length of the vessel and the y-axis represented the width. Due to symmetry, only one quarter of the vessel was measured. For the evaluation it was possible to apply these measured data to the entire vessel.

2.2

Stirring technique

A hyperboloid stirrer of the diameter D= T/4= 100 mm (Figure 3) was used in the experiments. The stirrer body, milled out of brass, was mounted on a steel shaft centered in the vessel. The clearence to the vessel's bottom was C= D/10= 10 mm. This stirring element is mainly used to suspend particles, where most of the energy brought into the fluid is needed to remove solids from the bottom. Therefore the above mentioned ratios with the comparatively low clearence proved to be very effective, because the energy is input into the part of the tank where it is required. The induced flow remains attached to the upper surface of the stirrer body. Hence, separation and resulting energy losses are minimized. The stirrer body was equipped with 8 transport ribs, which protrude 2 mm from the surface of the stirrer.

The required stirrer speed was set through the output voltage of the power supply (Gossen, SSP-Konstanter 62 N). This value was monitored by an encoder on the shaft of the electric motor Type E644 of the Electro Craft Cooperation.

A constant stirrer speed of 573 rpm was used for the measurements, which corresponds to a circumferential tip speed of 3 m/s. A Reynolds number of 95,500 was achieved by using water as test fluid. This velocity has shown to be sufficient to remove sludge from the bottom of the tank and to keep it suspended. This system has proven to be suitable for simulating the flow field of activated sludge basins in waste water treatment plants.

3

The ultrasound Doppler anemometry

Detailed characterization of the stirrer/stirred vessel system requires explicit knowledge of the mean and the turbulent flow field in the stirred vessel. This places high demands on the accuracy of the measuring system.

Similar to laser Doppler anemometry, the ultrasound Doppler anemometer, measures the local velocity by determining the Doppler shift caused by slip-free particles in the fluid. In contrast to LDA methods however, by using different time windows, measurements can be taken at several successive points along the ultrasound beam. The ultrasound signals are transmitted by a transducer and received again after reflection from the scattered particles. This measuring principle of ultrasound Doppler anemometry is shown schematically in Figure 4.

3.1

Basic principles of the ultrasound Doppler anemometry

In the following some fundamental background of the ultrasound Doppler anemometry is given, in particular, that there is a limitation in the maximum measureable velocity and the penetration length, which is inherent to the measurement technique. Other effects like the absorption of the ultrasound in solids and fluids, which also reduce the penetration of the beam and lead to a decreasing signal to noise ratio, are not discussed here.

The Doppler shift f_d is directly related to the velocity component U of the respective scattered particle, which is aligned with the beam propagation direction. The flow velocity can be determined without the need for further calibration of the measuring instrument, provided the velocity of sound in the fluid is known.

$$U = c \cdot \frac{f_d}{2 \cdot f_0} \qquad (1)$$

The measuring beam is effectively subdivided into successive measuring points by way of the fact that the device measures the Doppler shift frequency at different time instances following transmission of the ultrasound signal. The maximum penetration depth, i.e. the maximum measuring length over which a total velocity profile can be acquired is limited by the pulse repetition frequency f_{prf} and the signal to noise ratio:

$$L_{max} = \frac{c}{2 \cdot f_{prf}} \tag{2}$$

To obtain a single profile, 128 pulses are provided and evaluated for each measuring point. In order to fulfil the Nyquist sampling criterion for determining the Doppler frequency, which is done by a Fourier analysis, at least two pulses are required per period. For the maximum detectable Doppler frequency

$$f_{D_{max}} < \frac{f_{prf}}{2} \tag{3}$$

applies and therefore also the maximum measurable velocity is dependent on the pulse repetition frequency

$$U_{max} < \frac{c \cdot f_{prf}}{4 f_0} \quad . \tag{4}$$

A common criterion is therefore obtained which demonstrates the dependence of the maximum measurable velocity on the measuring length:

$$L_{max} \cdot U_{max} < \frac{c^2}{8 \cdot f_0} \tag{5}$$

This shows that large penetration depths can only be obtained at the cost of the maximum measurable velocity.

3.2

Analysis of the accuracy of UVP measurements

Statistical independence

In the case of measurements in turbulent flow, it is extremely important to ensure the statistical independence of the measured values, otherwise errors can occur in the calculation of average values and the turbulent fluctuations (rms value). The statistical independence is checked, according to Tropea (1993), using the integral time scale of the typical large-scale flow variations. For the fluid mechanics problem under investigation here, a characteristic length of L_1 = 100 mm corresponding to the diameter of the stirrer element used and a characteristic speed of U_{Tip} = 3 m/s corresponding to the circumferential tip speed of the hyperboloid stirrer were assumed. The integral time scale is therefore obtained as follows:

$$t_1 = \frac{L_1}{U_{Tip}} = \frac{0{,}1 \ \ [m]}{3{,}0 \ \ [m/s]} = 0{,}033 \ \ [s] \tag{6}$$

The integral time scale has the following characteristics:

- Signals at intervals of 2 t_I contribute to the average value as a single, statistically independent measured value.
- Signal values only become statistically independent when a period of 2 t_I lies between them.

The maximum sampling rate Ω, at which statistically independent velocity values are acquired, is obtained from these conditions as

$$\Omega = \frac{1}{2 \cdot t_I} = 15 \quad [\text{Hz}] \quad . \tag{7}$$

The time resolution of the measurements, calculated using the pulse repetition frequency for the 128 pulses, is 65,5 ms for the selected penetration length. For realizing a real-time data analysis, the time interval between two measurements is 69.8 ms or 14.3 Hz respectively. If this value is compared with the maximum sampling rate Ω, it becomes apparent that the velocity values obtained are statistically independent.

Statistical error

The following equation applies for the statistical error in the velocity measurement, according to Tropea (1993):

$$\varepsilon = \sqrt{\frac{z^2 \cdot \sigma_x^2}{N}} \tag{4}$$

This includes the standard deviation σ_x^2, which is obtained from the rms value; the number of measuring points N; and a factor z that characterizes the size of the confidence interval. With a confidence interval of 96 %, i.e. for z = 2 and an rms value measured in close proximity of the stirrer of 150 mm/s, the statistical error ε is specified in Table 2 for different values of N. For the relative error with respect to the maximum measurable velocity value (which was 181 [mm/s] in the measurement mentioned above, in close proximity of the stirrer), the relationship to N is given in Table 3.

3.3

Evaluation software

A flow chart of the evaluation procedure is shown in Figure 5, naming also the programmes used. The programmes printed in italics were developed specifically at the Department of Fluid Mechanics for the 3-dimensional presentation of results. This was necessary to obtain a graphical representation that allows a comprehensive insight into the fluid flow.

The programme *uvpgraph* allowed a fast evaluation of the binary data obtained by the Ultrasound Velocity Profile Monitor. The velocity and the rms value were calculated for every measuring point. It took into consideration that the sound veloctity in the wall differed from that in the fluid. The programme *quad2tec* had mainly the task to provide the data format which was needed for TECPLOT, a commercial software of Amtec Engineering, Inc., to visualize data records.

4

Results of the ultrasound Doppler measurements

With the ultrasound velocity technique, described in section 3, the entire velocity field was mapped out. To obtain the result that were presented in the following, a total of 2,200 separate profiles were recorded which involved a measuring time of 55 hours. From these separate profiles, 208 average velocity profiles were then calculated from which the relevant velocity components could be correlated to the 576 individual measuring points.

4.1

Graphical presentation of the flow field

The results measured with the UVP monitor were subdivided into different horizontal and vertical planes that could be displayed individually using the commercial post-processing software TECPLOT.

The velocity field for the flow was described on the one hand using vectors for a clear picture of the flow direction. On the other hand, the values of absolute velocity with respect to the circumferential speed of the stirrer were presented as coloured contoured surfaces that provide an overview of the global velocity distribution. When the fluid velocity relative to the stirrer circumferential speed are plotted, the velocity distribution for the measured geometric form is obtained independently of the stirrer speed. In highly turbulent stirred flows the average velocity and the turbulent fluctuations are directly proportional to the stirrer speed, so this allows the absolute velocities to be determined for any rotational speed in the area of turbulence. In addition, the values for the relative fractions of velocity components with respect to the absolute velocity was displayed as a coloured contoured surface in order to restore the velocity impression in the depth of a plane that had been lost in the two-dimensional vector representation of the plane.

A presentation in the form of coloured contours was also used for evaluating the local energy dissipation because this variable is a scalar and has no direction and cannot therefore be displayed in vector form.

The results for the horizontal planes are depicted on the following pages. It can be seen from the *vector presentation* (Figure 6) of the floor level that the stirrer drives the fluid right into the corners at a relatively high velocity whereby with careful design the deposit of solids in the corners can be prevented. If this corner flow is traced further in the subsequent plane, it is illustrated that a flow forms close to the wall that runs in the opposite direction to the main flow. This flow arose due to the strong axial flow in the corners following diversion of the floor flow to the vertical. With increasing height, this effect loses significance and the flow gradually transforms into a rotational flow about the stirrer axis. In planes z = 164 to z = 346, the horizontal projection of a vortex with the stirrer shaft at its centre is shown.

From a glance at the presentation of the *relative axial velocity* (Figure 7), in the central planes, the areas of increased axial flow can be seen clearly that form around the stirrer shaft. In these areas, the fluid was flowing back towards the stirrer. The other significant areas with a high axial flow component are the corners. These high relative velocities in the corners are found as far up as the upper planes; so even in the case of tall vessels, the hyperboloid stirrer can provide good stirring effects.

The graph of *relative velocity* (Figure 8) in the various horizontal levels shows that at a height of 34 mm, i.e. only 26 mm from the floor level, the flow velocity became significantly smaller. From the velocity distribution in the planes z = 34 mm and z = 60 mm, the areas of increased velocity at the edge of the vessel and in close proximity of the stirrer can be clearly distinguished. The high velocity at the wall was a result of the change in direction of the floor flow to the vertical. In the plane z = 60 mm, velocities of 0.03 x U_{tip}, i.e. 9 cm/s, were reached

here. The area of increased velocity around the stirrer was due to the return flow of the fluid driven upwards at the wall towards the stirrer. This is particularly clear in the presentation of *relative axial velocity* (Figure 7). In the planes z = 112 mm and z = 164 mm in Figure 7, the relatively low flow velocities in the two preceding lower planes are no longer present. These zones visible in form of dark blue coloured regions in the two lower planes presumably represent the vortex centres of the large scale vortex that forms in the lower corners. An evaluation of the vector presentation of the flow velocity for the vertical levels produced the value of approximately 70 mm for the horizontal distance of the vortex centre from the floor. In the subsequent planes, z = 216 mm and z = 268 mm, the high velocities at sections of the vessel wall can be detected again.

Whereas in the lower planes, these velocity peaks arose in a strip parallel to the x-axis, they were now found in an area parallel to the y-axis. The reason for this was presumably the upwards flow close to the wall overlapping with the clockwise rotating flow around the stirrer. This caused the velocity peak to move slowly in the direction of rotation of the stirrer. In the top two planes, z = 346 mm and z = 424 mm, the measured velocities had already fallen to a fifth of the maximum floor velocity. On the whole, in these planes, the measured velocities were distributed quite evenly over the entire plane.

The graph of the *turbulent velocity field* in the vertical direction (Figure 9) represents planes in a side view. In the plane y =7 mm, which shows the detail next to the wall, it can be seen clearly how the fluid was moved along the corners up to the surface. This upwards directed flow is along the whole wall visible even if it is not so marked in the heights of 346 mm and 424 mm. In a distance of 57 mm of the wall the above described ring vortex was formed in the lower left and right part of the vessel. These structures were becoming clearer and clearer with looking at the sequence of planes. The plane y =197 mm is nearly an intersection with the

stirrer shaft where the flow streams downwards along the shaft to be moved along the vessel's bottom to the wall and then again upwards to the surface. Because the coordinate y =200 mm is the middle of the tank the vector field is nearly symmetrical relating to the shaft.

From the presentation of the *local energy dissipation* (Fig. 10) it is clear that the largest portion of the input energy was concentrated in a ring-shaped area around the stirrer in the floor area. In the other areas, the energy input was significantly lower and remained practically constant over the entire height of the vessel. In the central planes, a value of around 1.0 was obtained for the local energy dissipation, i.e. the average energy component falling on this partial volume was transferred in its entirety, whereas in the upper levels the local energy input fell slightly as expected.

4.2

Interpretation of the results

The results show the applicability of the ultrasound Doppler anemometry to stirred vessel flows. The large-scale flow patterns generated by the hyperboloid stirrer were detected very well. Nevertheless there are some limitations, which restrict the obtainable information.

In the immediate vicinity of the stirrer, acoustic reflections of the stirrer and its shaft complicate the evaluation and interpretation of the signals. Also important to point out is the spatial resolution, which is given by the beam diameter, of more than 4 mm. As an example, the effect is shown in comparison with laser Doppler measurements in Figure 11. It concerns an angle-resolved measurement, which allows to take the periodic variations produced by the blades of the stirrer into account.

The intersection of the beams and hence the two dimensional plane of the measuring volume of the ultrasound Doppler measurements is marked. This graph explains why the

measuring points next to the stirrer in Figures 6 and 9 must not show the highest velocities. The vector presentation of the laser Doppler measurements makes clear that the fluid moves downwards before reaching the measuring volume of the ultrasonic Doppler measurement. Then the fluid flows along the bottom in the radial direction and spreads in a way, so that the high velocity is detected in the following measuring volume.

4.3

Determining the turbulence variables

The local energy dissipation in a stirred vessel can be determined via the constant C that takes on a characteristic value for the stirrer/stirred vessel system as follows Brodkey (1975):

$$\varepsilon_{loc} = C\frac{u_i'^3}{d_R} \tag{5}$$

Where the constant C can be calculated from the volume-related variation velocities :

$$C = \frac{\overline{\varepsilon_{ges}}}{\sum \frac{u_i'^3}{d_R}} \tag{6}$$

$$\sum u_i'^3 = \frac{\sum V_i u_i'^3}{V_{ges}} \tag{7}$$

The average power input $\overline{\varepsilon_{ges}}$ with respect to the mass inside the stirred vessel, can be obtained via the Newton number Ne of the stirrer element :

$$\overline{\varepsilon_{ges}} = \frac{P}{\rho V} = \frac{Ne \cdot n^3 \cdot d_R^5}{V} \tag{8}$$

It is also of interest to determine the microscales, that describe the smallest vortex that occurs in a turbulent flow, which are independent of the geometric size of the experimental set-up. The so-called Kolmogorov and Taylor microscales are commonly used here Landahl et al. (1986):

$$\eta = \left(\frac{\nu^3}{\varepsilon}\right)^{\frac{1}{4}} \quad \text{(Kolmogorov)} \tag{9}$$

$$\lambda^2 = \frac{\overline{u'^2}}{\left(\frac{\partial u'}{\partial x}\right)^2} \quad \text{(Taylor)} \tag{10}$$

The following approximate relationship exists between these two length values:

$$\frac{\lambda}{\eta} = Re^{\frac{1}{4}} \tag{11}$$

As can be seen from the above equation [15], as the Reynolds number of the flow increases, the difference between the two values also increases.

Assuming that the macro scale L for the turbulent stirrer flow corresponds to the stirrer diameter d_R, the turbulence values of Table 4 were obtained.

By setting C to "1" in the equation for determining the constant C, a characteristic length value of L = 6.7 mm is obtained, which corresponds to about a fifteenth of the stirrer diameter. The macro scale Λ for the largest vortex can be determined from this characteristic length using the formula from Brodkey

$$\Lambda = \frac{3}{8} \cdot L. \tag{12}$$

This gives a value of Λ = 2.18 mm which corresponds to the rib height of 2 mm to an acceptable degree of accuracy.

5

Conclusions

This investigation shows that the ultrasound Doppler anemometry is a useful technique for examining large-scale flows in model tank reactors. Because of the spatial resolution this technique is predestined for characterizing flows where no detailed information in the nearer vicinity of the stirrer are needed, e.g. for multi-stirrer configurations or stirrer flows with a superimposed in- and outflow.

Nevertheless, the most important goal of the investigations described above, to gain more knowledge about the turbulent large scale flow field induced by a hyperboloid stirrer, was attained. All the data gathered will help to improve the design of hyperboloid stirrers. Measuring the turbulent fluctuation velocities, it should now be possible to calculate the mass and heat transfer rates with higher accuracy. The acquired Kolmogorov micro scales allow the prediction of the minimum particle size that can be suspended by the hyperboloid stirring

system, Herdel (1982) and Höfken (1994). The obtained data will also be very useful to validate CFD-simulations.

References

Brodkey, R. S. : *Turbulence in Mixing Operations*, Academic Press, New York, 1975

Herndl, G. : *Stoffübergang in gerührten Suspensionen*, Dissertation, München, 1982

Höfken, M. : *Moderne experimentelle Methoden für die Untersuchung von Strömungen in Rührbehältern und für Rührwerksoptimierung*, Dissertation, Erlangen, 1994

Landahl, M., Mollo-Christensen, E. : *Turbulence and random processes in fluid mechanics*, Cambridge University Press, Cambridge, 1986

Kresta, S. M., Wood, P. E.: *The Flow-field Produced by a Pitched Blade Turbine: Characterization of the Turbulence and Estimation of the Dissipation Rate*, Chem. Eng. Sci., vol. 48, pp. 1761-1774, 1992.

Nicolaus, F. : *Suspendieren von Festkörpern in Flüssigkeiten durch Rührer*, Dissertation, München, 1961

Tropea, C. : *Statistische Ermittlung strömungsmechanischer Größen*, Vortrag auf dem Kurzlehrgang „Präzisions-Messungen mittels Laser-Doppler-Anemometrie und Phasen-Doppler-Anemometrie", Erlangen, 1993

Yianneskis, M, Popiolek, Z., Whitelaw J. H., *An Experimental Study of the Steady and Unsteady Flow Characteristics of Stirred Reactors,* J. Fluid Mech., vol. 175, pp. 537-555, 1987.

Yianneskis, M., Whitelaw, J. H., *On the Structure of the Trailing Vortices around Rushton Turbine Blades,* Trans. IChemE, vol. 71, Part A, pp. 543-550, 1993.

Yianneskis, M., Rutherford, K., Lee, K. C., *The Interaction of the Trailing Vortex Streams from Rushton Turbine Blades,* Seventh International Symposium on Applications of Laser Techniques to Fluid Mechanics, Lisbon, vol. 1, pp. 10.2.1-10.2.7, 1994.

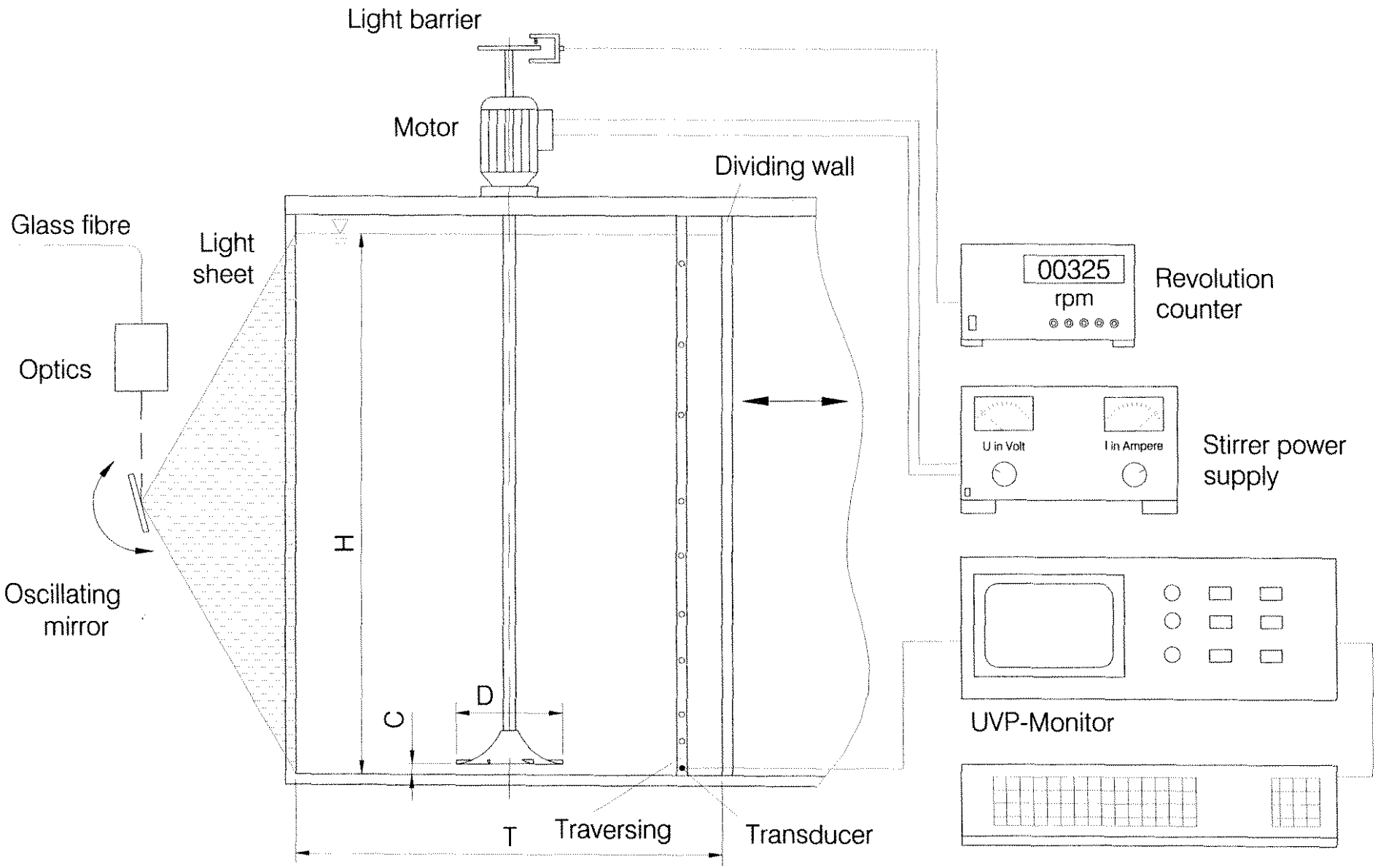

Fig. 1: Experimental set-up

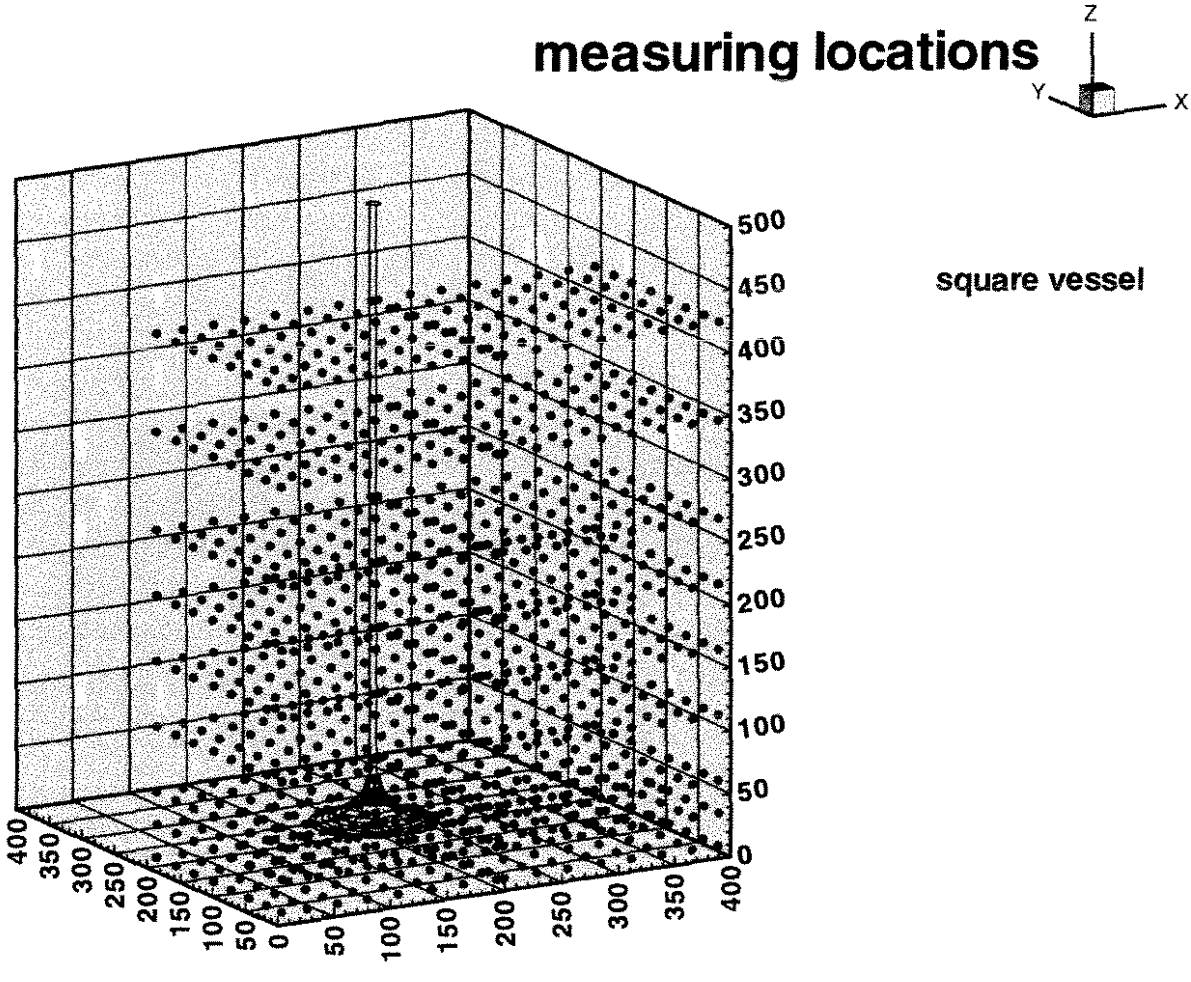

Fig. 2: Locations of the measuring points in the quadratic vessel

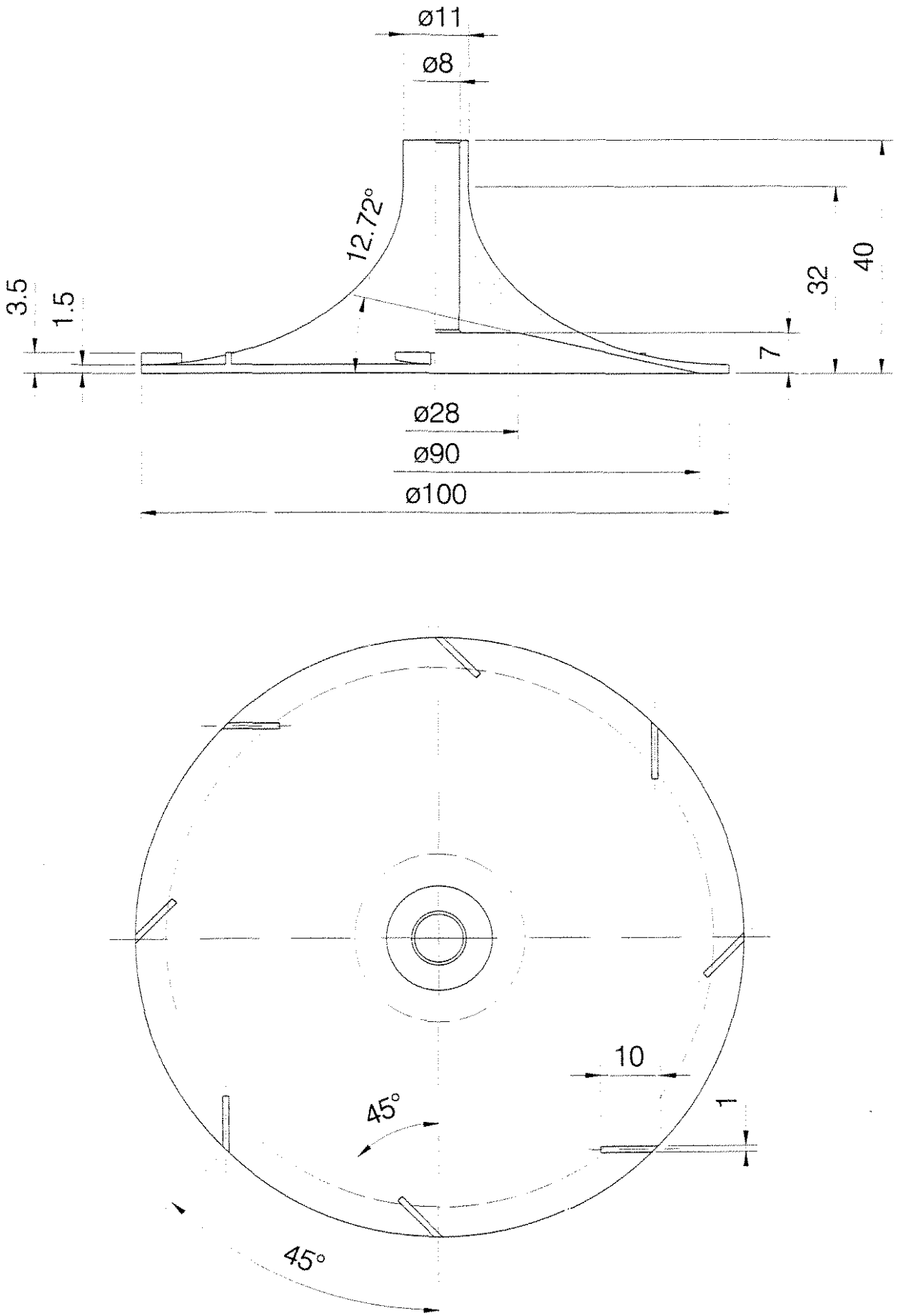

Fig. 3: Hyperboloid stirrer used

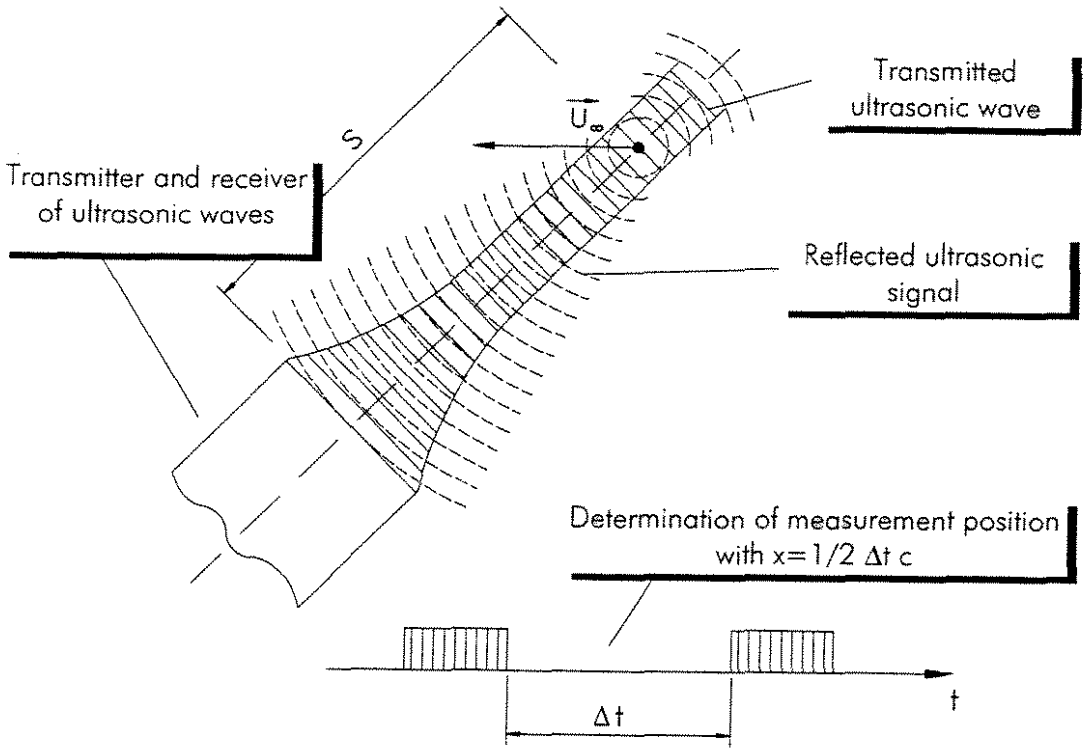

Fig. 4: Measuring principle of ultrasound Doppler anemometry

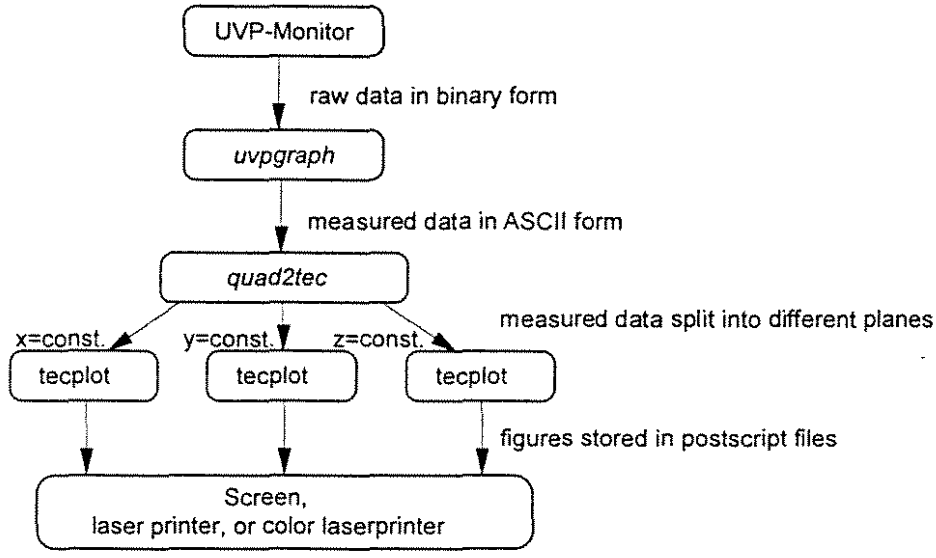

Fig. 5: The evaluation procedure from measured data acquisition to the printout

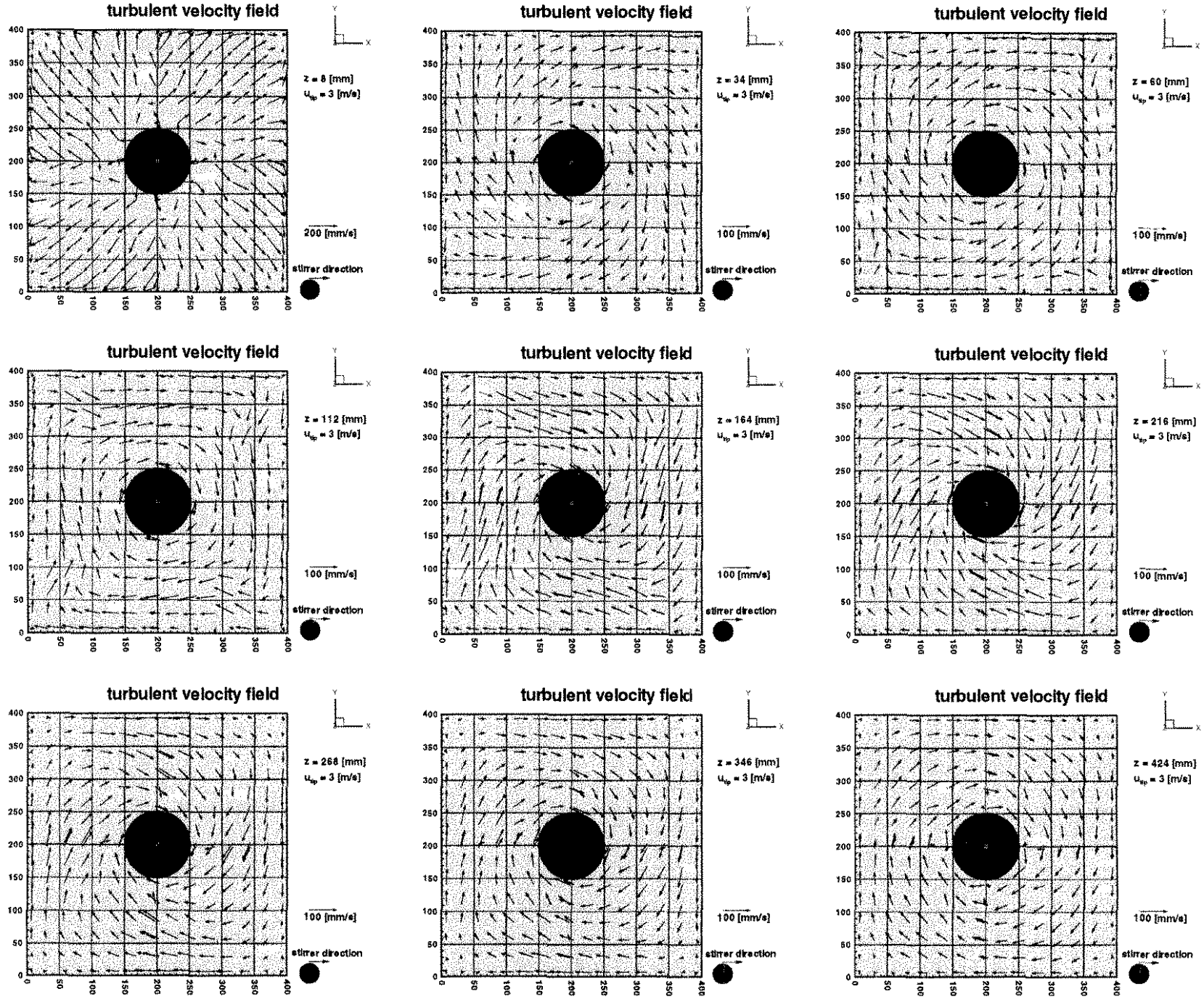

Fig. 6: Presentation of the vector field of velocity for the horizontal planes

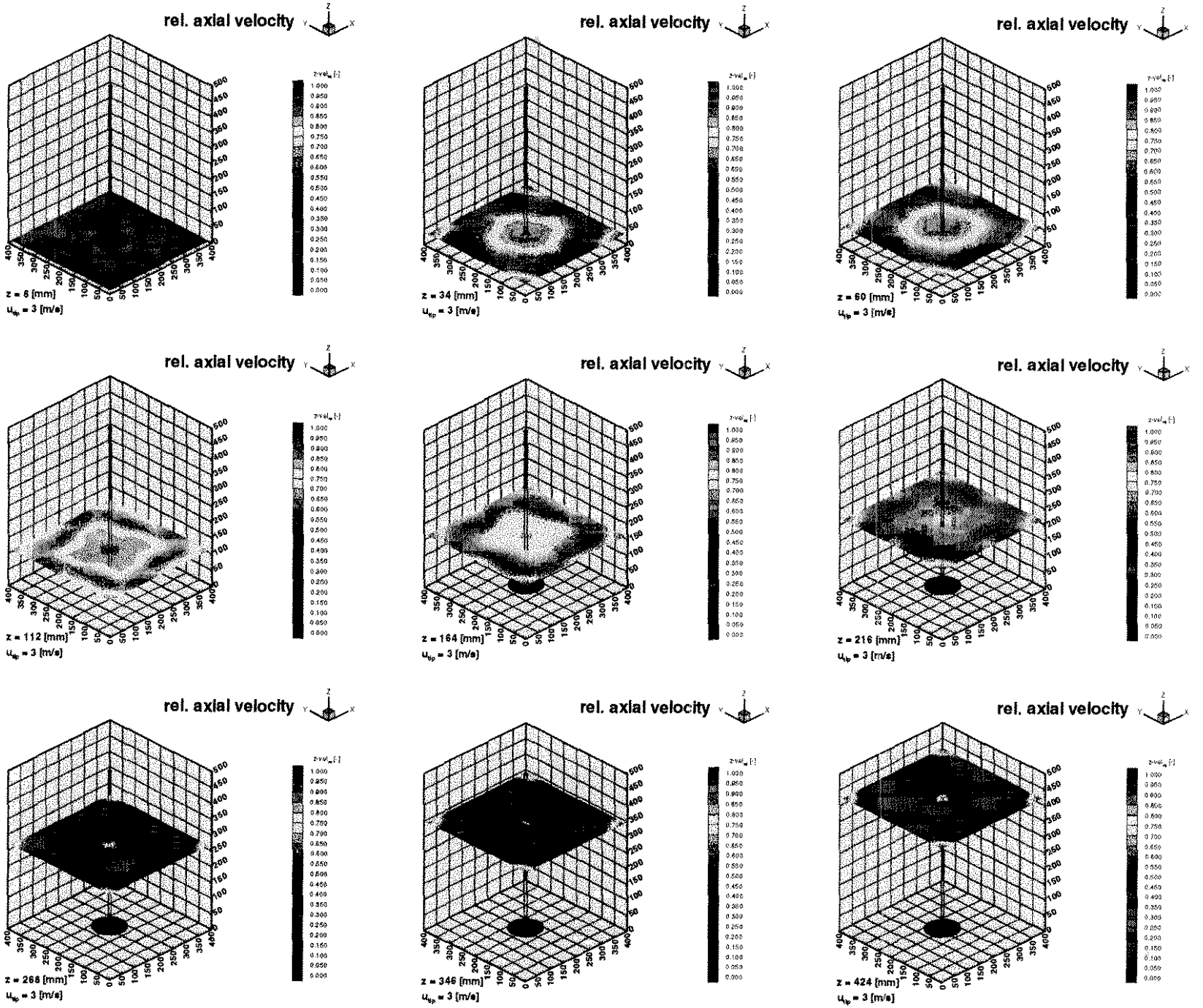

Fig. 7: Presentation of the relative axial velocity for the horizontal planes

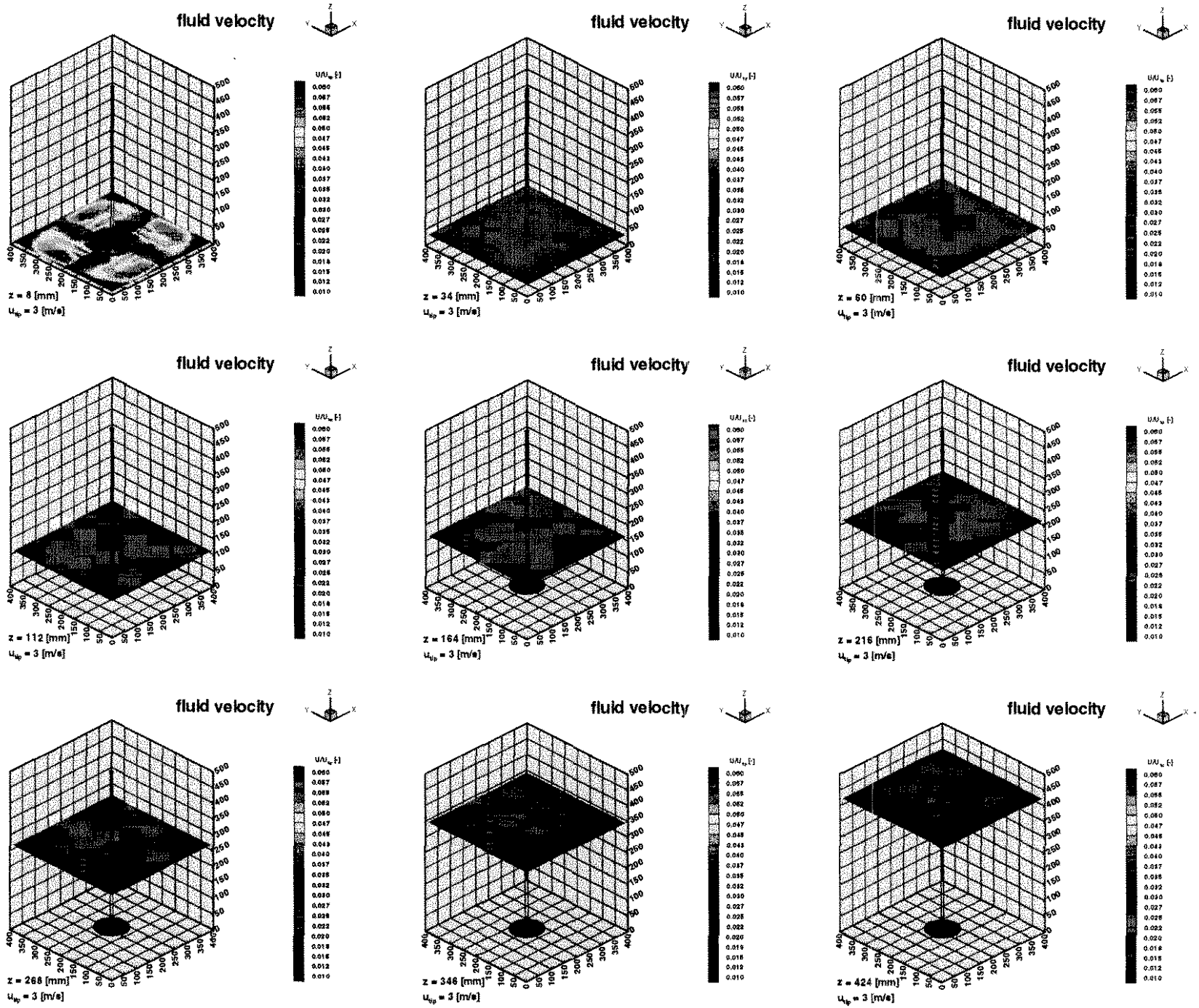

Fig. 8: Presentation of the nondimensional velocity U/U_{Tip} for the horizontal planes

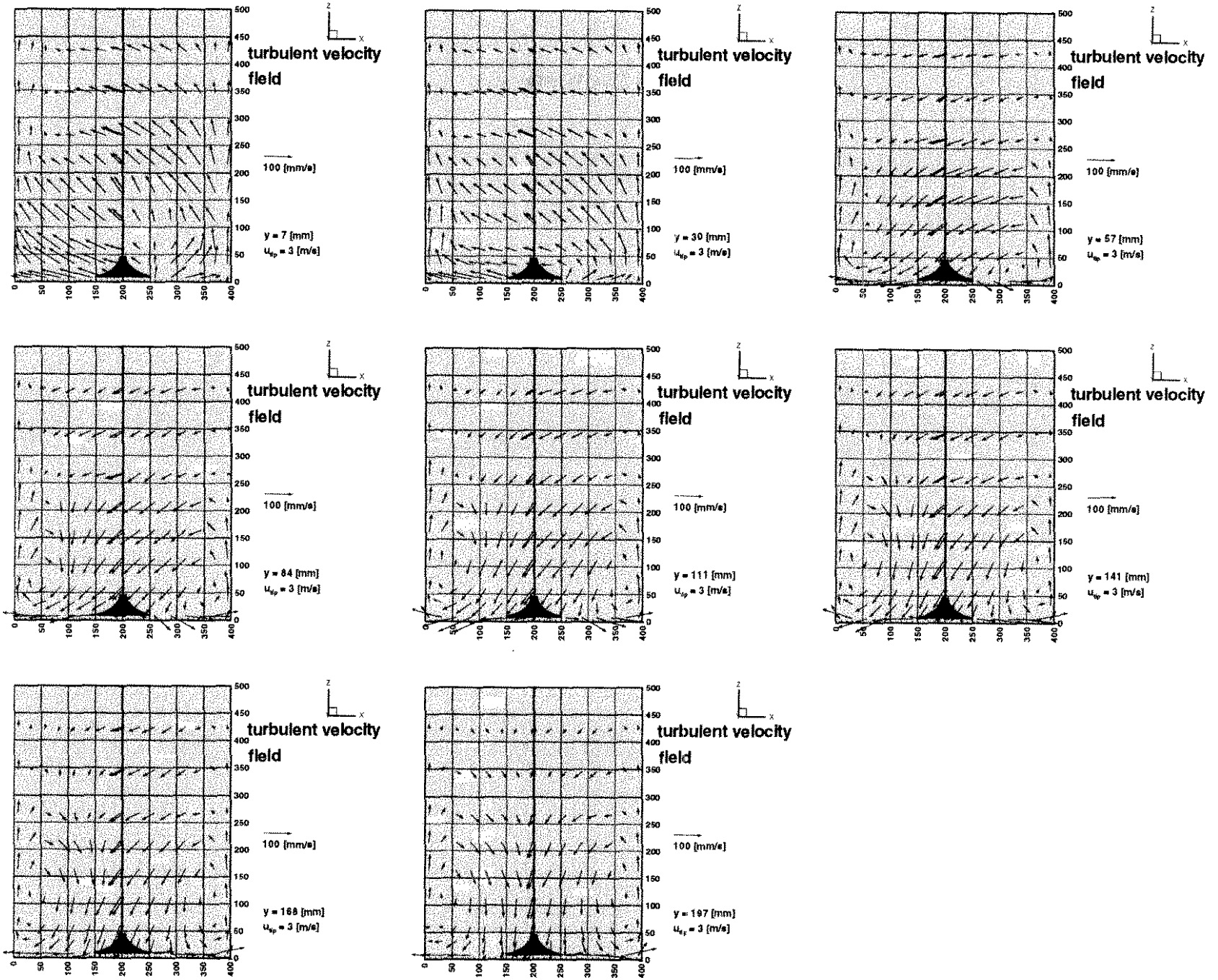

Fig. 9: Presentation of the vector field of velocity for the vertical planes

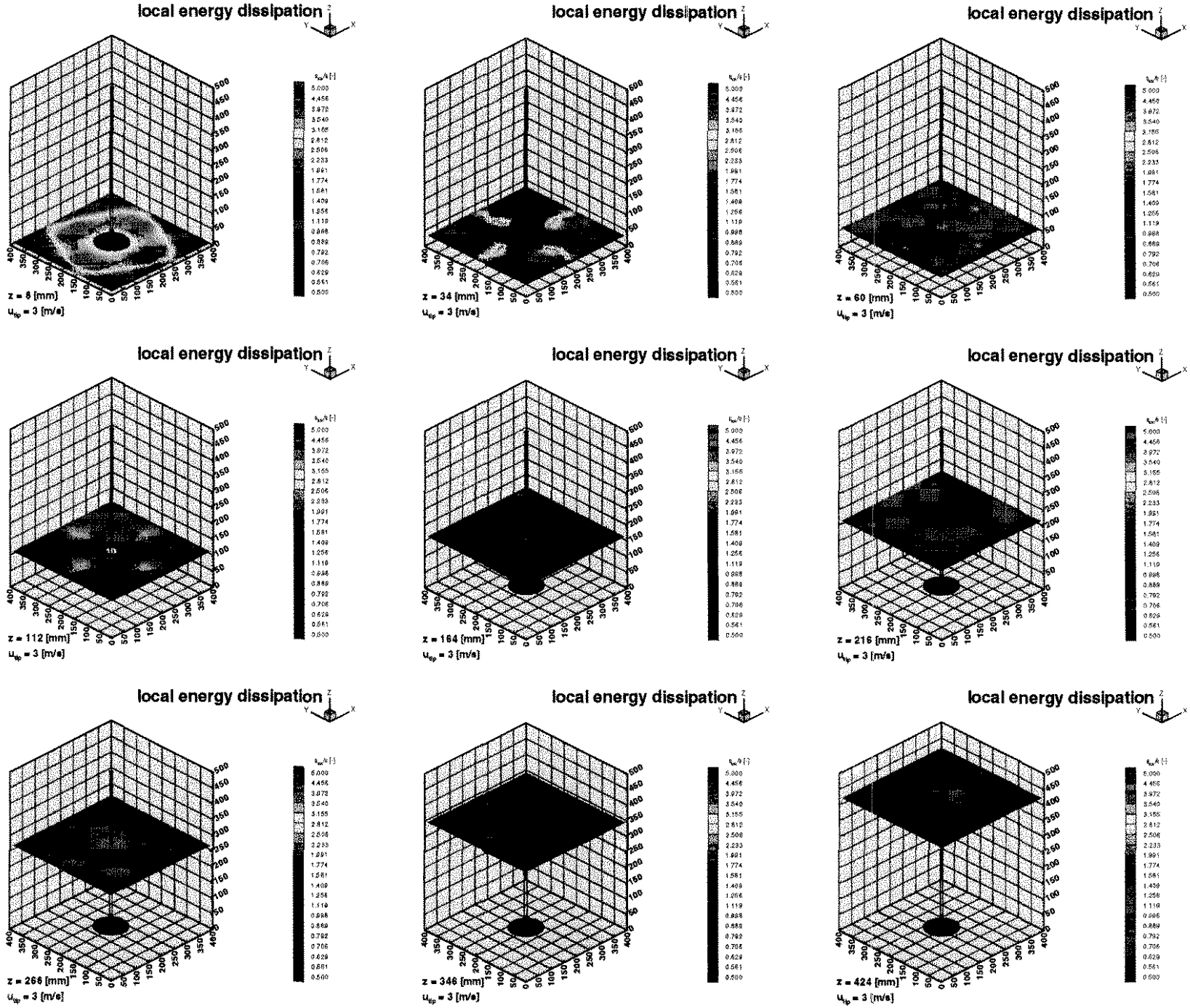

Fig. 10: Presentation of the local energy dissipation for the horizontal planes

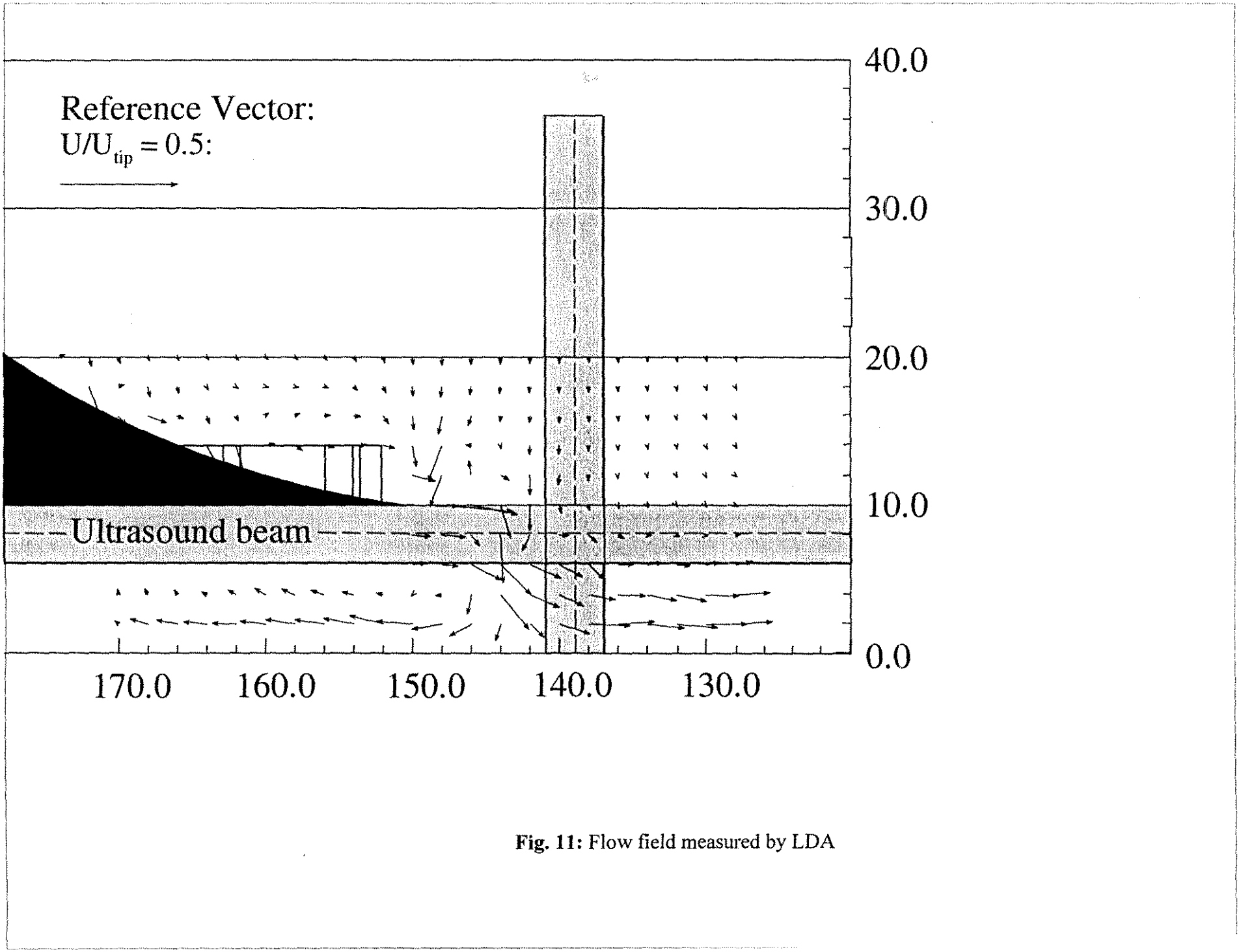

Fig. 11: Flow field measured by LDA

x-axis	7	30	57	84	111	141	168	197	-
y-axis	7	30	57	84	111	141	168	197	-
z-axis	8	34	60	112	164	216	268	346	424

Table 1: Coordinates of the measuring points in [mm] for the quadratic vessel

N	**20**	**50**	**100**	**200**
ε	±5,5 [mm/s]	±3,5 [mm/s]	±2,4 [mm/s]	±1,7 [mm/s]

Table 2: Number of measured values and statistical error

N	**20**	**50**	**100**	**200**
ε	±3,0 [%]	±1,9 [%]	±1,3 [%]	±0,9 [%]

Table 3: Number of measured values and relative error

Constant C	15.65
Micro scale (Taylor) λ	2.509 mm
Micro scale (Kolmogorov) η	0.143 mm

Table 4: Turbulence values for $L = d_R$

Acoustic Doppler velocity profilers: application to correlation measurements in open-channel flow

T. Rolland and U. Lemmin

Laboratoire de recherches hydrauliques
Ecole Polytechnique Fédérale de Lausanne
CH-1015 Lausanne, Switzerland

Running title: correlation measuements with acoustic Doppler velocity profilers

Postal address: same as above

Abstract Measurements with a monostatic and a bistatic acoustic Doppler velocity profiler in open-channel water-flow are used to calculate correlation functions. The instantaneous measurement of one or two components of the velocity vector allows to determine time-, space- and space-time-correlations with ease. It is verified that in this shear flow case the local mean velocity and the convection velocity coincide. For correlations of the vertical velocity the convection velocity is zero. Spectra characterize the flow field as isotropic. Extending the range of spectral resolution by two-gate cross-correlation is found to add at least one decade of resolution.

1 Introduction

Velocity and turbulence are important hydrodynamic parameters. Consequently, many instruments, working on a variety of principles, have been developed for their measurement. Among them, the pulse-to-pulse coherent acoustic velocity profiler (ADVP) has a unique combination of advantages:

- it can take instantaneous *velocity profiles*
  -- of all three velocity vector components simultaneously
  -- covering the total water column in open channel flow
  -- with a resolution of turbulence scales.
- it is non-intrusive.
- it works reliably in the presence of suspended particles.
- it can determine instantaneous particle *flux profiles.*

Its suitability for studies in rotating flows was first demonstrated by Takeda (1986). We have tested its feasibility for open-channel

laboratory-research (Lhermitte and Lemmin 1990; Lhermitte and Lemmin 1994) based on hardware systems and signal processing algorithms which we have developed and improved since.

Much has been learned about turbulent flow in boundary layers from measurements of correlations in time and space (Favre et al. 1957; Favre et al. 1958; Tritton 1967). More recently interest in correlation functions is renewed because they can provide useful information on coherent structures (Adrian 1988). Two-point correlation measurements have suffered in the past from instrument wake effects (Comte-Bellot and Corrsin 1966) which have been corrected by using a two beam LDA (Romano 1995) The profiling capacity of the ADVP may greatly enhance the possibilities of correlation measurements since it can measure several velocity components at more than 200 points along a line simultaneously and non-intrusively.

In this paper we will briefly review ADVP configurations and demonstrate the potential of different ADVP systems in measuring various types of correlations in open channel flow.

2 ADVP configurations

Depending on the flow conditions and on the aim of the investigations, different approaches and different configurations of the ADVP can be or have to be realized. In order to optimize the ADVP system in each case, a modular arrangement of the instrument is required. We will demonstrate the flexibility of such a modular system in two different configurations: a monostatic ADVP and a bistatic ADVP.

Different signal treatment methods exist to extract the velocity information from the measured Doppler phase shift between the emitted

and the backscattered signals. In the present analysis the pulse-pair algorithm (Lhermitte and Serafin 1984) is used which was found to be more reliable than the spectral analysis. In view of the good signal to noise ratio, the number of pulse-pairs was taken as N_{pp} = 32. Random phase coding (Lhermitte and Lemmin 1994) was used which significantly reduces the aliased echoes that may occur from multiple reflections on fixed surfaces.

2. 1
Monostatic ADVP

In a monostatic mode, one single acoustic transducer is used to emit and receive acoustic waves. ADVP velocity profiles have been taken by aligning the transducer with the direction of interest (Takeda 1995). A profile is obtained by gating the received signal to correspond to the pulse's time of flight to a certain depth. In open channel flow, vertical profiles of both the along axis and vertical velocity component are of interest. Thus a vertically pointing transducer can take a full profile of the vertical velocity in a horizontal open channel. In our study, this transducer has been placed below the channel bottom in a separate chamber separated from the channel flow by a Mylar window (Lemmin and Rolland 1996) and thus takes measurements without disturbing the flow. For the horizontal velocity component the transducer would have to be placed in the flow looking horizontally. In this case a vertical profile can only be taken by moving the transducer vertically and the multigate capability of the ADVP is of little use.

As an alternative, the transducer may be placed in the chamber below the channel bottom and tilted at an angle to the vertical. The radial velocity that this transducer measures contains contributions from the horizontal and the vertical velocity components. Under uniform flow

conditions we have shown that with three consecutive measurements with three transducers mounted as shown in Fig. 1a. mean vertical profiles of the mean velocities and the variances as well as the Reynolds stresses can be obtained. Investigating stationary open channel flow over rough and smooth beds, good agreement was found for all laws for the distribution of mean velocities and turbulence parameters (Rolland 1994; Lemmin and Rolland 1996).

However, the determination of turbulence parameters with this system is limited to uniform or very gradually varying flow. It is impossible to apply it to more rapidly accelerating or decelerating flows which are often encountered in natural water flows that we are interested in.

2.2
Bistatic ADVP

Recently we have therefore extended the ADVP-technique to a system which is capable to determine instantaneous profiles of at least two velocity components simultaneously with the resolution of turbulence scales.

In this new ADVP a pulse of sound waves is emitted only from a central transducer (Fig. 1b). As in the monostatic mode this transducer can also work as a receiver of the backscattered sound waves. Additional transducers placed around the emitter will serve as receivers for the backscattered signals coming from same pulse of sound waves. For convenience and ease of signal extraction, these receivers which have to be inclined towards the central emitter are normally placed symmetrically around the emitter. In that case any sound waves which are backscattered from a certain volume in the central beam will have the same time of flight to all the surrounding receivers. One pair of

opposingly inclined receivers is sufficient for the determination of two instantaneous velocity components. An additional pair in a plane perpendicular to the first one will allow to determine all three velocity components instantaneously.

For convenience this system is aligned here with the direction of the mean flow (the along axis flow in the open channel). In this case the two velocity components under consideration are the horizontal velocity u and the vertical velocity v. The emitted sound beam from which the velocity profile is determined is vertical with respect to the channel bottom. This is an advantage over the monostatic system where the profile has to be taken along an inclined sound beam. Details of the signal processing and the determination of the instantaneous velocities are given in Rolland (1994). Profile measurements made with the bistatic ADVP in an open channel with smooth bed are reported in Rolland and Lemmin (1996).

3 Correlation measurements

To evaluate the ADVP in turbulent open channel flow, the present experiments were conducted under uniform flow conditions in a recirculating glass-wall channel with a smooth steel floor. It is L = 43 m long, b = 2 m wide and 0.16% tilted. The measurements were made at 16 m from the channels entrance where the turbulent flow generated by wall friction is well-established and in equilibrium. Experiments conducted with the ADVP system were concerned with clear water (better than 98 percent transmissivity) which was permanently filtered. No seeding was done. Details of the installation and of the basic pulse-to-pulse coherent ADVP equipment operating at 1 MHz are given in

Lhermitte and Lemmin (1994); Lemmin and Rolland (1996) and Rolland and Lemmin (1996). Measurements reported here were made in uniform turbulent flow (Re = $U_1 h/\nu$ = 3.5 to 3.6×10^5; Fr = 0.79 to 0.87; bottom friction velocity u_* = 3.79 to 3.94 cms^{-1}). The water depth h in the present experiments was between 10 and 11 cm, the mean along axis velocity U_1 = 87 to 82 cms^{-1} and the aspect ratio b/h = 19.8 to 18.2. The vertical profile of the horizontal velocity component follows the logarithmic law for z/h < 0.2 and Coles' law of the wake in the outer layer (Lemmin and Rolland 1996).

3.1
Taylor's hypothesis

Taylor (1938) assumed that the velocity field is 'frozen' and convected downstream. In homogeneous turbulence the convection velocity is the same for all eddies and equal to the mean velocity U_j. This implies that a partial time derivative $\frac{\partial(..)}{\partial t}$ and a partial space derivative $\frac{\partial(..)}{\partial x_i}$ are related by

$$\frac{\partial(..)}{\partial t} = U_i \frac{\partial(..)}{\partial x_i} \qquad (1)$$

and that a fluctuating velocity $u(x,t)$ can be expressed as:

$$u(x,t) = u(x + U\tau, t + \tau) \qquad (2)$$

for not too large values of time lag τ (Townsend 1976). Taylor's hypothesis has been found valid for large Reynolds numbers and small turbulence intensities $(\overline{u_i^2})^{1/2} << U_i$. Within the above restrictions the use of the frozen flow assumption applies to all flows. However, when the

gradient of the mean velocity is large such as in boundary layers, the local convection velocity may deviate from the mean velocity.

A correlation in space ($\tau = 0$) may then be related to a correlation in time ($r = 0$; r determines the distance between two points of measurement) as

$$R_{11}^{N}(0,0,0;\tau) = R_{11}^{N}(U_1\,\tau,0,0;0) \qquad (3)$$

In this equation the superscript N indicates normalized correlations and the subscript 11 indicates that the correlations are measured in a direction r which is parallel to the direction of the mean flow. In the open channel this is a direction parallel to the channel bottom.

For the present correlation measurements the acoustic transducer of the monostatic system was placed horizontally in the axis of the channel looking into the flow in mid-depth ($z/h = 0.5$). The influence of the transducer on the measurements was minimized by setting the first gate of the profile at 12 cm ahead of the transducer face (diameter 3 cm). The gate spacing was 6 mm and simultaneous measurements were taken at up to 100 equally spaced gates.

Fig. 2 shows the comparison of the two correlation functions in eq.(3). The reference velocity in this case was not the mean velocity U_1 but the local mean velocity $\overline{u}$ at the depth of measurement. We find agreement between them for $r_1/h > 2$. The deviation for higher values of separation distance r_1 observed by Cenedese and Romano (1991) does not occur in our case because the flow is uniform and well established. For the same reason we do not observe the difference between the positive and the negative displacements either. The existence of uniformity and thus homogeneous turbulence can be made evident by comparing autocorrelation functions for different gates along the channel axis. If the condition of homogeneity is satisfied all autocorrelation

function have to be identical. This is demonstrated in Fig. 3 for three gates separated each time by 60 mm which have been acquired simultaneously. We have also compared autocorrelation functions of the horizontal velocity component with those of the vertical component. We find (Rolland 1994) that in the correlations of the vertical component the initial fall-off is at least twice as rapid as that of the horizontal component indicating that the integral scales of the vertical turbulence are smaller than those of the horizontal one. This agrees with the observations of Nezu and Nakagawa (1993) who have pointed out that in the outer region of the flow where our measurements were taken, turbulence intensity in the longitudinal direction is 1.45 to 1.8 times greater than in the vertical direction.

3.2
Spatial correlation

The vertically pointing transducer allows to establish the relationship between the vertical component of the velocity measured at a reference level (gate) and at other depths in the flow. The ADVP is well suited for this measurement because it is placed outside the flow field (Fig. 1a) and it does not require to invoke Taylor's hypothesis nor the use of a second sensor within the water column. Fig. 4 presents several examples of the spatial correlation functions. All data have been acquired in a single measurement. A systematic variation in the structure of the correlation function can be seen which depends on the reference level chosen. One may consider that the surface below the curve is representative for a correlation length related to a turbulence scale. The examples in Fig. 4 show that the scales of vertical turbulence are larger in the central part of the water column. They fall off as expected when the free surface or the channel bottom is approached.

3.3

Space-time correlation with time delay

As in the preceding measurements a horizontally pointing transducer at mid-depth and a vertically pointing transducer both working in the monostatic mode are used. The correlation functions are each time calculated from data obtained in a single multigate acquisition.

The results for the horizontal correlation function are shown in Fig. 5. For each separation distance, the correlation function passes through a maximum. The delay of this maximum τ_m is directly proportional to the separation ζ_m between the two gates in question. From these two parameters the convection velocity $u_c = \zeta_m / \tau_m$ can be calculated. In our case the convection velocity is always equal to the local mean velocity $\overline{u}$ at that depth. This observation confirms again that Taylor's hypothesis is valid in a shear flow if the local mean velocity $\overline{u}$ is used to transform a time signal into a space signal. Favre et al. (1957,1958) had already shown that in air shear flow Taylor's hypothesis is valid. However, in their case the convection velocity was generally equal to 0.8 $\overline{u}$. Romano (1995) has shown that in duct flow (using water) $u_c/\overline{u} = 1$ is approached for high Reynolds numbers. The amplitude of the maximum of the correlation functions decreases with increasing separation in contradiction to Taylor's hypothesis while the radius of curvature become larger at the same time. This was predicted and explained by Townsend (1976) and observed in all studies cited above. However, we note that after the initial fall-off the further decrease in our case is much less that seen before indicating that in uniform open channel flow the loss of correlation and thus of identity of the turbulence is less significant.

The same analysis can be carried out for the vertical velocity component obtained from the vertically pointing transducer. Results are

given in Fig. 6. This figure shows clearly that the convection velocity in the vertical direction is zero: the maxima of all curves fall onto the line $\tau = 0$. One may note a certain tendency that gates with the same distance from the reference level have a slightly higher correlation in the upward direction than in the downward direction. This can be interpreted to indicate that turbulence patterns move from the channel bottom towards the surface.

3.4
Iso-correlation patterns

The bistatic ADVP as indicated above can measure instantaneous vertical profiles of two velocity components over the whole water column. Assuming that Taylor's hypothesis is valid over the whole water column, time correlation functions determined over the whole water column can be interpreted as spatial correlation functions. Curves of iso-correlation can then be established for any given reference level. In the present study we will again take the reference level at mid-depth z/h = 0.5. The hydraulic conditions remained unchanged from the above monostatic measurements. Each of the cases discussed below results from one simultaneous recording of profiles of the two velocity components at 22 gates in the vertical.

In the first case, iso-correlation curves have been determined for the longitudinal velocity component. Results are shown in Fig. 7. It can be seen the iso-correlation curves are ellipses which are inclined by about 20° in the direction of the mean flow. The direction of inclination which is the line connecting for each gate those points that have the highest correlation is an indication of the direction of movement of the turbulence structures. This result agrees well with the observations made

by Blackwelder and Kovaznay (1972) and the calculations by Townsend (1976) for the theory of rapid distortion of isotropic turbulence.

In the second case, the same calculations as above have been carried out for the correlations for the vertical velocity component. The resultant iso-correlation curves are shown in Fig. 8. In this case the curves are again ellipses but their main axes all coincide with the vertical. Furthermore, a very rapid de-correlation is observed in the mean flow direction. As was already seen above, this indicates that vertical turbulence in the outer region is organized on smaller scales than the horizontal component. In the vertical, correlation above the level of reference extends to longer distances of separation than in the downward direction.

In the third case use is made of the simultaneous recording of profiles of two orthogonal velocity components. Normalized cross-correlations are determined between the horizontal velocity at the reference level and the vertical velocities measured at all other gate levels. Results are presented in Fig. 9 where a certain asymmetry with respect to the vertical line at the origin is observed. Correlations are stronger in the direction of the mean flow than in the opposite direction. This behaviour was already outlined by Townsend (1976) and is indicated by the cross-correlation curves given by Tritton (1967). It may also be noted that the cross-correlation is stronger towards the channel bottom than towards the free surface. This is reflected in the distribution of the Reynolds stresses which have their maximum on the channel bed.

4
Spectral analysis

Spectral analysis provides a statistical means to determine the distribution of turbulent energy between different frequencies which may in turn provide information on the distribution of spatial and temporal turbulence scales. Here we will calculate one-dimensional spectra on timeseries of the horizontal and the vertical component of the flow field invoking Taylor's hypothesis. The spectra have been obtained using standard FFT technique on partially overlapping subsets.

For the monostatic ADVP, the data obtained with the inclined transducers (Fig. 1a) have been analyzed. For stationary uniform flow the spectrum of the horizontal component can be extracted after some signal procession (Rolland 1994). The result is shown in Fig. 10 where the ADVP data have been compared with results from hot-film anemometer measurements which were taken afterwards at the same location. Good agreement is found between the two techniques. Energy containing scales are observed for frequencies $f < 0.1$ Hz. The inertial subrange starts between $0.1 < f > 1$ Hz and is well established for $f > 1$ Hz. The present ADVP spectra are limited to $f < 20$Hz while the inertial subrange extends to at least $f = 100$Hz as seen from the hot film measurements. This limit is due to the choice of $N_{pp} = 32$. The good agreement between the results from the two measuring techniques shows that the choice of N_{pp} was correct for eliminating parasitic signals from the ADVP velocity determination.

Spectra have also been obtained from the measurements with the bistatic ADVP. In this case, spectra for both velocity components were calculated for several depths (Fig. 11). No difference in the spectra with depth is observed. For the longitudinal components the peak in the energy containing scales agrees with the monostatic measurements. The inertial subrange is established over nearly two decades starting at $f = 0.1$ Hz. For the vertical component the range of the energy containing eddies is much broader and extends to 1 Hz. For the next decade the

inertial subranges of the two velocity components agree well. It is evident, as was seen already in the correlation analysis above, that the vertical velocity component is organized on smaller length scales than the horizontal component.

5
Correction for Doppler ambiguities

A spectral resolution to higher frequencies may at times be desirable. Two processes interfere with the resolution at higher frequencies and both occur also with laser and Radar systems. However, their consequences are more accentuated in acoustic systems because of the greater wavelength. The first process is attenuation caused by spatial averaging inside the measuring volume, biased by the coefficient of directivity of the emission. Little can be done about this effect. The second process is the Doppler ambiguity and generally this one is much more important than attenuation. Doppler ambiguity results in spectral broadening (Lhermitte and Lemmin 1994). This occurs because of the random transit of the scatterers across the measuring volume of finite dimensions from one sound pulse to the next.

Garbini et al. (1982) have suggested that the measured Doppler phase may be decomposed into a phase spatially averaged across the acoustic beam and an instantaneously fluctuating phase. Both contribute to the spectrum and the latter one mainly to the high frequency end. The pulse-pair algorithm is capable of extracting the velocity correctly from the ambiguity noise because it is a real time autocovariance algorithm. Thus, for a sufficiently large number of pulse pairs (Zrnic 1979) an estimate of the mean velocity inside the measuring volume can be

correctly made and spectra without Doppler ambiguity effects can be obtained as seen above.

The higher temporal resolution requires a reduction in N_{pp} which will in turn introduce the effect of the Doppler ambiguity. For measurements with transducers inclined to the direction of flow, Garbini et al. (1982) have shown that the Doppler ambiguity can be eliminated while the desired velocity information is maintained when signal timeseries from two gates measured in the same acoustic beam and at the same time are correlated. If the two gates are sufficiently close to each other (but not too close to avoid overlapping or shading) the cross-correlation is a good approximation of the autocorrelation function. We have shown (Rolland 1994) that for our measurement conditions two consecutive gates should be cross-correlated.

The results of the application of this procedure are shown in Fig. 12. In order to obtain the same temporal resolution (f = 100 Hz) as the hot film anemometer, the number of pulse pairs has to be lowered to $N_{pp} = 4$. The spectrum which results directly for $N_{pp} = 4$ is progressively affected by the Doppler ambiguity for frequencies f > 10 Hz. This can be eliminated when cross-correlating the signals between two consecutive gates instead. Some aliasing effects become visible in the resultant spectrum near f = 100 Hz. These can be eliminated by other means. Thus the range of spectral resolution of the ADVP can be expanded by applying the proper signal treatment methods. In order to show that the pulse pair algorithm automatically eliminates the Doppler ambiguity effects when N_{pp} is high enough, the spectrum for $N_{pp} = 32$ and the spectrum obtained by cross-correlation of two consecutive gates are compared in Fig. 13. The good agreement between the two spectral curves is evident.

Concluding remarks

The Acoustic Doppler Velocity Profiler has been evaluated for its use in boundary layer flow conditions in open channel flows. From the analysis it is evident that the ADVP hardware and the software algorithms applied to the extraction of the velocity vector are well suited for the analysis of turbulent flow characteristics without the need for a calibration procedure. Measurements can be taken rapidly with a degree of accuracy better than that of many conventional in situ sensors which at the same time stand to significantly modify the local flow conditions by intruding into the flow. The ADVP is easier to operate than laser velocimeters and essentially provides instantaneous velocity profiles instead of point measurements. This opens new research possibilities in the study of coherent structures (Shen and Lemmin 1996a).

Compared to existing instrumentation, the ADVP profile measurements take only a small fraction of the time for the same resolution. Furthermore, since ADVP profile measurements are taken simultaneously under the same flow conditions, the resultant profiles are found to be smoother than those taken in sequence by existing instruments. Still higher spatial and temporal resolution can be achieved by using a higher acoustic frequency.

We have also tested the same ADVP in rivers and lakes (Lemmin et al. 1995; Lemmin and Jiang 1996). In these environments, typical values of the sampling frequency needed for correctly studying turbulence are about 10 Hz. The ADVP systems of the type discussed here seem to be the most appropriate instrument. The presence of particles in low to medium concentration in the flow does not influence the acoustic system at all, a great advantage over the LDA. Therefore the pulse-to-pulse coherent technique presented here appears to be a rather promising tool in field

studies. In the laboratory the presence of particles, their concentration and the variance may be investigated by exploiting the profiles of backscattering intensity information provided by the ADVP at the same time (Shen and Lemmin 1996b). This information, combined with the instantaneous velocity profile can be used for detailed studies of sediment transport fluxes (Shen and Lemmin 1996c).

In conclusion, the investigations carried out so far have already shown the potential of the high frequency ADVP as a valuable tool for hydraulic research under a large variety of conditions. More sophisticated techniques for beam focalization (Hurther and Lemmin 1996), data acquisition and signal processing or beam scanning techniques may have to be further investigated before the optimal configuration and the range of application of a high frequency ADVP designed for hydraulic research can be fully determined. It can be expected that these developments will extend the capabilities of the acoustic systems to advance the understanding of the turbulent water flows.

Acknowledgment

The continuous encouragement by Prof. W.H. Graf is greatly appreciated. This study was financed by the Swiss National Science Foundation grant Nr. 20-39'495.93. We are grateful for the support.

References

Adrian, R. J. (1988) Linking correlations and structure: stochastic estimation and conditional averaging. Near wall turbulence; Zoran Zaric Memorial Conf. Eds. S. J. Kline and N. H. Afgan. New York, N.Y., 420-436.

Blackwelder, R. F., and L. S. G. Kovaznay (1972) Time scale correlations in a turbulent boundary layer. The Physics of Fluids 15:

Cenedese, A., and G. P. Romano (1991) Experimental testing of Taylor's hypothesis by L.D.A. in highly turbulent flow. Exp. Fluids 11: 359-367.

Comte-Bellot, G., and S. Corrsin (1966) The use of a contraction to improve the isotropy of grid-generated turbulence. J. Fluid Mech. 25: 657-682.

Favre, A. J., J. J. Gaviglio, and R. J. Dumas (1957) Space-time double correlations and spectra in a turbulent boundary layer. J. Fluid Mech. 2: 313-342.

Favre, A. J., J. J. Gaviglio, and R. J. Dumas (1958) Further space-time correlations and spectra in a turbulent boundary layer. J. Fluid Mech. 3: 344-356.

Garbini, J. L., F. K. Forster, and J. E. Jorgensen (1982) Measurement of fluid turbulence based on pulsed ultrasound techniques (part I and II). J. Fluid Mech. 118: 445-505.

Hurther, D., and U. Lemmin (1996). Using an annular curved array transducer for bistatic ADVP applications. Laboratoire de Recherches Hydrauliques, EPFL, Lausanne, Switzerland.

Lemmin, U., and R. Jiang (1996) Vertical velocity structure and eddy scale distribution in the water column of the stratified Lake of Geneva. Mixing and dispersion in stably stratified flows. Dundee, U.K., Institute of mathematics and its application.

Lemmin, U., R. Jiang, and S. A. Thorpe (1995) Finescale dynamics of stratified waters near a sloping boundary of a lake. IUTAM symposium on physical limnology, Broome, Australia, 115-124.

Lemmin, U., and T. Rolland (1996) An acoustic velocity profiler for laboratory and field studies. J. Hydr. Eng. ASCE, in press.

Lhermitte, R., and U. Lemmin (1990) Probing water turbulence by high frequency Doppler sonar. Geophys. Res. Letters 10: 717-720.

Lhermitte, R., and U. Lemmin (1994) Open-channel flow and turbulence measurement by high-resolution Doppler sonar. J. Atm. Ocean. Tech. 11: 1295-1308.

Lhermitte, R., and R. Serafin (1984) Pulse-to-pulse coherentDoppler signal processing techniques. J. Atm. Oceanic Technol. 4: 293-308.

Nezu, I., and H. Nakagawa (1993) Turbulence in open-channel flows. A.A. Balkema. Rotterdam.

Rolland, T. (1994). Développement d'une instrumentation Doppler ultrasonore: application aux écoulements turbulents en hydraulique. EPFL Lausanne, Switzerland.

Rolland, T., and U. Lemmin (1996) A two-component velocity profiler for use in turbulent open-channel flow. J. Hydr. Res. accepted.

Romano, G. P. (1995) Analysis of two-point velocity measurements in near wall flows. Exp. Fluids 20: 68-83.

Shen, C., and U. Lemmin (1996a) A tristatic Doppler velocity profiler and its application to turbulent open channel flow. Advances in turbulence VI Ed. S. G. e. al. Lausanne, Kluwer Academic Publishers. 483-486.

Shen, C., and U. Lemmin (1996b) Two-dimensional acoustic sediment flux profiler. Meas. Sci Technol. submitted.

Shen, C., and U. Lemmin (1996c) Ultrasonic measurements of suspended sediments: a concentration profiling system with attenuation compensation. Meas. Sci. Technol. 7: 1191-1194.

Takeda, Y. (1986) Velocity profile measurements by ultrasound Doppler shift method. Int. J. Heat Fluid Flow 7: 313.

Takeda, Y. (1995) Velocity profile measurements by ultrasonic Doppler method. Exp. Thermal and Fluid Sci. 10: 444-453.

Taylor, G. I. (1938) The spectrum of turbulence. Proc. Roy Soc London A 164: 476-490.

Townsend, A. A. (1976) The structure of turbulent shear flow. Cambridge University Press. Cambridge. 429.

Tritton, D. J. (1967) Some new correlation measurements in a turbulent boundary layer. J. Fluid Mech. 28: 439-462.

Zrnic, D. S. (1979) Estimation of spectral moments from weather echoes. IEEE Trans. Geosci. Electron. 17: 113-128.

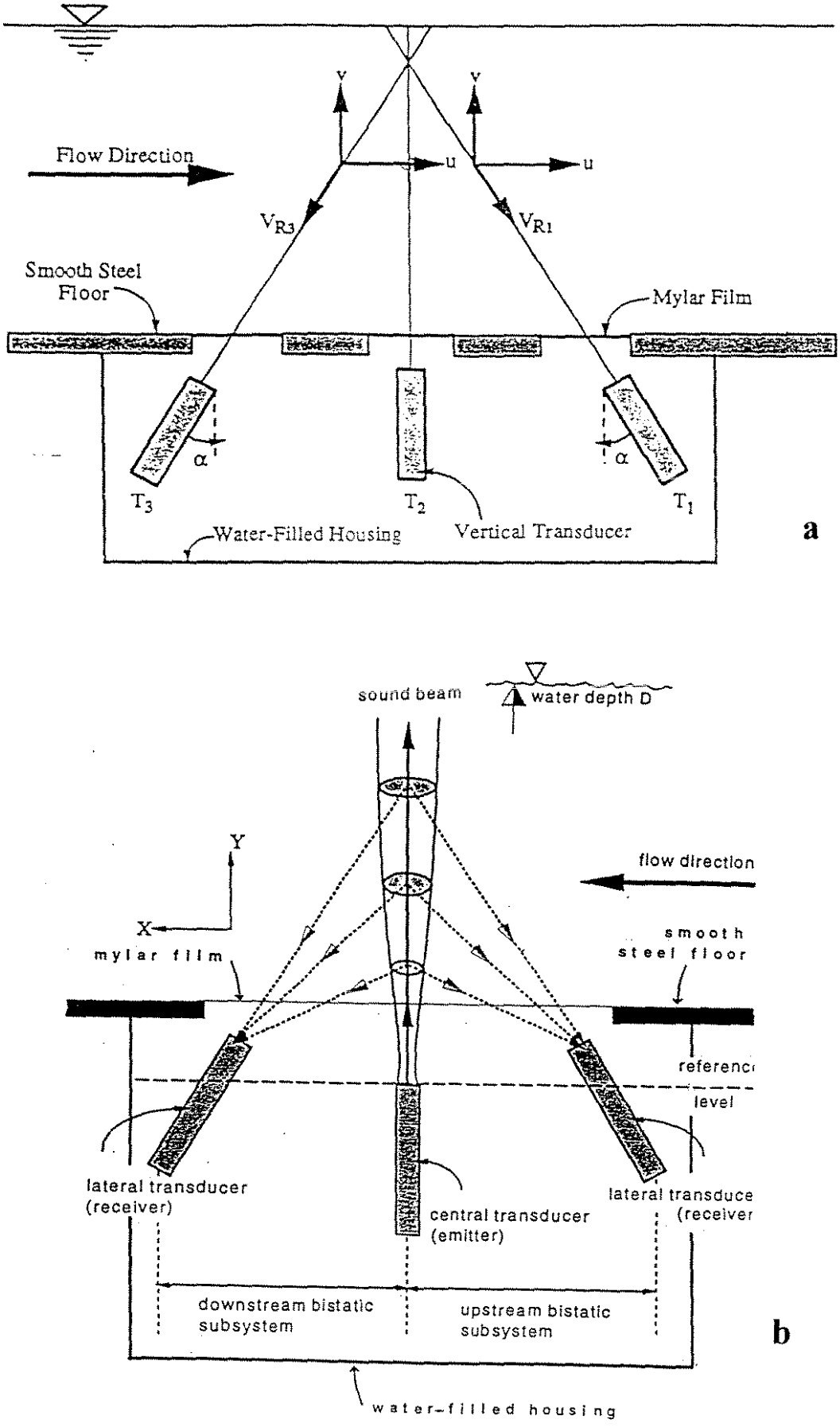

Fig. 1a,b. Acoustic Doppler velocity profiler layouts: **a**: Monostatic ADVP; **b**: Bistatic ADVP.

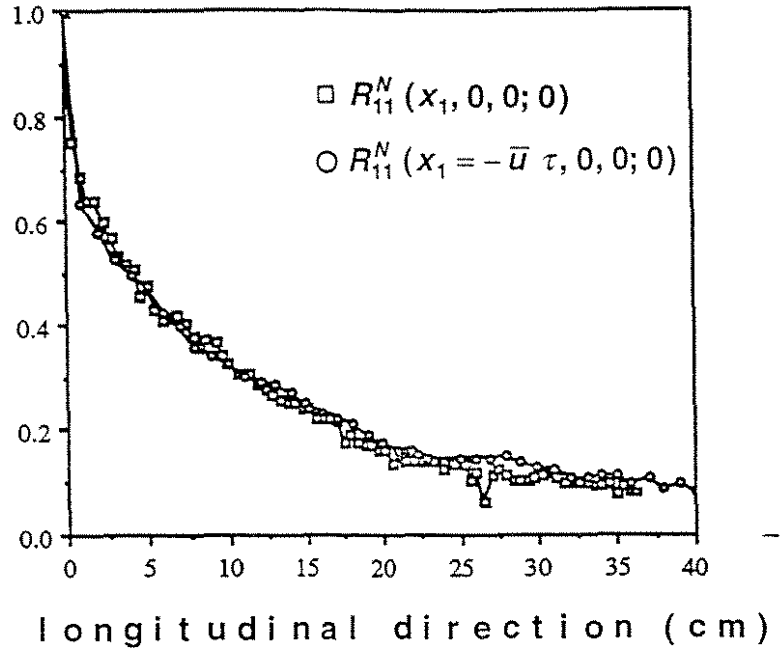

Fig. 2. Spatial correlation functions of the horizontal velocity component at z/h = 0.5 measured with the monostatic ADVP.

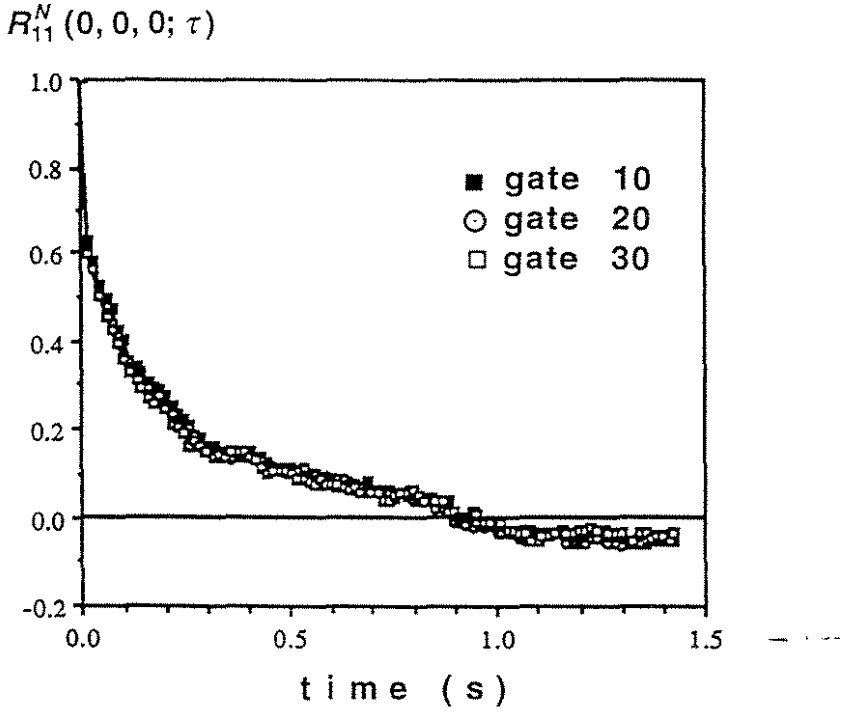

Fig. 3. Auto-correlation functions of the horizontal velocity component at z/h = 0.5 for different gates measured with the horizontal monostatic ADVP.

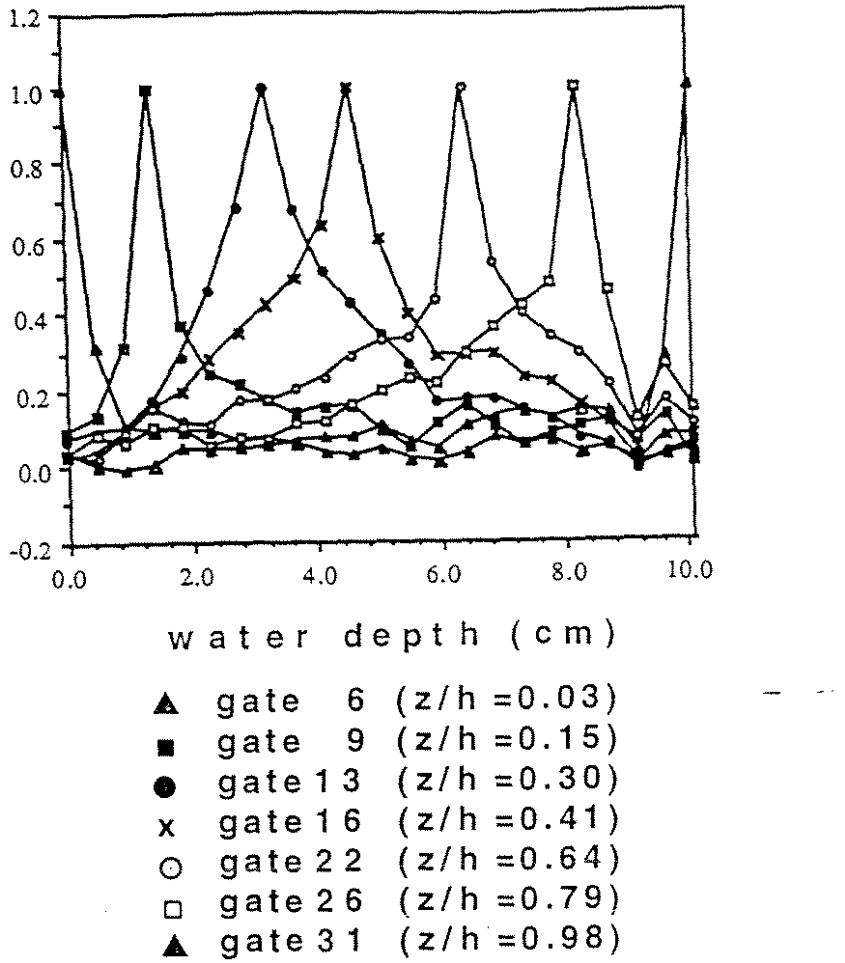

Fig. 4. Spatial correlation functions of the vertical velocity component for different reference gates measured with the vertical monostatic ADVP.

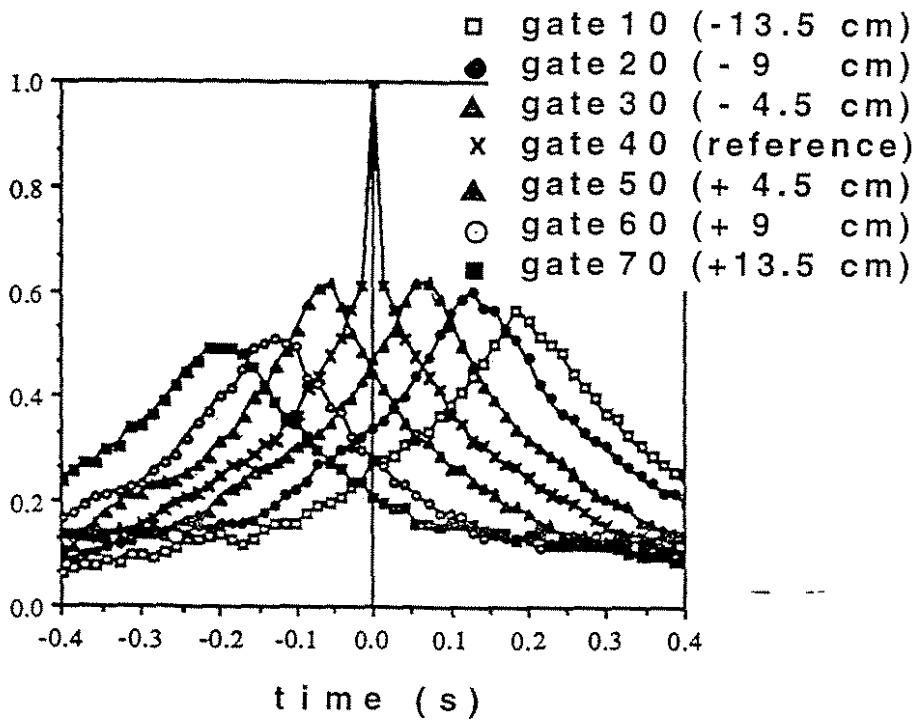

Fig. 5. Space-time correlation functions of the horizontal velocity component at z/h = 0.5 measured with the horizontal monostatic ADVP.

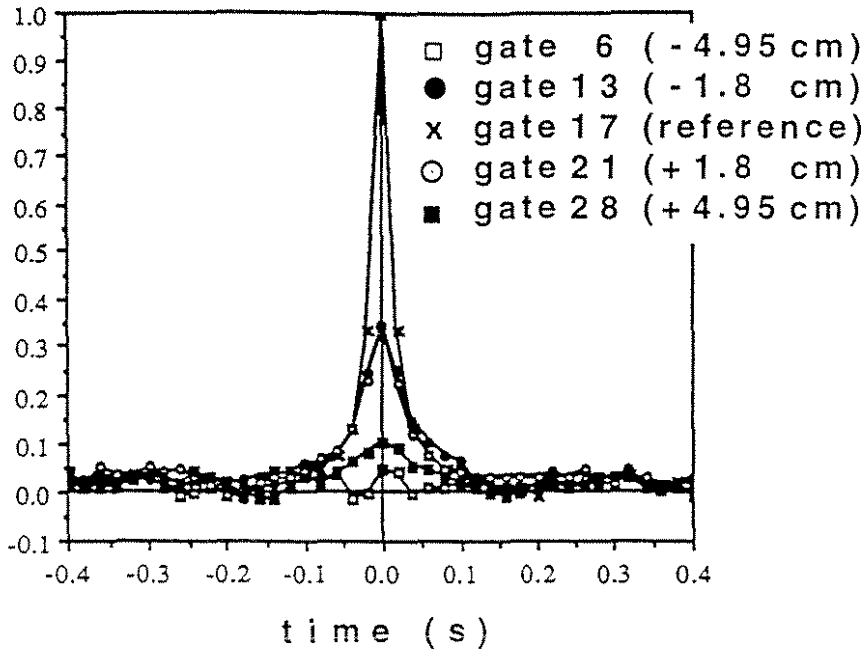

Fig. 6. Space-time correlation functions of the vertical velocity component measured with the vertical monostatic ADVP.

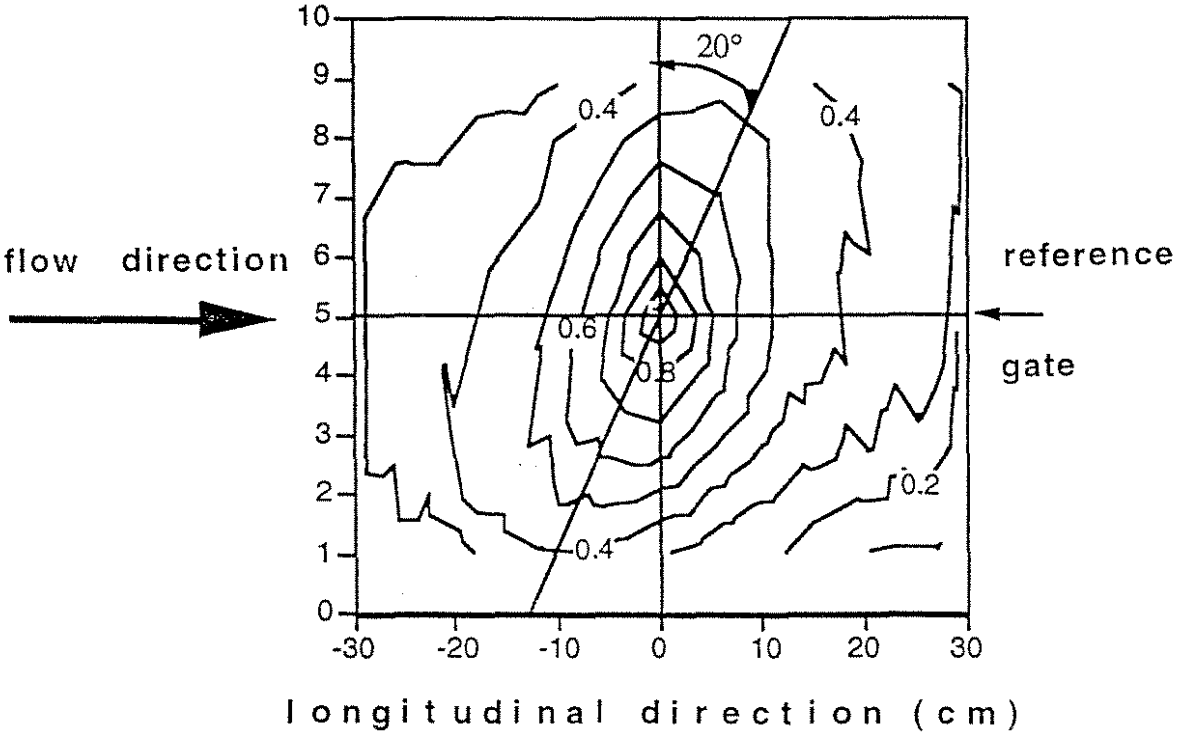

Fig. 7. Iso-correlation pattern of the horizontal velocity component for the full water depth measured with the bistatic ADVP.

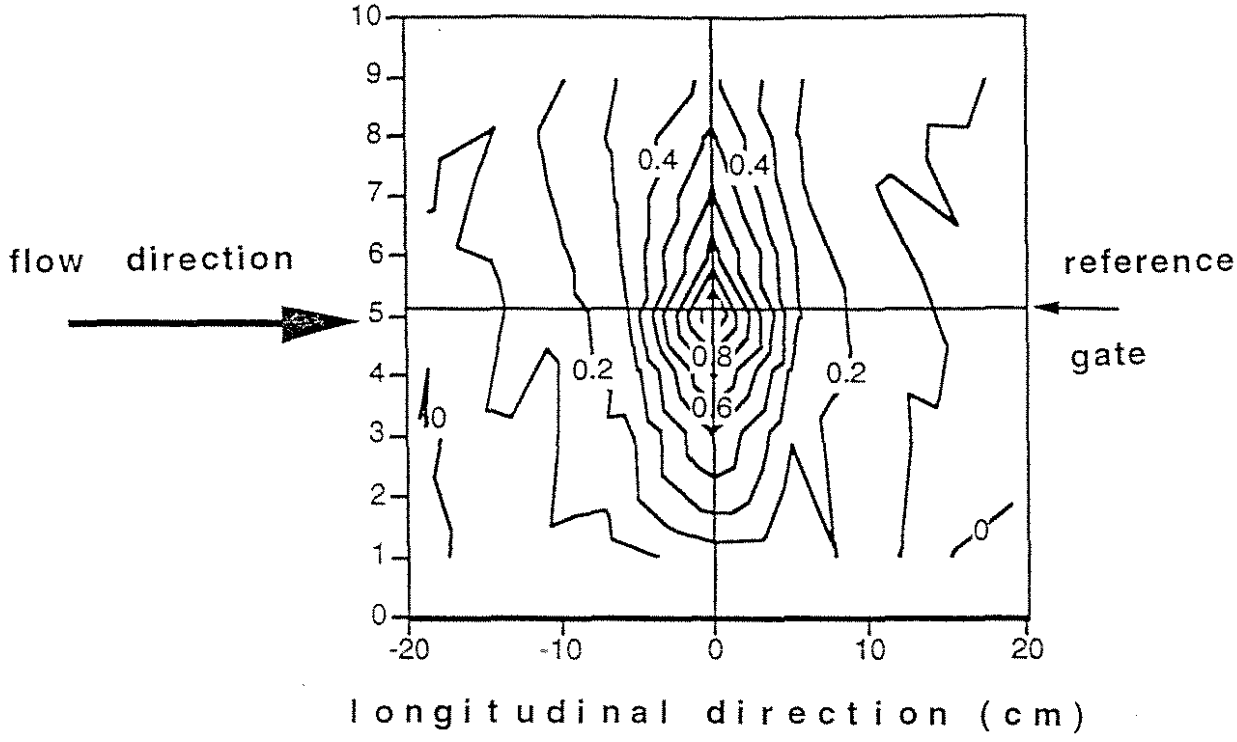

Fig. 8. Iso-correlation pattern of the vertical velocity component for the full water depth measured with the bistatic ADVP.

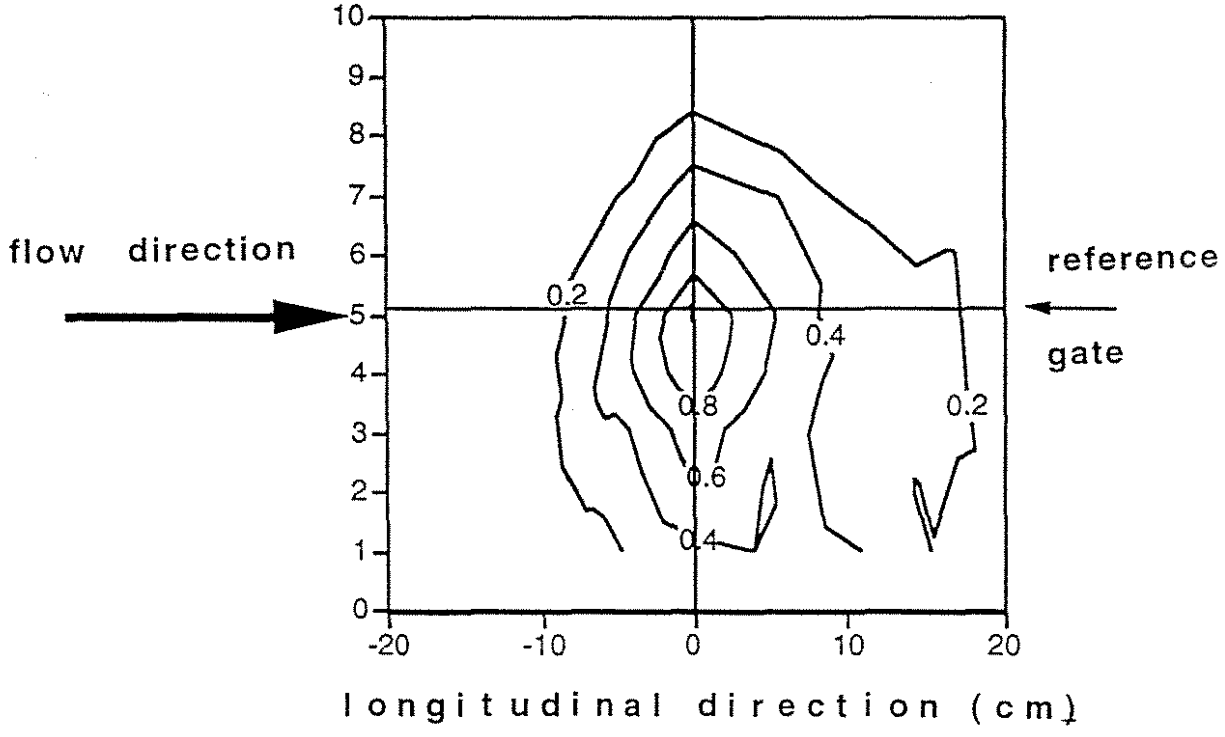

Fig. 9. Iso-cross-correlation pattern between the horizontal velocity component measured at z/h = 0.5 and the vertical velocity component for the full water depth; measured with the bistatic ADVP.

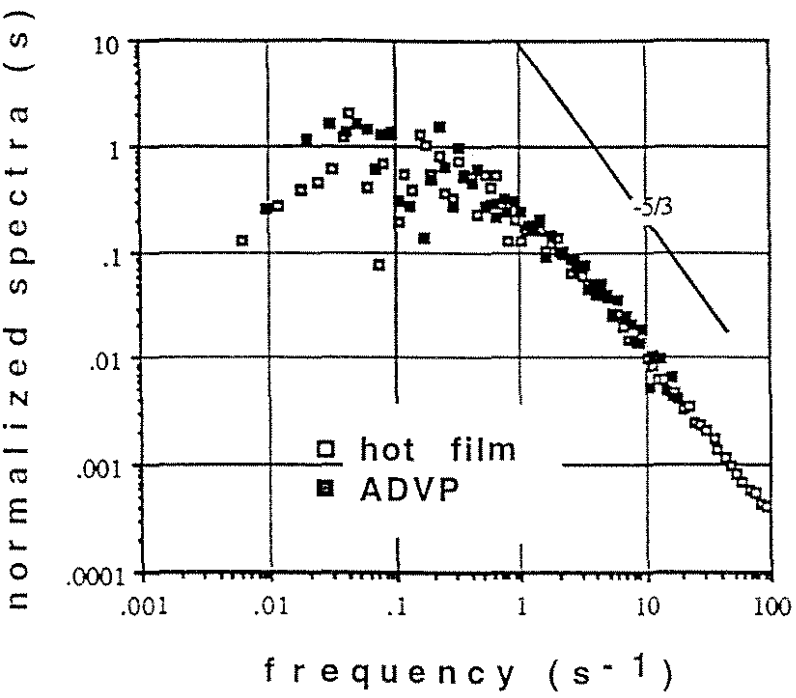

Fig. 10. Spectrum of the horizontal velocity component measured with the inclined monostatic ADVP and with the hot film anemometer.

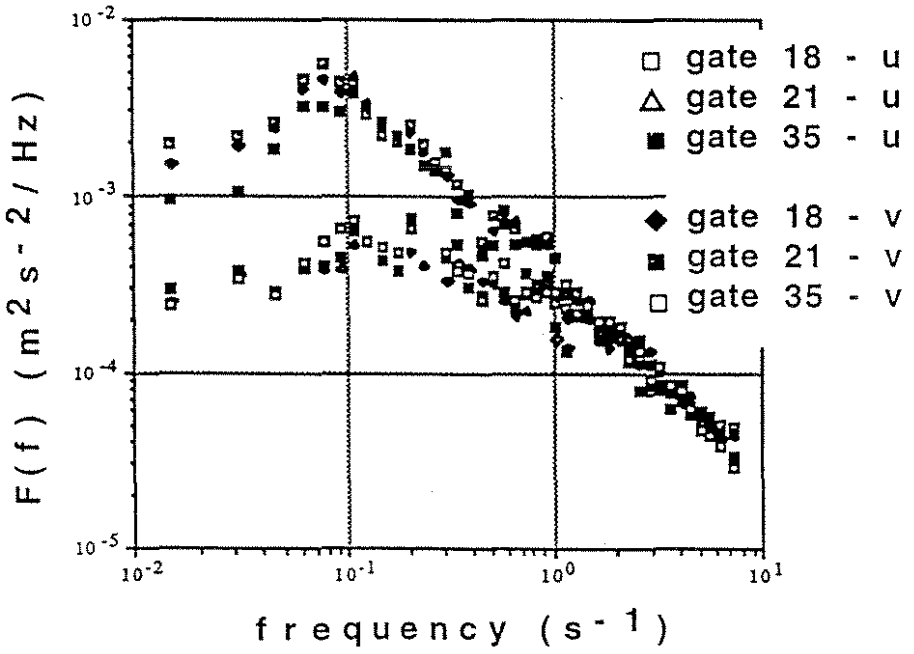

Fig. 11. Spectra of the horizontal and the vertical velocity components at different depths measured with the bistatic ADVP.

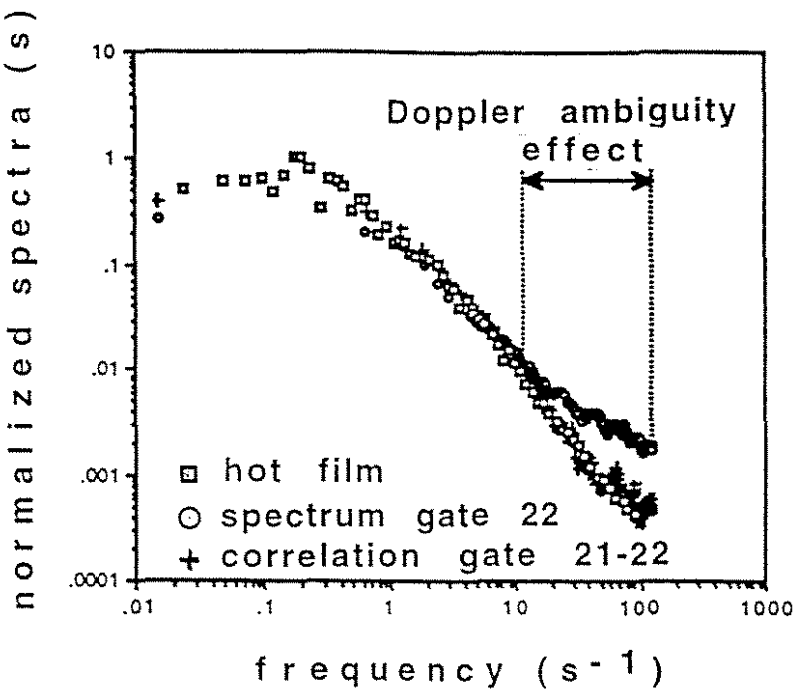

Fig. 12. The Doppler ambiguity effect and its elimination. Spectra of the horizontal velocity component measured with the inclined monostatic ADVP and with the hot film anemometer.

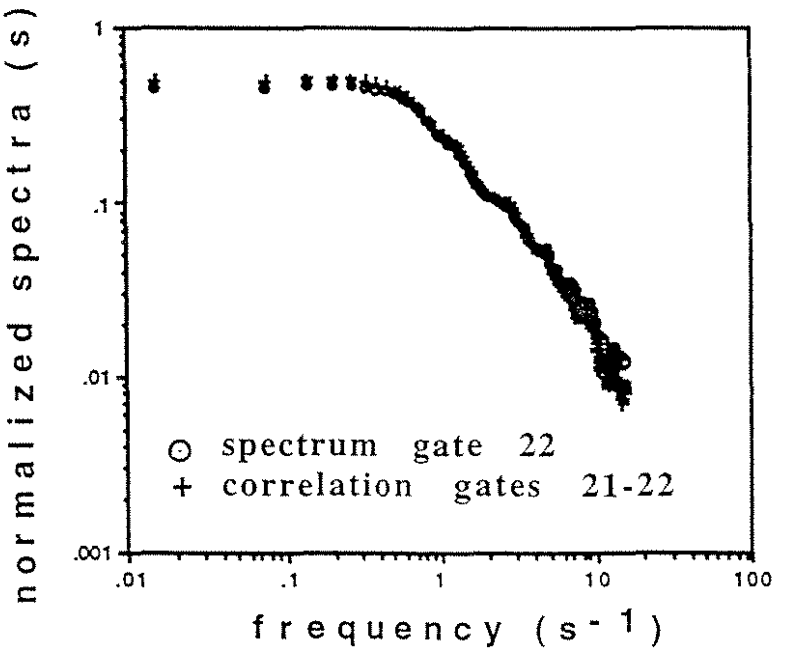

Fig. 13. The Doppler ambiguity effect and its elimination. Spectrum of the horizontal velocity component measured with the inclined monostatic ADVP and N_{pp} = 32 compared to the spectrum obtained by the two gate cross-correlation procedure.

MEASUREMENT SYSTEM AND MULTI-DIMENSIONAL FLOW CHARACTERISTICS OF BUBBLY COUNTERCURRENT FLOW

- Effects of Air and Water Flow Rates -

Shirong ZHOU [1],Masanori ARITOMI [1], Junji MIZOGUCHI [2],

Yasushi TAKEDA [3] and Michitsugu MORI [4]

1 Tokyo Institute of Technology, 2-12-1 Ohokayama, Meguro-ku, Tokyo, 152 Japan
TEL +81-3-5734-3063, FAX +81-3-5734-2959

2 Shibaura Institute of Technology, 307 Tameihara, Fukasaku, Omiya, 330 Japan
TEL +81-48-687-5058, FAX +81-48-687-5116

3 Paul Scherrer Institut, Wurenlingen and Villigen, CH-5232, Villigen, Switzerland
TEL +41-56-310-3568, FAX +41-56-310-3131

4 Tokyo Electric Power Co., 1-1-3 Uchisaiwai-cho, Chiyoda-ku, Tokyo, 100 Japan
TEL +81-45-585-8932, FAX +81-45-585-8943

Contact person: Masanori ARITOMI
Professor
Research Laboratory For Nuclear Reactors,
Tokyo Institute of Technology
2-12-1 Ohokayama, Meguro-ku, Tokyo,152 Japan
TEL +81-3-5734-3063, FAX +81-3-5734-2959

ABSTRACT

The authors have developed a new measurement system which consisted of an ultrasonic velocity profile monitor and a video data processing unit in order to clarify its multi-dimensional flow characteristics in bubbly flow and to offer a data base to validate numerical codes for multi-dimensional two-phase flow. In this paper, the proposed measurement system was applied for fully developed bubbly countercurrent flows in a vertical rectangular channel. At first, both bubble and water velocity profiles and void fraction profiles in the channel were investigated statistically. Next, turbulence intensity in the channel was defined as a standard deviation of velocity fluctuation in a continuous liquid phase, and the two-phase multiplier profile of turbulence intensity in bubbly countercurrent flows was clarified. In addition, the distribution parameter and drift velocity used in the drift flux model were calculated directly from these profiles.

1. INTRODUCTION

In the study of two-phase flow, the knowledge of bubbly and liquid velocities is required for better understanding of transport phenomena in two-phase flow systems. The void fraction is the most important parameter for engineering use, e.g. for the design of nuclear reactors, steam boilers, evaporating equipment, refrigerating equipment, etc. Recently, many concepts of future light water reactor (LWRs), in which passive and simplified safety functions are actively introduced into their safety features, have been proposed such as the AP-600 design (Tower et al. 1988) and the SBWR design (Duncan 1988) in order to reduce their construction cost, to improve their reliability and maintainability and so on. However, since passive safety features are functioned by the law of nature, the driving force is much smaller than that induced by active ones. Multi-dimensional two-phase flow may, therefore, appear after their safety features are activated. Consequently, it is necessary with regard to passive safety features to be able to simulate multi-dimensional flow characteristics even for the two-phase flow which can be regarded as one dimensional flow for active ones.

The two-phase flow shows essentially multi-dimensional characteristics even in a simple

channel. The safety analysis codes such as the TRAC (Liles et al. 1979) and RELAP5 (Ransom et al. 1981) treat the flow basically as one dimensional flow and introduce multi-dimensional convection effects in a macroscopic way due to a lack of a fundamental data base for establishing the model of multi-dimensional two-phase flow dynamics. It is one of the important problems to establish an analytical method of multi-dimensional two-phase flow to verify analytically the effectiveness of passive safety features. It is also one of the most important subjects in the research of two-phase flow dynamics to clarify its multi-dimensional flow characteristics.

Recently, an ultrasonic Doppler method for velocity profile measurement has been developed for liquid flow measurements by Takeda (1995). It can measure a local velocity profile instantaneously as a component in the ultrasonic beam direction, so that a velocity field can be measured in space and time domain (Takeda 1994). The authors have developed a new measurement system composed of Ultrasonic Velocity Profile Monitor (UVP) and a Video Data Processing Unit (VDP) to measure multi-dimensional flow characteristics in bubbly flow (Aritomi et al. 1996), which can measure simultaneously the multi-dimensional flow characteristics of bubbly flow such as velocity profiles of both gas and liquid phases and a void fraction profile in a channel, an average bubble diameter and an average void fraction.

In this paper, the proposed measurement system was applied to fully developed bubbly countercurrent flows in a vertical rectangular channel in order to understand the multi-dimensional flow characteristics and to offer a data base to validate numerical codes for multi-dimensional two-phase flow. At first, both bubble and water velocity profiles and void fraction profiles in the channel were investigated statistically under various conditions of both air and water flow rates. Next, turbulence intensity in the channel was defined as a standard deviation of velocity fluctuation in a continuous liquid phase, and the two-phase multiplier profile of turbulence intensity in the channel was measured as a ratio of the standard deviation of velocity fluctuation in a bubbly countercurrent flow to that in a water single phase flow. In addition, concerning the drift flux model, the distribution parameter and the drift velocity

were calculated directly from these profiles, and were compared with the correlation proposed for bubbly countercurrent flows.

2. EXPERIMENTAL APPARATUS AND MEASUREMENT PRINCIPLE

2.1 Experimental Apparatus

Figure 1 shows a schematic diagram of an experimental apparatus. Air and water were used as working fluids. The experimental apparatus was composed of a water circulation system, an air supply system, a test section and a measurement system. The test section was a vertical rectangular channel of 10mmx100mmx500mm made of Plexiglas as shown in **Fig.2**. The measurement system consisted of the UVP, the VDP and a personal computer to record and treat data.

Water was fed into the upper tank and flowed downward in the test section. The water level in an upper tank was kept constant with an overflow nozzle which was connected to a lower feedwater tank. The flow rate was regulated by a flow control valve and measured by an orifice flowmeter which were installed at the downstream end of the test section. Adopting this flow control system, the water flow rate could be kept constant for hours. Microparticles of nylon powder were suspended in water to reflect ultrasonic pulses. Water temperature is kept constant by a subcooler.

The air supply system consisted of a compressor and a pressure regulation valve. Bubbles were injected from three needles located near the bottom of the channel. The air flow rate was measured by a float flowmeter and regulated by another flow control valve. As a result, the air flow rate could be kept constant for hours. Pressure transducers and thermocouples were installed at several points in the loop to monitor the flow condition. A personal computer acquired the readings from these sensors for an on-line control of the experimental condition.

An ultrasonic transducer was installed on the outside surface of the front wall of the channel with a contact angle θ of 45° and a gap between the transducer and the wall was

filled with a jelly to prevent a reflection of ultrasonic pulses on the wall surface as shown in **Fig.2**. After both air and water flow rates were set up at the desired values, 9,216 (1,024x9) velocity profiles along a measured line were measured under one experimental condition to treat them statistically. It takes about 30 minutes to get them. The hydrostatic head was simultaneously measured as a pressure drop between the pressure taps installed on the side wall using a differential pressure transducer to get an averaged void fraction.

An outline of video camera equipment is shown in **Fig.3**, which consists of an 8mm video camera, a light source and a translucent sheet to unify the luminance brightness. The speed, diaphragm and gain of the video camera can be manually regulated and a speed of 60 flames per second can be obtained. After videotaping, the video digital data were recorded in a personal computer through an image converter. The picture elements are 640x240 dots, the color is monotone, and the brightness resolution is 1/256. Since the measurement method of the VDP was described in our previous work (Aritomi et al. 1996), its description is omitted here.

The experimental conditions are tabulated in **Table 1.**

2.2 Measurement Principle of UVP

Since the detailed information of the proposed measurement system was reported in our previous work (Aritomi et al. 1996), its measurement principle is described briefly and to the point in this paper.

The working principle of the UVP is to use the echo of ultrasonic pulses reflected by microparticles suspended in the fluid. An ultrasonic transducer takes roles of both emitting ultrasonic pulses and receiving the echoes, that is, the backscattered ultrasound is received for a time interval between two emissions.

The position information, x, is obtained from the time lapse, τ, from the emission to the reception of the echo:

$$x = c\tau / 2 , \tag{1}$$

where c is a sound speed in the fluid. An instantaneous local velocity, $u_{UVP}(x_i)$, as a component in the ultrasonic beam direction, is derived from the instantaneous Doppler shift frequency, f_D, in the echo:

$$u_{UVP} = cf_D / 2f , \tag{2}$$

where f is the basic ultrasonic frequency (4MHz). The velocity resolution is 0.75mm/s for our proposed system. Horizontal position, y, and axial velocity, u, can be expressed by

$$y = \Delta x \cdot i \cdot \sin\theta , \tag{3}$$

and

$$u = u_{UVP} / \cos\theta , \tag{4}$$

where $\triangle x$ is a spatial resolution, which is 0.74 mm for our proposed system, i is the number of the reception of the emission echo.

A probability density function includes the velocity information of both phases. Assuming that each probability density function of both phases can be expressed by a normal distribution,

$$N[\bar{u},\ \sigma^2](u) = \frac{1}{\sqrt{2\pi\sigma^2}} \exp\left[-\frac{(u - \bar{u})^2}{2\sigma^2}\right] . \tag{5}$$

The probability density function of mixture velocity is given by

$$P_u(y,u) = \varepsilon(y)N[\bar{u}_G(y),\sigma_G^2(y)](u) + (1 - \varepsilon(y))N[\bar{u}_L(y),\sigma_L^2(y)](u) . \tag{6}$$

where $\bar{u}_G$ and $\bar{u}_L$ are average velocities of gas and liquid phases respectively, σ_G and σ_L

are standard deviations of both phases respectively and ε is the probability of bubble existence. These five variables, $\bar{u}_G$, $\bar{u}_L$, σ_G, σ_L and ε, are calculated numerically and iteratively by the least squares method. An example of the probability density function obtained from the UVP data is representatively shown in **Fig.4**.

As long as a bubble exists, the ultrasonic pulse is reflected at its surface, so that the bubble velocity can be always detected as the interfacial velocity. On the other hand, the ultrasonic wave is not reflected in water where a microparticle does not exist. As a result, water velocity is not always measured in the profile. Hence, it is necessary to revise the probability of bubble existence as follows:

$$\kappa(y) = P_s(y)\ \varepsilon(y), \tag{7}$$

where $P_s(y)$ is the probability of data existence. $\kappa(y)$ is called the probability of bubble data existence in this work.

The average void fraction was obtained by measuring the hydrostatic head or from the VDP data. Assuming that the local void fraction is proportional to the local probability of bubble data existence and that the proportional constant, k, is uniform in the channel since it is dependent on bubble size and configuration, the average void fraction is expressed by

$$<\alpha> = k\int_A \kappa\, dA / A = k<\kappa> . \tag{8}$$

The proportional constant, k, was calculated from measured average void fraction, $<\alpha>$, and measured average probability of bubble data existence, $<\kappa>$. Then, local void fraction, $\alpha(y)$, is given by

$$\alpha(y) = k\ \kappa(y) . \tag{9}$$

The UVP specification used in this work is tabulated in **Table 2**.

3. RESULTS AND DISCUSSION

3.1 Multi-dimensional Flow Characteristics

Velocity profiles of both phases in the channel were measured with the UVP. At first, the effects of air flow rates on flow characteristics in bubbly countercurrent flows was investigated for both low and high water flow rates. The experimental results are shown in **Figs.5(a)** and **(b)**. Since it is very difficult to measure the velocities near the wall with significant accuracy due to an ultrasonic beam diameter of 5mm, they are omitted in these figures. Water downward velocities become higher toward the center of the channel from the wall in the same tendency as water single phase flow. In contrast with this, bubble velocities are higher near the wall than those in the core. Relative velocity was defined by a difference between the bubble and water velocities. Relative velocity profiles were calculated from the results shown in **Figs.5(a)** and **(b)** and are shown in **Figs.6(a)** and **(b)**. It can be seen from these figure that the relative velocities are almost constant in the whole channel and are scarcely varied with changes in the water flow rate. It is clear from **Figs.5** and **6** that the flow characteristics of bubbly countercurrent flow is strongly dependent on the water velocity which is a continuous phase and that a bubble rising velocity is induced by the difference between the buoyancy and interfacial drag force. As a result, in fully developed bubbly countercurrent flow with the almost same bubble diameter in the channel, the relative velocities are almost equal in the whole channel. Since air flow rates are much lower than water ones under the present conditions, the velocity profiles of both phases are scarcely varied even if the air flow rate increases.

Next, the effects of water flow rates on flow characteristics in bubbly countercurrent flows was also investigated for both low and high air flow rates. The experimental results are shown in **Figs.7(a)** and **(b)**. It can be seen from the figure that water velocities become higher but their profiles are scarcely influenced with an increase in a water flow rate. However, bubble rising velocities become lower but their profiles are still hardly affected under the

present conditions. With an increase in water flow rate, an impact pressure at bubble generation nozzles becomes larger and bubble rising velocity decreases. Relative velocity profiles were calculated from the results shown in **Figs.7(a)** and **(b)** and are shown in **Figs.8(a)** and **(b)**. It can be seen from these figures that the relative velocities are almost constant in the whole channel and are scarcely varied with changes in the air flow rate.

3.2 Void Fraction Profiles

The hydrostatic head is obtained from the measured differential pressure and average void fraction is calculated by

$$(\Delta P / \Delta Z)_{Head} = \rho_G <\alpha> g + \rho_L (1 - <\alpha>) g \ , \tag{10}$$

because friction loss is negligibly small due to low water flow rates. According to Eqs.(8), (9) and (10), $\alpha(y)$ can be calculated. The threshold brightness (Aritomi et al. 1996), which identifies the bubble surface, influences evaluation of the average bubble diameter and void fraction even though it does not affect the number of bubbles, the threshold brightness was calibrated. A comparison of average void fractions obtained by the hydrostatic head and by the VDP is shown in **Fig.9**. The void fractions obtained by the VDP agree well with those obtained by the hydrostatic head.

A bubble diameter is calculated from its volume by assuming that it is spherical. The relationship between average bubble diameters and average void fractions is shown in **Fig.10**. With an increase in a water flow rate, an impact pressure at bubble generation nozzles becomes larger and a bubble rising velocity decreases as shown in **Figs.7(a)** and **(b)**, so that the average bubble diameter becomes larger. In addition, as an air flow rate increases, the average bubble diameter increases because the air pressure in the bubble generation needles is enlarged.

Figures 11(a) and **(b)** show the typical measured results of a probability profile of bubble data existence. The probability of bubble data existence means that a bubble exists in an

ultrasonic pulse path when the pulse is emitted. It is clearly seen from the figure that the probability of bubble data existence increases with air and water flow rates increase. A void fraction profile in the channel can be calculated from Eqs.(8) and (9) and the measured probability profile of bubble data existence. The effects of air flow rates on the void fraction profile for both low and high water flow rates are shown in **Figs.12(a)** and **(b)**, respectively. It can be seen from these figures that void fraction profiles are almost flat in bubbly countercurrent flows except for those near the wall. Since air flow rates are much lower than water ones under the present experimental conditions, water velocity profiles are scarcely varied even with a change in air flow rates. As a result, bubble velocity is dependent on the water velocity profile as shown in **Figs.5** and **7**. The void fraction is, consequently, enlarged with an increase in air flow rates as shown in **Figs.12(a)** and **(b)**. This tendency appears more strongly for higher water flow rate. Next, the effects of water flow rates on the void fraction profile for both low and high air flow rates are shown in **Figs.13(a)** and **(b)**, respectively. As the water flow rate increases, the bubble rising velocity is decreased, so that void fraction becomes larger. This tendency appears more remarkably with an increase in the air flow rate.

3.3 Turbulence Intensity Profile

As a general rule, the turbulence intensity in a bubbly flow is larger than that in liquid single phase flow because bubbles agitate the flow. In this work, the turbulence intensity is defined as a standard deviation of water velocity fluctuation in a continuous liquid phase, σ_L given by Eq.(6). Typical results in a water single flow and a bubbly countercurrent flow are shown in **Figs.14** **(a)** and **(b)**, respectively. In a water downward flow, the turbulence intensity has the maximum value near the wall and becomes lower with going toward the center of the channel in the same manner as a single phase flow because the gradient of longitudinal velocities is higher near the wall. On the other hand, in a bubbly countercurrent flow, the turbulence intensity becomes higher with going toward the center of the channel and has the maximum value in the center of the channel. Fluctuation of bubble upflow in the core

is larger than that near the wall because the restriction of the boundary is weakened. This fact indicates that bubbles agitate the flow in a continuous liquid phase.

Since local velocities were measured not at a point but on the area because of an ultrasonic beam diameter of 5mm, the absolute value of the standard deviation in a water phase is not significant. Hence, The ratio of the standard deviation ratio in a bubbly countercurrent flow to that in a water single phase flow is selected as two-phase multiplier of turbulence intensity, $\sigma_{LTPF}/\sigma_{LSPF}$. **Figures 15(a)** and **(b)** show the effects of air flow rates on the two-phase multiplier of turbulence intensity for both low and high water flow rates, respectively. The two-phase multiplier of turbulence intensity becomes larger with going toward the center of the channel. It can be seen from these figures that $\sigma_{LTPF}/\sigma_{LSPF}$ are enhanced with increases in air flow rates. This tendency becomes more notable with an increase in the water flow rate.

Next, the effects of water flow rates on the profile of $\sigma_{LTPF}/\sigma_{LSPF}$ for both low and high air flow rates are illustrated in **Figs.16(a)** and **(b)**, respectively. As the water flow rate increases, the profiles of $\sigma_{LTPF}/\sigma_{LSPF}$ are scarcely varied at a low air flow rate but becomes larger at a high one.

Typical measured results of velocity profile of both phases, $u_G(y)$ and $u_L(y)$, void fraction profile, $\alpha(y)$, and two-phase multiplier profile of turbulence intensity, $\sigma_{LTPF}/\sigma_{LSPF}$ are tabulated in **Table 3** as a data base to model multi-dimensional two-phase flow and validate its numerical codes. j_L, j_G, D_b mean specific velocities of water and air and the average bubble diameter, respectively, y is the horizontal position and H is the width of the channel, 10mm.

3.4 Distribution Parameter and Drift Velocity

The drift flux model proposed by Zuber and Findlay (1965) is widely applied to two-phase flow analysis codes. The following notations are introduced:

$$\langle F \rangle = \frac{\int_A F dA}{A} \tag{11}$$

and

$$\langle F \rangle = \frac{\langle \alpha F \rangle}{\langle \alpha \rangle} \tag{12}$$

where F is a variable and A is a flow channel cross section. In the drift flux model, local drift velocity, v_{gj}, and the distribution parameter, C_0, are defined as follows:

$$v_{gj} = u_G - j \ , \tag{13}$$

and

$$C_O = \langle \alpha j \rangle / \langle \alpha \rangle \langle j \rangle \ , \tag{14}$$

where j is volumetric flux and defined by

$$j = j_G + j_L = \alpha u_G + (1 - \alpha) u_L \ . \tag{15}$$

Since it was difficult to measure velocity profiles of both phases and void fraction profiles directly, in many previous works, average void fractions were measured under various conditions of $\langle j_G \rangle$ and $\langle j_L \rangle$, and C_0 and V_{gj} were determined by

$$\frac{\langle j_G \rangle}{\langle \alpha \rangle} = C_0 \langle j \rangle + \langle v_{gj} \rangle = C_0 \langle j \rangle + V_{gj} \ . \tag{16}$$

In this work, velocity profiles of both phases and void fraction profiles can be measured. Local drift velocity is given by

$$v_{gj}(y) = [1-\alpha(y)][u_G(y) - u_L(y)] \ . \qquad (17)$$

Substituting experimental results of $u_G(y)$, $u_L(y)$ and $\alpha(y)$ into Eqs.(14), (15) and (17), the distribution parameters and the drift velocity were calculated and the results are shown in **Figs.17** and **18**, respectively. It can be seen from **Figs.12** and **13** that the void fraction profiles are nearly flat except for those near the wall. Consequently, the distribution parameter is almost 1.0. Substituting properties of air and water into the correlation proposed by Zuber and Findlay (1965), $V_{gj} = 0.231m/s$. The results shown in **Fig.18** are identical to this value.

4. CONCLUDING REMARKS

The measurement system composed of the UVP and the VDP was applied to measure flow characteristics of bubbly countercurrent flows. The following insights are clarified:

(1) Water downward velocities become higher with leaving the wall but bubble rising velocities decreases because of higher water velocities. The relative velocities between both phases are scarcely varied in the channel.

(2) Void fractions in the channel are almost constant except for those near the wall.

(3) For the bubbly countercurrent flow, the turbulence intensity is greater than that in water single phase flow and increases with going toward the center from the wall.

(4) The two-phase multiplier of turbulence intensity increases with increases in air and/or water flow rates. Moreover, the effects of air flow rates on the two-phase multiplier of turbulence intensity is greater than that of water flow rates.

(5) Concerning the drift flux model, the distribution parameter is 1.0 for bubbly countercurrent flow and the drift velocity is the same value as proposed for bubbly upflows.

This work was performed at the Tokyo Institute of Technology in collaboration with the Tokyo Electric Power Company and the Paul Scherrer Institut.

REFERENCE

Aritomi, M., Zhou, S., Nakajima, M., Takeda, Y., Mori, M., and Yoshioka, Y. (1996),

Measurement system of bubbly flow using ultrasonic velocity profile monitor and video data processing unit. J. Nucl.Sci Technol., **33** 915–923.

Duncan, J.D. (1988), SBWR: A simplified boiling water reactor. Nucl. Engrg. Des., **109**, 73–77.

Liles, D.R. et al. (1979), TRAC–P1A: An advanced best–estimate computer programs for PWR LOCA analysis. NUREG/CR–0665.

Ransom, V.H. et al. (1981), RELAP5/MOD1 code manual. Vol. 1 System and numerics, NUREG/CR–1827.

Takeda, Y. (1994), Decomposition of the modulated waves in a rotating couette system. Science, **263**, 502–505.

Takeda, Y., (1995), Velocity profile measurement by ultrasonic doppler method. Experimental Thermal and Fluid Sci., **10**, 444–453.

Tower, S.N., Schulz, T.L. and Vijuk R.P. (1988), Passive and simplified system features for the advanced westinghouse 600 MWe PWR, Nucl. Engrg. Des., **109**, 147–154.

Zuber, N. and Findlay J.A. (1965), Average volumetric concentration in two–phase flow systems, Trans. ASME, J. Heat Transfer, **87**, 453–468.

Table 1 Experimental conditions

System pressure	Atmospheric pressure
Water specific velocity	−0.06, −0.12m/s
Air specific velocity	0.00195 - 0.00418m/s

Table 2 The specification of the Ultrasonic Velocity Profile Monitor

Basic ultrasonic frequency	4MHz
Maximum measurable depth	758mm (variable)
Minimum spatial resolution	0.74mm
Maximum measurable velocity	0.75m/s (variable)
Velocity resolution	0.75mm/s (variable)
Measurement points	128
The number of profiles	1,024

Table 3 Measured results of the UVP

j_L = −0.06(*m/s*) , j_G =0.00195(*m/s*) , D_b = 3.23(*mm*)

y/(H/2)(mm)	u_G(*m/s*)	u_L(*m/s*)	α	$\sigma_{LTPF}/\sigma_{LSPF}$
0.000	0.205	−0.053	0.008	1.837
0.105	0.176	−0.059	0.010	1.558
0.211	0.169	−0.064	0.012	1.912
0.316	0.166	−0.069	0.013	2.089
0.421	0.163	−0.073	0.013	2.391
0.526	0.156	−0.075	0.014	2.739
0.632	0.150	−0.076	0.014	3.036
0.737	0.141	−0.076	0.015	3.281
0.842	0.135	−0.078	0.015	3.358
0.947	0.132	−0.080	0.015	3.347

j_L = −0.06(*m/s*) , j_G = 0.00327(*m/s*) , D_b = 3.83(*mm*)

y/(H/2)(mm)	u_G(*m/s*)	u_L(*m/s*)	α	$\sigma_{LTPF}/\sigma_{LSPF}$
0.000	0.198	−0.061	0.012	2.751
0.105	0.182	−0.066	0.015	2.325
0.211	0.170	−0.071	0.017	2.571
0.316	0.167	−0.075	0.018	2.999
0.421	0.165	−0.079	0.019	3.151
0.526	0.161	−0.082	0.020	3.412
0.632	0.156	−0.082	0.020	3.940
0.737	0.150	−0.083	0.021	4.340
0.842	0.147	−0.084	0.021	4.472
0.947	0.148	−0.085	0.020	4.387

j_L = −0.06(*m/s*) , j_G = 0.00418(*m/s*) , D_b = 4.34(*mm*)

y/(H/2)(mm)	u_G(*m/s*)	u_L(*m/s*)	α	$\sigma_{LTPF}/\sigma_{LSPF}$
0.000	0.183	−0.066	0.017	3.228
0.105	0.172	−0.073	0.020	2.810
0.211	0.165	−0.079	0.023	2.975
0.316	0.164	−0.082	0.025	3.313
0.421	0.164	−0.084	0.025	3.693
0.526	0.163	−0.087	0.026	4.067
0.632	0.159	−0.087	0.026	4.707
0.737	0.155	−0.089	0.026	5.011
0.842	0.153	−0.089	0.026	5.003
0.947	0.149	−0.092	0.026	4.797

Table 3 Measured results of the UVP

j_L = -0.12m/s) , j_G =0.00195(m/s) , D_b = 3.70(mm)

$y/(H/2)(mm)$	$u_G(m/s)$	$u_L(m/s)$	α	$\sigma_{LTPF}/\sigma_{LSPF}$
0.000	0.105	−0.097	0.017	1.304
0.105	0.094	−0.110	0.020	1.385
0.211	0.087	−0.121	0.021	1.483
0.316	0.083	−0.131	0.023	1.778
0.421	0.080	−0.136	0.024	2.260
0.526	0.068	−0.140	0.026	2.628
0.632	0.064	−0.143	0.027	3.019
0.737	0.071	−0.143	0.026	3.434
0.842	0.060	−0.144	0.027	3.407
0.947	0.070	−0.142	0.025	3.559

j_L = -0.12(m/s) , j_G = 0.00327(m/s) , D_b = 4.37(mm)

$y/(H/2)(mm)$	$u_G(m/s)$	$u_L(m/s)$	α	$\sigma_{LTPF}/\sigma_{LSPF}$
0.000	0.105	−0.092	0.033	1.677
0.105	0.098	−0.106	0.036	1.823
0.211	0.092	−0.120	0.039	1.921
0.316	0.092	−0.128	0.042	2.318
0.421	0.093	−0.134	0.043	3.009
0.526	0.096	−0.137	0.044	3.785
0.632	0.095	−0.139	0.044	4.334
0.737	0.093	−0.141	0.045	4.673
0.842	0.092	−0.141	0.045	4.916
0.947	0.089	−0.142	0.045	4.894

j_L = -0.12(m/s) , j_G = 0.00418(m/s) , D_b = 5.06(mm)

$y/(H/2)(mm)$	$u_G(m/s)$	$u_L(m/s)$	α	$\sigma_{LTPF}/\sigma_{LSPF}$
0.000	0.111	−0.104	0.049	2.269
0.105	0.108	−0.117	0.051	2.527
0.211	0.107	−0.127	0.055	2.760
0.316	0.106	−0.134	0.060	3.412
0.421	0.107	−0.134	0.062	4.311
0.526	0.110	−0.134	0.062	5.148
0.632	0.108	−0.134	0.064	6.032
0.737	0.108	−0.132	0.063	6.496
0.842	0.108	−0.130	0.064	6.666
0.947	0.107	−0.132	0.065	6.541

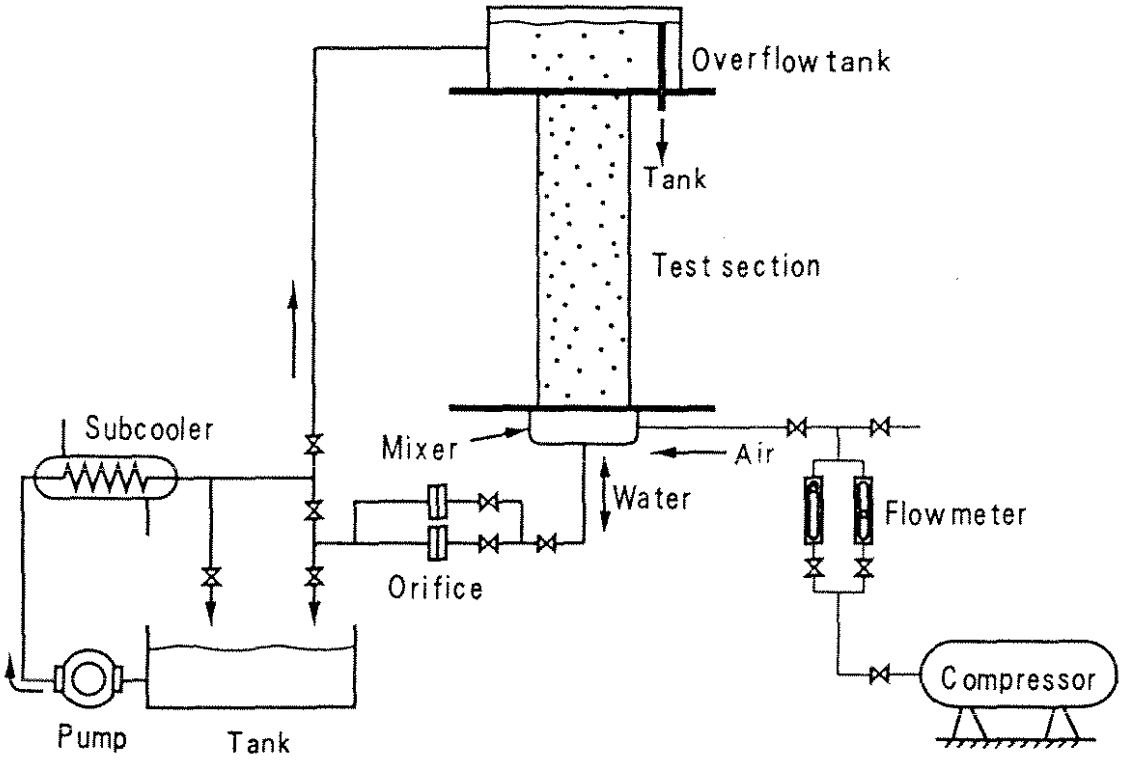

Fig.1 A schematic diagram of experimental apparatus

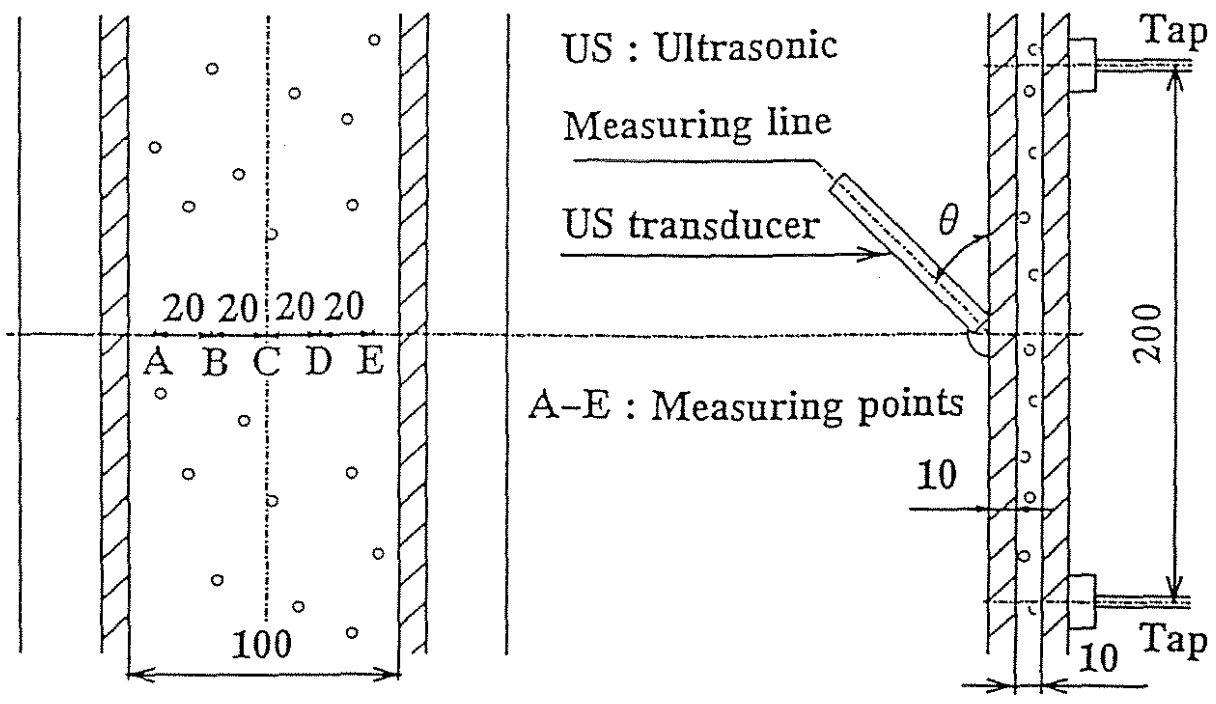

Fig.2 Test section

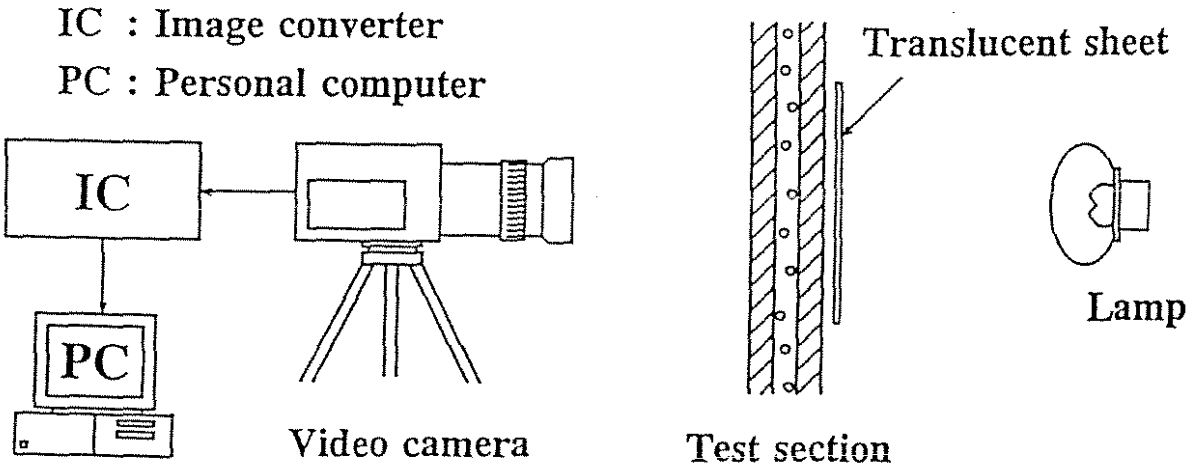

Fig.3 An outline of video camera equipment

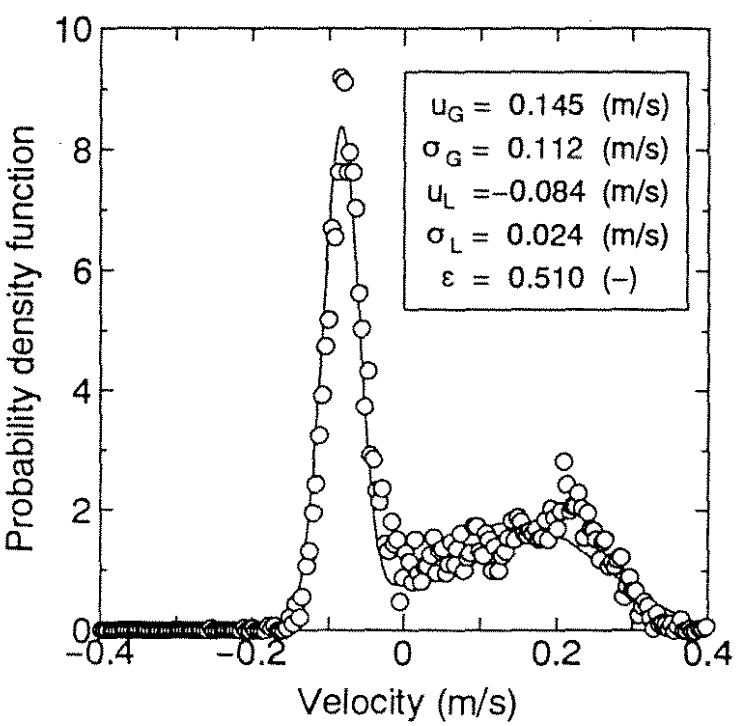

Fig. 4 A typical probability density function

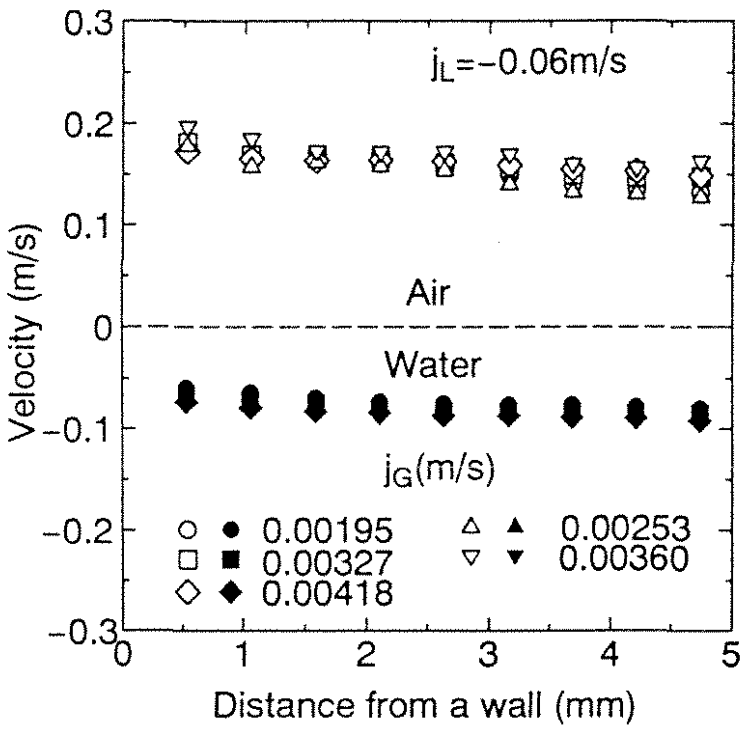

(a) Low water flow rate

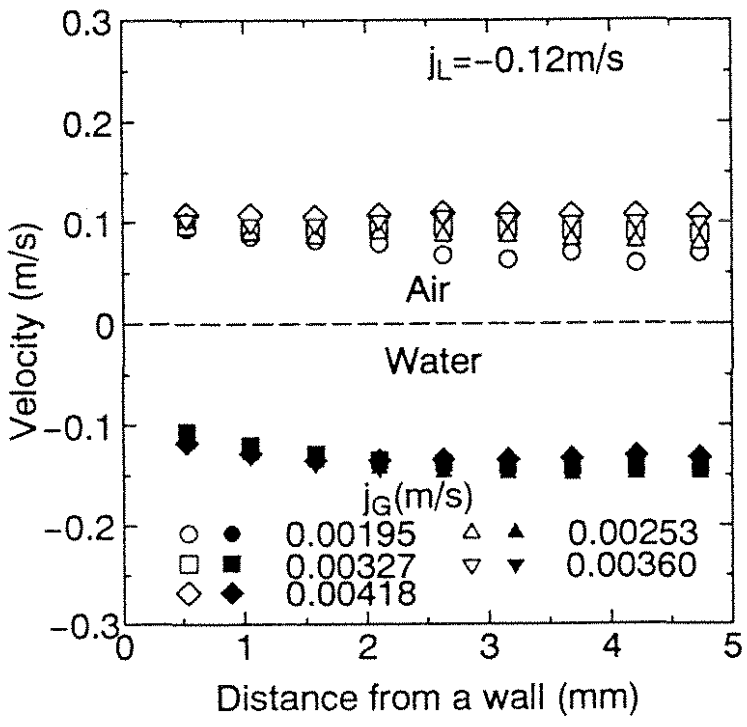

(b) High water flow rate

Fig.5 Velocity profiles of both phases in reference to air flow rates

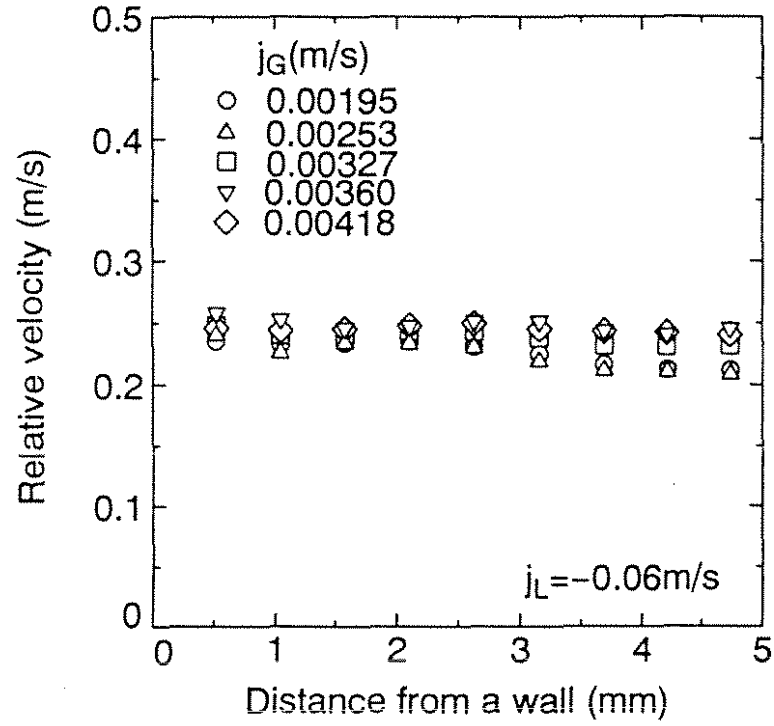

(a) Low water flow rate

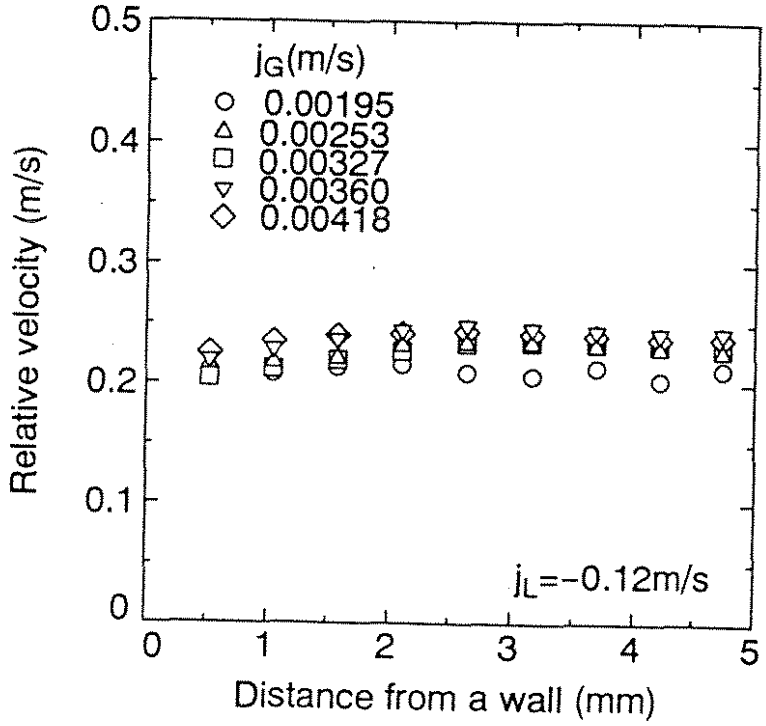

(b) High water flow rate

Fig.6 Relative velocity profiles in reference to air flow rates

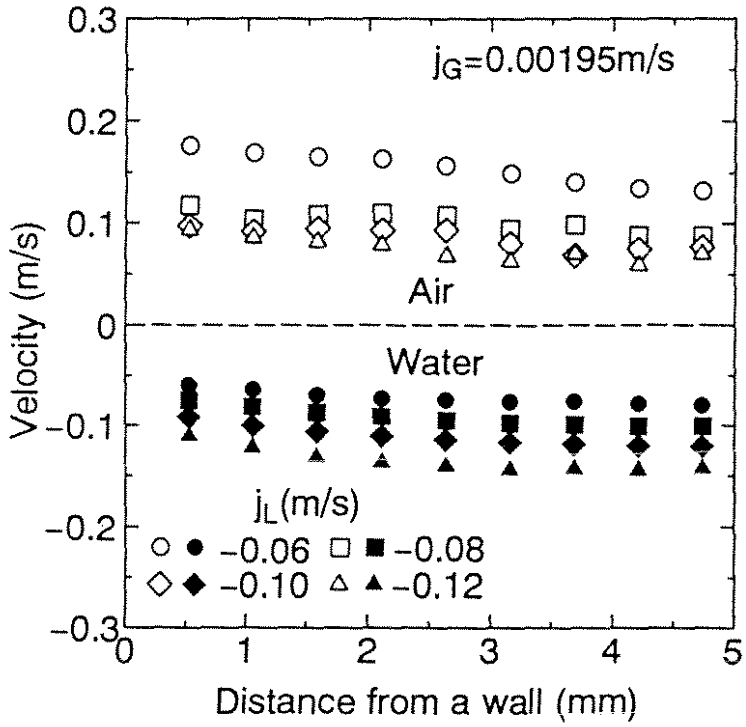

(a) Low air flow rate

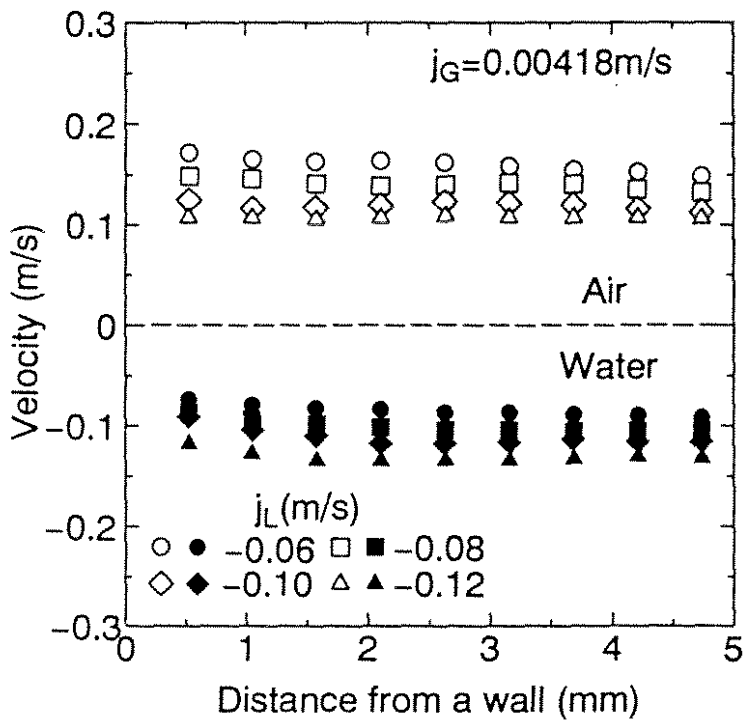

(b) High air flow rate

Fig.7 Velocity profiles of both phases in reference to water flow rates

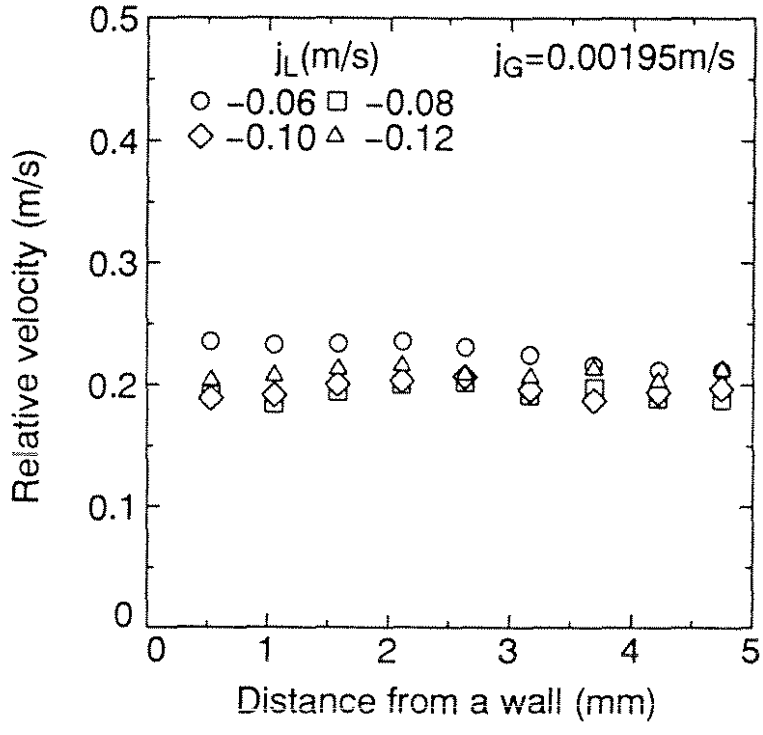

(a) Low air flow rate

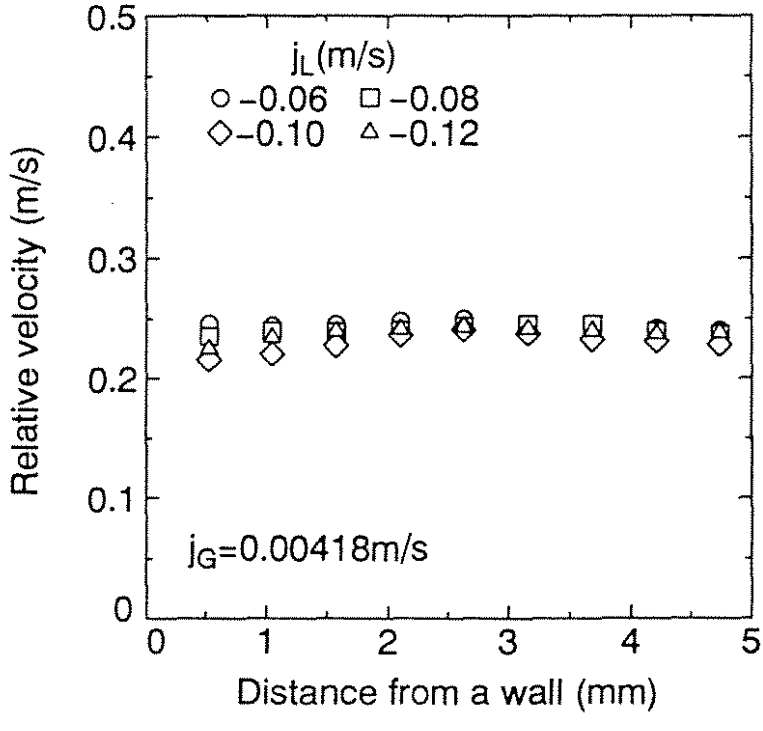

(b) High air flow rate

Fig.8 Relative velocity profiles in reference to water flow rates

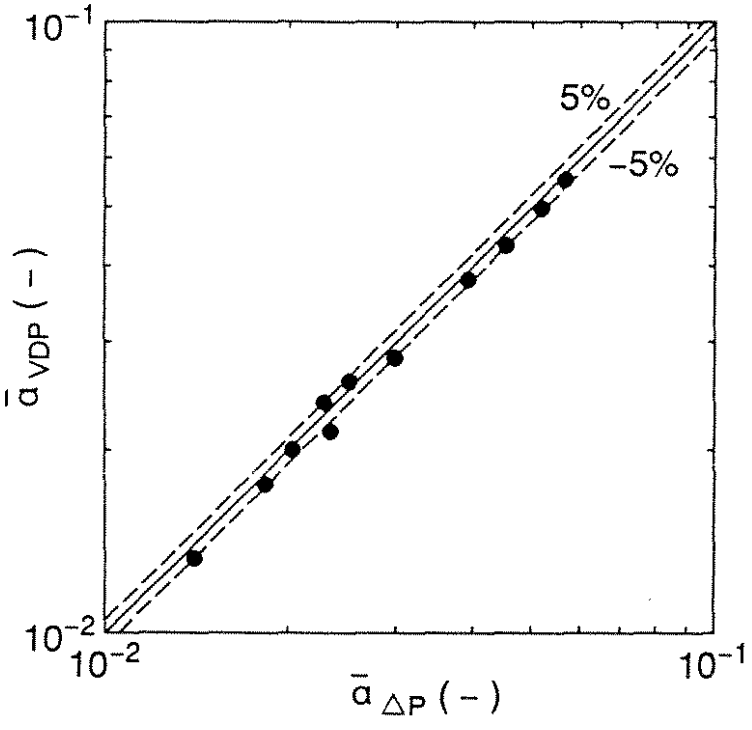

Fig.9 A comparison of average void fractions measured by hydrostatic head with those by the VDP

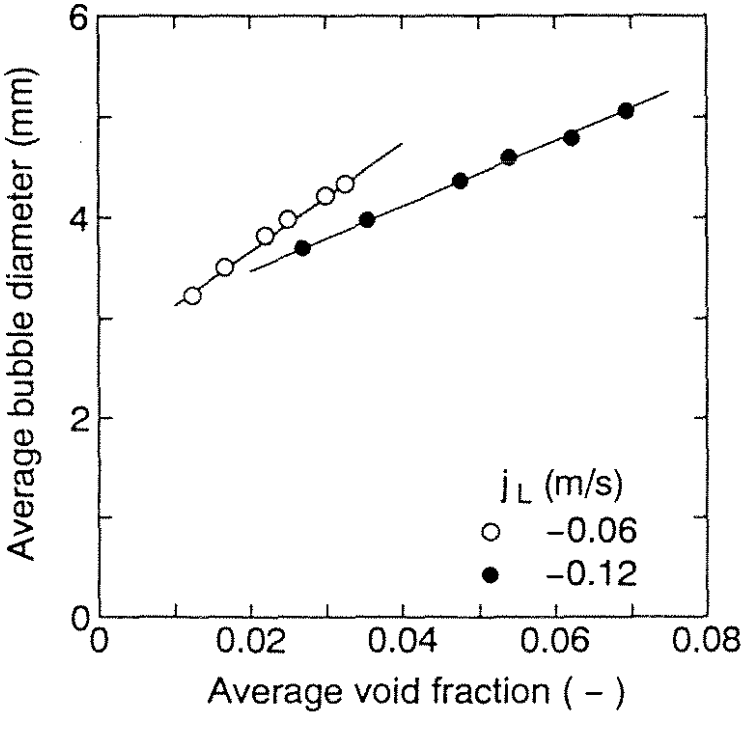

Fig.10 Average bubble diameter

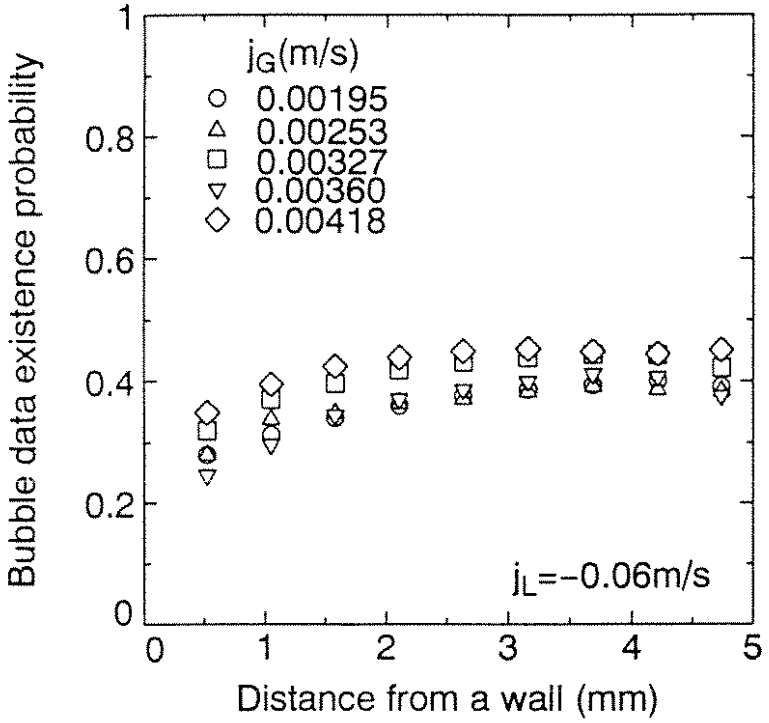

(a) Effect of air flow rates

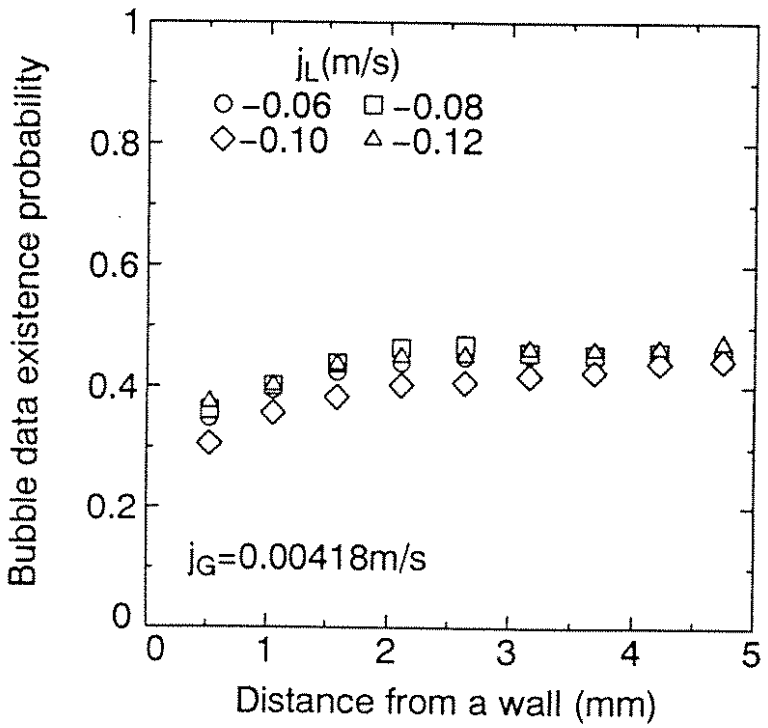

(b) Effect of water flow rates

Fig.11 Bubble data existence probability profiles in reference to air or water flow rates

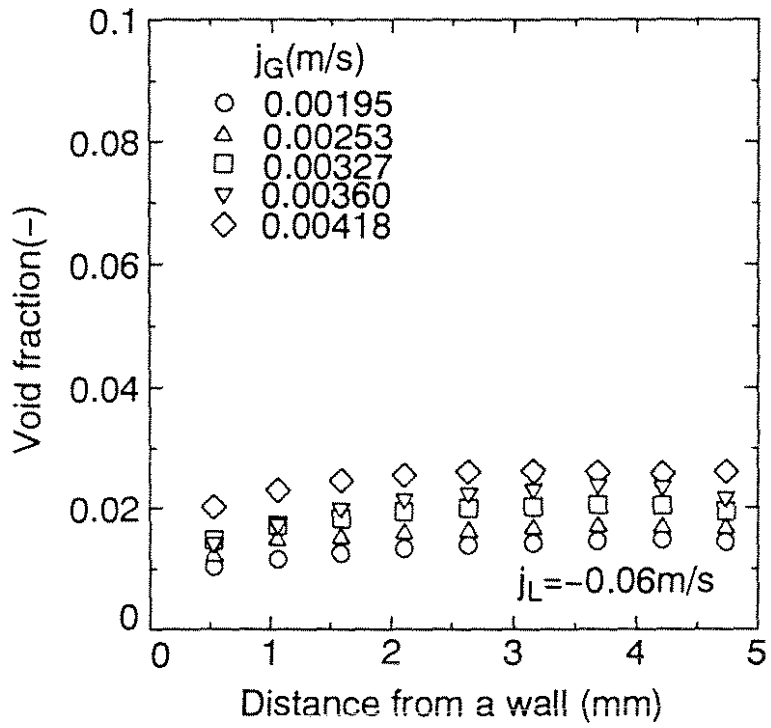

(a) Low water flow rate

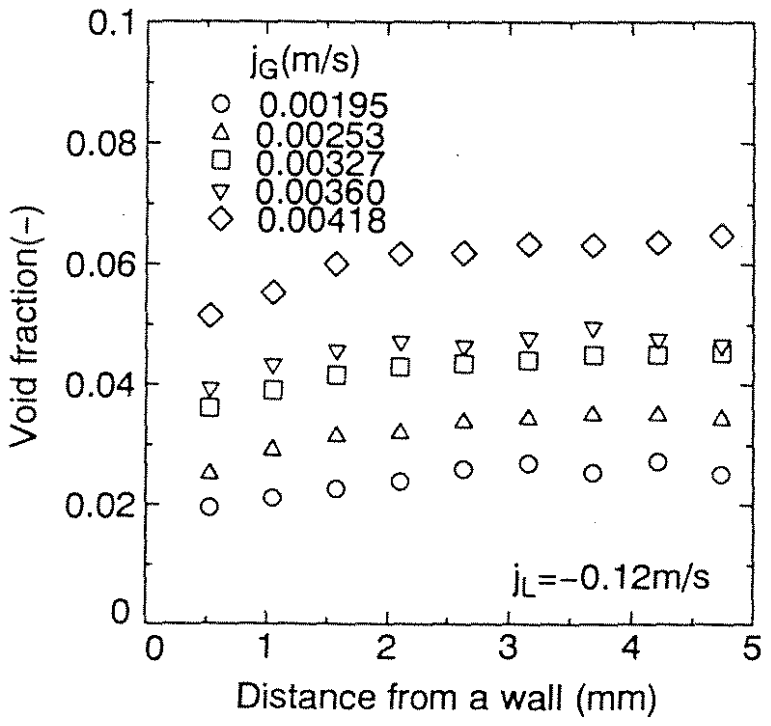

(b) High water flow rate

Fig.12 Void fraction profiles in reference to air flow rates

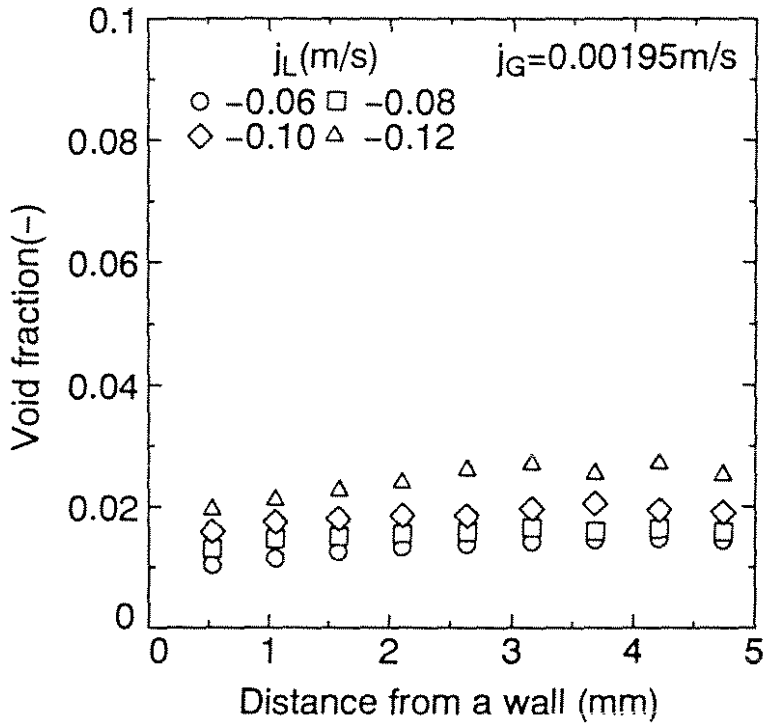

(a) Low air flow rate

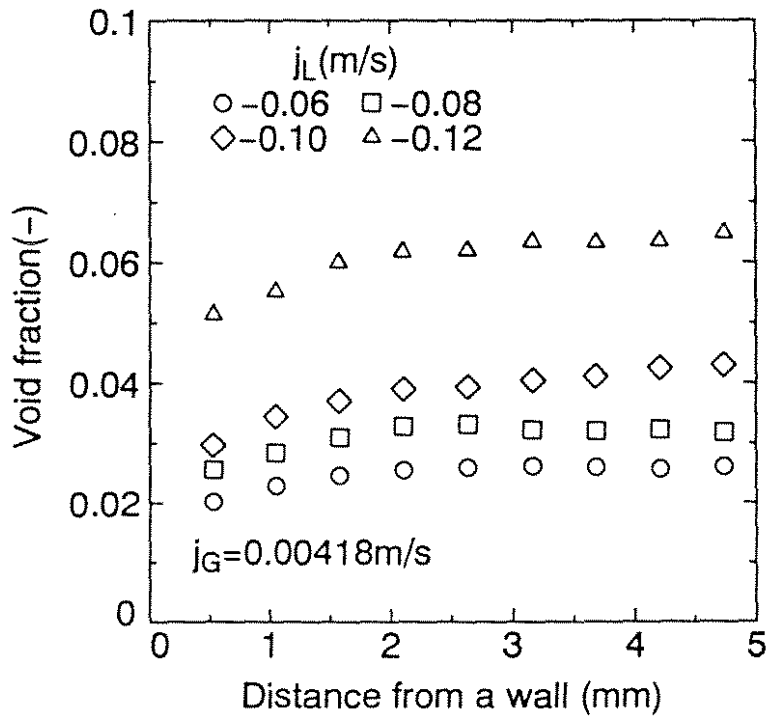

(b) Higher air flow rate

Fig.13 Void fraction profiles in reference to water flow rates

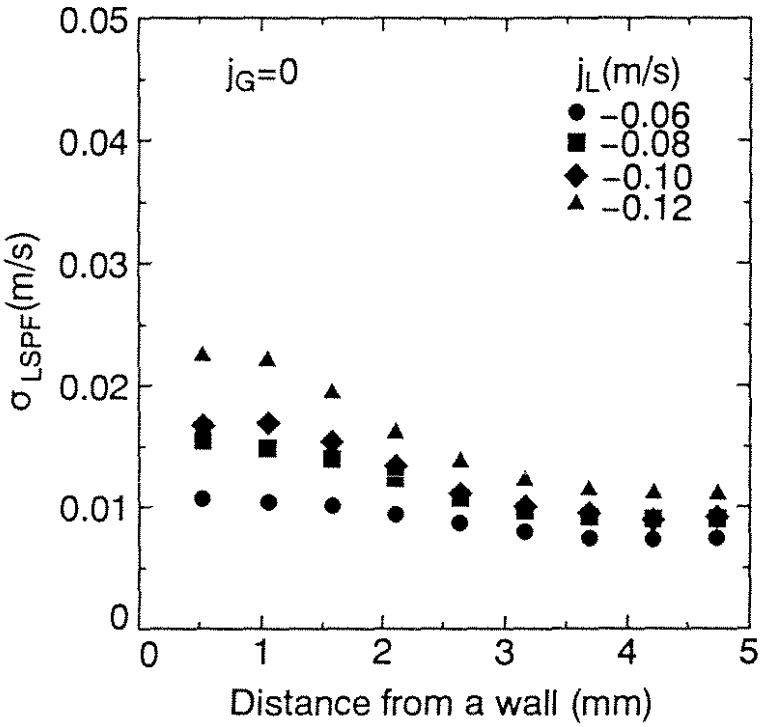

(a) Water downward flow

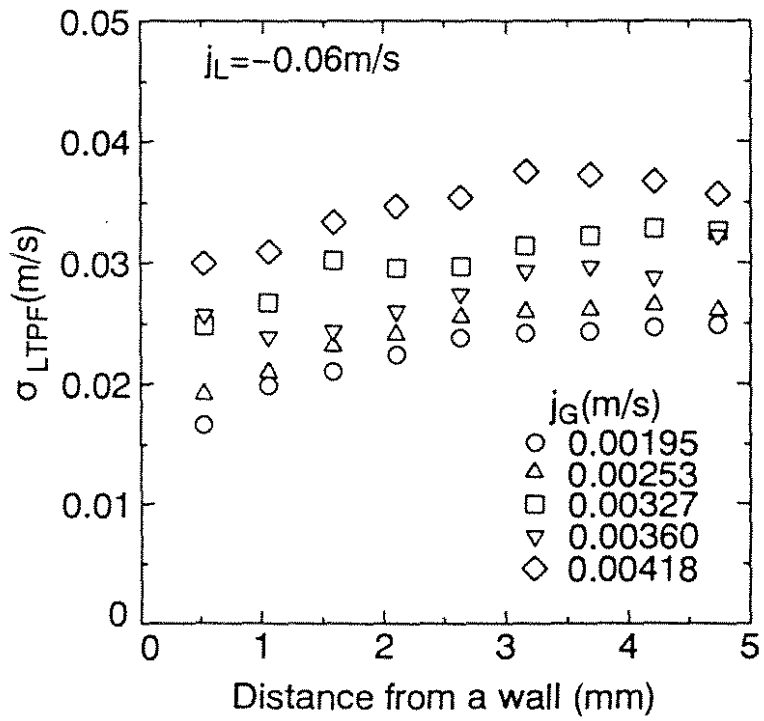

(b) Bubbly countercurrent flow

Fig.14 Typical standard deviation profiles of velocity fluctuation

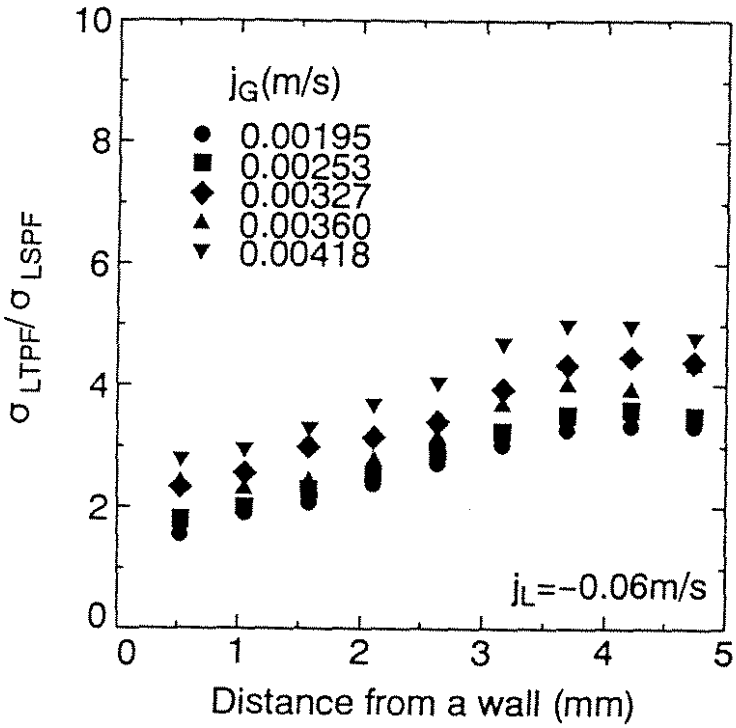

(a) Low water flow rate

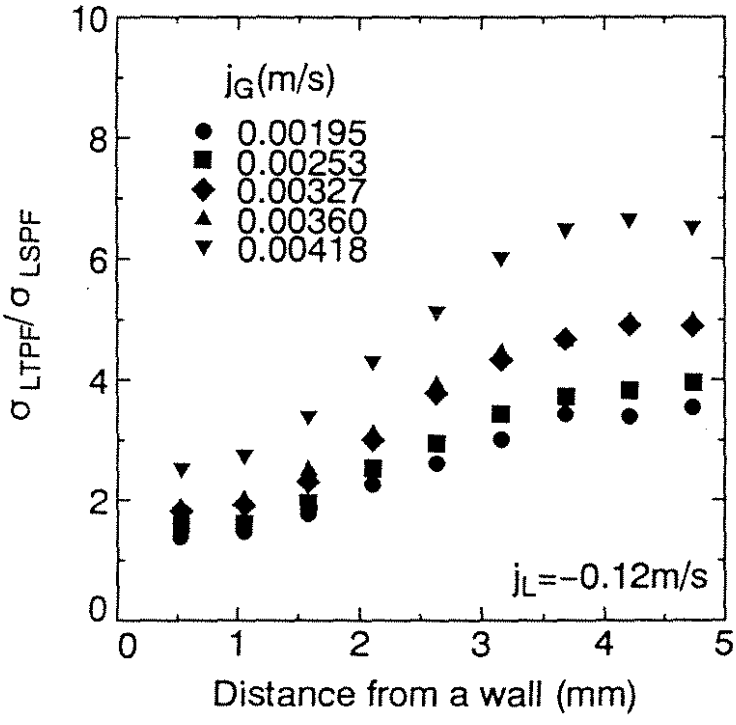

(b) High water flow rate

Fig.15 Turbulence intensity multiplier profiles

in bubbly countercurrent flows in reference to air flow rates

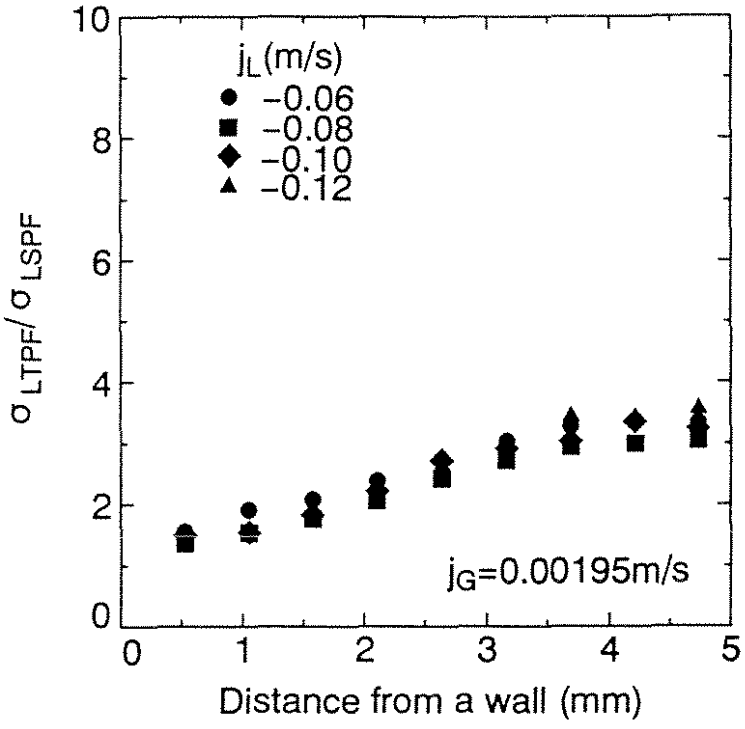

(a) Low air flow rate

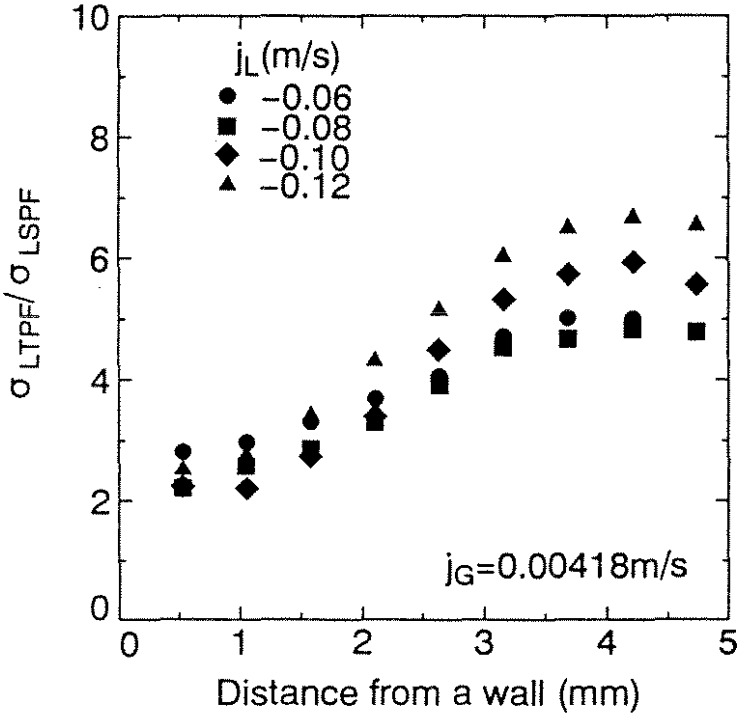

(b) High air flow rate

Fig.16 Turbulent intensity multiplier profiles

in bubbly countercurrent flows in reference to water flow rates

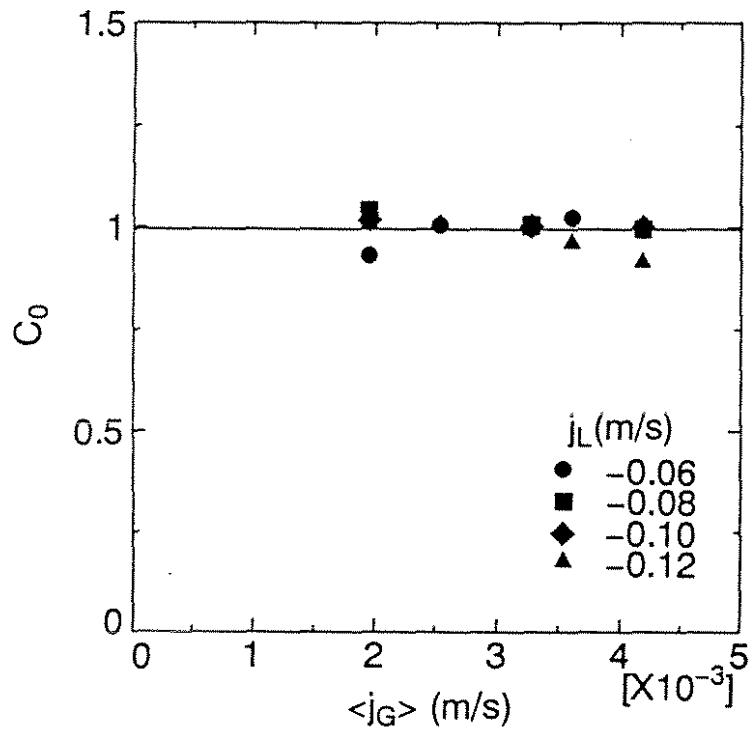

Fig.17 Distribution parameter of the drift flux model in bubbly countercurrent flow

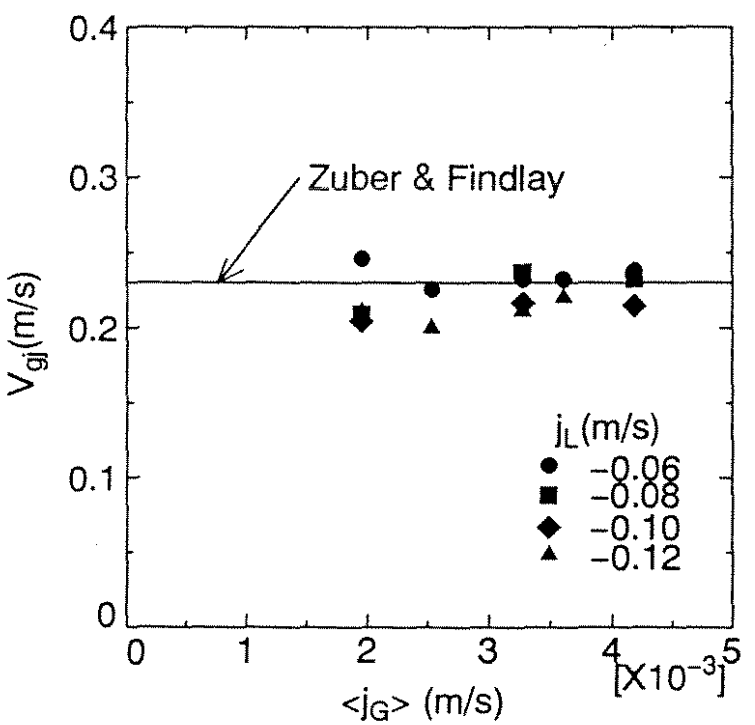

Fig.18 Drift velocity of the drift flux model in bubbly countercurrent flow

ON THE SPATIO-TEMPORAL STRUCTURE OF THE CYLINDER WAKE

I. Peschard[①], P. Le Gal[①] and Y.Takeda[②]

[①]Institut de Recherche sur les Phénomènes Hors Equilibre

UM 138, CNRS - Universités d'Aix-Marseille I & II

12, Avenue Général Leclerc,13003 Marseille, France

[②]Laboratory for Spallation Neutron Source

Paul Scherrer Institute

CH-5232 Villigen PSI, Switzerland

ABSTRACT

The wake of a short aspect ratio cylinder placed in a uniform flow is experimentally investigated. After having characterized the temporal behavior of the Bénard-Von Kàrmàn vortex shedding by the use of a classical hot-wire anemometer, an ultrasound anemometry technique is applied to study the spatial critical behavior of the envelope of the transversal velocity of the wake. It is shown that this envelope which represents the spatial form of the global mode of the wake, follows universal scaling lawswhich are in agreement with a second order phase transition. In a second set of experiments, the behavior of the longitudinal velocity fluctuations is also investigated. It has also been discovered that there is a special point several diameters behind the cylinder, which plays a role of a wave maker. Finally, for very small aspect ratio cylinders, symmetric vortex shedding is reported and modeled using a system of coupled oscillators equations.

List of symbols

Symbol	Unit	Physical Property
A	mm/s or a.u	amplitude of velocity oscillation.
A_{max}	mm/s	maximum of amplitude of velocity oscillation
c_2	-	non linear parameter of Landau equation
d	mm	diameter of cylinder
l	mm	length of cylinder
$\Gamma=l/d$	-	aspect ratio of cylinders
x	mm	longitudinal downstream coordinate
y	mm	transversal coordinate
x/d	-	normalized longitudinal downstream coordinate
y/d	-	normalized transversal coordinate
x_{max}	mm	reduced position of the maximum of amplitude
R	-	Reynolds number
R_c	-	critical Reynolds number
ε	-	reduced Reynolds number $(R-R_c)/R_c$
δ	mm	typical viscous length
ω_0	-	natural frequency of the shedding

1

Introduction

The goal of this study is to analyse the temporal and the spatial features of the classical Bénard-Von Kàrmàn wake of a cylinder. Although this wake is certainly the most popular flow in fluid mechanics, many problems about its spatio-temporal structure remain open. Recently, it has been proved by several authors (Sreenivasan et al (1986), Provansal et al (1987), Dusek et al (1994) and Schumm et al (1994)) that the Bénard-Von Kàrmàn vortex street shed by a cylinder, appears via a Hopf bifurcation at a critical Reynolds number R_c. When neglecting the three-dimensional features of the wakes, the normal form for this bifurcation is called the Landau equation and reads simply:

$$\frac{dA}{dt} = (\varepsilon + i \omega_0) A - (1 + i c_2) |A|^2 A \qquad (1)$$

where A is a complex order parameter representing the lateral velocity measured at one location in the wake, ε the reduced Reynolds number $((R - R_c)/R_c)$, ω_0 the natural frequency (without the non linear correction) of the shedding at Reynolds number R and c_2 a parameter corresponding to this frequency variation with the finite amplitude oscillations of the velocity field. The universal value for c_2 is equal to -2.7 (see for instance Dusek et al (1994)) for infinitely long circular cylinder. In fact, Albarède and Monkewitz (1992) have shown that this model of two-dimensionnal wake can be extended to the case of the three-dimensionnal wake, and in particular in order to interpret the "chevron shedding" observed by Williamson (1989). Moreover, it has also been shown by Albarède and Provansal (1995), that when the aspect ratio of the cylinder is small enough, only the first mode (along the axis of the cylinder) of vortex shedding can be observed. In these conditions, the temporal behavior of the wake is accurately described by the Landau equation. Of course, the coefficients of the model have to be estimated again as they depend on the aspect ratio of the cylinder. In particular, it is known from Lee and Budwig (1990) that the critical Reynolds number increases when the aspect ratio of the cylinder is decreased. Although these substantial progress achieved by these theoretical and experimental investigations concerning the temporal behavior of the wake,

Goujon-Durand et al (1994) and later, Zielinska and Wesfreid (1995) and Wesfreid et al. (1996) stressed on the signification of the amplitude A of the global mode. They showed experimentally and numerically that A has to be a norm of the spatial amplitude distribution of the wake which is different from a local amplitude as it was usually considered in experiments. Analysing the deformation of the spatial envelope of the wake oscillations with the Reynolds number , they were able to prove by hot wire mappings of the flow or direct numerical simulation of the wake, that the position x_{max} (on the downstream direction) of the maximum A_{max} of the velocity oscillation, approaches the cylinder as the Reynolds number increases. Moreover, they showed that A_{max} obeys the Landau equation and that x_{max} varies with a power law of the Reynolds number. These results are in complete agreement with the prediction from a second order phase transition.

The present experimental investigation, which is based on a new and particularly well-adapted anemometer, namely an ultrasound velocity profiler, brings a verification of this critical behavior of the wake near its threshold. Then, motivated by some of these measurements, we present some original visualizations of a varicose instability of the wake behind a very small aspect ratio cylinder.

2

Experimental arrangement and techniques

Our experimental facility consists of a water loop and is fully described by Le Gal et al (1996). The test section is 20 mm high and 128 mm wide. The water velocity can be varied between 0 and 1 m/s. It is measured by a home-made flow-meter and the back-ground turbulence intensity of the flow has been estimated by a hot-wire anemometer as about 0.5 %. To avoid the emergence of three-dimensionnal shedding, a small aspect ratio cylinder having a diameter d equal to 4 mm, is positionned on one of the horizontal walls of the channel. Its length is l=20 mm (l/d=5) and it is in close contact with the other horizontal wall. As the cylinder touches the opposite wall and because no end-plates have been used to control the boundary conditions, horse-shoe vortices are created in the boundary layers of the walls of the

water tunnel, around the ends of the cylinders. However, it is observed by visualisations and by ultrasound measurements that the alternate vortex shedding in the bulk flow is only slightly affected by the presence of these vortices. In the first part of this study, a classical hot-wire study of the temporal behavior of the wake is performed with a pobe placed seven diameter downstream the cylinder (x/d=7, y/d=0). The parameters of the Landau equation are calculated by a classical procedure based in particular on the impulse response of the wake. Then, its spatial shape is studied by ultrasound anemometry whose operation principle is ultrasound echography. An ultrasonic 4 MHz frequency pulse is emitted through the water flow by a piezoelectric probe having a diameter of 8 mm. The sound beam (roughly 5mm in diameter) propagates inside the flow and is reflected by 100 microns hydrogen bubbles which are generated by a electrolysis of water using a 0,1 mm platinium wire stretched across and at midheight of the channel, 100 mm upstream of the cylinder. When the piezoelectric transducer recieves the echoes back, the anemometer calculates the position of the reflecting bubbles by the time delay between the emitted and the recieved pulse, as well as the Doppler shift they generate because of their own velocity. More details about this technique can be found in Takeda et al (1993). When correctely seeded, the flow can be analysed by the measurements of instantaneous velocity profiles projected onto the direction of the sound beam. We performed to two sets of experiments. In the first, the ultrasound probe is placed in a groove machined in the middle plane of the side-wall of the channel. By this configuration, the transversal velocity profiles can be measured along lines crossing the main flow in the y direction. The transversal velocity profiles are recorded every 69.8 ms (or for some experiments, every 135.3 ms), in 128 spatial positions separated by 0.74 mm. 1024 instantaneous profiles are then recorded for several Reynolds numbers R. In the second set of experiments, the ultrasound probe is positionned inside the water flow, 80 mm downstream of the cylinder (x/d= 20) and 2 mm on its side (y/d= 0.5) in such a manner that longitudinal velocity profiles can be recorded.

3

Hot-wire determination of the temporal features of the wake

In the experimental conditions described in section 2, the critical Reynolds number R_c is determined by a careful hot-wire study of the wake. In particular, when studying the impulse response of the wake at different Reynolds numbers, the shedding frequency and the decay rate of the oscillations are obtained under the threshold. This study is then completed above the threshold, where the amplitude and the frequency of the saturated regimes are measured. The critical value (R_c=102±2) that we obtain agrees perfectly well with the previous study of Lee and Budwig (1990) concerning small aspect ratio cylinder wakes. The determination of the coefficient c_2 leads to a value equal to -1±0.1 which completes the study of Albarède and Provansal (1995). Figure 1 shows the evolution of the frequency (a) and of the square of the amplitude (b) of the wake, measured on the axis, at 7 diameters downstream the cylinder. The change of slope of the frequency curve is reminiscent of the non linear feature of the wake oscillation and the ratio between the two slopes leads to the deternination of the c_2 coefficient. Note also on Figure 1-b, that the prediction of the Landau equation - i.e. that the amplitude of the saturated oscillations above the threshold has to be proportionnal to the square root of the threshold distance- seems to be valid only for Reynolds numbers less than 160. Above this value, we note a saturation of the square of the amplitude that deviates from the linear prediction. Next section which presents a global description of the wake will give an explanation of this saturation.

4

Ultrasound measurements of the spatial shape of the global mode

Modelling the Bénard-Von Kàrmàn instability in terms of global modes, needs to represent the velocity wake fluctuations by the product of two independent functions linked to the

temporal and to the spatial evolutions of the velocity field. As we saw in the previous section, the main temporal features of the wake can be described by local measurements of the velocity flow. On the contrary, the spatial behavior of the periodic disturbances is much more difficult to study because traditionnal anemometry techniques (hot wire or laser anemometry) need heavy mappings of the flow. The ultrasound profile monitor presents in this context a new and interesting alternative.

4.1

Transversal velocity profiles

The early experimental studies of Mathis (1983) showed already that the envelope of the fluctuations of the wake possesses a maximum whose position varies with the Reynolds number. More recently, the experimental work of Goujon-Durand et al (1994) and Wesfreid et al. (1996) and the numerical investigations of Zielinska and Wesfreid (1995) have shown that the wakes of triangular bodies present a critical behavior at Reynolds numbers close to the instability threshold. In particular, it is shown that the amplitude and the position of the maxima of the transversal velocity oscillations obey power laws of the Reynolds number.

Using the ultrasound profiler, we measured the complete profiles of the transversal velocity at 8 different longitudinal positions downstream the cylinder and for several Reynolds numbers. Figure 2-a presents such a space-time diagram recorded at a Reynolds number of 132 at the position x/d = 6. The 2-D Fourier Transform of this space-time diagram is then calculated and band-pass filtered, in order to improve the visualisation of the vortex shedding (see Figure 2-b). The gray level coding permits to observe the periodic oscillation of the transversal velocity due to the vortex shedding. As shown by Dusek (1996), the transversal velocity mode is symmetric versus the flow axis as it can be seen by our measurements. This corresponds to the classical alternate vortex shedding or to the sinuous mode of the wake. Then, taking the temporal Fourier Transform for each of the 128 space points, it is possible to compute the spatial distribution of the squared amplitude of the

fundamental mode at those longitudinal positions. These profiles are then displayed on the same diagram giving a three-dimensionnal view of the global mode of the circular cylinder wake. Figure 3 shows these spatial shapes of the wake as the Reynolds number increases. It can be observed that the energy profiles of the first x-location profiles has a double hump near the cylinder. Further downstream, these profiles are transformed into a single peak. We will come back later on this double hump structure, and analyse for now the evolution of the main peak. Plotting the amplitudes taken by these profiles at y=0, we show on Figure 4 the deformation of the global mode with the Reynolds number. The deformation which can be easily observed, is at the origin of the amplitude saturation displayed on Figure 1-b. We observe a rapid increase of the amplitude of oscillation from zero near the cylinder, up to a maximum A_{max} whose position x_{max} varies between 9 and 5, when increasing the Reynolds number. Then, the decrease of these envelopes far away from the cylinder can be interpreted as a viscous relaxation of the far wake.

It is then easy to compute the evolution of the position and level of the maximum of the mode as a function of the Reynolds number. The logarithmic representations of figure 5-a and 5-b show the critical behavior of the envelops as already observed by Goujon-Durand et al (1994), Zielinska and Wesfreid (1995) and Wesfreid et al.(1996). Moreover, we confirm the exponent of the power laws (1/2 for the amplitude A_{max} and -1/2 for the position x_{max}) observed by these authors. Note that these exponents are in complete agreement with a second-order phase transition model of the wake. An improvement of the Landau model can be acchieved when adding to equation (1) a second-derivative-term in the x direction. In order to enhance the scale-invariance structure of the wake, we renormalize the amplitude and the space by using A_{max} and x_{max}. Figure 6 shows that the different envelopes now collapse onto a single curve.

As already mentioned, very near the cylinder (x/d between 1 and 4), the energy of the global mode presents a double hump structure (see Figure 3). In fact, they correspond to measurements which were realised at longitudinal positions inside the recirculation eddies formed behind the cylinder. Therefore, the double hump structure corresponds to a wave propagation on each side of the cylinder. We show such a space-time measurement for R=120

and x/d=2, in Figure 7-a). As in Figure 2, we use the Fourier Transform and a band-pass filter to enhance the wake structure (Figure 7-b). It can be observed that the oscillations on each side of the cylinder, are in phase, but for some Reynolds numbers, it has also been possible to observe for some periods of time, oscillations in phase opposition. In this case, the shedding is a mixture of a symmetric and anti-symmetric oscillations. Figure 8 shows for a Reynolds number of R=150 and a longitudinal abscissa x/d=3, such a case of mixing between the varicose (anti-symmetric transversal velocity fluctuations) and the sinuous (symmetric transversal velocity fluctuations) mode. We will confirm further the presence of the varicose mode of vortex shedding in section 5, where a visual study of very short aspect ratio cylinders is presented.

4.2

Longitudinal velocity profiles

The ultrasound probe is now placed inside the water channel, aligned with the x axis in order to measure the longitudinal velocity fluctuations from the longitudinal location x/d=20 up to the cylinder. Because this mode is odd, its amplitude is null along the x axis, and we placed the probe at the transversal position y/d= 0.5. Figure 9-a and 9-b give space-time diagrams obtained by the ultrasound profiler. As it can be clearly observed on these figures, two systems of waves which are generated from a position around x/d=3.5 downstream of the cylinder. The waves propagating in the downstream direction between x/d=3.5 and 20 correspond to the alternate shedding of the travelling vortices. The other waves propagate to the upstream direction between x/d=3.5 and the cylinder on the edge of the stationnary recirculating eddies. These experimental observations of the cylinder wake, may confirm the theoretical predictions of the existence of a region of the flow where the instability is of "absolute type" as it is defined in the review of Huerre and Monkewitz (1990).

5

Visualization of very short aspect ratio cylinder wakes

To verify the presence of the varicose mode of vortex shedding, we placed in the water channel, cylinders having aspect ratios Γ as small as 0.5. The wake is visualized by injecting (at an appropriate very small rate) white dye by small holes placed at the middle of the transversal plane, at the rear face of the cylinder. Figure 10 presents a sequence of snapshots obtained at different Reynolds numbers. As predicted by Lee and Budwig (1990), the threshold of the vortex shedding is pushed toward high Reynolds numbers. Moreover, as it can be seen on figure 10, the first instability of the wake in such conditions is of varicose type. For this particular cylinder, this instability occurs for a Reynolds number around 440. Although the main features of the flow are two-dimensional, we believe that it is the three-dimensional structure (and not shedding) of the near wake which is at the origin of this varicose mode. Under this threshold, the wake remains stationary with the formation of large recirculating eddies behind the cylinder (see Figure 10-a). Above the threshold, a symmetric oscillation develops on each side of the recirculating eddies (Figure 10-b-c). We note also on these snapshots the existence next to the cylinder of a dead water zone which traps the dye. The extension of this region is approximatively one half of a diameter. When increasing the Reynolds number, the varicose mode generates a symmetric vortex street. Finally for R=800 (Figure 10-e), the classical alternate shedding appears. First both modes exist together, but for R=900 (see Figure 10-f) the alternate shedding and its associated Bénard-Von Kàrmàn vortex street dominate the wake. A physical interpretation of this phenomenon can be proposed if we consider the oscillating wake as the result of the coupling between two shear layers which have a thickness given by viscous effects and which are located on each side of the cylinder. Following the work we made on two coupled wakes (see Peschard and Le Gal (1996)), we propose to model these two unstable shear layers by two linearly coupled Hopf bifurcations of the type described by equation (1). As it was demonstrated for two wakes, the in-phase mode appears for strongly coupled oscillators and the phase-opposition mode appears for weakly coupled wakes. We can therefore extrapolate these observations to the case of a single wake. The two shear layers have a thickness approximately

given by the viscous scale of the flow: $\delta=\nu/U$ where ν is the kinematic viscosity of the fluid and U its velocity. It is then easily shown that the ratio between the distance separating the shear layers and their thickness is $d/\delta = R$. Therefore, near the threshold of very small aspect ratio cylinders ($R_c \cong 500$), this ratio which gives the coupling strengh between the oscillators, is large and our model predicts a phase-opposition locking which gives a varicose mode of vortex shedding. On the contrary, large aspect ratio cylinders have relatively close shear layers: $d/\delta \cong 50$ and then are strongly coupled. The sinuous mode appears in this case. Note that a similar oscillators model based on coupled Van der Pol oscillators has been recently proposed by Lopez-Ruiz and Pomeau (1996). They obtained similar results to ours (Peschard and Le Gal (1996)) to interpret the transition between a varicose and a sinuous mode of vortex shedding phenomena. Note also that a similar mode selection (see for instance Thomas and Prakash (1990)) works generally for two-dimensional jets: undeveloped "flat" profiles jets are unstable to the varicose mode (weakly coupled shear layers) contrary to well developed parabolic profile jets (strongly coupled shear layers) which are unstable to the sinuous mode.

6
Conclusion

The present experimental study of small aspect ratio cylinder wakes has confirmed and revealed new phenomena occuring on the vortex shedding. First, a classical hot wire anemometry study showed that even small aspect ratio ($\Gamma=l/d=5$) cylinder wakes still appear via Hopf bifurcations. The parameters of the bifurcation agree fairly well with the existing linear or non linear data. Following Westfreid and co-workers, it was also proved that the spatial shape of the global mode of the wake obeys universal phase transition laws. This last study was realized by the use of an ultrasound anemometer that permits to avoid extended mapping of the flow. Transversal and longitudinal velocity profile measurements have been successfully performed. At 3.5 diameters downstream the cylinder, we observe the existence of a special location from where waves are emitted in the downstream and upstream

directions. This may be the signature of the so-called absolute instability of the wake. The ultrasound measurements revealed also the presence of a symmetric vortex shedding. The presence of this varicose mode has then been checked by flow visualisation on a very small aspect ratio cylinder (l/d=0.5). An interpretation in terms of coupled oscillators was finally presented where the aspect ratio of the cylinders drives the coupling between the shear layers which develop on each side of the cylinders.

References

-**Albarede P; Monkewitz P** (1992) A model for the formation of oblique shedding and "chevron" patterns in cylinder wakes, Phys. Fluids A 4: 744-756.

-**Albarède P; Provansal M** (1995) Quasi-periodic cylinder wakes and the Ginzburg-Landau model, J. Fluid Mech. 291: 191.

-**Dusek J** (1996) Spatial structure of the Bénard-Von Kàrmàn instability, Eur; J; Mech. B/Fluids 15 (3): 330.

-**Dusek J; Le Gal P; Fraunié Ph** (1994) A numerical and theoretical study of the first Hopf bifurcation in a cylinder wake, J. Fluid Mech. 264: 59-80.

-**Goujon-Durand S; Wesfreid JE; Jenffer P (1994)** Downstream evolution of the Bénard-Von Kàrmàn instability, Phys. Rev. E 50: 308.

-**Huerre P; Monkewitz P (1990)** Local and global instabilities in spatially developing flows, Annu. Rev. Fluid Mech. 22: 473.

-**Lee T; Budwig R** (1990) A study of the effect of aspect ratio on vortex shedding behind circular cylinders, Phys. Fluids A 3 (2): 309-314.

-**Lopez-Ruiz R; Pomeau Y** (1996) Non linear transition between two oscillation modes. (A model for the release of vortices behind a circular cylinder), submitted to Phys. Rev. E.

-**Mathis C** (1983) Propriétés des composantes transverses dans l'écoulement de Bénard-Von Kàrmàn aux faibles nombres de Reynolds. Thèse de l' Univ. de Provence, France.

-**Peschard I; Le Gal P** (1996) Coupled wakes of cylinders, Phys. Rev. Lett. 77 (15):3122-3125.

-**Provansal M; Mathis C; Boyer L** (1987) Bénard-von Karman instability: transient and forced regimes, J. Fluid Mech. 182: 1-22.

-**Sreenivasan KR; Strykowski PJ; Olinger DJ** (1986) Hopf bifurcation, Landau equation and vortex shedding behind circular cylinders, Proc. Forum on Unsteady Forum Separation (ed. K. N. Ghia), ASME FED, 52: 1-13.

-**Schumm M; Berger E; Monkewitz P** (1994) Self-excited oscillations in the wake of two-dimensional bluff bodies and their control, J. Fluid Mech. 271: 17-53.

-**Takeda Y; Fischer WE; Sakakibara J; Ohmura K** (1993) Experimental observation of the quasi periodic modes in a rotating Couette system, Phys. Rev. E 47: 4130.

-**Thomas FO; Prakash KMK** (1991) An experimental investigation of the natural transition of an untuned planar jet. Physics of Fluids A 3 (1): 90-105.

-**Wesfreid JE; Goujon-Durand S; Zielinska BJA** (1996) Global mode behavior of the streamwise velocity in wakes, J. Phys. II, France, 6 : 1343-1357

-**Williamson CHK** (1989) Oblique and parallel modes of vortex shedding in the wake of a circular cylinder at low Reynolds numbers, J. Fluid Mech. 206: 579-627.

-**Zielinska BJA; Wesfreid JE** (1995) On the spatial structure of global modes in wake flow, Phys. Fluids 7: 6.

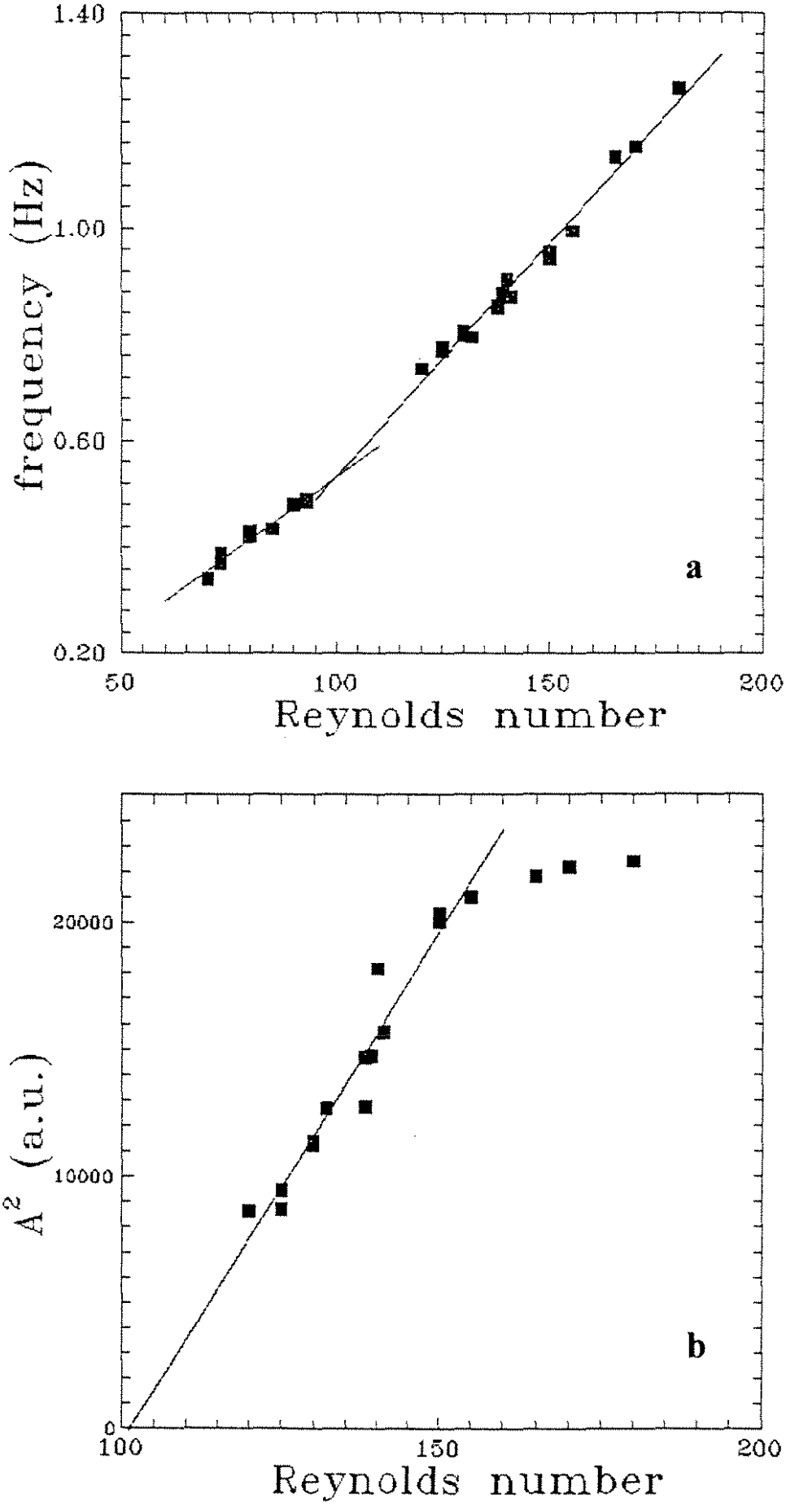

Figure 1: a) Variation of the wake frequency with the Reynolds number. b) Variation of the energy of the oscillations versus the Reynolds number. Note the saturation around R=160.

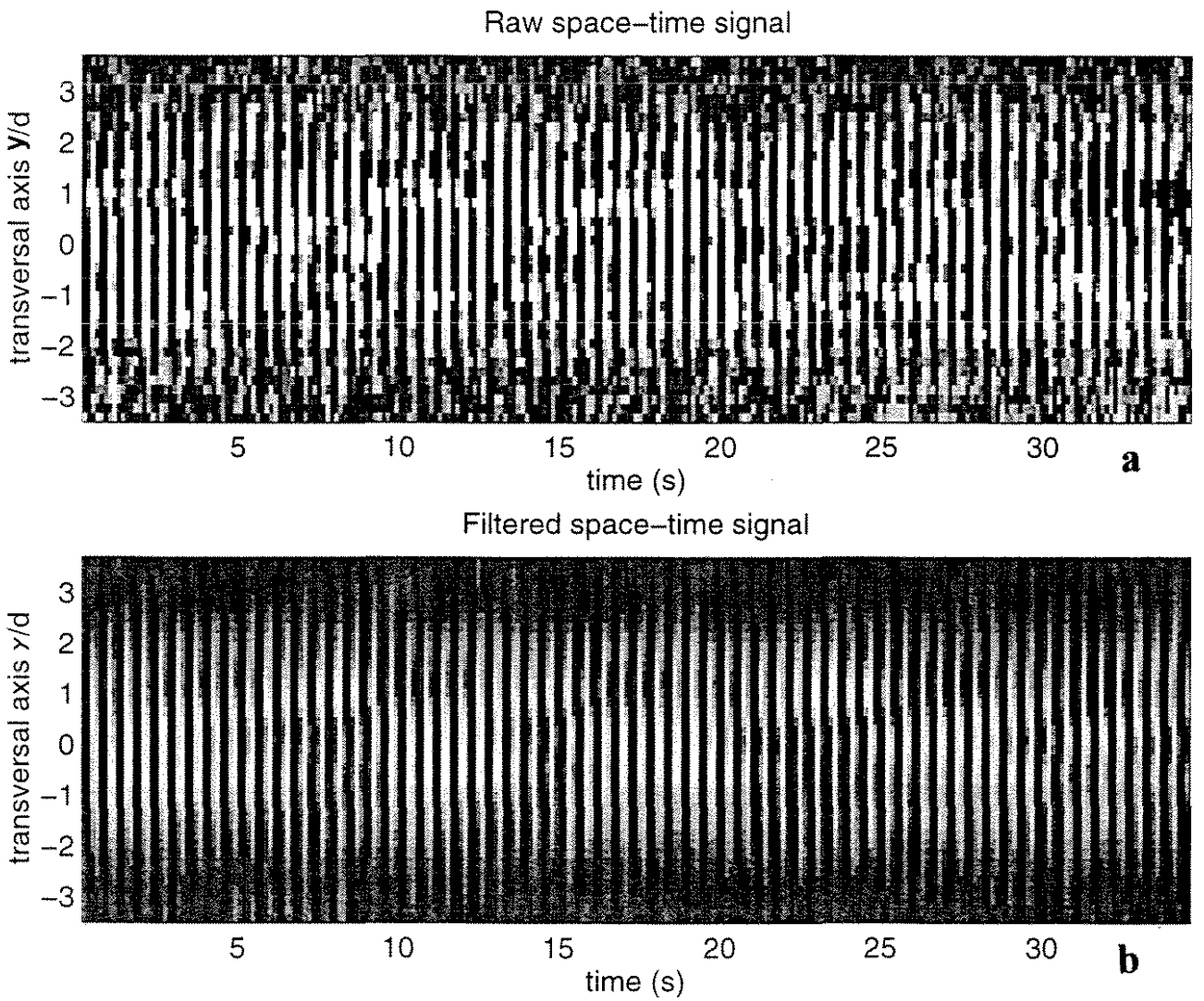

Figure 2: Space-time diagram of the transversal velocity component, a) raw data, b) filtered data (R=132, x/d=6).

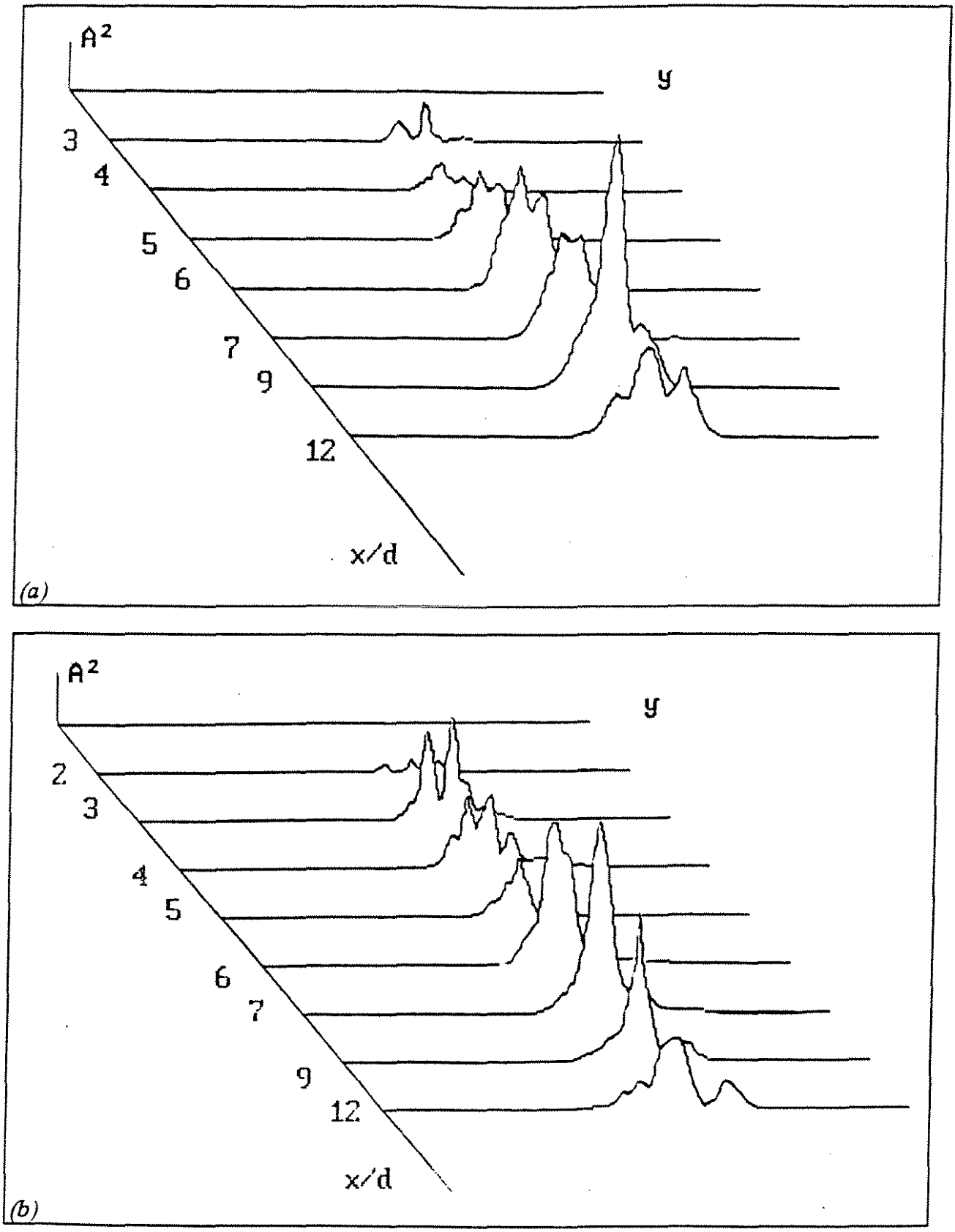

Figure 3: Three-dimensional representation of the spatial energy distribution of the transversal velocity oscillations. a)R=122, b) R= 142

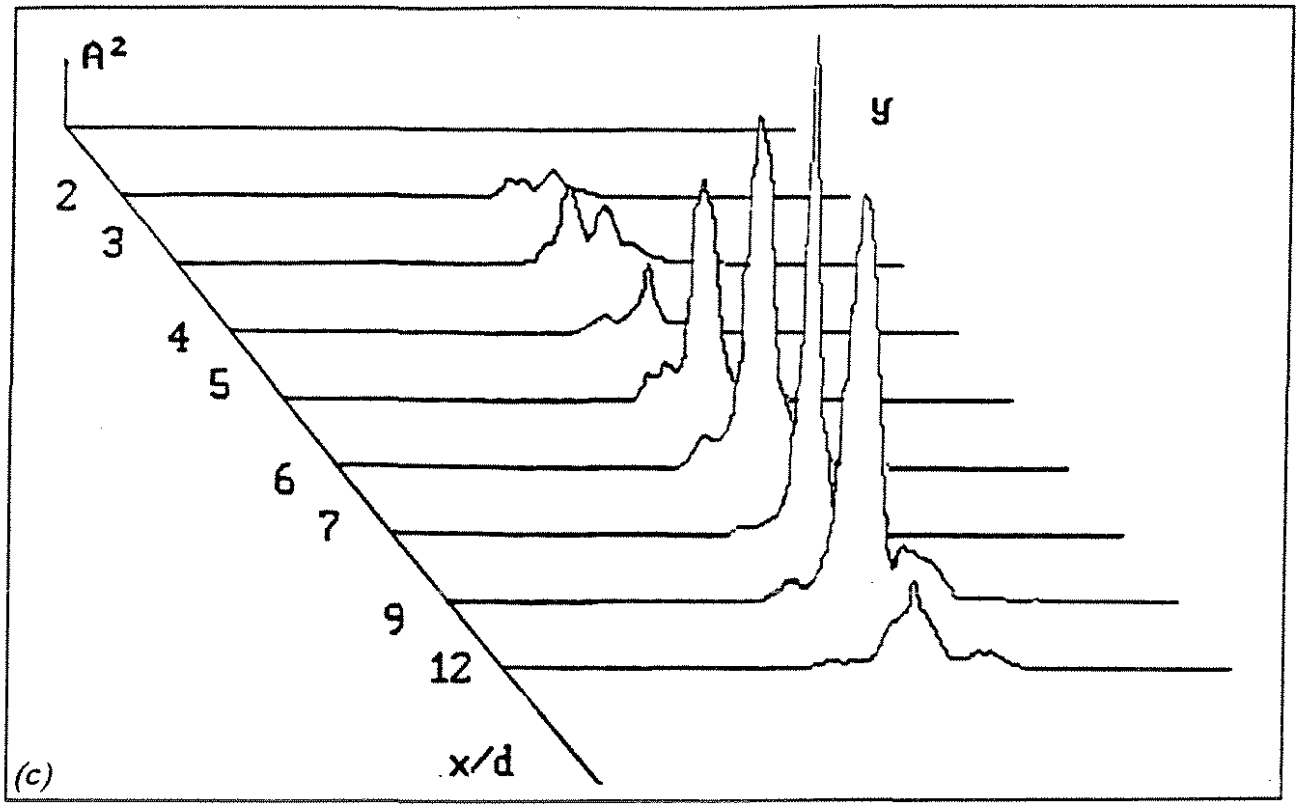

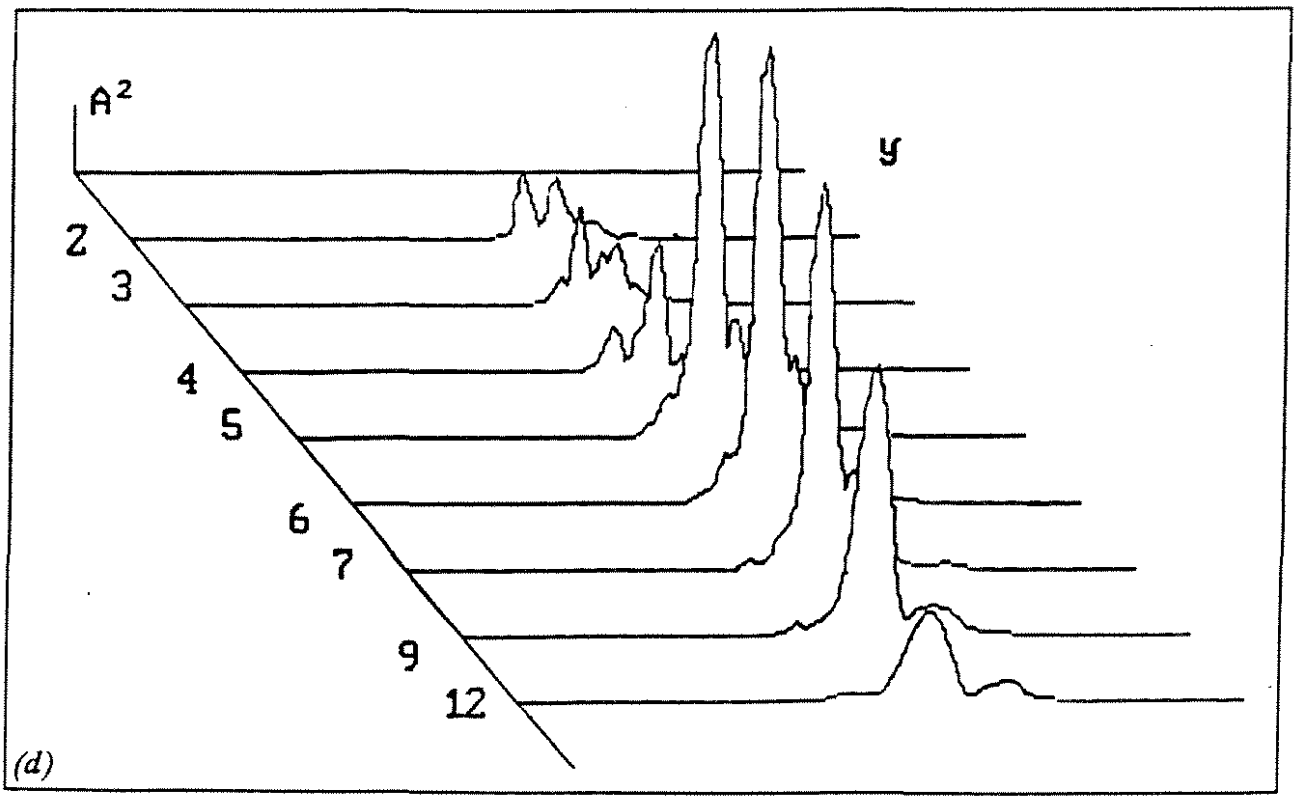

Figure 3: Three-dimensional representation of the spatial energy distribution of the transversal velocity oscillations. c)R= 170, d)R=185

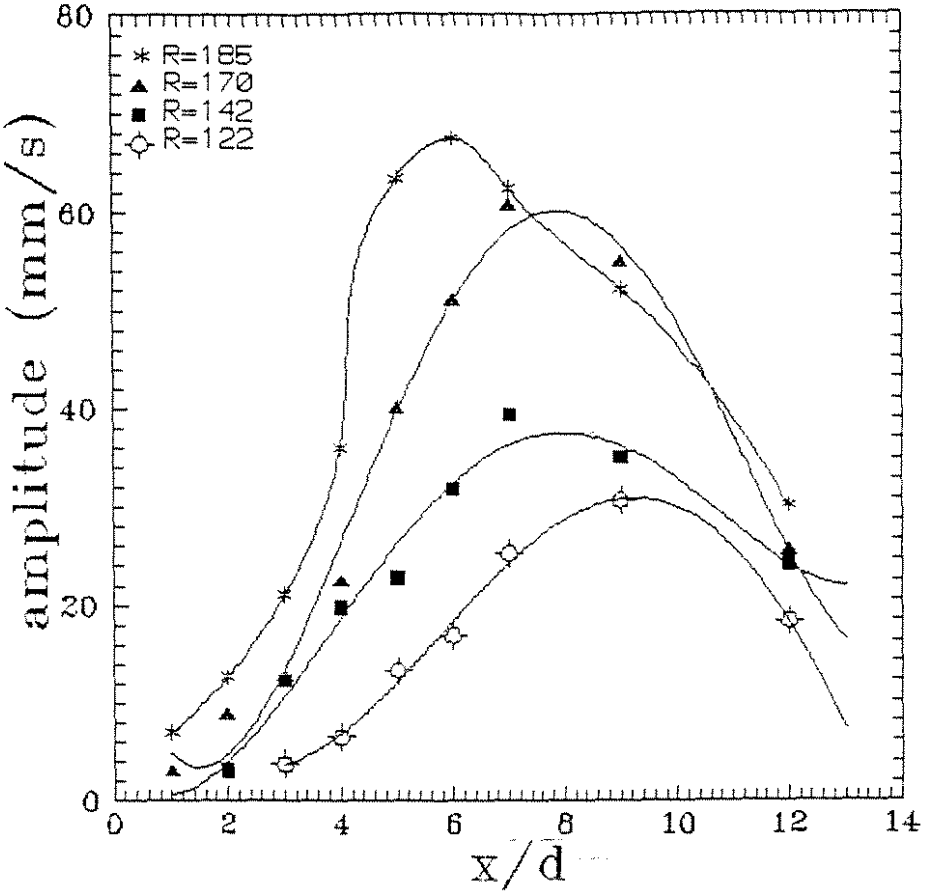

Figure 4: Amplitude of the transversal velocity oscillations downstream the cylinder (y/d=0) versus x/d for different Reynolds numbers.

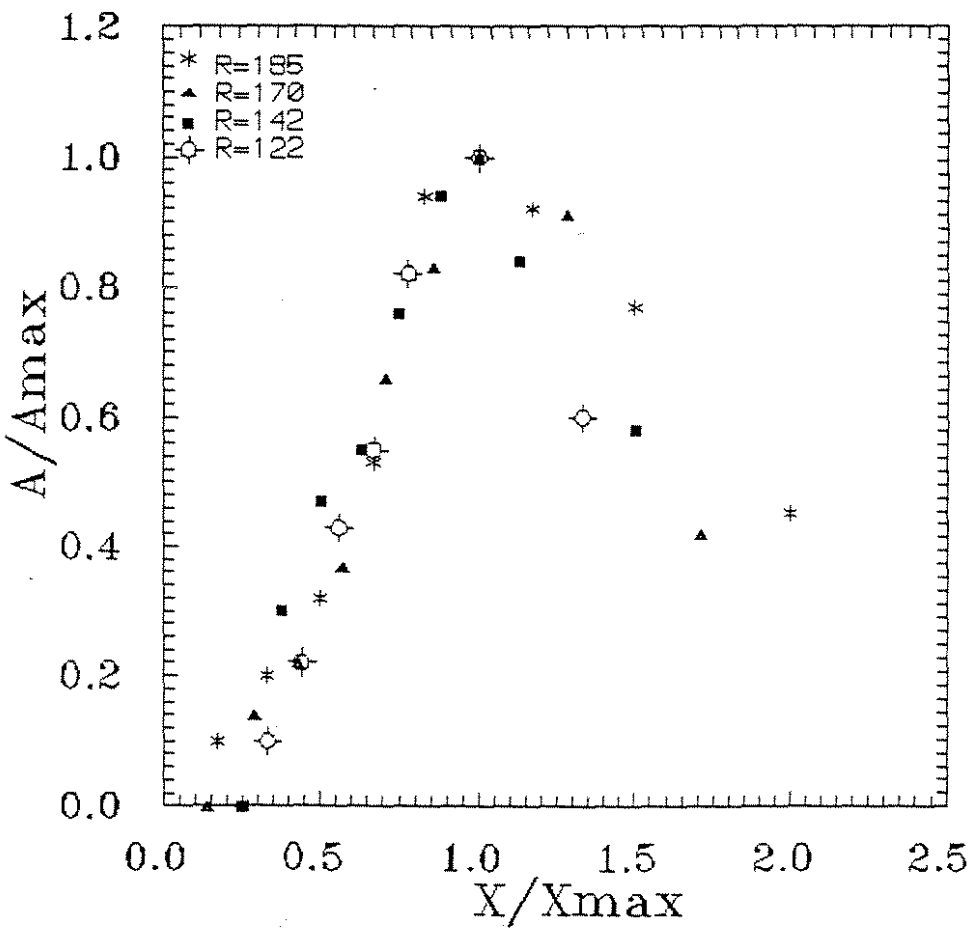

Figure 6: Renormalized amplitude of the transversal velocity oscillations downstream the cylinder (y/d=0) versus the renormalized longitudinal coordinate.

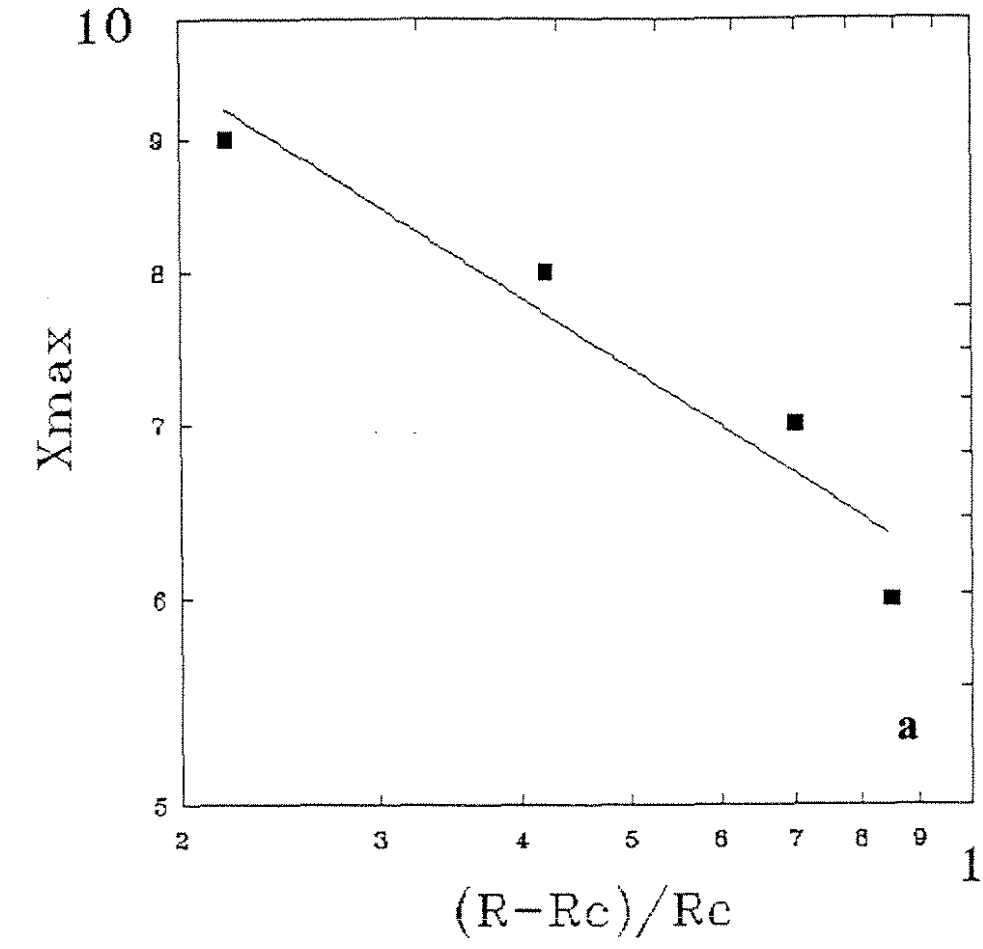

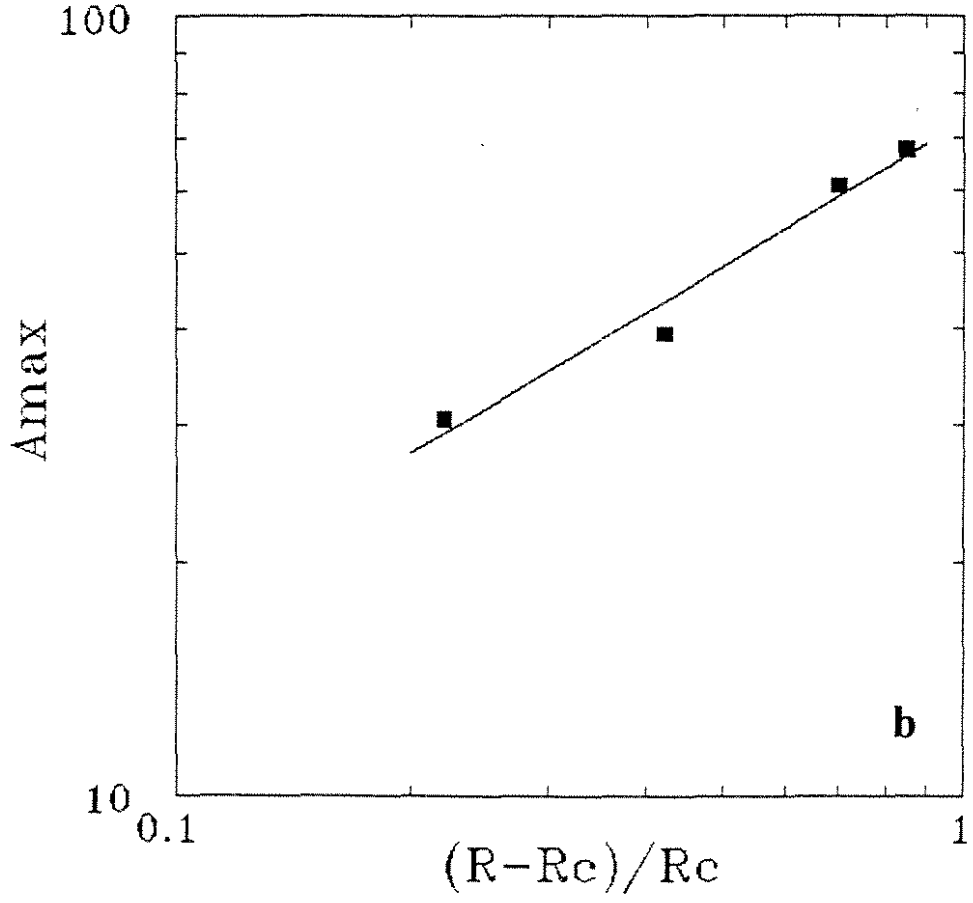

Figure 5: Log-Log plot of the position x_{max}(a) and of the amplitude A_{max} (b) of the maximum of the transversal velocity oscillations as a function of the Reynolds number.

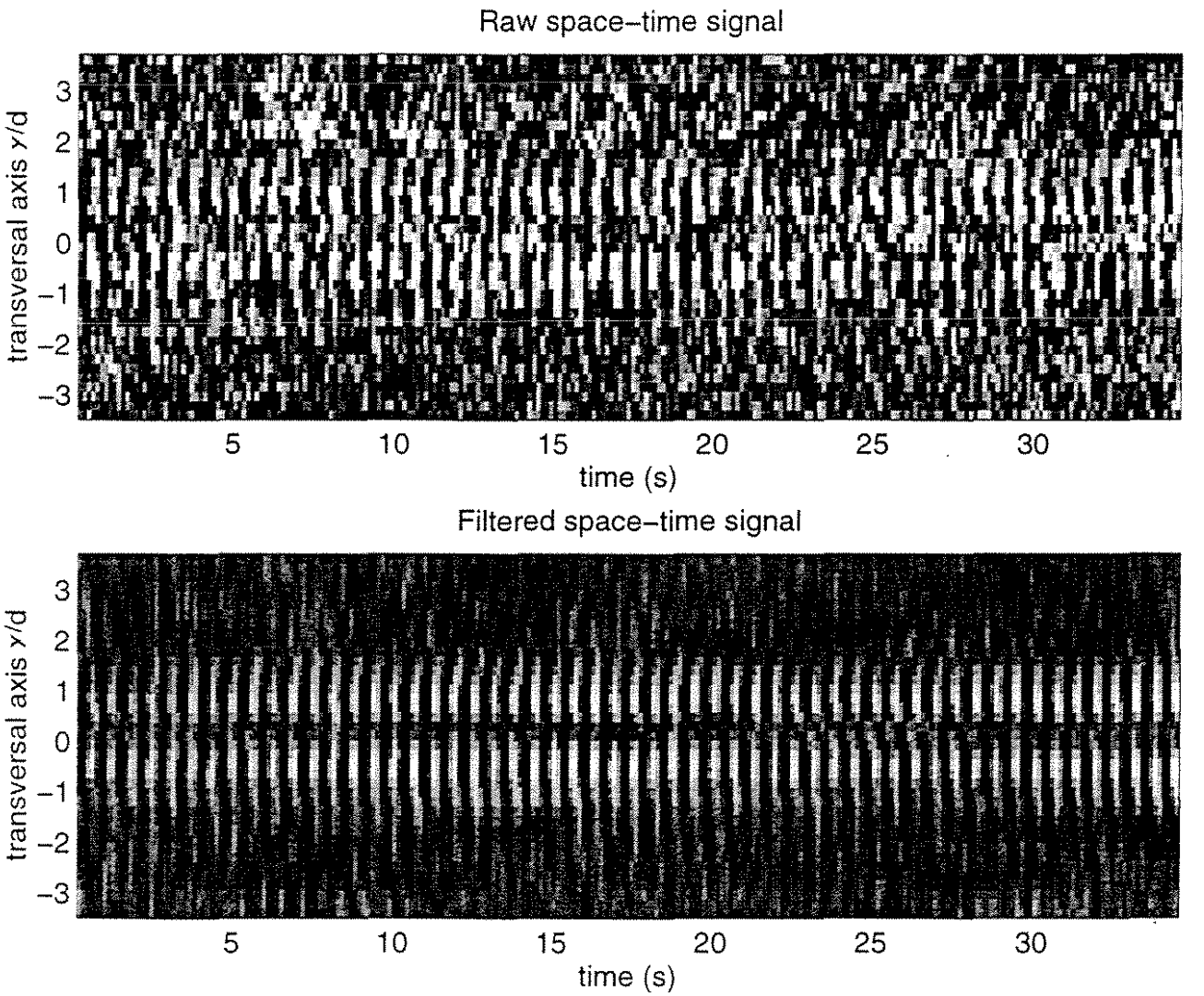

Figure 7: Spatio-temporal diagram of the transversal velocity component (R=120, x/d=2), gray scale coding of the velocity, a) raw data, b) filtered data. Note the sinuous mode of vortex shedding.

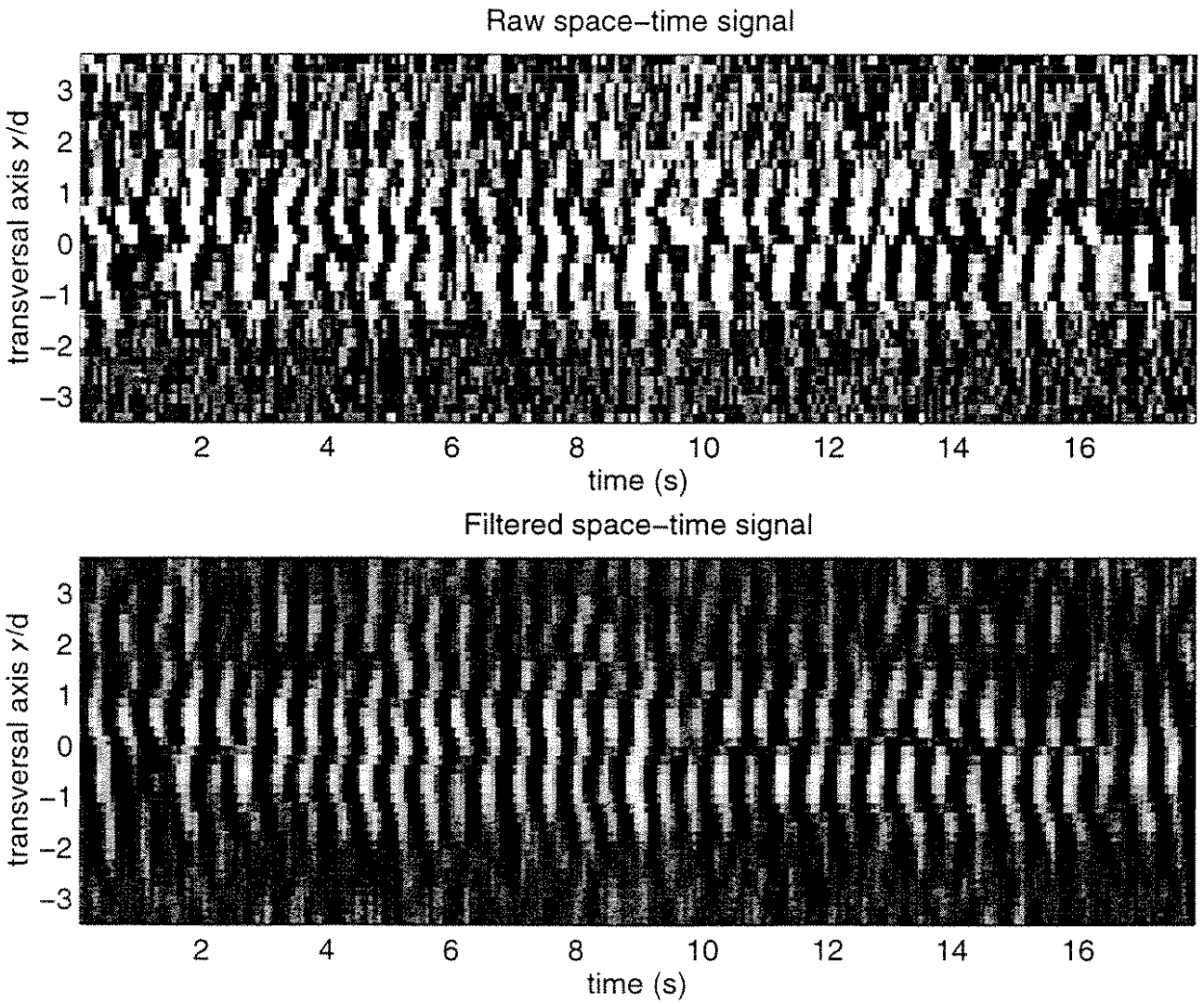

Figure 8: Space time diagram of the transversal velocity component (R=150, x/d=3), gray scale coding of the velocity, a) raw data, b) filtered data. Note the mixing of varicose and sinuous mode of vortex shedding.

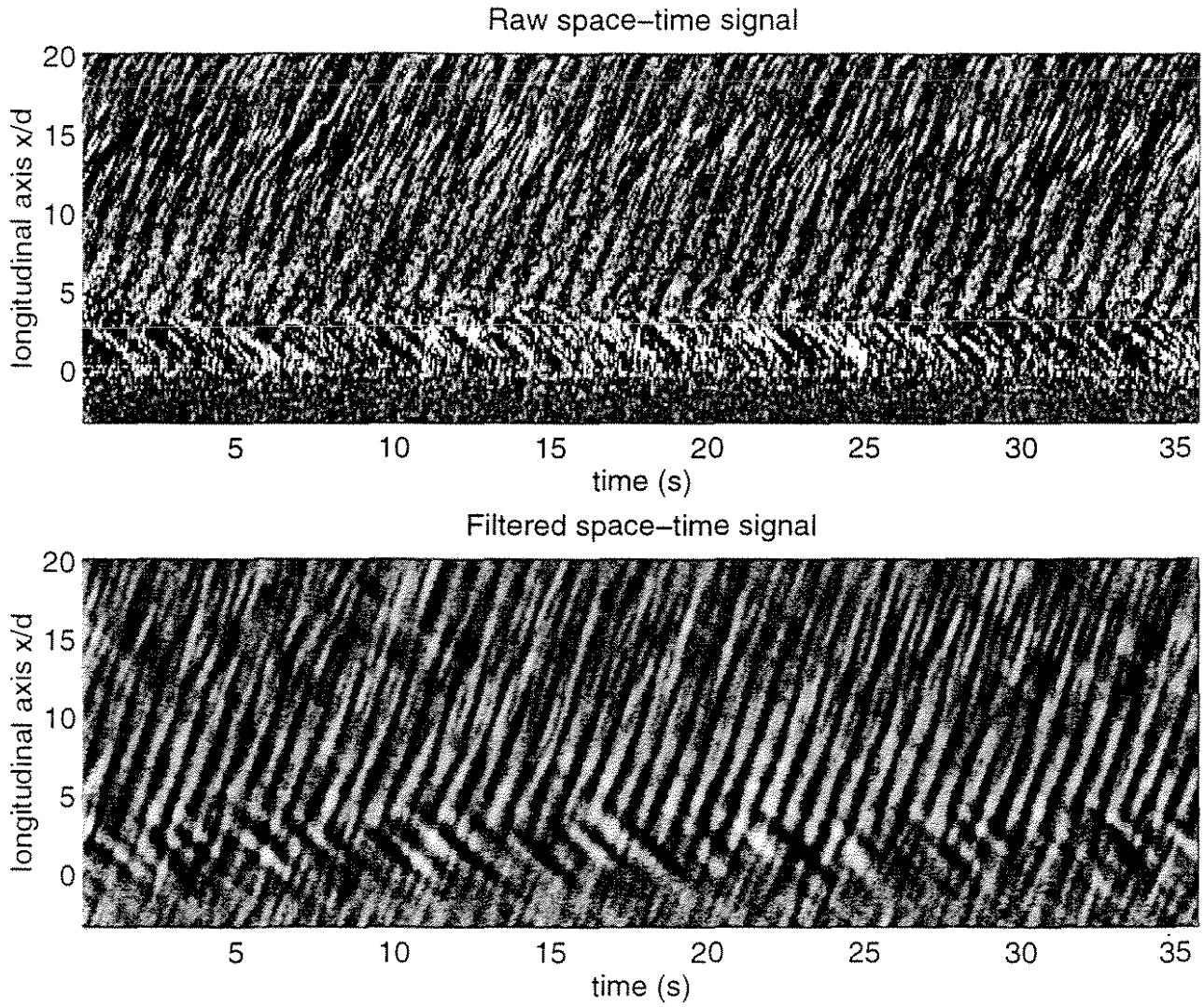

Figure 9: Spatio-temporal diagram of the longitudinal velocity component (R=132, y/d=0.5), gray scale coding of the velocity, a) raw data, b) filtered data.

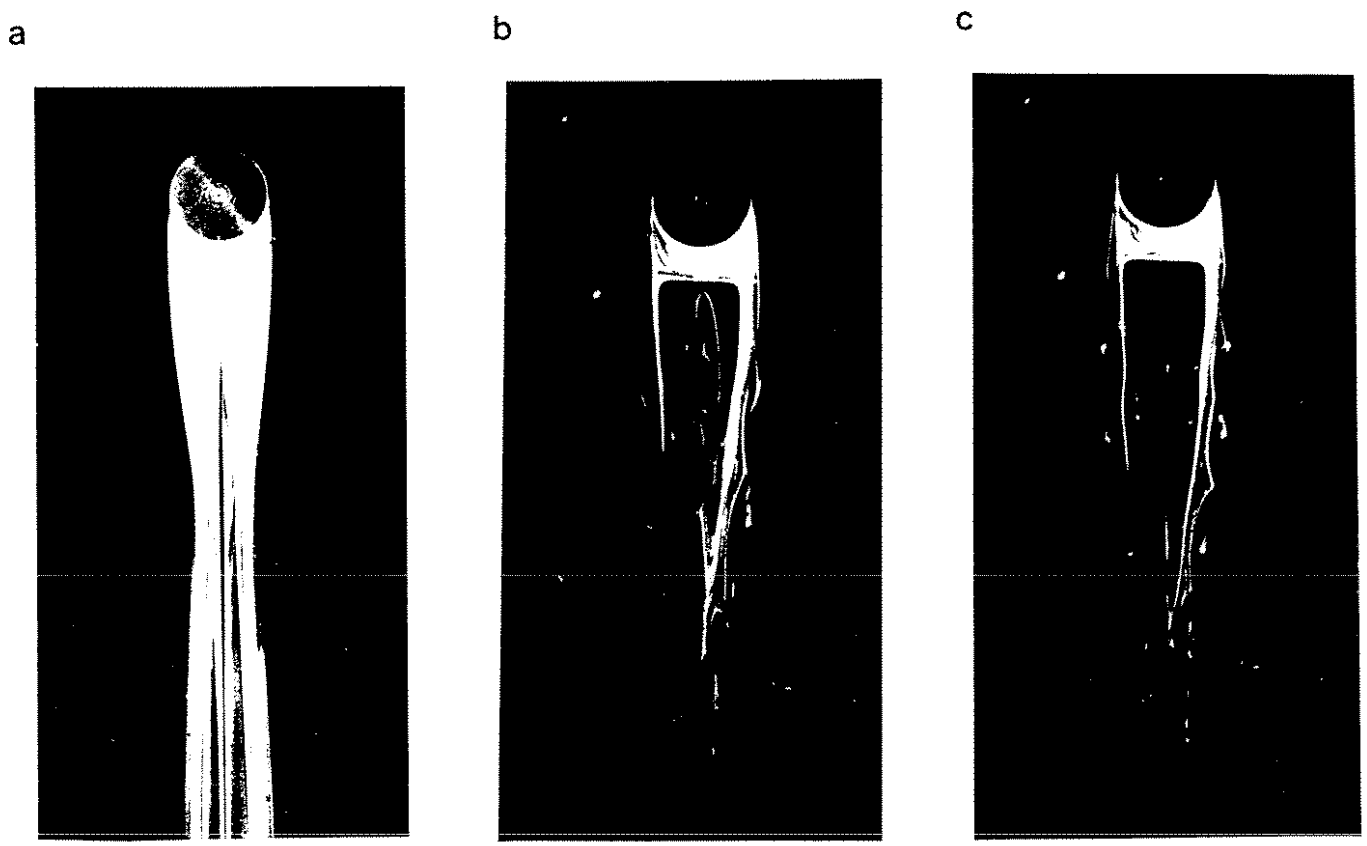

Figure 10: Snapshots of the near wake of a very small aspect ratio cylinder (l/d=0.5). a) R=300, b) R=450, c) R=500, d) R=750, e) R=800, f) R=900.

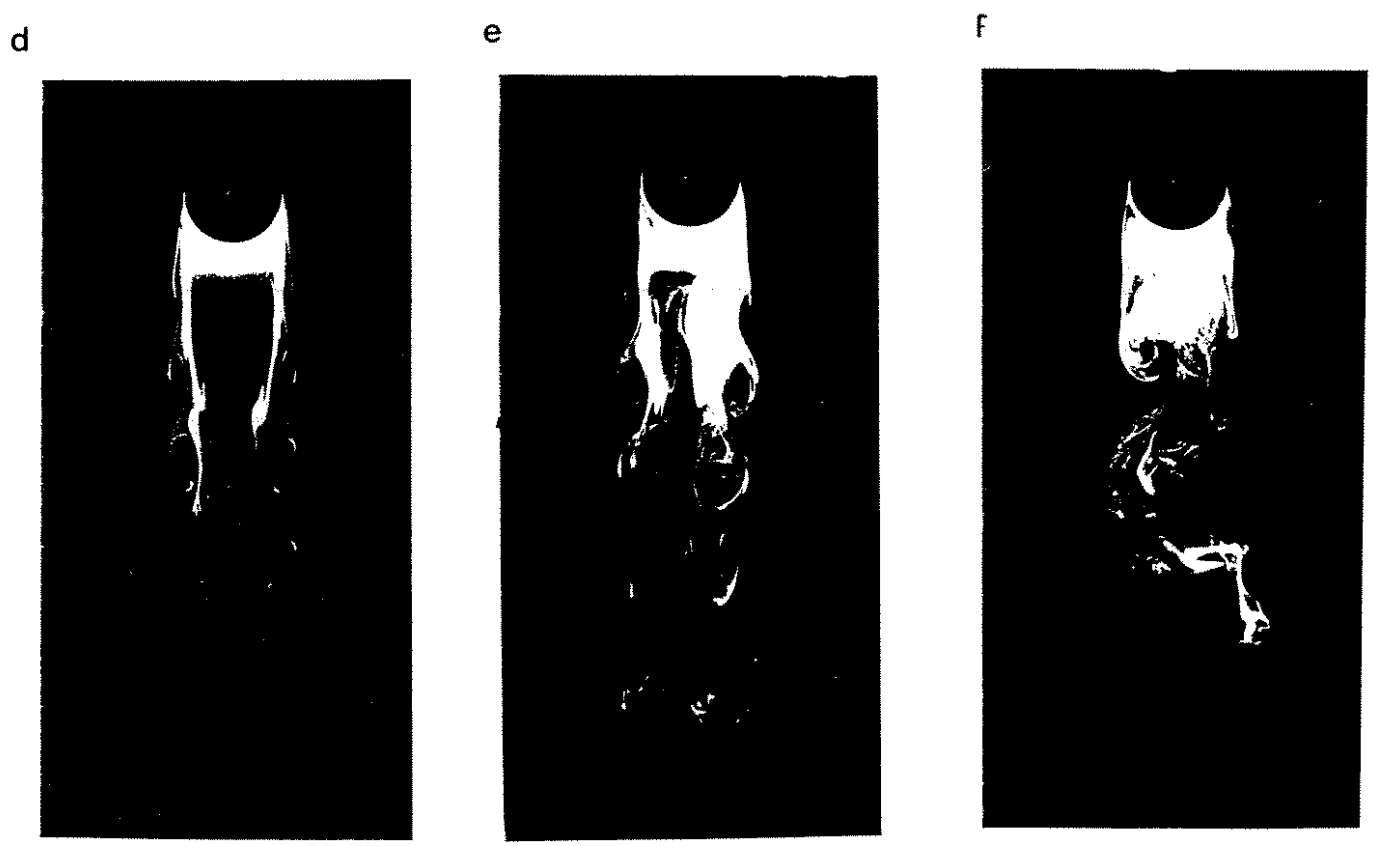

An experimental study on a wake of a torus body using UVP monitor

Authors: **Yoshihiro Inoue[1], Shintaro Yamashita[2], and Masaya Kumada[2]**

Institution: Department of Mechanical Engineering, Suzuka College of Technology

Running head: Y. Inoue et al. / A wake of a torus body

Titles and Address: [1] Department of Mechanical Engineering, Suzuka College of Technology, Suzuka, Mie 510-02, Japan

[2] Department of Mechanical Engineering, Gifu University, Gifu 501-11, Japan

Abstract. A flow around a torus body has a complicated three-dimensional structure, and it is difficult in this flow to measure a spatiotemporal field of velocity by means of conventional methods such as hot-wire anemometers. In this study, the wakes of the tori with the diameter ratio of 3 and 5 are investigated in an axisymmetric and oblique postures mainly for the Reynolds number of 1500. The vortical structures are observed by the flow visualization techniques, and instantaneous velocity profiles in the x- and y-directions are measured with an ultrasonic velocity profile monitor (UVP). The time history of the instantaneous velocity profile is presented, and the spatial distribution of power-spectrum and two-point correlation coefficient are analyzed. A system for multi-line measurements of the UVP is developed, and a velocity field conditionally averaged for vortex shedding is shown.

List of symbols

D	center-line diameter
d	cross-sectional diameter
R_{11}	correlation coefficient
Re	Reynolds number
r_x	streamwise spacing between two points
St	Strouhal number
U_0	mainstream velocity
U_c	convection velocity

U, V	mean velocity components in the x- and y-directions
u, v	fluctuating velocity components
$\tilde{u}$, $\tilde{v}$	instantaneous velocity components
u', v'	rms values of fluctuating velocity
x	distance in the mainstream direction
y	distance parallel to the symmetry plane of the flow and normal to the x-axis
x_{tr}, y_{tr}	position of the transducer tip
α_{tr}	angle between the measuring line and x-axis
θ	oblique angle of the torus against the mainstream
ω_z	vorticity

1 Introduction

Flows around a three-dimensional bluff body and three-dimensional separated flows are of great interest in the field of fluid mechanics. The vortex formation process even in a wake of a two-dimensional bluff body like a straight cylinder (Williamson, 1995), however, is not made clear yet, because of its three-dimensionality and unsteadiness. Many difficult problems related to the flow structure in the near wake remain to be solved. Axisymmetric bluff bodies have received attention from many investigators for their simple geometrical shape and wide variety of practical applications: for example, a disk (Calvert, 1967; Higuchi et al., 1996), a sphere (Sakamoto and Haniu, 1990) and a ring (Takamoto, 1987; Miau et al., 1992). On the other hand, a body of revolution at an angle of attack in a uniform flow has been also investigated to understand the topology of three-dimensional separated flow (Tobak and Peake, 1982).

In the present study, the structure of a wake behind a torus body has been investigated; the torus is a ring with a circular cross-section. This flow is a basic one applicable to many problems, including bio-fluid mechanics for DNA polymer, properties of flow with micelles, and the drag and heat transfer performance for helical heating tubes.

The flow around the torus has a three-dimensional complicated structure, and so far few studies have been made from the engineering and fundamental points of view. Monson (1983), who made free-fall experiments with different tori in a viscous fluid, found the drag data in the viscous regime and a variety of flow patterns against a projected area solidity. Also, Amarakoon et al. (1982) obtained

the drag on the torus falling in a viscous liquid contained by tanks of different cross-sections. In analytical studies for low Reynolds numbers, Johnson and Wu (1979) employed a singularity method for Stokes flow and obtained force coefficients for various motions of the torus. Goren and O'Neill (1980) solved exactly the equations of creeping fluid motion using toroidal coordinates and computed the resisting forces for toroids with various solidities.

Recently, Leweke and Provansal (1995) investigated the wakes behind four rings with different aspect ratios in a wind tunnel. They yielded the Strouhal curves in the periodic regime and transition range, and identified the periodic vortex shedding modes, that is, the parallel mode and helical oblique modes. Furthermore, they studied the ring wake using a dynamical wake model involving a Ginzburg-Landau amplitude equation and compared its predictions with their experimental data.

Our present experiments were carried out in a water channel using a flow visualization technique and an ultrasonic Doppler method. The ultrasonic velocity profile (UVP) monitor developed by Takeda (1995) yields spatiotemporal information on the velocity, so that the wake structure of the torus is made clear in this study, both in the cases of a zero inclination and oblique postures of the torus.

2 Experimental methods

2.1 Test rig

Experiments were performed in a free-surface water channel. Water preserved in the underground pit is pumped up and introduced through a control valve into the channel. The flow settled by means of a straightener and screens is contracted into a test section. The layout around the test channel is shown in Fig. 1. The channel is 700 mm wide, 3 m long, and 500 mm deep at the top of the weir. The torus body is suspended on a circular rod, whose other end is fixed at a rotatable table on the channel, in the middle of a cross section 1 m downstream from the contraction end. An ultrasound transducer is held in a tip of a streamline-shaped support, which is fastened to a traversing device.

The flow field and coordinate system are shown in Fig. 2. The cross-sectional diameter and center-line diameter of the torus body are defined as d and D, respectively. A ratio D/d is a geometrical parameter of the torus, and in this study the cases of $D/d = 3$ and 5 with $d = 30$ mm are investigated. An inclination of the symmetry axis of torus to the mainstream direction presents an attitude of the torus. The oblique angle θ was varied in the range of 0° to 85°, and the zero inclination, that is $\theta = 0$, is an axisymmetric posture. A dynamical parameter of the flow is the Reynolds number, which is

based on a free stream velocity U_0 and the cross-sectional diameter d in the present study. The free stream velocity remains constant at 50 mm/s, and the Reynolds number Re is nearly equal to 1500. The origin of co-ordinates is on a plane of symmetry of the torus body and at the center of its rim, and the x-axis is taken to be coincident with the mainstream direction. The flow visualization by a hydrogen-bubble technique and measurements with the UVP monitor were made on the symmetry plane of the flow, i.e., the x-y plane.

2.2 UVP monitor and multiplexer

The UVP monitor used in this study is a model X3-PS (Met-Flow). The hydrogen bubbles, which were generated and seeded from a cathode wire by the electrolysis of water, were utilized as particles reflecting the ultrasound. The cathode wire is a platinum wire of 20 μm diameter and positioned upstream of the torus, as shown in Fig. 1.

A basic frequency of the ultrasonic transducer is 4 MHz (IMASONIC), and the other measuring parameters are shown in Table 1. The arrangement of the ultrasound transducer is shown in Fig. 2. A location and orientation of measuring line are presented in terms of the position of the transducer tip, x_{tr} and y_{tr}, and of an angle from the x-axis, α_{tr}. Therefore, the velocity $\tilde{q}$ instantaneously detected by the UVP monitor is a function of α_{tr},

$$\tilde{q}(x_i, y_i) = \tilde{u}(x_i, y_i) \cos \alpha_{tr} + \tilde{v}(x_i, y_i) \sin \alpha_{tr}, \tag{1}$$

and the measuring positions are

$$\begin{aligned} x_i &= x_{tr} + (\xi_{st} + \xi_{ch}\, i) \cos \alpha_{tr}, \\ y_i &= y_{tr} + (\xi_{st} + \xi_{ch}\, i) \sin \alpha_{tr} \quad (i = 0, 1, \cdots, 127), \end{aligned} \tag{2}$$

where ξ_{st} and ξ_{ch} are the starting depth and channel distance of the UVP monitor, respectively. The transducer arrangements and spatial measuring parameters adopted in this experiment are also listed in Table 1.

A multi-measurement system applied to conditionally averaging the velocity profiles is shown schematically in Fig. 3, and a setting of a reference transducer is given in the last column of Table 1. Two transducers are alternately switched by a multiplexer (64-System, JcAIR), which is controlled together with the UVP monitor by a personal computer (FMV-Series, FUJITSU). The time period of the transducer switching is 145 ms.

3 Results and discussion

3.1 Axisymmetric wake at zero inclination

Flow visualization and vortex shedding frequency

The flows visualized by a hydrogen-bubble method are shown in Fig. 4. Mean flow fields for D/d = 3 and 5 are axisymmetric, but the vortical structures for these flows are different from each other. In the near wake region of $D/d = 5$, say within about 1 D downstream of the torus, the inside and outside shear layers roll up alternately; they are separated from the caliber and circumference of the torus, respectively, and the vortex rings are shed downstream. In the case of $D/d = 3$, however, no vortex ring is discernible in this visualization picture, and the periodic variation of the velocity is rather observed near the axis of symmetry of the torus.

There is a dominant frequency of the fluctuating velocity in the wake of the torus at the zero inclination, probably corresponding to the vortex shedding. In order to estimate the dominant frequencies, measurements of the fluctuating velocity were made in a range of $600 < Re < 2700$ at x = 150 mm, where the inside and outside cylindrical shear layers separated from the torus roll up and periodic vortex structures are observed, as shown in Fig. 4. The variation in the vortex shedding frequency, represented in the Strouhal number $St = f d / U_0$, against the diameter ratio is shown in Fig. 5; the present data are for $Re \approx 1500$, and compared with rings having a sharp-edged cross-section (Takamoto, 1987) and two circular cylinders (Bearman and Wadcock, 1973). Takamoto (1987) has suggested in his investigations of the rings that there exists a structural change of the wake between $D/d = 4.5$ and 5.0. Monson (1983) also found that the patterns of the torus wake may be classified into three categories by the projected area solidity, $S = 4\,(D/d) / (D/d + 1)^2$, and that there is a sudden change between two flow patterns at $S \approx 0.6$ ($D/d \approx 4.4$). In the present experiments the tori with D/d = 3 and 5 were used; on referring to the above studies, the former corresponds to a disk mode which has an oblique loop wake structure typically generated by solid bodies, and the latter to a ring wake mode which consists of coherent axisymmetric structures. The vortex shedding frequencies for the torus were almost similar to the wake of two circular cylinders, and they remained almost unchanged for both regimes of the torus wake. No discrepancy seems to explicitly appear between the two wake modes in the shedding frequency in contrast to the wake of the ring model. In the wake of the torus with $D/d = 3$, however, the peak of the power spectrum is relatively smaller and much broader than that with D/d =5.

Figure 6 shows the change in the dominant frequencies with respect to the Reynolds number for the ring wake mode ($D/d = 5$) together with the results measured by Leweke and Provansal (1995) in the wake of the torus with $D/d = 10$. Leweke et al. have found from their careful experiments that transition from a stationary to an oscillating wake occurs at $Re \approx 50$, and that there are a periodic regime nearly in the interval $50 < Re < 190$ and a transition regime in $180 < Re < 350$. The Reynolds numbers in the present experiments are slightly above the transition regime, and by reference to the wake of a circular cylinder (Williamson, 1995), flows in this interval seem to be associated with a disorganized motion by a fine-scale three-dimensionality. It is observed from our results that the Strouhal number is nearly constant and slightly decreases as the Reynolds number increases above 1000. This behavior is probably the same for the circular cylinder (Blevins, 1995).

Spatiotemporal velocity field

Figures 7(a) and (b) show time histories of the instantaneous profile of the velocity component $\tilde{u}$ in the x-direction. The radial distances of measuring lines which are parallel to the x-axis are 30 mm and 50 mm for the diameter ratio of 3 and 5, respectively, and these positions nearly correspond to the inside separated shear layers. In the case of $D/d = 5$, the regions of higher and lower velocities appear alternatively and regularly in the time and/or streamwise directions and transfer linearly in the x-t plane. This slope indicates a convection velocity of flow structure, and the value estimated here in this case is 0.80 times the free stream velocity U_0. On the other hand, for $D/d = 3$, the regularity of the flow structure is found downstream of about $x = 150$ mm, and the convection velocity is smaller than that for $D/d = 5$.

Spatiotemporal contour maps of the instantaneous velocity component in the y-direction are shown in Figs. 8(a), (b) at $x = 150$ mm and Figs. 8(c), (d) at $x = 300$ mm; the abscissae denote the time and the ordinates are the lateral distance. The figures clearly show the flow patterns in the space-time field, in which the flow direction is right to left. The map for $D/d = 5$ at $x = 150$ mm (Fig. 8(b)) shows clearly the anti-symmetric contour patterns; thus the flow is symmetric with respect to $y = 0$, and the regions of the positive and negative velocities are arrayed with a spatiotemporally regular pattern. In the near field at $D/d = 3$ (Fig. 8(a)), there is a flow toward the center axis in the outer shear layer, and the regions of the positive and negative velocities are scattered about $y \approx \pm 40$ mm temporally. In the downstream position, $x = 300$ mm for $D/d = 5$ (Fig. 8(d)), it can be seen that the

regular patterns are clear and the structural arrangement of the flow remains almost unchanged both in the time and lateral directions. On the other hand, at $D/d = 3$ (Fig. 8(c)), a flow pattern is considerably altered compared with the upstream cross section; the regions of the positive and negative velocities become larger bulks than at the upstream position due to an absorption of the vortices and have a tendency to be located about $y = 0$. It seems that this modification of the velocity profile is connected with the transition of the flow structure from the cylindrical vortex to the vortex loop (see also in Fig. 4(a)), which was suggested by Sakamoto and Haniu (1990) for a wake of a sphere.

Flow structure

The space correlation of fluctuating velocities at two points separated in the main flow direction is useful for a structural analysis of flow, while its measurement is difficult by means of the method of hot-wires, because the upstream probe greatly disturbs the flow. For this reason, the UVP monitor has an advantage over the other velocity measurement methods and can measure such quantities without error due to the probe-induced disturbance.

The coefficient of space correlation is defined as,

$$R_{11}(x, y; r_x, r_y, \tau) = \frac{\overline{u(x, y; 0, 0, 0)\ u(x, y; r_x, r_y, \tau)}}{u'(x, y; 0, 0, 0)\ u'(x, y; r_x, r_y, \tau)}, \tag{3}$$

in the two-dimensional field. Although spatiotemporal parameters are r_x, r_y and τ, only r_x is changed as a variable and the others remain constant. The correlation coefficients are computed at various y.

Figures 9(a) and (b) show the contour maps of two-point correlation coefficients at the reference position of $x = 150$ mm for the diameter ratio of 3 and 5, respectively. As shown in Fig. 9(a), no coherent structure of the flow at $D/d = 3$ can be found except in the neighborhood of the axis of symmetry. In contrast, it can be seen at $D/d = 5$ (Fig. 9(b)) that the regions of the positive and negative correlation coefficients appear periodically in the x-direction; the streamwise length scales of this flow have a same value over the wake, except near $y = 0$ and $y = \pm 90$ mm, where mean velocity gradients in the y-direction dU/dy are nearly equal to 0.

The wake of the torus of $D/d = 5$ exhibits well-organized motion in comparison with $D/d = 3$. This organized structure consists of the inside and outside vortex rings, shed from the torus body and counterrotating with each other, which corresponds to the axisymmetric parallel mode. In order to

confirm this phenomenon, a conditionally averaging method is utilized in the present study. The multi-line measurements with two ultrasonic transducers were carried out and instantaneous velocity profiles at two different locations were sampled almost simultaneously, that is, with a very short interval of 145 ms; one measuring-line is fixed for a reference velocity fluctuation, and the other is moved in the wake. The reference signal is that obtained by rectifying the fluctuating velocity by a band-pass filter, and the time when the reference signal reaches a positive peak is used as a trigger for each cycle.

Figure 10 shows the conditionally averaged vector map ($\langle u \rangle - U_c$, $\langle v \rangle$), where U_c is the convection velocity and estimated at 0.80 U_0 in the preceding section. Vorticities can be deduced from the conditionally averaged velocity field. The vorticity in the x-y plane ω_z is defined as

$$\omega_z = \frac{\partial v}{\partial x} - \frac{\partial u}{\partial y}, \tag{4}$$

and velocity gradients are computed by polynomial approximation. Figure 11 shows a contour map of the vorticity. As shown in Figs. 10 and 11, the vortical structure is symmetric with respect to the axis of symmetry of the torus, and clockwise and counterclockwise vortex rings alternatively arrange in the streamwise direction. A center of the inside vortex rings locates at the radial distance of about 50 mm from the symmetry axis of the torus and a center of the outside vortex rings at the radial distance of about 90 mm. Values of mean velocities in the mainstream direction at the centers of the inside and outside vortex rings, which were utilized as the convection velocity of the vortex ring by Takamoto (1987), are 0.81 U_0 and 0.77 U_0, respectively.

3.2 Flow fields for oblique posture

Figures 12(a)-(f) show the flows at Re = 600 visualized by the electrolytic precipitation method, in which the torus with the diameter ratio of 3 was set up in the oblique postures of $\theta = 0°$, 15°, 30°, 45° and 80°, and the behaviors of the shear layer separated from the torus perimeter are visible by white precipitates. In the axisymmetric case (Fig. 12(a)), the separated shear layer is a cylindrical form rolling up at $x \approx 4d$ (see also in Fig. 4(a)).

For $\theta = 15°$ and 30° (Figs. 12(b) and (c)), the separated flow from the torus forms a cylindrical layer with an axis nearly coincident with the mainstream direction and rolls up at almost the same downstream distance from the leading edge of the torus body. After that, the vortex ring is broken

up into two parts because of an interaction between the outside and inside shear layers. One part exists in the side where the torus rim is inclined upstream, i.e., $y > 0$, and vortex filaments are periodically shed into the wake and have a vortex-loop structure, as shown in a side view for $\theta = 30^\circ$ (Fig. 12(f)). Another part in the downstream-inclined side ($y < 0$) is quasi-periodic at different intervals compared with the upstream-inclined side. For $\theta = 45^\circ$ (Fig. 12(d)) the flow shows almost the same configuration as the preceding case, but the regularity of flow structure in the downstream-inclined side vanishes. For $\theta = 80^\circ$, shown in Fig. 12(e), the intermittent flow through the inside of the torus and the separated flow from the trailing edge were synchronized at a nearly constant interval.

The 3-D maps of power spectra dependent on f and y in the cross section of x = 150 mm are shown in Figs. 13(a)-(d) for the various oblique postures of the torus with $D/d = 5$; a one-dimensional power spectrum $S_{22}(f)$ is obtained by Fourier transforming a time-series data set of 512 points measured by the UVP monitor, where f denotes a frequency. For the axisymmetric flow at $\theta = 0$, the spectral map is symmetric with respect to $y = 0$ and shows two peaks of single frequency of $f \approx 0.34$ Hz at $y \approx \pm 90$ mm. In the case of $\theta = 15^\circ$, the peak frequency in the upstream-inclined side ($y > 0$) increases compared with $\theta = 0$, the one in the downstream-inclined side ($y < 0$) decreases and its power is considerably reduced. In the downstream-inclined side at $\theta = 45^\circ$, no peak is distinguished in the frequency domain, and two ridges become evident in the region of $y < 0$. For $\theta = 80^\circ$, there appears one peak for each spectral ridge with the axis of $y = 0$ between.

Non-dimensional peak frequencies are plotted against the oblique angle in Fig. 14, together with the experimental results of a circular disk by Calbert (1967). When the torus is set with axisymmetric posture (say $\theta = 0$), the Strouhal number is about 0.2. If the torus assumes an oblique posture, the Strouhal numbers in the upstream- and downstream-inclined sides become different from each other; the former increases and the latter decreases with increasing the oblique angle θ up to about $\theta = 30^\circ$. By further increasing θ, the peak in the power spectrum in the downstream-inclined side disappears up to about $\theta = 60^\circ$, and in this range of θ the Strouhal number in the upstream-inclined side is nearly constant or slightly decreases with θ. If θ goes over 60°, the peak in the power spectrum in the downstream-inclined side appears again, and the Strouhal number coincides with the one in the upstream-inclined side which decreases with increasing θ. This variation of the Strouhal number or the peak frequency in the spectrum with respect to the oblique angle θ indicates that the structure of the wake of the inclined torus is altered with θ; four categories can be identified in the situations of θ

$= 0°$, $0° < \theta < 30°$, $30° < \theta < 60°$ and $\theta > 60°$, respectively.

It is found by our previous work for the inclined torus body (Inoue et al., 1995) that a maximum value of lift is obtained at $\theta \approx 60°$, and that the direction of the moment of force acting on the torus is different from each other for $0° < \theta < 70°$ and $70° < \theta < 90°$. These phenomena seem to correlate with the transition of the flow regimes shown in the present experiment.

4 Concluding remarks

The flow structures behind the torus body set with axisymmetric and oblique postures were investigated by the flow visualization technique and UVP monitor. Qualitative explanations were given for the vortical structure in terms of flow visualization. Instantaneous flow pattern, various quantities, including streamwise two-point correlation and power spectral density of fluctuating velocity, and conditionally averaged velocity profiles were analyzed from the data set measured by the UVP monitor. These quantities made clear the structural properties of the wake of the torus.

In the axisymmetric wake at zero inclination, it is confirmed that there were two modes of flow structure. At the lower diameter ratio, the disk mode is observed and consists of the cylindrical shear layer and oblique vortex loop. The streamwise change of these flow structures is clearly found in the time history of the instantaneous velocity profile. At the higher diameter ratio corresponding to the ring wake mode, the counterrotating vortex rings alternately are shed from the torus with regularity. This phenomenon is reflected in the streamwise two-point correlation and conditionally averaged vorticity field. In the case of $D/d = 5$ at $Re \approx 1500$, the convection velocity of the vortex ring is estimated at $0.80\ U_0$.

The vortex shedding frequencies remain almost unchanged for both regimes within the present experiments, and no discrepancy explicitly appears between two wake modes in the shedding frequency. In the ring wake mode, the Strouhal number is nearly constant and slightly decreases as the Reynolds number increases above 1000.

In the oblique postures of the torus, the change in the flow structure with respect to the oblique angle can be made clear by the transverse variations in the power spectrum and behavior of the peak frequencies in the space and frequency domains. The flow patterns can be identified in four categories of $\theta = 0°$, $0° < \theta < 30°$, $30° < \theta < 60°$ and $\theta > 60°$, respectively.

Acknowledgement

The authors wish to express their appreciation to Dr. Ing. Yasushi Takeda of Paul Scherrer Institut for his advice on the UVP system.

References

Amarakoon A M D; Hussey R G; Good B J; Grimsal E G (1982) Drag measurements for axisymmetric motion of a torus at low Reynolds number. Phs. Fluids. 25: 1495-1501

Bearman P W; Wadcock A J (1973) The interaction between a pair of circular cylinders normal to a stream. J. Fluid Mech. 61: 499-511

Blevins R D (1995) Vortex-structure interaction. In: Fluid Vortices. (ed Green, S I). pp 533-574, Netherlands: Kluwer Academic Pub.

Calvert J R (1967) Experiments on the flow past an inclined disk. J. Fluid Mech. 29: 691-703

Goren S L; O'Neill M E (1980) Asymmetric creeping motion of an open torus. J. Fluid Mech. 101: 97-110

Higuchi H; Anderson R W; Zhang J (1996) Three-dimensional wake formations behind a family of regular polygonal plates. AIAA J. 34: 1138-1145

Inoue Y; Okugawa T; Yamashita S (1995) An experimental study on the properties of the 3-dimensional flow around a torus. Proc. 72nd JSME Spring Ann. Meeting. (Tokyo). 3: 63-64

Johnson R E; Wu T Y (1979) Hydromechanics of low-Reynolds-number flow. Part 5. Motion of a slender torus. J. Fluid Mech. 95: 263-277

Leweke T; Provansal M (1995) The flow behind rings: bluff body wakes without end effects. J. Fluid Mech. 288: 265-310

Miau J J; Chiu E G; Chou J H (1992) Laser-sheet flow visualization of the confined wake behind a ring. Fluid Dynamics Research. 9: 255-265

Monson D R (1983) The effect of transverse curvature on the drag and vortex shedding of elongated bluff bodies at low Reynolds number. Trans. ASME J. Fluids Eng. 105: 308-322

Sakamoto H; Haniu H (1990) A study on vortex shedding from spheres in a uniform flow. Trans. ASME J. Fluids Eng. 112: 386-392

Takamoto M (1987) A study of the wake structure behind bluff rings. Bull. National Research Laboratory of Metrology. 36: 445-537

Takeda Y (1995) Velocity profile measurement by ultrasonic Doppler method. In: Experimental Thermal and Fluid Science. Vol. 10, pp 444-453, New York: Elsevier Sci. Inc.

Tobak M; Peake D J (1982) Topology of three-dimensional separated flows. Ann. Rev. Fluid Mech. 14: 61-85

Williamson C H K (1995) Vortex dynamics in the wake of a cylinder. In: Fluid Vortices. (ed Green, S I). pp 155-234, Netherlands: Kluwer Academic Pub.

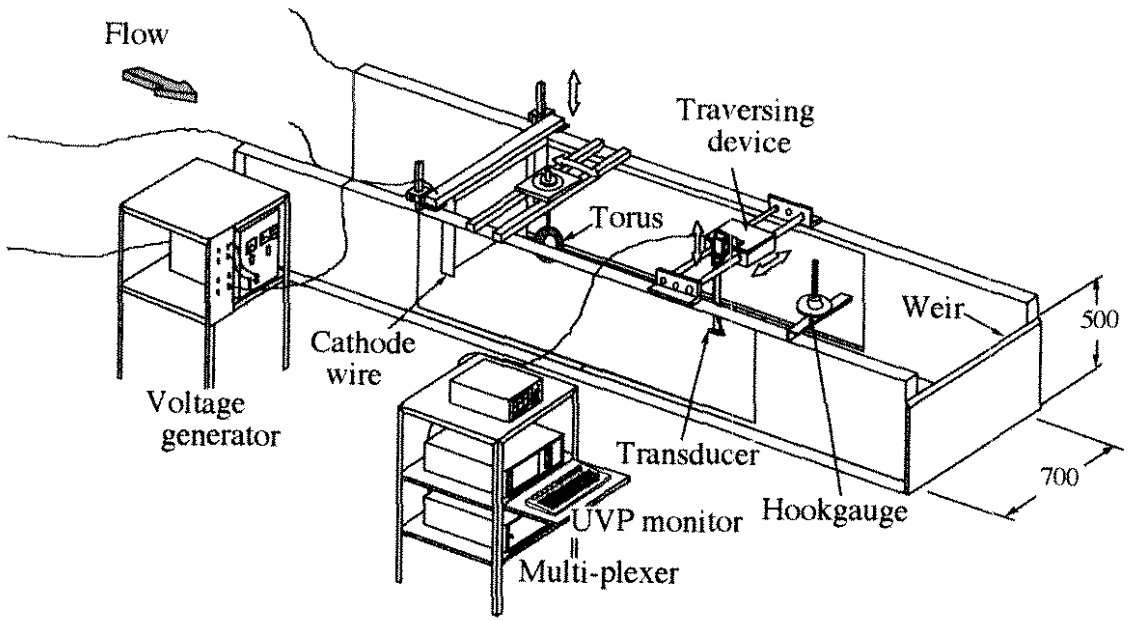

Fig. 1. Sketch of the test section

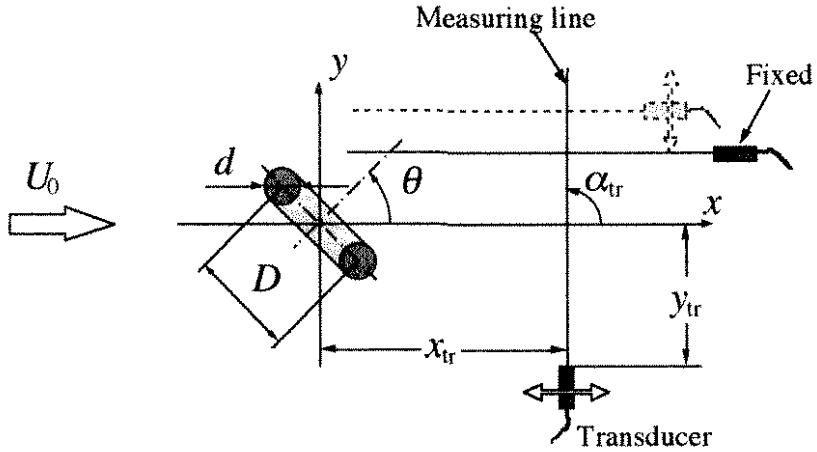

Fig. 2. Flow field and coordinate system

Table 1. Specifications of UVP measurement

	x-direction	*y*-direction	Ref. TRD
α_{tr} (deg)	180	90	180
x_{tr} (mm)	590	90 ~ 420	690
y_{tr} (mm)	-198 ~ 198	273	45
ξ_{st} (mm)	20	15	←
ξ_{ch} (mm)	4.44	3.70	←
Emission voltage	150 V		
Basic frequency	4 MHz		
Pulse repetition frequency	978 Hz		
Number of pulse repetition	16		
Cycles per pulse	4		

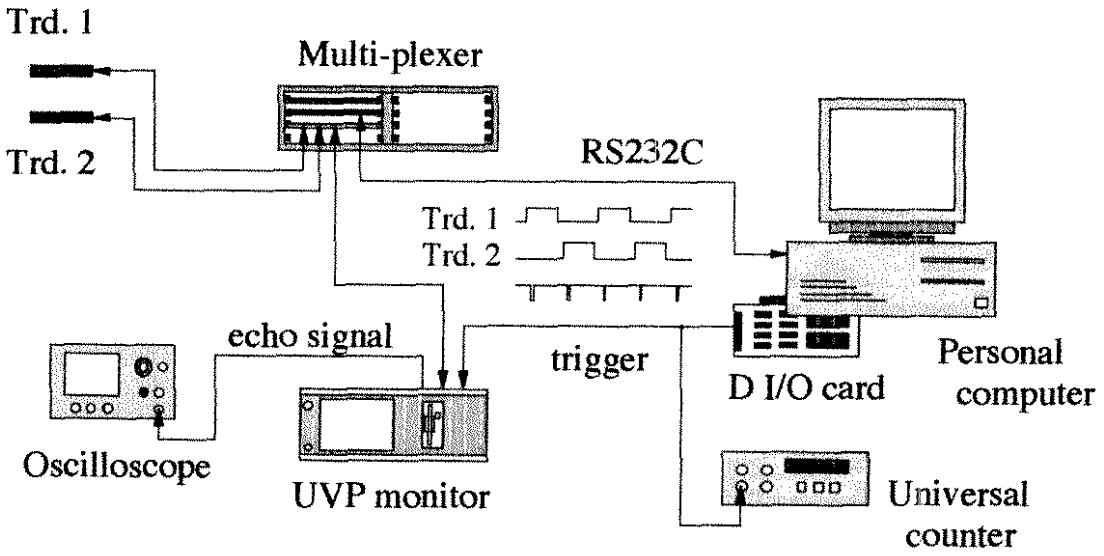

Fig. 3. Multi-line measurement system

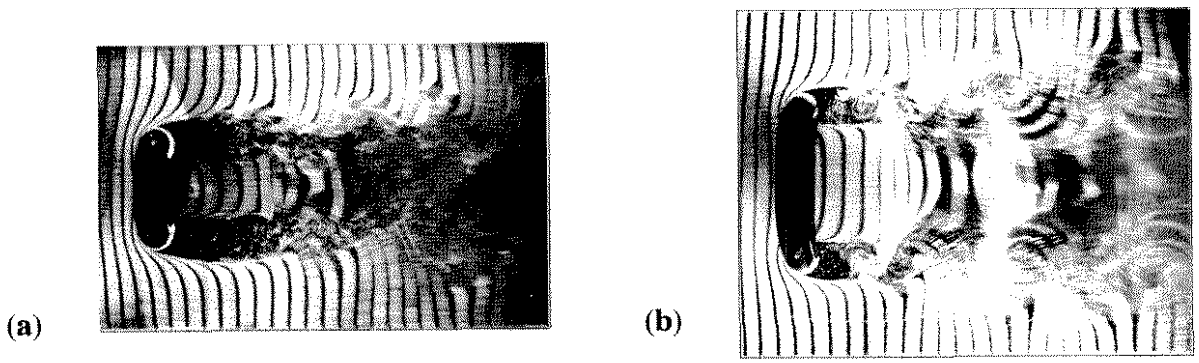

Fig. 4. Flow visualizations at $\theta = 0°$ by the hydrogen bubble method. (a) $D/d = 3$; (b) $D/d = 5$.

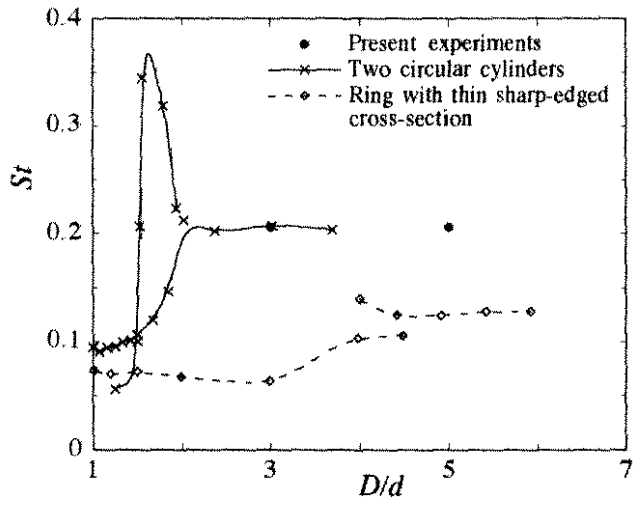

Fig. 5. Variation of Strouhal number with geometrical parameter *D/d*

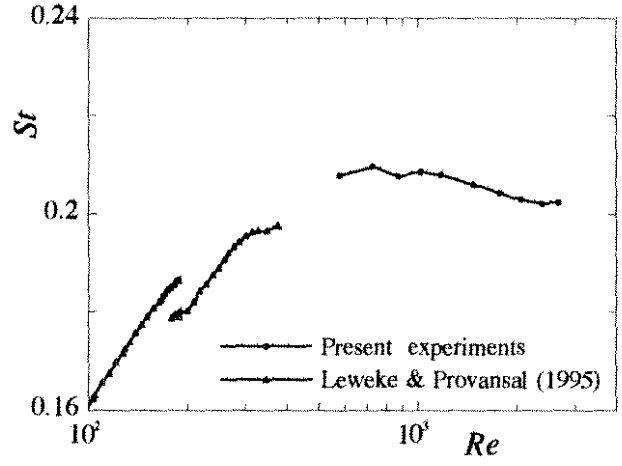

Fig. 6. Strouhal-Reynolds number relationship in the ring wake mode

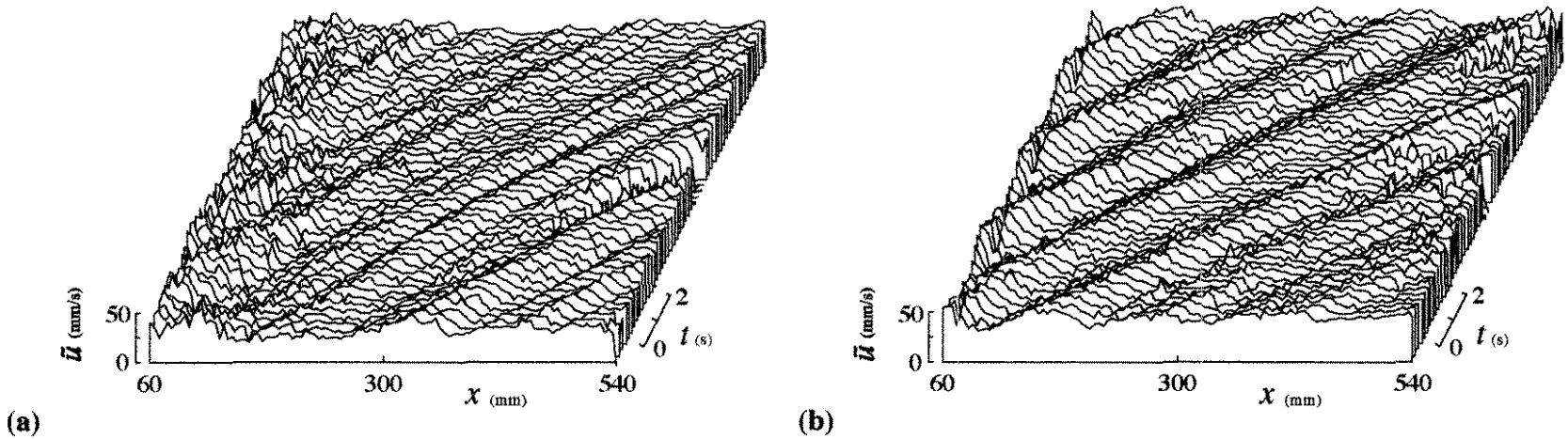

Fig. 7. Time history of the streamwise distribution of velocity component $\tilde{u}$. (a) $D/d = 3$; (b) $D/d = 5$.

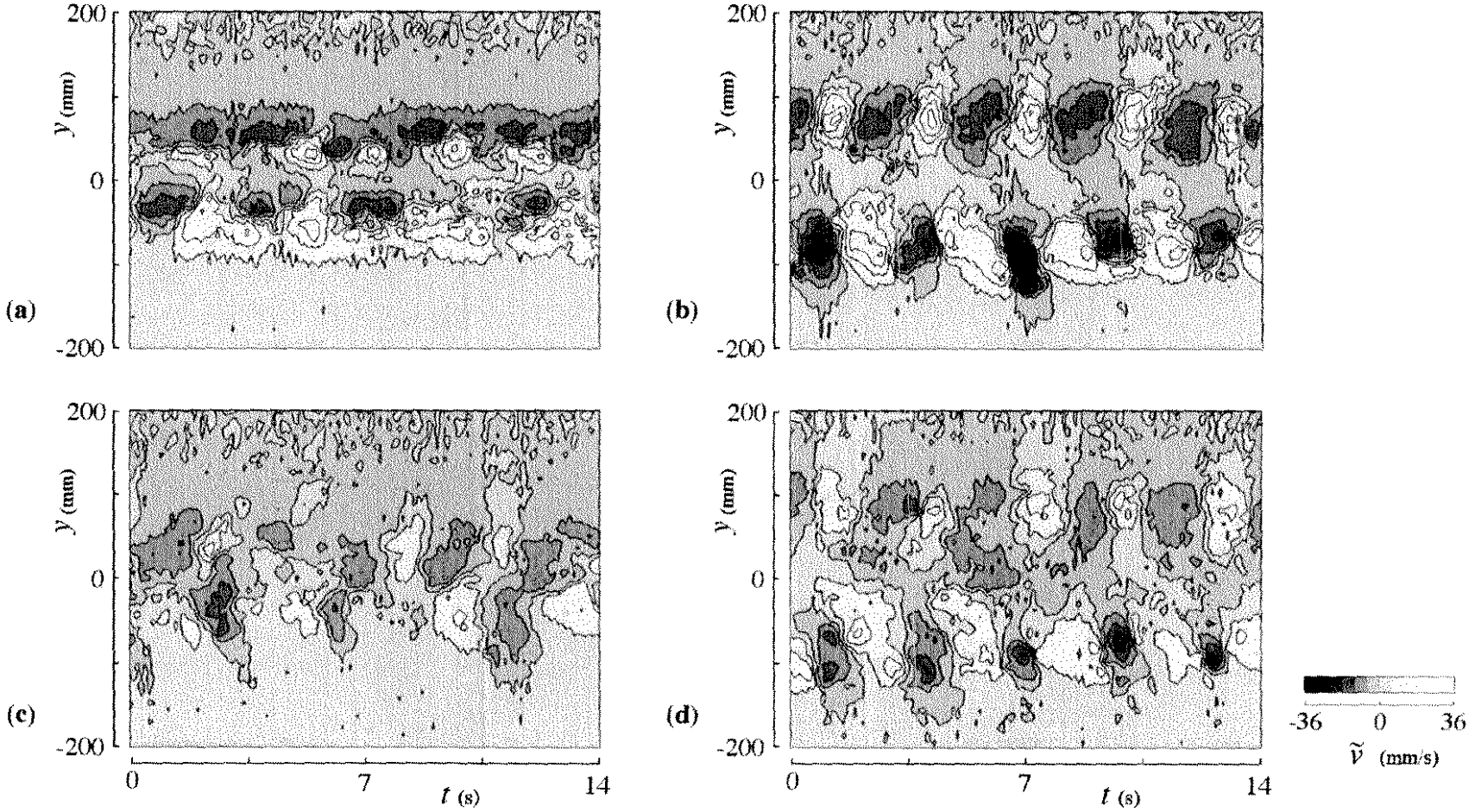

Fig. 8. Velocity contour maps in the y-t field of component $\tilde{v}$. (a) $D/d = 3$, $x = 150$ mm; (b) $D/d = 5$, $x = 150$ mm; (c) $D/d = 3$, $x = 300$ mm; (d) $D/d = 5$, $x = 300$ mm.

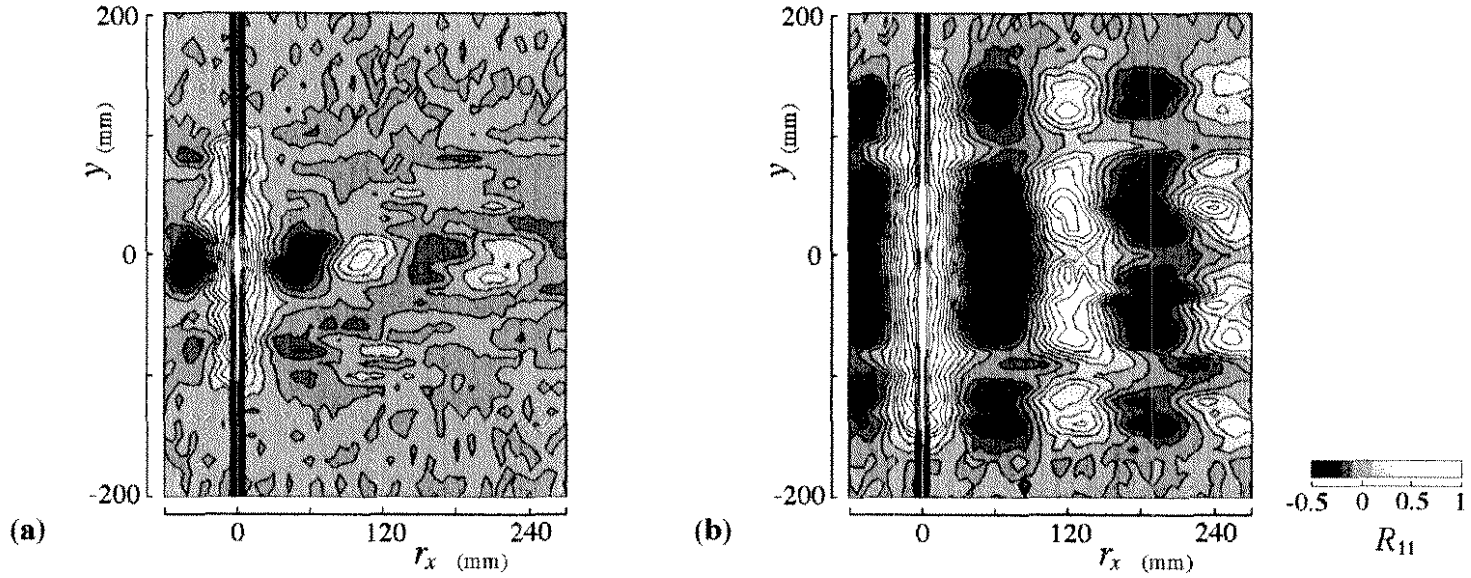

Fig. 9. Contour maps of the two-point correlation coefficient in the streamwise direction. (a) $D/d = 3$; (b) $D/d = 5$.

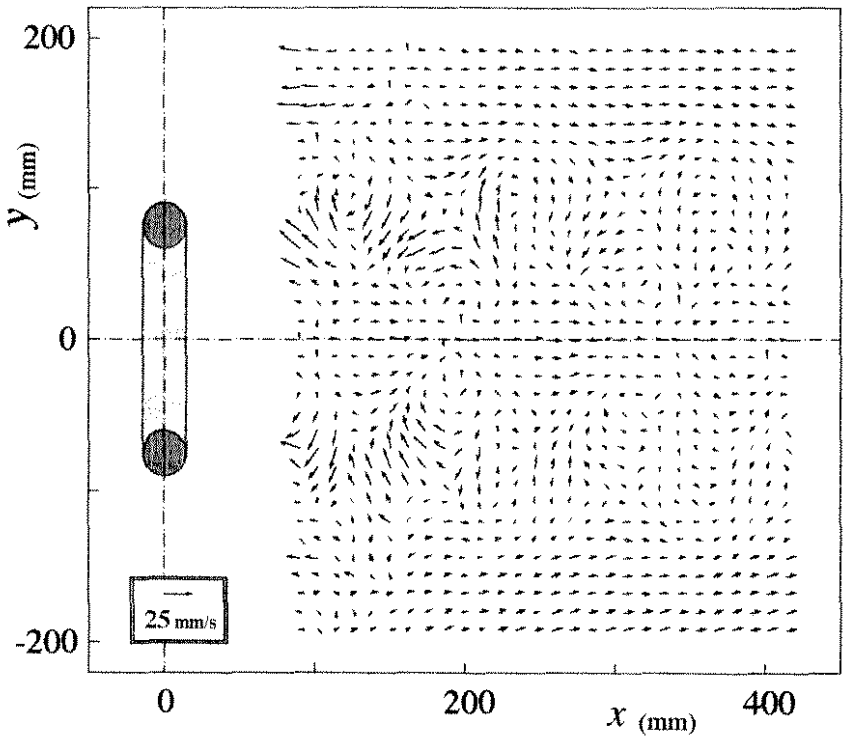

Fig. 10. Vector map of conditionally averaged velocity

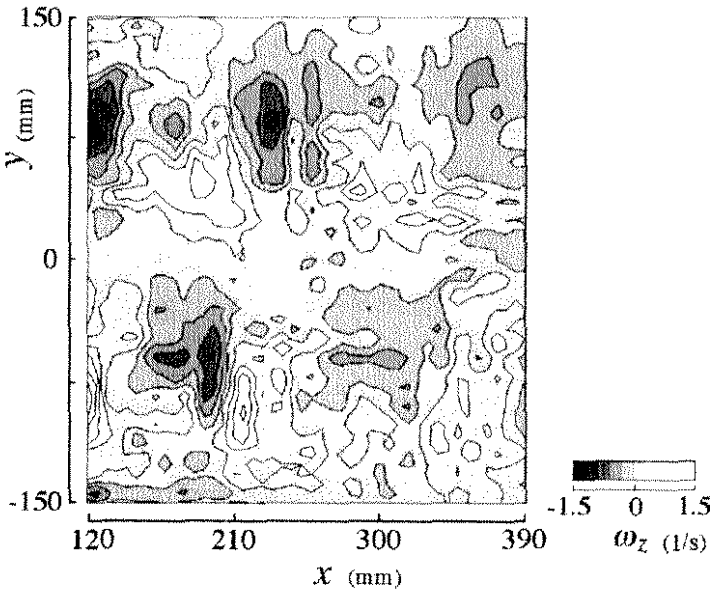

Fig. 11. Contour map of vorticity

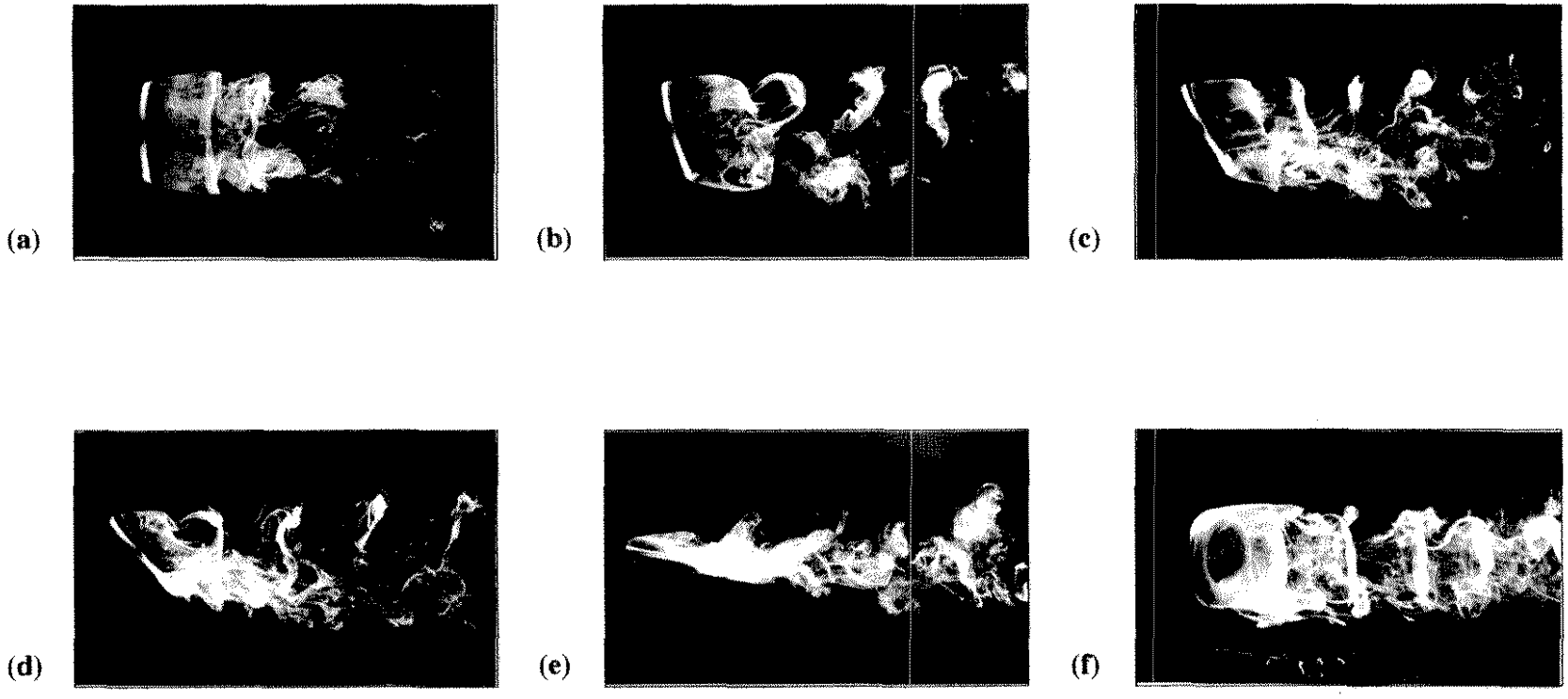

Fig. 12. Flow visualizations of the torus with $D/d = 3$ by the electrolytic precipitation method. Top-views at (a) $\theta = 0°$; (b) $\theta = 15°$; (c) $\theta = 30°$; (d) $\theta = 45°$; (e) $\theta = 80°$, and (f) side-view at $\theta = 30°$.

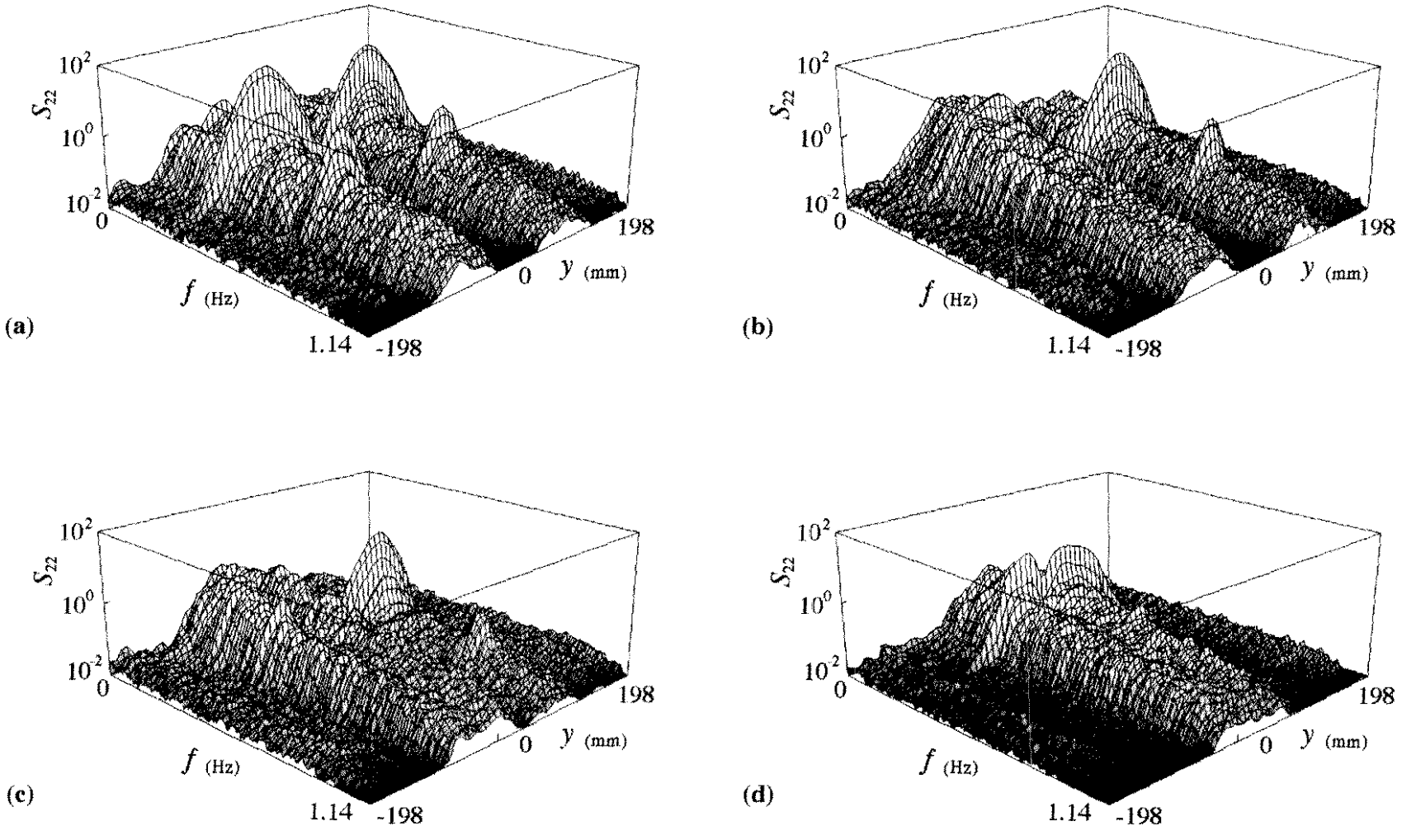

Fig. 13. Transverse variations in the power spectrum of the velocity component v in the wake of the torus with $D/d = 5$. (a) $\theta = 0°$, (b) $\theta = 15°$, (c) $\theta = 45°$ and (d) $\theta = 80°$.

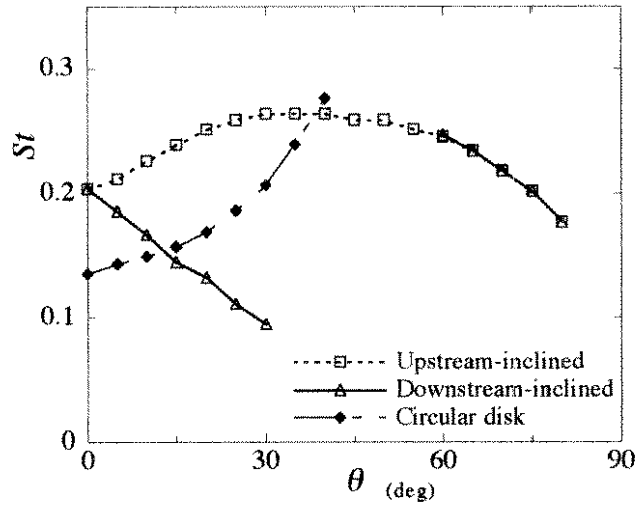

Fig. 14. Variation of Strouhal number with oblique angles θ

An experimental investigation on thermal striping. Mixing phenomena of a non-buoyant jet with two adjacent buoyant jets as measured by ultrasound Doppler velocimetry

A. Tokuhiro

Reactor Engineering Section, Safety Engineering Division, Oarai Engineering Center
Power Reactor and Nuclear Fuel Development Corporation (PNC)
4002 Narita, Oarai-machi, Ibaraki-ken, Japan 311-13

Abstract Experiments were conducted to investigate the thermal mixing phenomena of three quasi-planar vertical jets, one unheated surrounded by two heated jets. Velocity measurements of a *reference* single-jet and the triple-jet configurationwere taken by ultrasound Doppler velocimetry while temperature data were taken from 39 thermocouples traversed vertically. We found from a *hydrodynamic* perspective that beyond the exit region, our single-jet data behaved like previous single-jet data. In contrast the triple-jet exhibited for example, up to 20 times the root-mean-square velocity values in the downstream regions, especially in between the heated and unheated jets. In particular for equal jet exit velocities (3 jets), U_{avg}=0.5 m/s and a temperature difference between the jets, $\Delta T = T_{hot} - T_{cold} = 5°C$, we found that the convective mixing predominantly takes place at axial distances, z/D_h = 2.0 to 4.5, where D_h is the hydraulic diameter of the exit nozzle. Spanwise the mixing span a range, $x/D_h \sim 2.25$, centered about the unheated jet; that is, the regionbetween the heated and unheated jets.

List of symbols

Symbol	Unit	
D_h	10^{-3} m	hydraulics diameter of the inlet channel
Gr	-----	Grashof number, = $(g\beta\Delta T\, z^3/\nu^2)$
L	10^{-3} m	length of the inlet channel
Pr	-----	Prandtl number, = (ν/α)
Re	-----	Reynolds number of inlet channel, = (UD_h/ν) or (Uz/ν)
Ri	-----	Richardson number, = Gr/Re^2
$T_{hot}, T_{cold}, \Delta T, t'$	[°C]	temperature of heated, unheated jets, temperature difference between the two at the exit, root-mean-square of temperature
U_{avg}, U_o	10^{-3} m/s	characteristic velocity, velocity at the exit of the nozzle
$U_{ctr,max}$	10^{-3} m/s	maximum centerline velocity of the velocity profile
w'	10^{-3} m/s	root-mean-square velocity of w-component
x	10^{-3} m	transverse (cross-stream) coordinate
z, z_{uc}	10^{-3} m	axial coordinate as measured from jet exit and axial core length
α	m^2/s	thermal diffusivity
β	1/K	coefficient of thermal expansion
ν	m^2/s	kinematic viscosity

1

Introduction

Thermal striping refers to random thermal cycling of reactor structures and components as a result of fluid-structure interaction; that is, striping is likely a description of the cold and hot (thermal) *stripes* or plumes and jets that a solid boundary must withstand due to *preferential or inefficient* mixing of typically coolant flowing through and exiting the core. The net result of this striping is undesirable since *thermal fatigue* of materials can lead to structural and material failure. Thermal striping as a phenomenological problem in LMFBRs was already recognized in the early 1980s by Wood (1980), Brunings (1982) and has subsequently been considered by Betts, Bourman and Sheriff (1983), Moriya et al. (1991) and in recent years by Muramatsu (1994).

We note here that, although the phenomena taken as a whole involve fluid-structure interaction, the analytical and experimental efforts have generally been divided into structural and thermal-hydraulic investigations. In the present work, we focus strictly on the thermal-hydraulic aspects; that is, mainly the convective mixing of a multiple number of jets at different temperatures. The number of jets can range from a single-jet, which has been most extensively studied, to two jets flowing side-by-side, at a relative angle or co-axially and with a relative velocity (and/or temperature) to each other. In fact co-axial jets of sodium have been investigated by Tenchine and Nam (1987) while Tenchine and Moro

(1995) compared the results of sodium and air jet experiments. Investigation of more than two jets seems to be rare. Thus besides its relevance to LMFBR thermal-hydraulics, a study of a multiple number of vertical jets at either the same or different densities (temperatures), may be of general interest to the heat transfer community.

In the present study, we carried out water-based experiments in a test facility simulating the mixing of one centrally located jet sandwiched by two adjacent and buoyant jets at higher (hotter) temperature. One objective of the study was to demonstrate the applicability of ultrasound Doppler velocimetry for velocity measurements. By applicability we mean velocity measurements in the flow field of relevance. Subsequently we first obtained and evaluated the hydrodynamic information concerning the nature of mixing between thermally-stratified jets. Then with the addition of temperature data we were able to assess the thermal-hydraulics of mixing.

2 Experiment

2.1 Experimental facility

Figure 1 shows the experimental loop including the test section. Except for the test section, the rest of the facility functions as a support system shared by two other experiments. The facility thus consists of the thermal striping test section set within a larger rectangular tank, a loop heater/exchanger for supplying hot water, a head tank in order to control the water-level, a filter to extract contaminants within the loop, an air-to-loop heat exchanger for supplying cold or cooled water back into the loop as well as a general purpose lab water supply tank. Several turbine flowmeters as well as orifice plate type devices, a system of valves and all the connecting piping are as depicted.

A more detailed view of the test section itself is shown in Figure 2. The test section is immersed within a rectangular tank measuring 2438W x 2438H x 671D [W-width, H-height, D-depth, all mm], and is itself a partially enclosed rectangular region measuring 400W x 950H x 176.5D. As noted in the top view, two acrylic plates sandwich the four rectangular blocks thereby restricting the spread of the exiting jets in these directions. The idea was to constrain the jet to a finite width and to "view" it as quasi two-dimensional within this geometry. The right and left sides are however, open so that even with overflow mechanism at the top of the test section there may be some recirculating flow through the sides. A prominent feature of the tank is the large viewing glass windows on both the *front, back* and *right side* of the tank. This feature was included primarily for laser-based measurements and flow visualization techniques. Below the test section are three rectangular channels defined by four equally rectangular blocks. The central channel functions as the "cold" jet while the adjacent two are "hot". The hot and cold jets are supplied from separate sources, the cold source being centrally situated, flowing first through an expansion and then through a flow constriction. The hot source is on the other hand supplied from the right-hand-side into a lower chamber. The flow then weaves its way past the

cold pipe and enters symmetrically through a one-sided rectangular constriction. The exit of the nozzle is a block elevated 75 mm from the reference *groundplane* of the tank.

The other prominent components of the test facility is the traversing thermocouple array and the UVP transducer holder fixed to the left arm of the traversing mechanism. A schematic is shown in Figure 3 along with the exit blocks. The moving mechanism consisted of two vertical and parallel pillars (OD 45mm), between which a "bridge" served as a mounting bracket for the thermocouples. This bridge is fixed and moves up and down with the pillars. The traversing thermocouple array consists of 39 thermocouples facing vertically downward and horizontally spaced 5 mm apart over a 190 mm span. The last 5 mm of each of 39 thermocouples are directly exposed to the flow, while beyond this point the T/C is insulated for a length of 50 mm. The T/Cs are threaded and bonded to an horizontal arm and contained either in the right or left arms. The two arms enter through the top of the rectangular tank. The thermocouple are T-type, constantan copper-nickel with an expected measurement error of 0.5°C. Operationally three T/Cs malfunctioned (No. 5, 6, 14 numbering from left) and could not be used for data acquisition.

Velocity measurements were taken using the Met-Flow Model X-1 Ultrasound Velocity Profile [UVP] (1992) monitor with a single, Delrin-encased (temperature limit ~ 80°C) piezo-electric transducer [TDX] operating at 4 MHz. The transducer had an active crystal diameter of 6 mm. The UVP works on the principle of ultrasound Doppler echography; that is, the position and velocity information are evaluated respectively from the detected time-of-flight and the Doppler-shift frequency at each of 128 locations. From these 128 locations, a componental velocity profile is constructed along the measurement line (ML) of the ultrasonic beam. By componental it is understood that the velocity vector oriented either toward or away from the face of the transducer (from the sign of the Doppler shift) and the magnitude is measured at each of the 128 "coin-like" volumetric elements during each of the 1024 measurement intervals. The real-time corresponding to 1024 measurement intervals is adjustable depending largely upon the preference (and experience) of the user, though it should be based on the phenomenon of interest in the flow; that is, based on estimates of the time-scales associated with various transport phenomena, the user is able to select either a short or long time span between measurements. The UVP can thus detect transient phenomena during a minimum time-span of 30 msec to minutes and hours. The device has been developed and tested most notably by Takeda (1986, 1991*a*, 1991*b*).

The ultrasound is reflected from tracer particles, typically a plastic powder with a nominal size of 50-100 μm (ρ = 1.02 kg/m^3), that are added to the test medium (water). One should note that the inherent assumptions in using this measurement technique are that: 1) the tracer particles accurately reflect the velocity profile of the liquid state and 2) the modification of the flow field due to addition of tracer particles; that is, the particle-to-fluid interaction, is of minor consequence to the measured profile.

Additionally, it is assumed that particle-to-particle interactions are negligible since the concentration of tracer particles, i.e. on the order of 100 grams per 4000 liters (3988) of water, is physically very low. Finally, regarding the former, we assume that there is no slip (relative) velocity between tracer particle and liquid; that is, the particle moves exactly as a fluid element would, as dictated by the initial and boundary conditions of the flow. As for the positioning of the transducer, it was held in place by a short piece of pipe through which the transducer was inserted (and held) and the output signal travels through a 4m long cable. The typical measurement time was of the order of 1-3 minutes.

2.2 Conditions of UVP and temperature measurements

For the data presented in this paper, the average exit velocity of both the single- and triple-jet experiments was 0.5 m/s with an estimated error of 0.1 m/s. The temperature difference between the cold and each of the hot jets was held to 5°C in all cases with an estimated error of 0.75°C. UVP measurements were conducted with the transducer fixed at either the right or left locations with respect to the jet(s) (see Figs. 2, 3). Measurements were taken axially, along the z-axis, at 5 mm intervals up to approximately 550 mm above the imaginary *"0"-plane* in most cases. For all the data present here, the UVP transducer was oriented at an angle of 10° with respect to the horizontal. The selection of the 10° angle was in reality an experimental compromise between a sufficient number of axial locations, which we sought in order to follow the flow development, and the detection of the larger, axial vector component relative to the horizontal component of the actual jetting flow.

3
Results

3.1 Photographs and Video Images

We first present in Figures 4 and 5 digitized image sequences of respectively, the single- and triple-jets extracted from video as a qualitative introduction. The images have been taken with laser-sheet (argon laser) illumination from the side with Rhodamine dye added to the test medium. An horizontal line tracing the laser sheet beam is clearly visible on the top surface of the 4 blocks. Since a normal speed video camera operating at 27 frames/sec was used the images of course missed flow phenomena too fast for it to record. Nevertheless, the single-jet, or rather an ideal planar jet, is said to consist of the following: 1) an *exit region*, which ideally has a *flat, square* or *top-hat* velocity profile but which of course depends on the upstream flow rectification, 2) a *mixing layer* or *developing region* where, as indicated in Figure 6, the mixing layer dynamics on both sides of the jet take place and the velocity profile changes, and 3) a *developed* or *self-preserved region* where the velocity profile is essentially *preserved* even as the jet disperses (widens) spatially. Additionally, one often mentions the *core flow* or *core* of the jet that describes the central region of the jet and additionally the *entrained flow* or *entrainment region*, which describes the flow that is swept into the jetting flow from the surrounding,

along the edge of the jet. Thus, it is clear that a turbulent planar jet would have both spatial (x, z) and temporal (time) dependence. Note that in the present set-up the axial coordinate is the z-axis and the spanwise or width-wise distance is the x-axis. Finally in order to facilitate our presentation, we refer to the buoyant jets as the "hot" jets and the non-buoyant, central jet as the "cold" jet.

3.2 UVP velocity profiles: Single-jet and Triple-jet

Figure 7a) shows a representative set of average velocity profiles of the single-jet taken by the UVP. The axial distances (z) have been chosen to clearly display the changes in the profile with downstream locations and thus represents the distance from the groundplane as indicated in Fig. 3. The abscissa depicts the 128 channels (0-127) along the ultrasound beam, a distance equivalent to 284 mm as noted. In Fig. 7b) we show one profile (z=45 mm) and its associated standard deviation profile in order to explain details of the profile itself. The actual profile as measured for example by the transducer depicted in Fig. 3 is the inverted image of Fig. 7b); that is, recall that with respect to the transducer, flows coming toward it are "--" (negative) and those flowing away are "+" with regard to the sign of the Doppler shift. This does not in any way change the information content of the depicted velocity profile. We thus see that a prominent feature is the peaked, jet-like profile in the central region. Additionally, to the sides of this central region are the entrained-flow regions which show flow of approximately equal magnitude and *on-average* of opposite sign with respect to the transducer. We say *on-average* here because the mixing layer-generated entrained flow dynamically changes direction and magnitude during the measurement period. We observed this while analyzing many sets of 1024 profiles per set of UVP velocity data. However, on average they are of opposite sign. We note that overall although narrower the velocity profile in Fig. 7b and in Fig. 6 are similar. Returning to Fig. 7a) we have artificially inverted the right-hand-side of the profile taken at z=45 and shown it as a dotted line to qualitatively illustrate the similarity with the developing jet depicted in Fig. 6. As for the standard deviation distribution the twin peaks and the valley in between appear to characterize the edge and core of the jet.

As a matter of comparison between our (isothermal) single-jet data with that from past investigations we show in Figure 8 the axial decay of the centerline velocity with those of investigators as noted. The data of past investigators have been extracted form Cheremisinoff (1986) and are represented by linear regression lines above the so-called velocity core length, z_{uc}. The core length corresponds to the axial point below which the data assumes a quasi-constant value ($z_{uc} \sim 4$). To the best of our knowledge the past data are for isothermal air jets. Note that there are variations in slope and magnitude even for identical fluids. Except for the exit region ($z < 0.8$) for which Cheremisinoff presents no data our data is consistent with past investigations.

Figure 9a) shows a representative set of average velocity profiles of the triple-jet at several coincidental axial locations as those in Fig. 7. Due in part to the number of jets (3) and the interaction between them the individual profiles are much more difficult to discern in this figure. We also include the profile near the maximum measured location, z = 535 mm, instead of at z = 350 and also provide data at z = 195. We next present in Fig. 9b) one profile and its associated standard deviation distribution at z = 45. The velocity profile taken here with the transducer at the right is clearly distorted, especially the left jet. The approximate location of the exit nozzles are indicated by triangular symbols on the x-axis. Note that similarly to Fig. 7b) the core and edges of each jets, certainly for the left and center jets are identifiable from the standard deviation profile. The left edge of the right jet is also evident. While details of the distorted profile are discussed later, we present respectively in Figs. 9c) and d) a composite triple-jet velocity profile and an idealized profile. The composite profile was constructed by taking one-half of the profiles from respectively the left and right transducer orientations and joining them at the center.

Figure 10 shows the calculated Root Mean Square (RMS) velocity distribution versus axial distance for both the single- and triple-jet, the latter for both left and right UVP transducer orientations. The triple-jet data were taken on two different occasions so that although operational conditions were nearly identical, it is likely that thermohydraulic conditions were not *exactly* reproduced. The single-jet data is for an isothermal jet. The average exit velocity in all three cases was 0.5 m/s. Figures 11a)-f) then show the estimated spanwise distribution (x-direction) of the ratio of the triple-jet RMS to that of the single-jet RMS with the axial location as the parameter. The data are shown in groups of four for clarity while for each type of jet, the RMS value has first been normalized by its own spanwise average velocity. The triple-to-single jet RMS ratio has been calculated at 8 spanwise regions, each containing velocity data (16 points) over a 35.5. mm span. Eight regions were selected since it was thought that a distribution consisting of 128 points would reveal fine detail not necessarily characteristic of the spanwise variation which might be revealed in a segment-wise average. Our objective was thus to qualitatively or semi-quantitatively reveal the difference in the normalized RMS distribution of the triple-jet versus the single-jet. After varying the number of regions we settled on 8 regions as representative of the spanwise variation.

3.3 Temperature data

The spanwise temperature distribution at selected axial locations is shown in Figure 12. Several points to the left are missing due to malfunctioning thermocouples. Each point represents a temperature averaged over ~ 20.5 seconds containing some 1025 samples. We note that the spatial resolution and span over which the velocity and temperature data were taken did not coincide; that is, the UVP data was taken over a length of 284 mm with a resolution of 2.21 mm whereas the thermocouples span 190 mm at 5 mm intervals. We mention this fact because it is of significance when combining velocity and temperature data. We next show in Figure 13 the corresponding spanwise distribution of the standard

deviation at selected axial stations. Compared to Fig. 11 the z-locations have here been selected to show the gradual change near the exit (z = 20, 30, 40 mm) and at or near the maximum magnitude (z = 120, 130, 140 mm) using Fig. 10 as a guide. Figure 14 is the temperature equivalent to Fig. 10 for velocity. Except that here we show the normalized RMS with the normalization factor being the spanwise averaged temperature.

Next in Figure 15 we show an iso-contour plot of the calculated turbulent heat flux distribution. The figure has been generated from separate calculations of w' and t', which respectively represent the velocity and temperature fluctuations as a function of (x,z). We have equated w' and t' to the RMS values as presented. Recall that the quantity w' is not strictly the z-component of velocity fluctuation since the UVP-TDX was oriented at 10° with respect to the horizontal; that is, it includes primarily the w' component but also a small contribution from u'. In addition since the traversed increments for temperature and velocity were of different sizes, some interpolation had to be performed in order to fill-in missing data. As a matter of approach, the *coarser* (larger traverse increments) temperature data was taken as the basis onto which the *finer* velocity data was adapted, so that interpolation would be minimized. Fortunately, both the temperature and velocity data have nearly equivalent *resolution* up to $z \sim 275$ ($0 \sim x \sim 180$), which also appears to be the region of relevance for thermal mixing. It is clear from the figure that beyond $z \sim 300$, the distribution shows largely *linear* patterns (straight lines) which are the result of sparsely recorded data points and interpolation between these points. We thus settled on a semi-quantitative presentation of the turbulent heat flux distribution.

Finally in Figure 16 we plot the frequency versus the axial distance of the first six peaks ordered in terms of "power" for the triple-jet. The frequencies were generated by applying a fast Fourier transform without any windows to the velocity profiles and characterize the hydrodynamic fluctuations inherent in our flow. They represent the fluctuations along the ultrasound beam. The ordering based on the power gives a measure of the turbulent kinetic energy associated with each frequency of the flow.

4

Discussion of results

4.1 UVP velocity profiles: Single-jet and Triple-jet

The images in Figs. 4 and 5 were presented to orient the reader and to facilitate the discussion to follow. A brief introduction regarding a way to view the UVP measured velocity profile was given based on single-jet data (Figs. 7). We subsequently verified that the our single-jet data, for example the centerline decay velocity was consistent with past experimental data (Fig. 8), even though most of the past data used air as the test medium. We then presented the average velocity and its associated standard deviation profiles for the triple-jet in Figs. 9a) and b).

In Fig. 9b) we note first that the jet exits are spanwise located along the abscissa at approximately x ~ 32, 64 and 96. The velocity profile taken at z = 45 (black symbol) show two slightly distorted peaks at the right and center but each with a shape similar to a single-jet profile. The profile corresponding to the right jet (x ~ 32), as taken from the right however, shows a distorted, twin-peaked shape. And although not shown, when taken from the left, the left jet showed a similarly distorted and twin-peaked profile. This inconsistency, that the distorted portion of the profile corresponds to the jet closest to the transducer, may be due to inadequate amplification of the echoes returning from the ultrasound wave reflecting tracer particles. That is, the linear amplification (versus distance from the transducer) which has been applied, although adequate for the distant channels (measurement volumes), appears insufficient for the (near) jetting region in question. The other distinct possibility is that due to the 10° orientation of the transducer, different axial segments of each jet is detected. As mentioned the 10° angle was in reality a compromise between including the contribution from the expectedly larger vertical component of velocity along the ultrasound beam (measuring line) to that of measuring as near identical axial segments (same z-locations) of the three jets as possible. In Fig. 9c) we have sketched the transducer at both right and left positions and also depict some of the just so-described details. Finally in Fig. 9d) we present a composite profile of the triple-jet with the left and right one-half portions taken with the transducer respectively from the right and left. The profile overlaps in channel number at the center and represents an undistorted profile of the triple-jet.

4.2 Comparison of triple-jet to single-jet velocity data

Fig. 10 depicts the axial distribution of the normalized *RMS* for both the single- and triple-jets, the latter for both right [R] and left [L] transducer orientations. While there are some differences in the triple-jet data the marked contrast is between the single- and triple-jets. In fact the triple-jet reaches values larger than what one might expect as a "rule-of-thumb"; that is, roughly three times the single-jet value (see $2 < z/D_h < 7$). Furthermore, the overall trend is different than the single-jet, which in comparison steadily increases up to $z/D_h \sim 11$ where it appears to reach a quasi-constant value. We note that in Gebhardt et al. (1988) the fully-turbulent region of an isothermal (or non-buoyant) axisymmetric jet, based on the axial distribution of the turbulent intensity, is reached at approximately 10 diameters downstream from the exit. If we can expect our quasi-planar jet to behave similarly then, for our average exit velocity-based Reynolds number of $Re \sim 2 \times 10^4$, our datum points have yet to reach a fully-turbulent state. Equally, that the peak intensity spans our measurement limit of $z/D_h \sim 15$ is different from the quoted work. The triple-jet in contrast, beyond a local minimum at $z/D_h \sim 1.2$, shows a rapid increase to a maximum value at $z/D_h \sim 6$ and thereafter an equally rapid decrease to a quasi-contant value at $z/D_h \sim 9$. From these data alone one could partially conclude that the "hydrodynamic" mixing of the hot and cold jets occurs within 2 to 10 diameters of the exit nozzle. By hydrodynamic we mean just based on velocity data while we acknowledge that the flow is thermal-hydraulic. Interestingly enough, beyond $z/D_h > 10$ the isothermal single-jet's RMS exceeds that of the

thermally-stratified triple-jet's. Since data of an isothermal triple-jet and/or a buoyant single-jet are not available at present we could not isolate nor fully assess the influence of (thermal) buoyancy on the turbulent mixing process. However, it does not appeal to physical reasoning that an isothermal triple-jet's RMS value would suddenly decrease to less than a single-jet's in comparison. So we believe it likely that either the energy content of the buoyant triple-jet is depleted due to thermal mixing and/or some form of turbulence suppression occurs; that is, something analogous to re-laminarization of turbulent mixed convective flows near the laminar-to-turbulent transition.

Since **Fig. 10** depicts the spanwise averaged RMS-values, it suppresses any details of the flow especially in-between the jets. We thus show in Fig. 11a)-to-f) the ratio of the normalized RMS of the triple jet to that of the single jet. Both the single- and triple-jet RMS-values are normalized by their respective spanwise average velocities. The thinking behind this particular way of data presentation was as follows. Since we are primarily interested in the convective mixing at the edge of each jet where potentially the largest temperature gradients are located, we do not necessarily need to look at the fine details of the spanwise velocity profile (for example Fig. 9a). In other words, even though this data is available, we know in advance some regions of interest of the triple-jet's configuration. Therefore, while we expect a fluctuating velocity signature within each of the 128 measurement volumes, we can afford to spatially average (or lump) the velocity level in segments; that is, we can spatially-average over a number of volumes and select the number of segments representative of the flow. Figs. 11a)-f) therefore show the triple-jet data taken from the right, normalized by the single-jet, also taken from the right-side. The legend in each figure shows the axial location at which the ratio was calculated. Since there was a discrepancy between single- and triple-jet measurement locations, a calculation of the RMS ratio at the same axial position was not always possible. Thus, where the locations differed, the axial locations are as noted.

It is clear from these plots that from $z \sim 70$ ($z/D_h \sim 1.96$) to about $z \sim 200$ ($z/D_h \sim 5.6$), the RMS of the triple-jet is larger (≥ 1) than that of the single-jet. In fact, between $95 \leq z \leq 120$ ($2.66 \leq z/D_h \leq 3.36$), the ratio can be as large as 20. Specifically the large values are reached typically in regions "3" and "6" which correspond respectively to the range $154.4 \leq x \leq 189.9$ mm and $225.4 \leq x \leq 260.9$ mm from the face of the transducer positioned at left (see Fig. 3). These regions substantially overlap the width of the two exit nozzle blocks located *in-between* the hot and cold jets. This gives strong support to localizing the thermalhydraulic mixing of our thermally-stratified jets. On the other hand, beyond $z \sim 300$ ($z/D_h \sim 8.39$), except for the left-most and right-most regions where the ratio is nearly one or slightly larger, the central region shows a value of less than one. This trend is consistent with Fig. 10 for $z/D_h \geq 10$. This means that the dynamics of convective mixing below $z \sim 300$ are such that the resulting RMS of the triple-jet especially in the region adjacent to and including the cold jet, falls below that of even an isothermal single-jet. In other words, just based on the RMS velocity data the

thermal mixing appears to take place (transverse to the flow of the jet) such that the turbulence is in effect "depleted" in the central region.

4.3 Temperature measurements

We next present in Figs. 12 and 13 the spanwise average temperature and its associated standard deviation profiles respectively at selected axial locations. The axial distances were selected for clarity in presentation and to correspond as much as possible to the velocity profiles. Note that at z = 20 [mm] the profile clearly indicates the presence of a central cold jet (T ~ 25.5°C) and two hot jets (T ~ 30.8°C), while in-between (to the right and left of z ~ 90) the temperature assumes the "approximate average" of 28°C over a span of 30 mm on either side of the cold jet. Near the regions of the individual jets, the temperature gradient is very sharply defined. At a distance 50 mm further downstream, at z = 70 mm, the "mixing" of the thermally-stratified streams appears well under way and the profile reflects this as the gradients (to either side) between the hot and cold jets have decreased (e.g. 100 < x < 108); that is, the temperature gradient, although still larger than at successively higher axial distances, is smaller in comparison to z = 20. By z = 180 then, the temperature gradients between the hot/cold streams are much smaller and overall, the thermal mixing brings about a "flattening" of the spanwise temperature profile. From z = 20 to 180, the axial center of the cold jet has increased in temperature (from 25.5°C) to nearly 29°C while the hot jets have decreased in temperature from 30.8°C to 29.5°C, which is a smaller absolute change than for the cold jet. The apparent reason for this is the presence of two hot jets which transfer heat to the single cold jet. Beyond z = 180 the temperature profile does not change significantly and resembles the profile at z = 180. Thus except for z = 500 we have not shown the profiles at z = 200, 300 and 400 mm.

As for the standard deviation distribution, the profile shows for example at z = 20, a "twin-peaked" profile similar to Fig. 7b for velocity while in between the jets there is a "plateau" or flat region describing temperature uniformity. At z = 30 however, the profile is already changing as the magnitude of the plateau regions increases relative to the twin-peaks of the central jet. This trend continues at z = 40. One can also see that the profile near the hot jets does not change as much as the region surrounding the cold jet. This appears to be an early indication of the thermal mixing at these lower axial locations. By z = 80, the overall fluctuation level has increased markedly and the profile itself has changed dramatically. In fact, most of the thermal fluctuations are clearly in between the hot and cold jets, while there appear to be smaller "peaks" located on the far side (see right jet, z ~ 164) of each of the hot jets. Note too that the relative width of the cold jet's core region remains fairly unchanged (compare z = 40, 80) and that a local minimum value exists up to z ~ 140 but no longer at z = 180. This means, at least qualitatively, that the thermal mixing has not yet reached (spanwise) the core of the cold jet at 80 < z < 140. This is, however, no longer the case at z = 180 where the "defect" seen at z < 140

has all but disappeared. Beyond z = 180 the profile assumes a gradually decreasing Gaussian-like distribution such that at z = 500, the magnitude is less than 1% of the average at that location.

We asserted from a hydrodynamic point of view, based on the RMS velocity data, that mixing most likely takes place over the axial span, $70 < z < 250$ ($2 < z/D_h < 7$) and in particular, in contrast to the single-jet, the mixing is especially accentuated in the region in-between the jets. We would thus expect much of the thermal convective mixing to occur *in-between* the cold and hot jets as well. We first show however, in Fig. 14 the normalized RMS value for temperature along the axial direction. This figure shows that consistent with the RMS data for velocity, the RMS for temperature reach their largest values, say over 1%, along $60 < z < 300$ mm ($1.68 < z/D_h < 8.4$). The axial span over which thermal convective mixing takes place approximately coincide as expected.

For the conditions given in this work the non-dimensional groupings, mainly the Reynolds (Re), Grashof (Gr) and Richardson ($Ri = Gr / Re^2$) numbers calculated at the mean exit temperature of 27.5°C and based on the hydraulic diameter D_h were as follows: $Re = 2.1 \times 10^4$, $Gr = 8.75 \times 10^5$ and $Ri = 1.98 \times 10^{-3}$. If the Ri-number is taken as the ratio of buoyancy to inertial forces, then conditions at the exit are dominated by forced flow. Equally the local, axial distance-based Ri-number calculated on the difference between the minimum and maximum velocity and temperature yield respectively at z = 120, 535 mm: $Ri (z = 120) = 6.89 \times 10^{-3}$ and 15.5×10^{-3}. So it does appear that the buoyancy force increases relatively to the inertial force from an axial location where mixing is vigorous (z = 120 mm) to where it is essentially complete (z = 535 mm). However, our flow at z =535 mm is still predominantly jet-like and not plume-like.

In Figure 15, we presented an iso-contour plot of the estimated turbulent heat flux distribution that we derived from separate calculations of the RMS for velocity, w', and temperature, t', both as a function of (x,z). We previously noted true nature of w' due to the inclination of the ultrasound transducer. It is by coincidence that the spanwise turbulent heat flux is the one calculated and is also the quantity which may hold more significance in terms of evaluating the thermal mixing. That is, if the spanwise mixing is efficient and thus the heat energy is dissipated, the thermal striping impact is lessened on any solid boundary which the flow encounters. In other words, at a given axial location, the uniformity in the spanwise temperature distribution is a measure of the thermal mixing which has taken place below it. So in spite of the compromises made in matching the velocity and temperature fields, the figure strongly supports our view that there is significant *convective mixing* of thermal energy contained in the two heated jets mostly to the cold jet. This is carried out for an average exit nozzle velocity of 0.5 m/s and $\Delta T = T_{hot\ jet} - T_{cold\ jet} = 5°C$, along an axial span $70 \sim z \sim 160$ mm or when non-dimensionalizing with the exit nozzle's hydraulic diameter, $z/D_h \sim 2.0$ to 4.5. In addition, the corresponding spanwise width where most of this mixing takes place is $x/D_h \sim 2.25$ centered about the axis of the central (cold) jet.

Finally in Fig. 16 we have shown the axial distribution of frequency of the first six peaks ranked in terms of their "power" which is a measure of the turbulent kinetic energy associated with the flow. It seems clear that there are two frequencies, one at approximately 2.25 HZ and the other at 0.7 Hz, dominant in the flow with a transition from the higher to lower frequency at roughly z = 300. Additionally the frequency mode f = 2.25 Hz is established within the first z < 80 mm from the jet exits and coincides with the span over which thermal mixing is thought to occur. It is therefore likely that especially for a low Prandtl number fluid like sodium (Pr ~ 0.001) that both hydrodynamic and thermal fluctuations are characterized for a flow of this type (and under similar conditions) by frequencies of order 2 Hz. That is, if our water data primarily yields frequencies 0.7 and 2.25 Hz, with the large thermal diffusivity (and smaller viscosity) of sodium we would expect "thermal frequencies" in a similar range. In fact these two frequencies are within the range observed by Brunings (1982), 0.1 to 2.0 Hz, who measured temperature fluctuations in a thermal striping experiment using sodium. We also mention in closing that the transition from 2.25Hz to 0.7 Hz signifies a change in the nature of the flow. Although we plan to investigate this further the transition at z = 300 roughly corresponds to the axial location beyond which Fig. 5 and other video-images suggest a composite single-jet like structure with a virtual origin for the triple-jet. It is also the approximate axial location where the triple-jet's RMS reaches a quasi-constant magnitude equivalent to that of the single-jet.

5

Conclusions

An experiment investigating the thermal-hydraulic mixing of three quasi-planar, vertically flowing (water) jets was conducted. In the experiment the central jet was at a lower temperature than the two adjacent jets which were at the same temperature. The jets flowed into a large volume of water initially at the central jet's temperature. The average exit velocity (and flowrate) of the three jets was equal. Velocity measurements were taken using an ultrasound Doppler velocimeter while temperature data were taken from an traversed array of thermocouples. The velocimeter yielded velocity profiles consisting of 128 points along its measurement line which were constructed from the echo signals received from ultrasound reflecting particles moving with the flow. Except for some apparent difficulty in the echo signal processing (amplification) in the region close to the transducer both single- and triple-jet configurations yielded satisfactory velocity data. In fact a plot of the centerline decay velocity of our single-jet was in agreement with data extracted from past investigations. In addition velocity measurements yielded a measure of the flow fluctuations; that is, the standard deviation associated with the average velocity provided, in addition to the temperature data, a means of evaluating the turbulent nature of the flow and the mixing process.

As for the triple-jet some expected similarities to the single-jet were observed, but generally the triple-jet exhibited an elevated level of fluctuations associated with the flow expressed in terms of the standard deviation of the velocity signal. In fact in comparison to the single-jet, normalized RMS values were as much as 20 times as large in the region between the buoyant and non-buoyant (central) jet. Beyond z ~ 300 (z/D ~ 10) however, due in part to thermal convective mixing of the jets, RMS of the single, isothermal jet exceeded the triple-jet. We thus partially concluded that for equal average jet exit velocities of U_{avg} = 0.5 m/s and a central-to-adjacent jet temperature difference $\Delta T = 5°$ (30°C and 25°C) most of the convective mixing between the thermally-stratified jets occurs over an axial distance of $z/D_h \sim 2.0$ to 4.5 where D_h is the hydraulic diameter of the exit nozzle. The mixing was on-average centered about the axis of the central jet and span a width, $x/D_h \sim 2.25$. In fact most of the convective mixing takes place in the region defined by the edges of the central jet and the right and left edges of the adjacent jets; that is, in the regions in-between the cold and hot jets.

Finally a brief look into the spectral nature of the measured data revealed two primarily frequencies associated with the flow, these being a dominating frequency of 2.25Hz established within the first 80 mm from the exit and a lower frequency of 0.7 Hz appearing beyond a transition at approximately z ~ 300 mm downstream.. From these results we were led to reason that for a low Prandtl number fluid such as sodium temperature fluctuations would more than likely occur at similar frequencies.

Acknowledgments

The author would like to thank PNC for his appointment as PNC International Fellow. The authors also recognize the efforts of Mr. Ito and Mr. Onuma who diligently conducted the experimental measurements, maintained the data and prepared the UVP and temperature data which were analyzed in order to prepare this report.

References

Betts C; Bourman C; Sheriff N (1983) Thermal striping in liquid metal cooled fast breeder reactors, 2nd Int'l Topical Mtg. on Nuclear Reactor Thermal Hydraulics, NURETH-2, Santa Barbara, CA, USA, vol. 2, 1292-1301

Brunings J E (1982) LMFBR thermal-striping evaluation, Interim report, Rockwell International Energy Systems Group, Canoga Park, CA, USA , Research Project 1704-11, EPRI-NP-2672

Cheremisinoff N P (1986) ed. In: Encyclopedia of Fluid Mechanics, Dynamics of Single-Fluid Flows and Mixing, vol. 2, Houston, USA: Gulf Publishing Co.

Moriya S; Ushijima S; Tanaka N; Adachi S; Ohshima I (1991) Prediction of Thermal Striping in Reactors. Int'l Conf. Fast Reactors and Related Fuel Cycles, Kyoto, Japan, vol. 1, 10.6.1 - 10.6.10, Oct. 28 - Nov. 1

Muramatsu T (1994) Development of thermohydraulics computer programs for thermal striping phenomena, Specialists meeting on correlation between material properties and thermohydraulics

conditions in LMFRs. IAEA Working Group on Fast Reactors, IWGFR/90, Aix-en-Provence, France, November 22-24

Gebhardt B; Jaluria Y; Mahajan R L; Sammakia B (1988) In: Buoyancy-Induced Flows and Transport, Reference Edition, New York: Hemisphere Publishing Corporation

Takeda Y (1986) Velocity profile measurement by ultrasound Doppler shift method, Int. J. Heat and Fluid Flow. 8:313-318

Takeda Y (1991*a*) Development of an ultrasound velocity profile monitor, Nucl. Eng. Design. 126: 277

Takeda Y ; Kobayashi K (1991*b*) Ultrasonic flow visualization of transient behavior of Taylor vortex flow. In: Experimental and Numerical Flow Visualization, ASME FED-128, 231

Tenchine D; Nam H-Y (1987) Thermal hydraulics of co-axial sodium jets. Am. Inst. Chem. Engrs. Symp. Ser. 83(257):151-156

Tenchine D ; Moro J-P (1995) Comparative analysis of sodium and air mixing jets experiments. 8th IAHR Working Group Mtg. Adv. Nucl. React. Thermohydraulics, Rez, Czech Rep., June 13-15

Ultrasound Velocity Profile monitor (1992) Model X-1, Met-Flow SA, Lausanne, Switzerland

Wood D S (1980) Proposal for design against thermal striping. Nuclear Energy. 19(6): 433-437

Figure 1. Schematic of experimental loop.

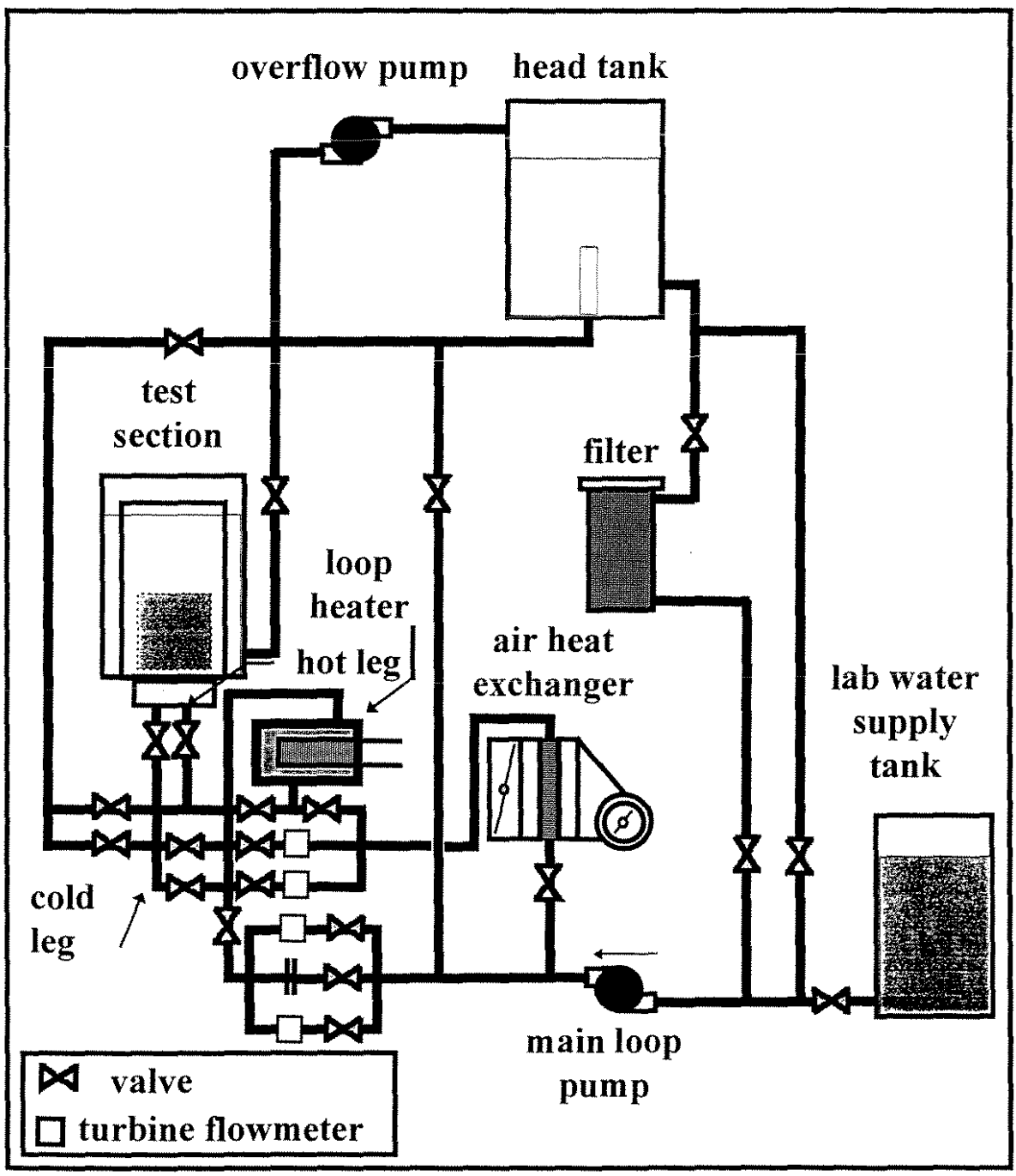

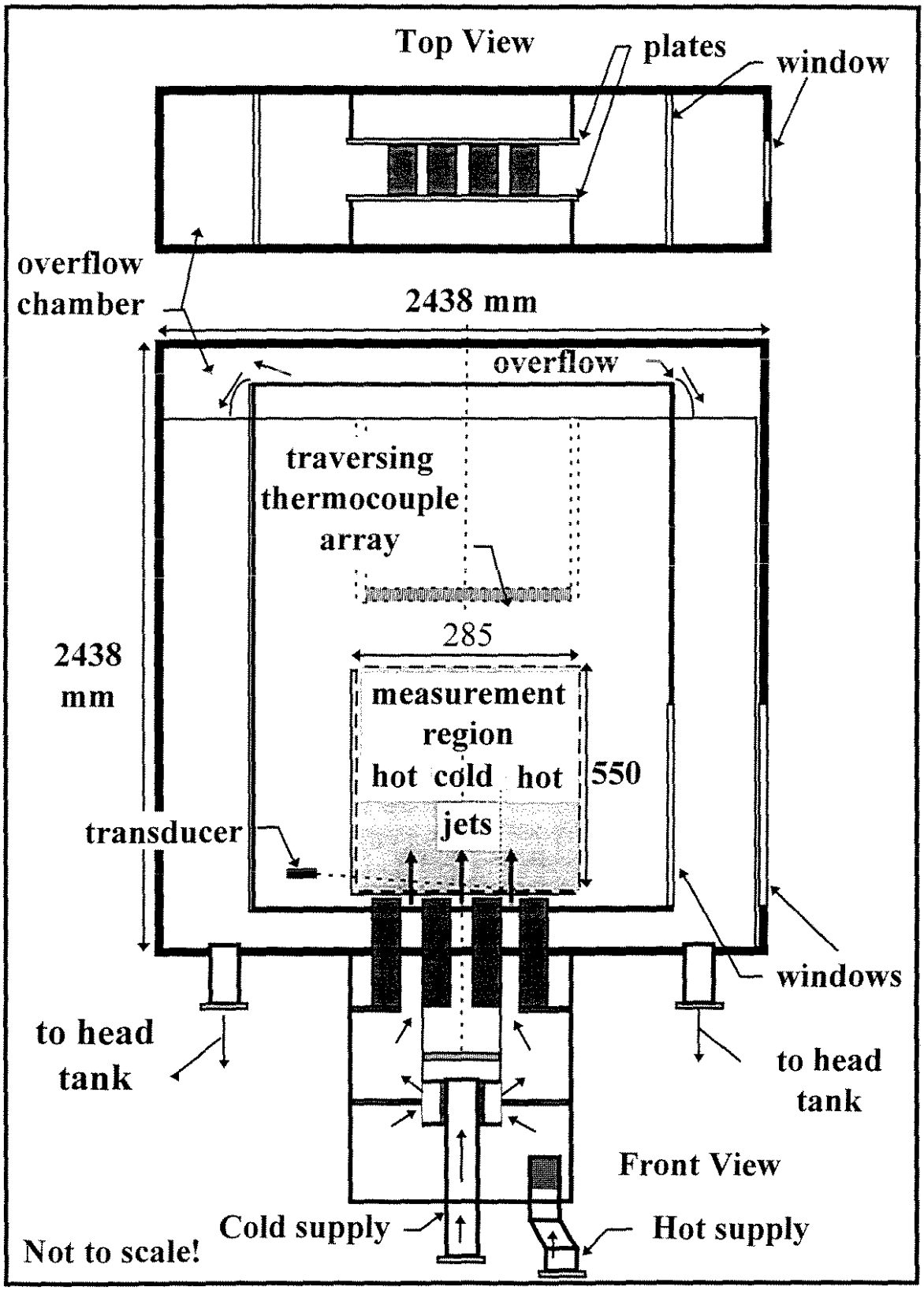

Figure 2. Schematic of test section.

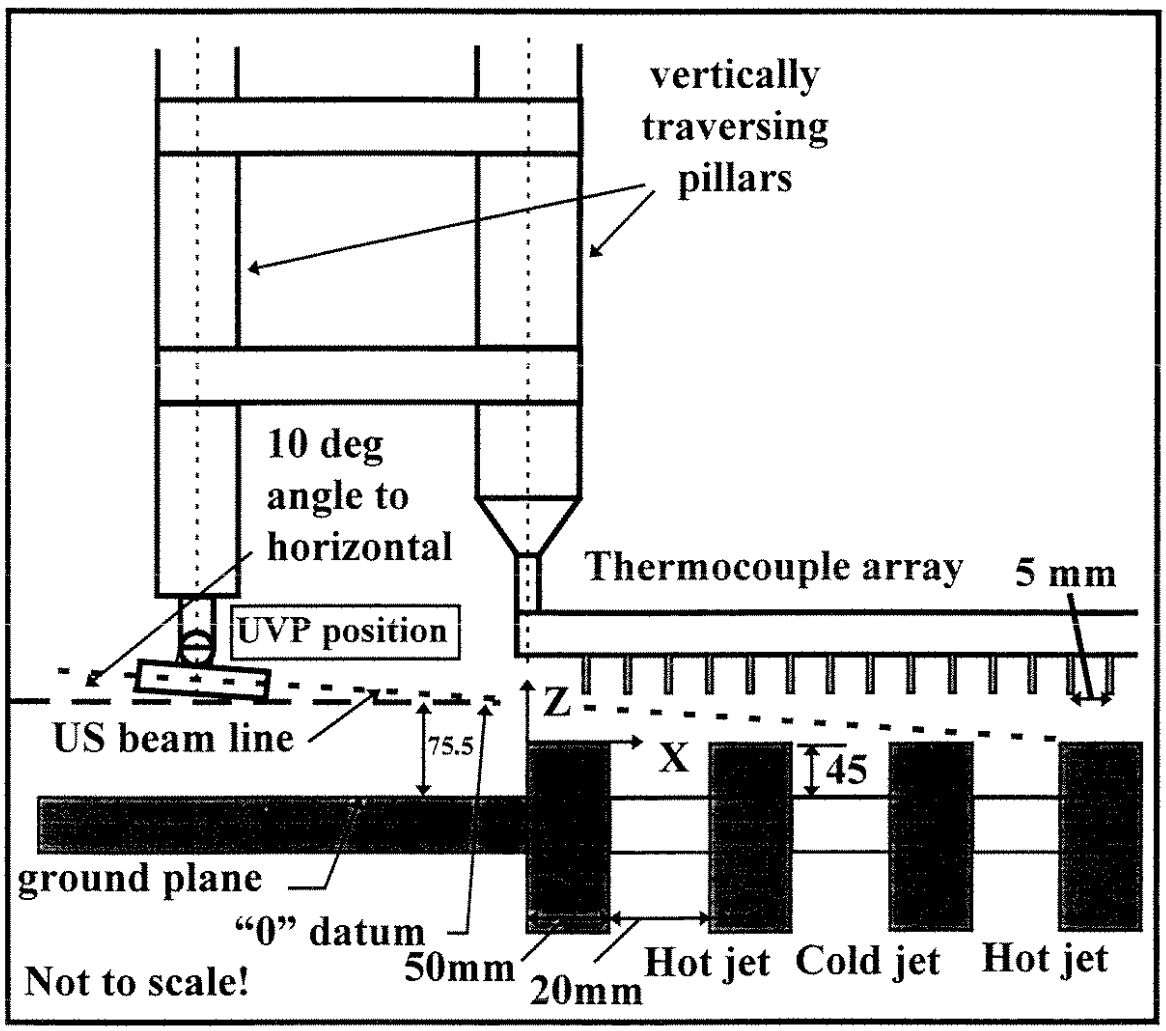

Figure 3. Schematic of instrumentation set-up. Close-up of the UVP transducer orientation and traversing thermocouple array.

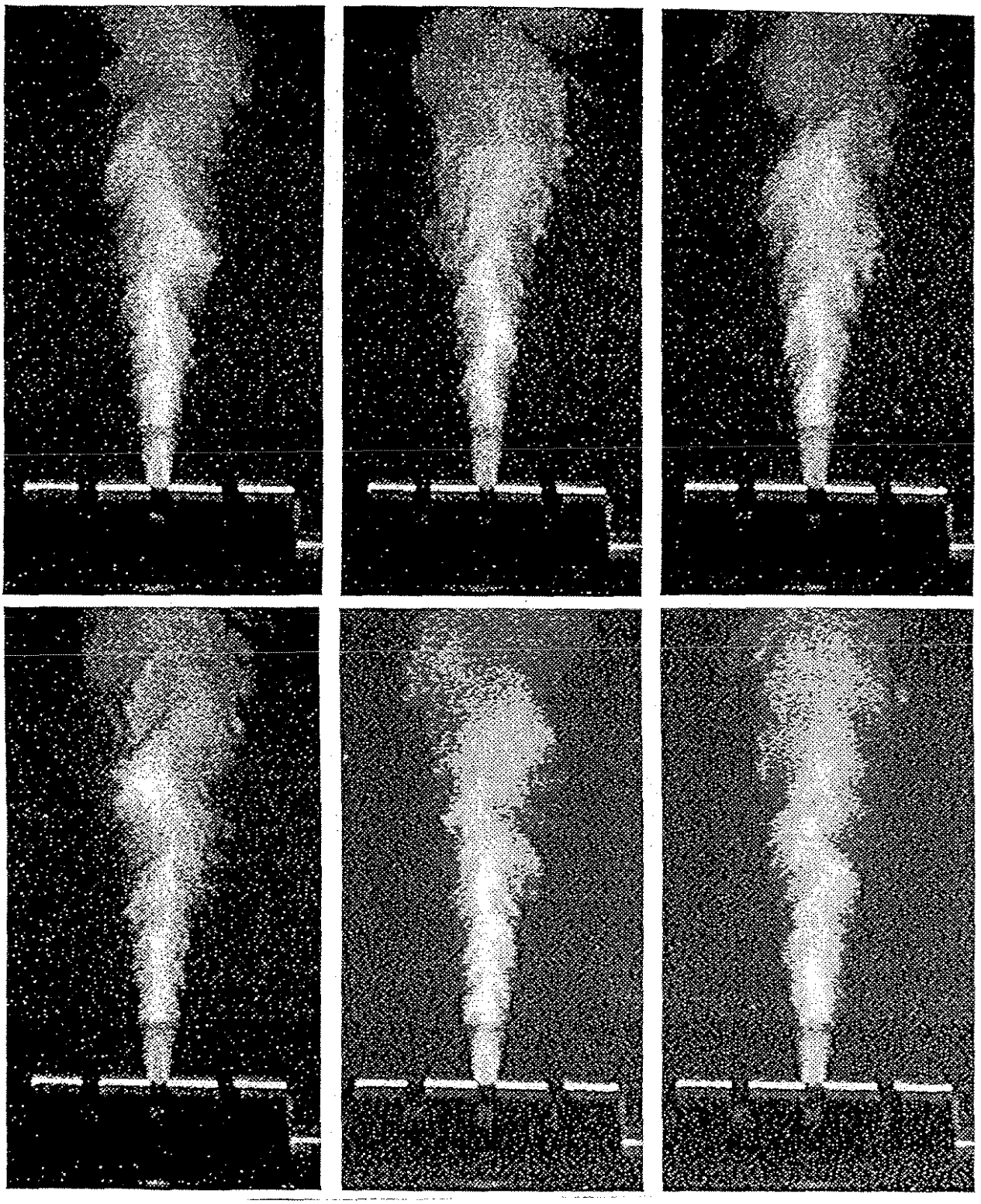

Figure 4. A sequence of 6 snapshot images digitized from video of the single-jet.

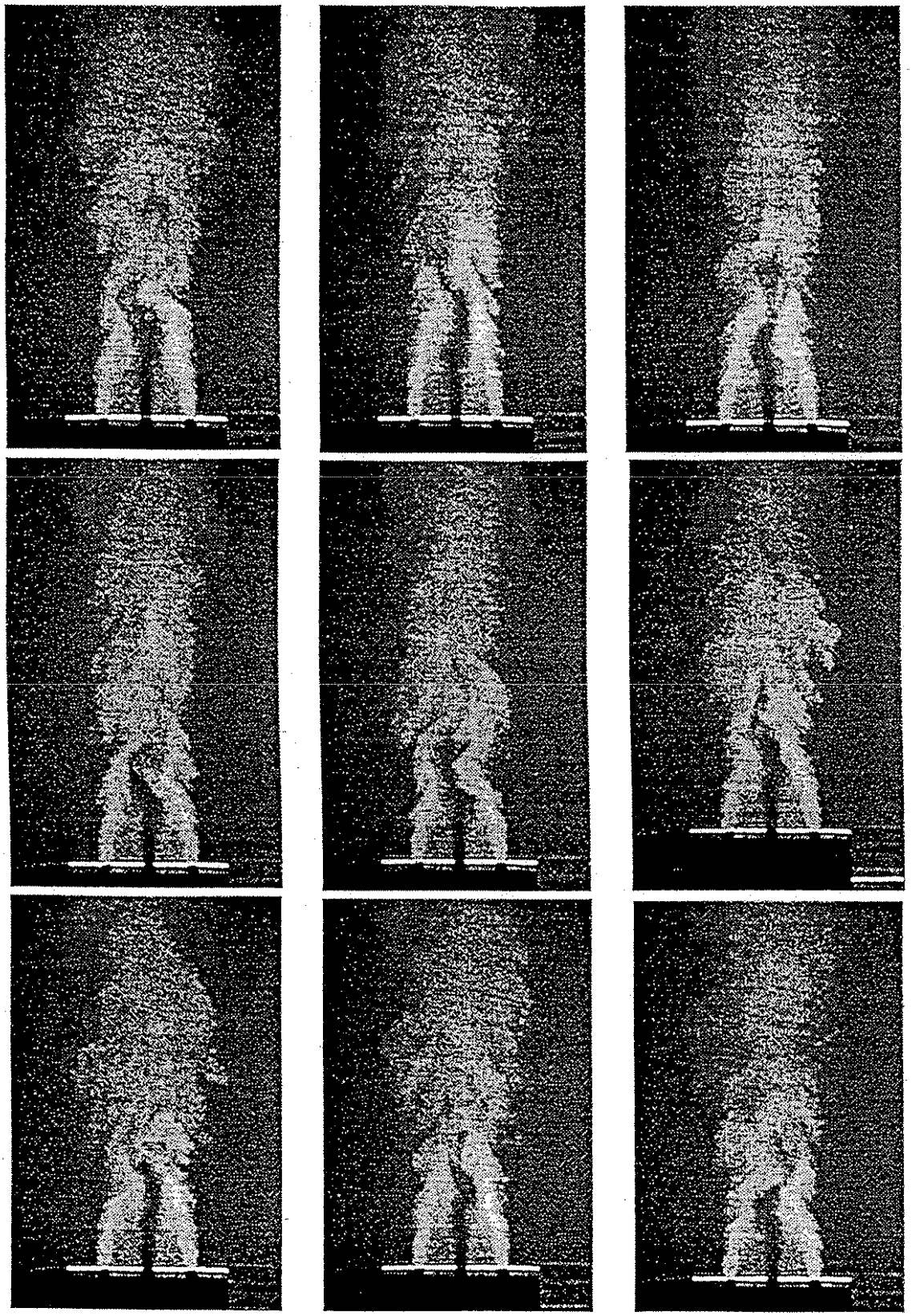

Figure 5. A sequence of 9 snapshot images digitized from video of the triple-jet.

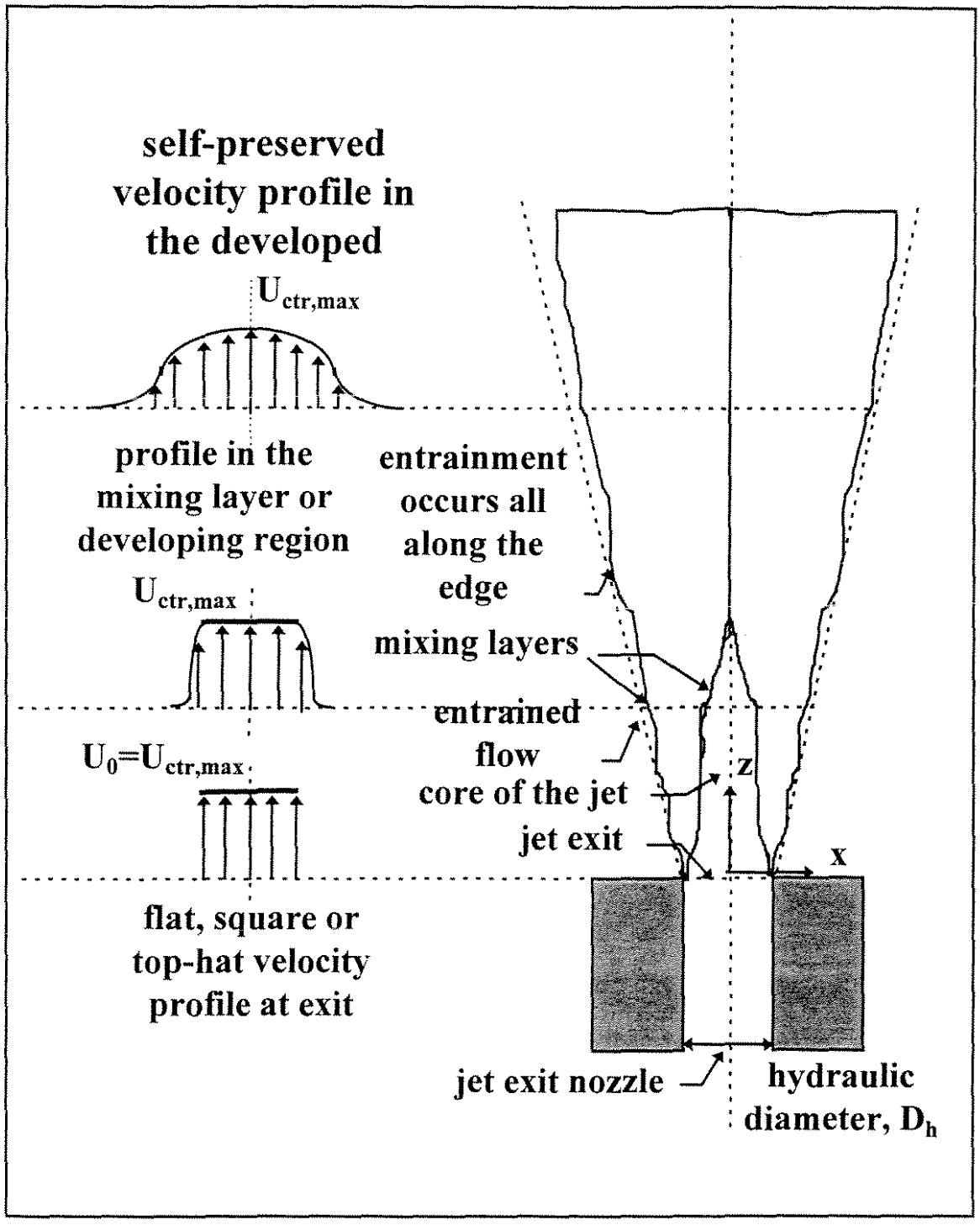

Figure 6. Idealized velocity profiles at 3 axial locations and a qualitative sketch of a plane turbulent jet. *Cf.* Tennekes and Lumley.

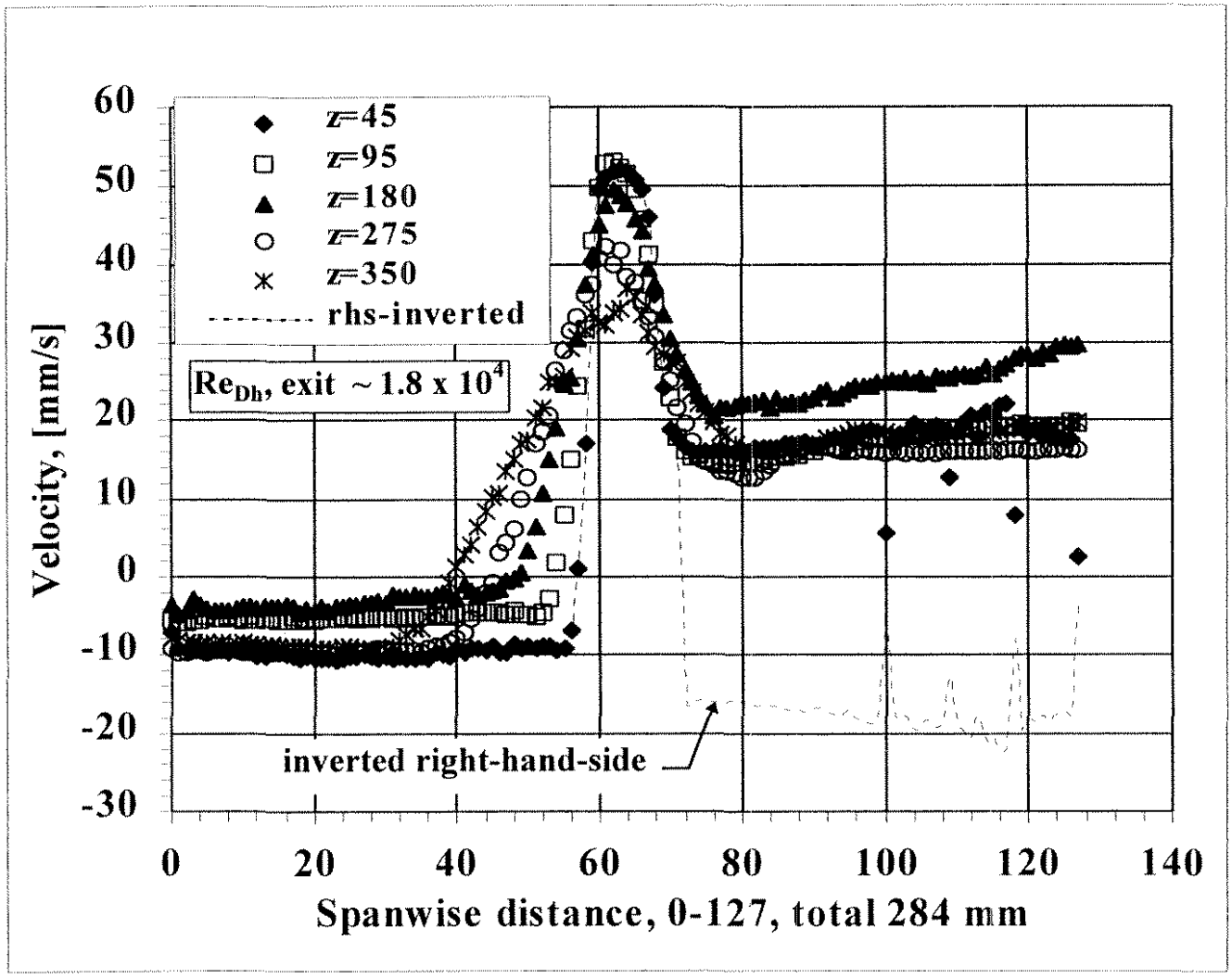

Figure 7a). Average velocity profile of the single-jet at selected axial locations.

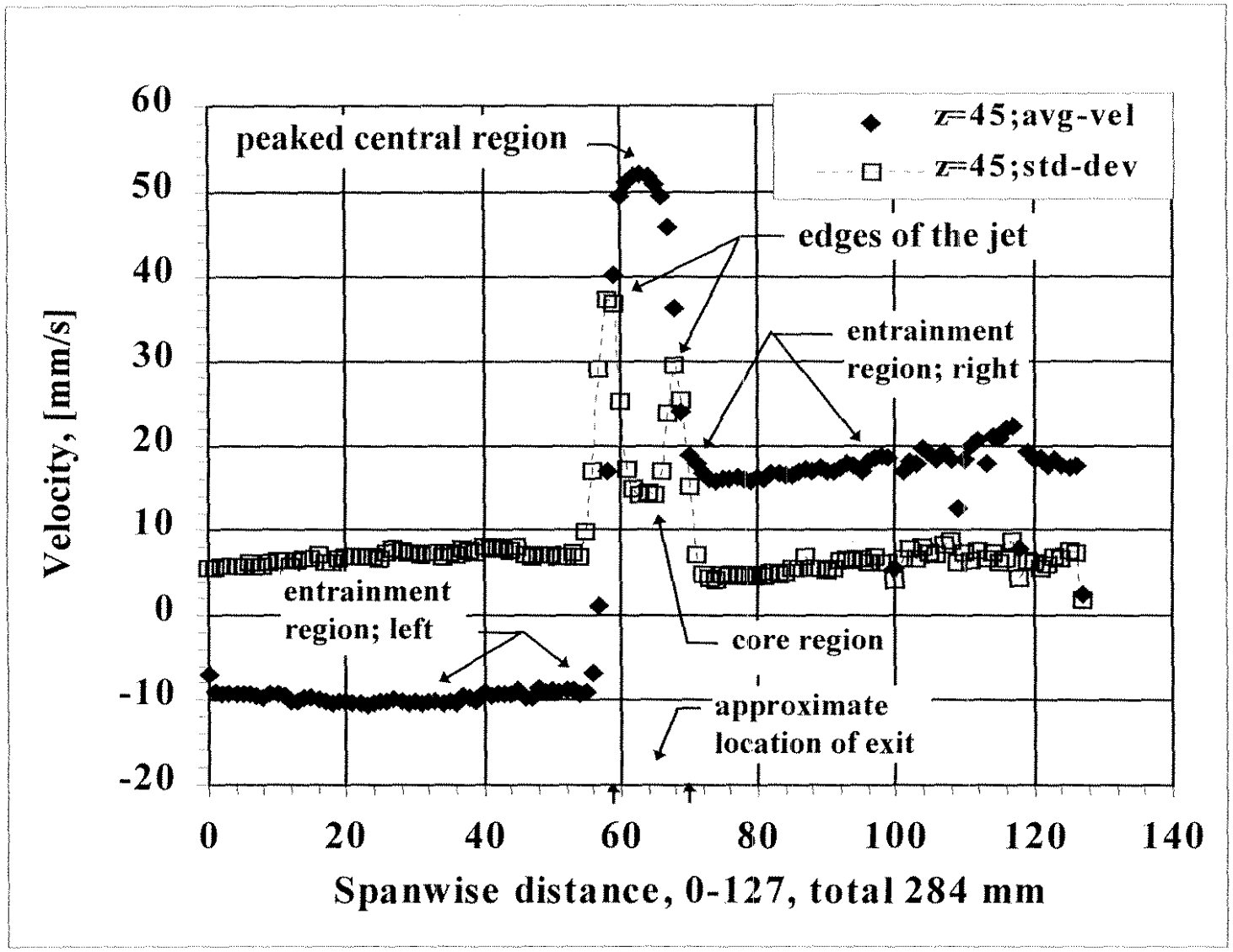

Figure 7b). Average velocity and standard deviation profiles of the single-jet at selected axial distances.

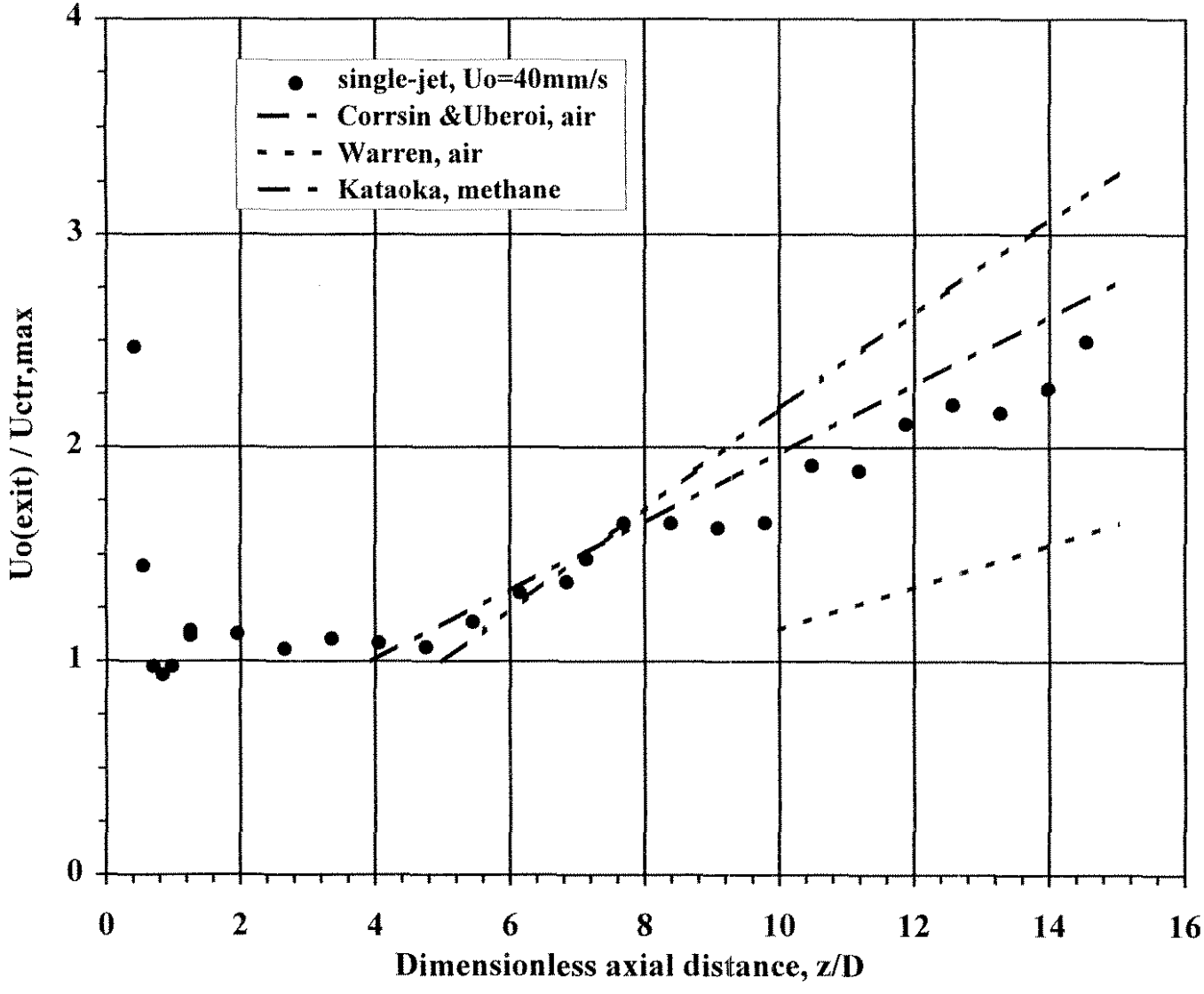

Figure 8. Axial decay of centerline velocity; a comparison of single-and triple-jet data with past data.

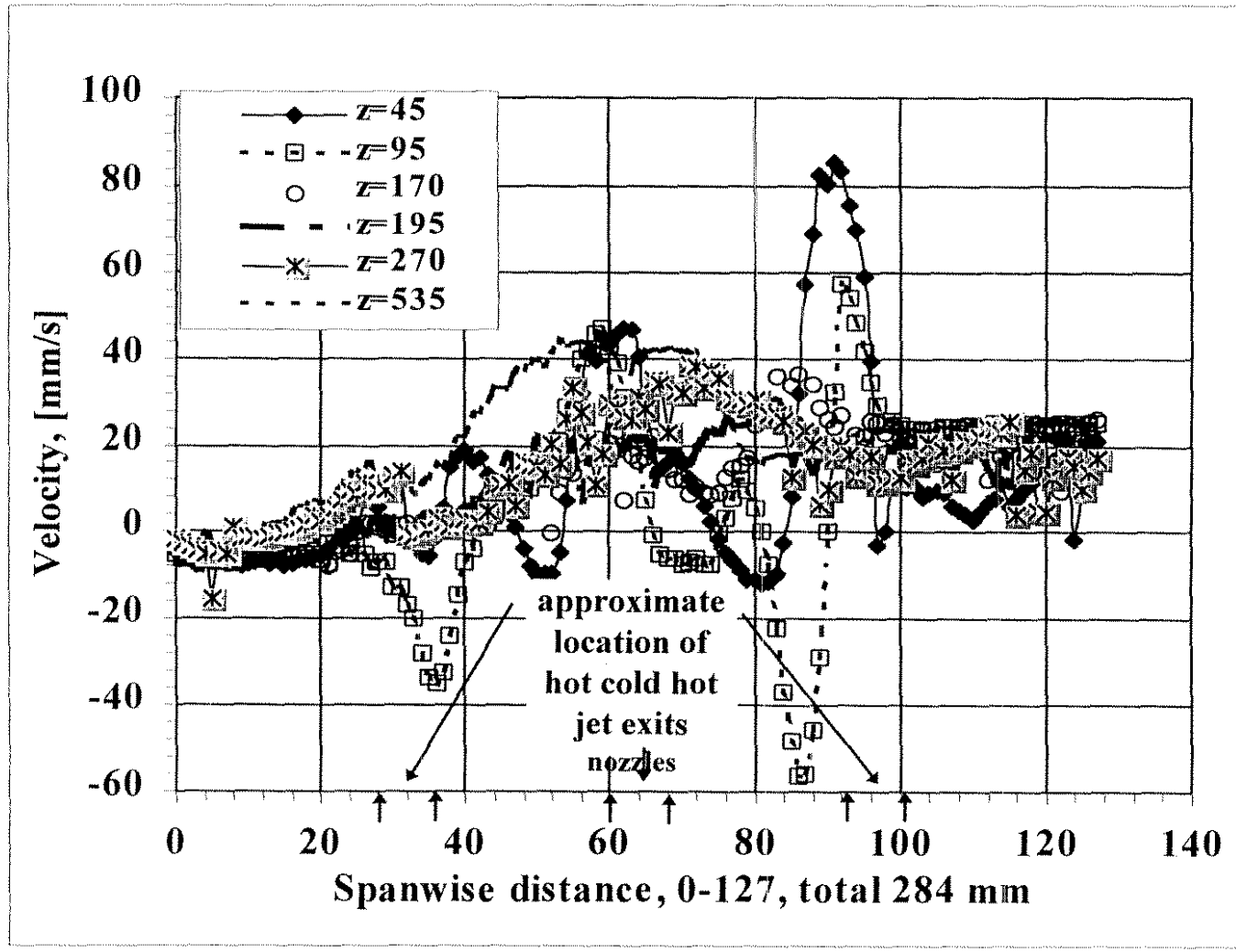

Figure 9a). Average velocity profile of the triple-jet at selected axial locations.

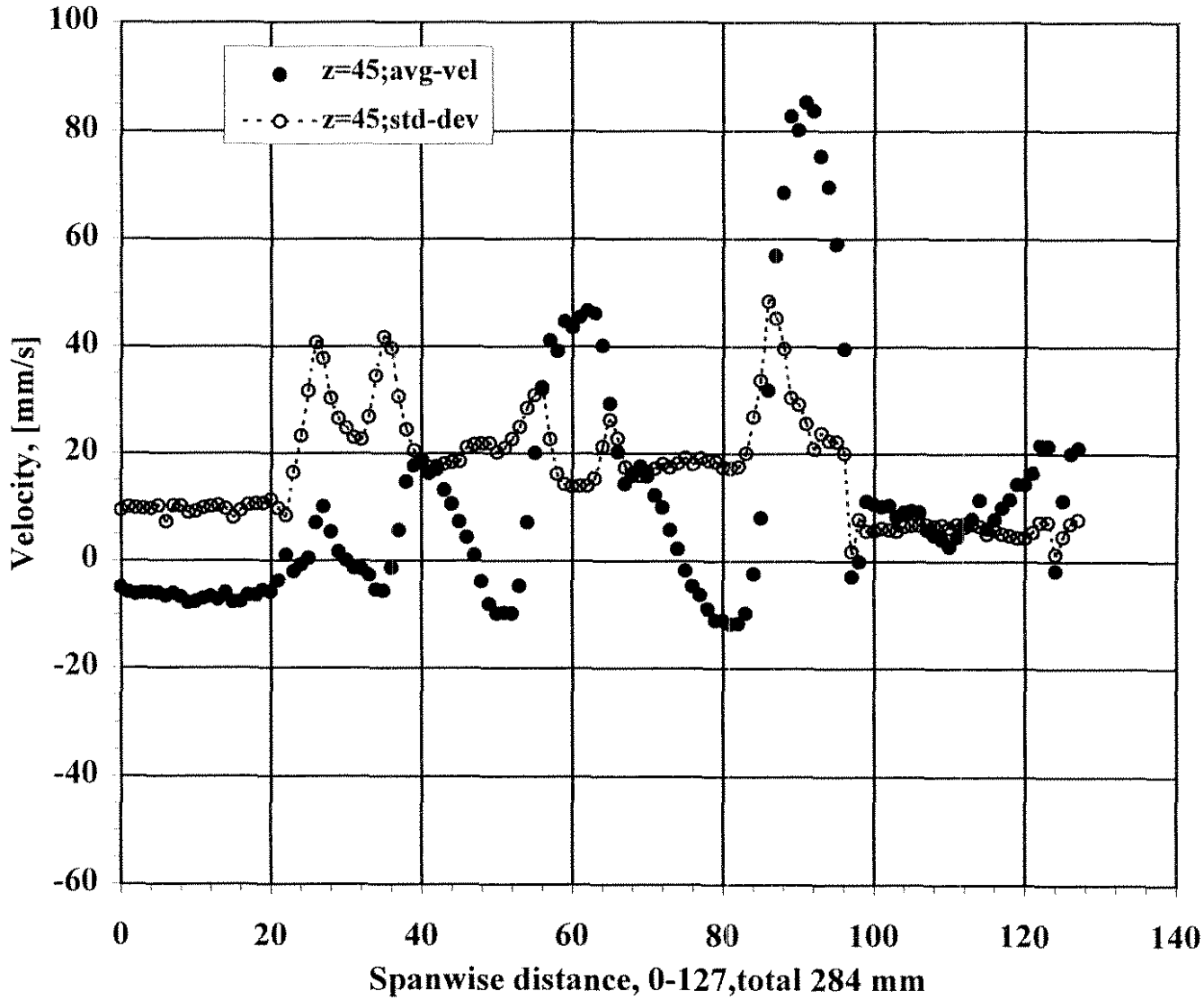

Figure 9b). Average velocity and standard deviation profiles of the triple-jet at selected axial locations.

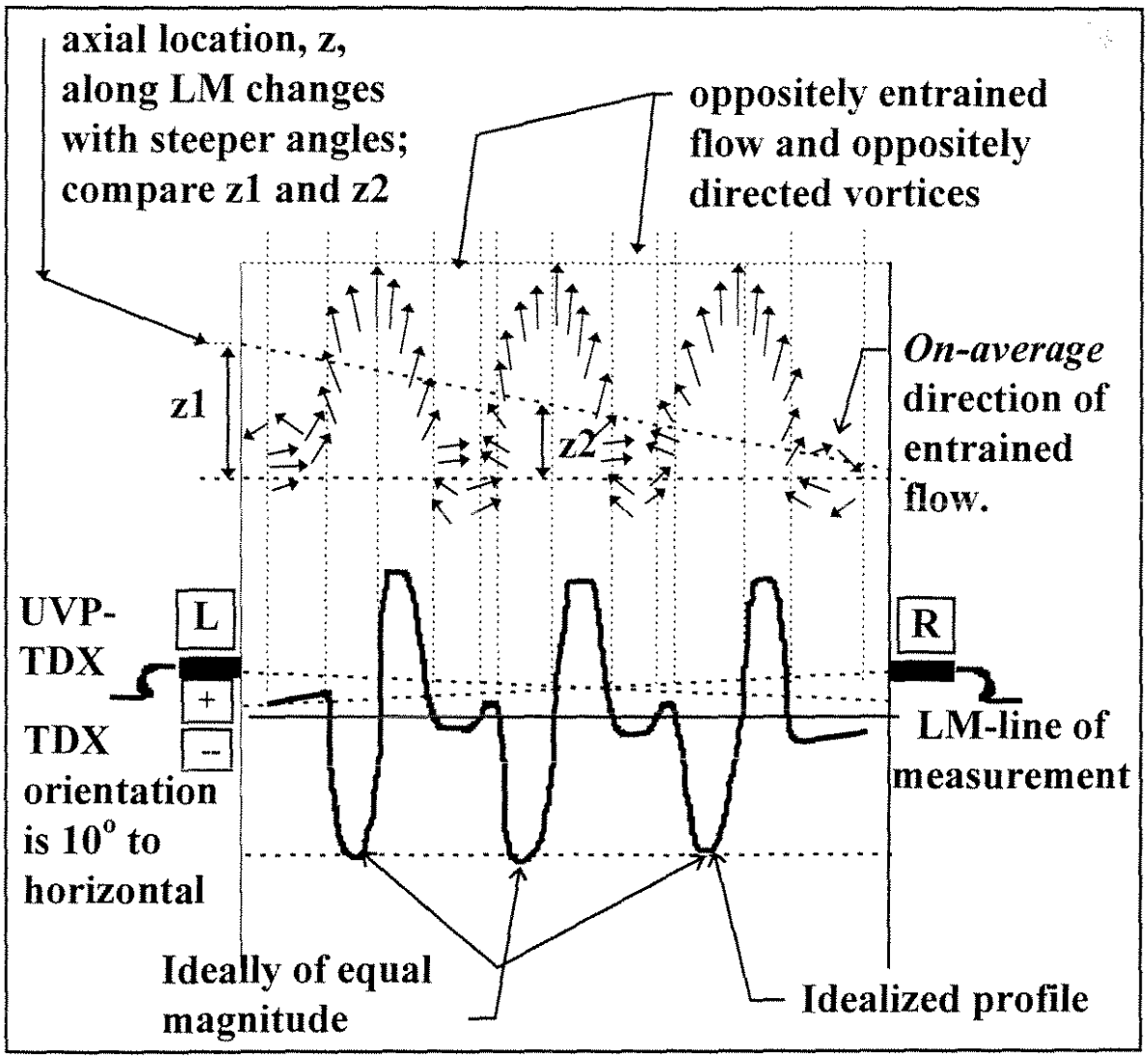

Figure 9c). Qualitative sketch of idealized triple-jet velocity profile and features.

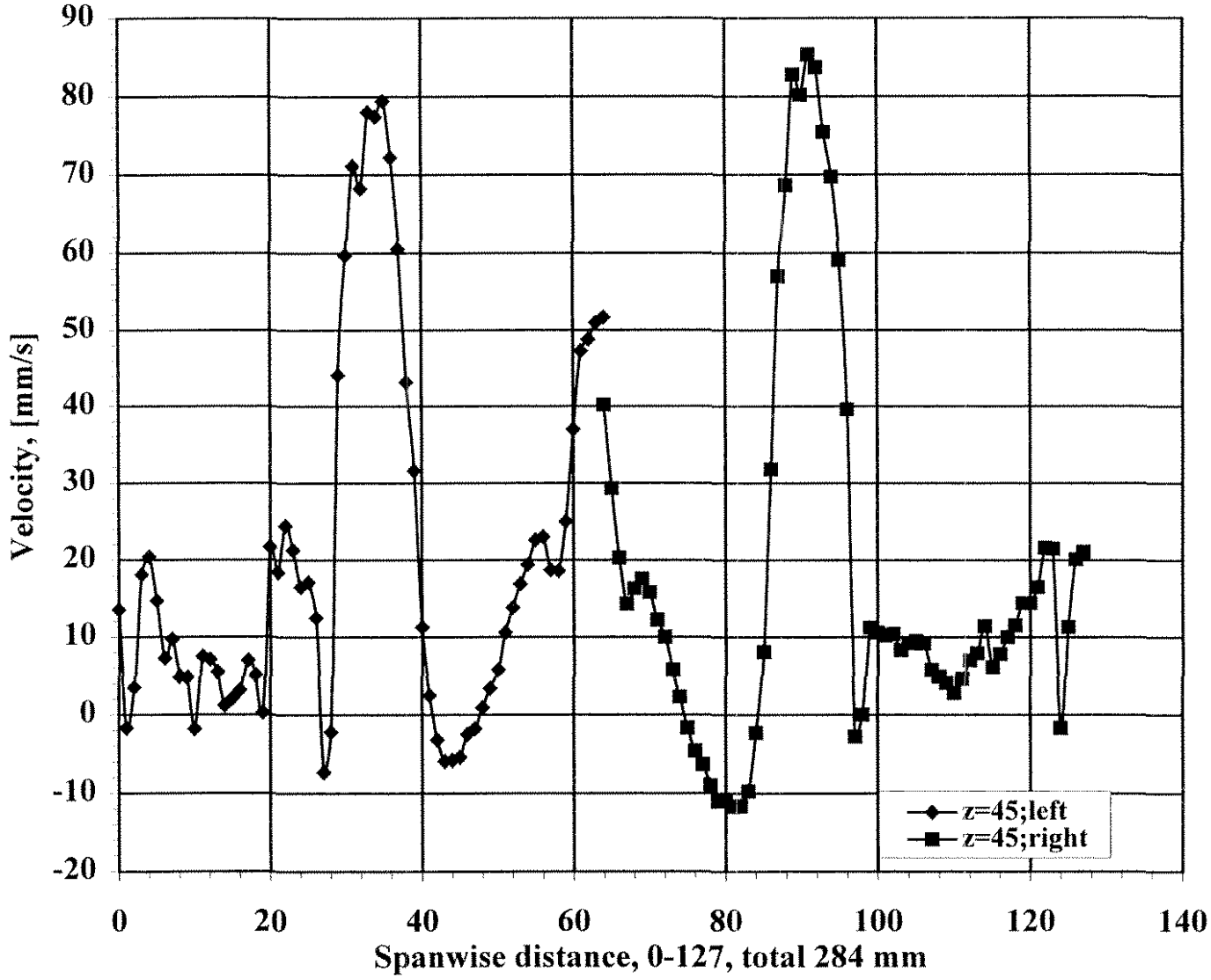

Figure 9d). Composite average velocity profile of triple-jet.

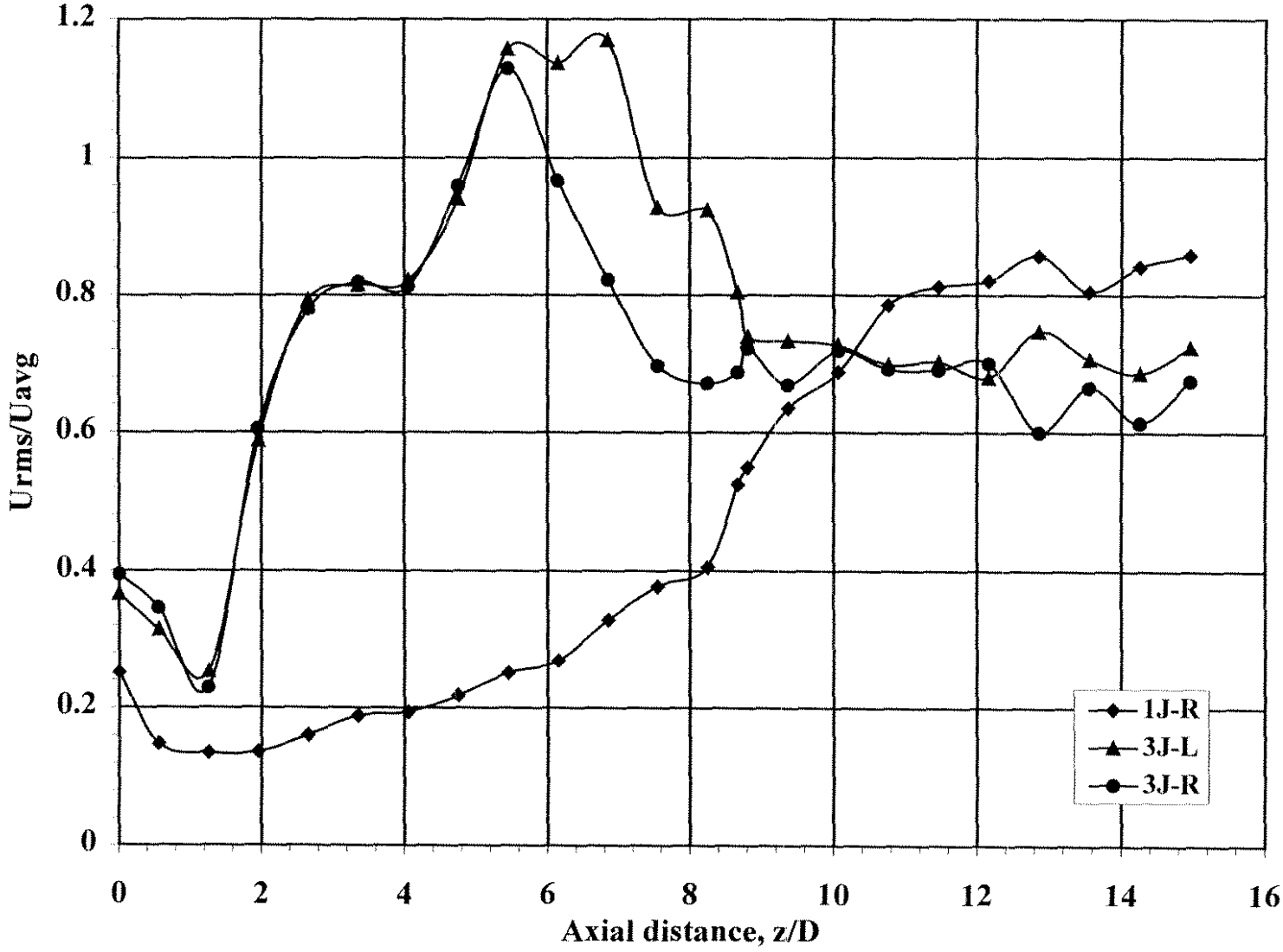

Figure 10. Comparison of the normalized RMS for velocity versus axial distance, z/D, of single- and triple-jets.

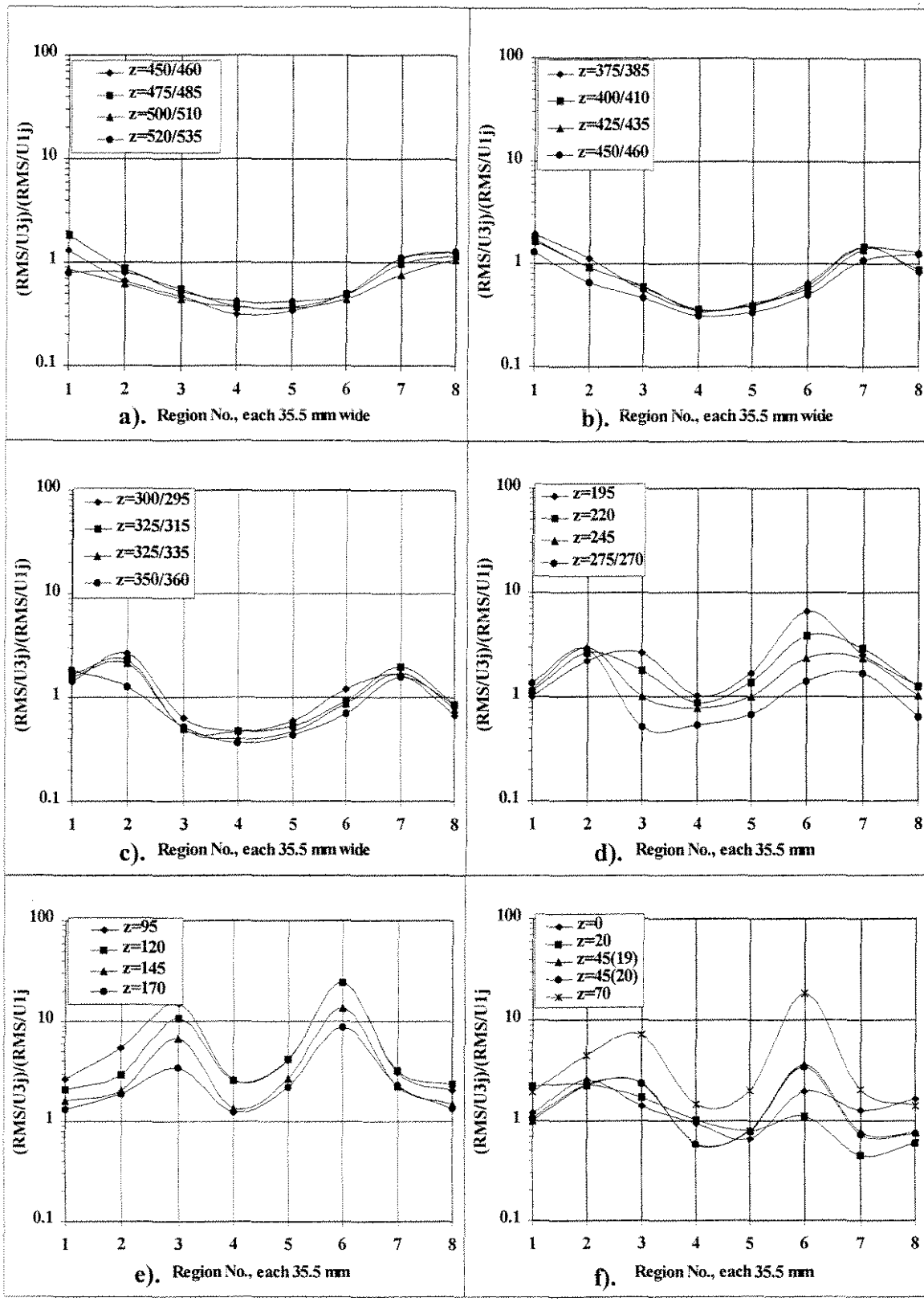

Figure 11a) - f). Spanwise distribution of the ratio of normalized RMS of the triple-jet to the single-jet as averaged regionally (1-8) and with the axial distance as a parameter.

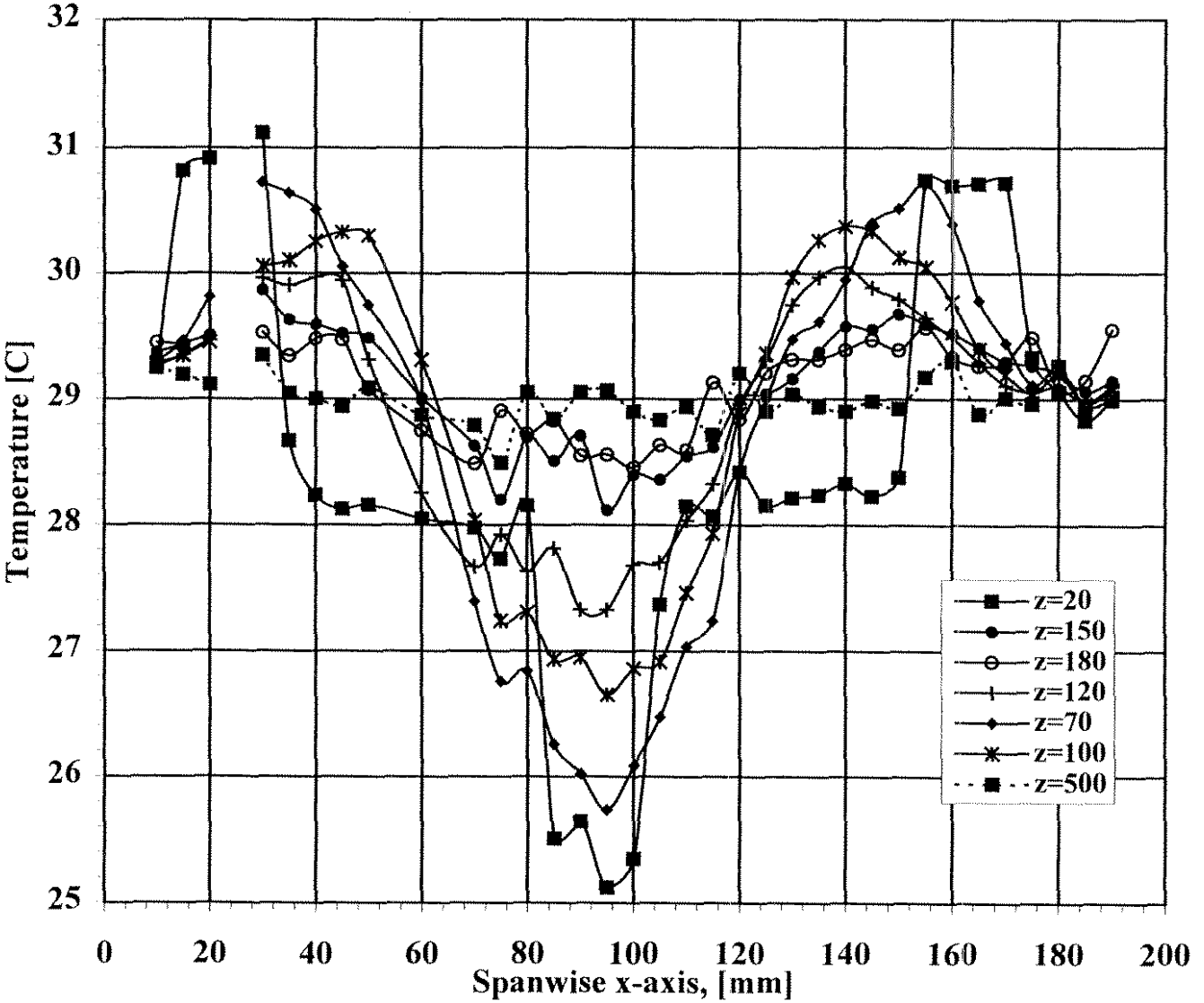

Figure 12. Spanwise temperature distribution of the triple-jet at selected axial locations.

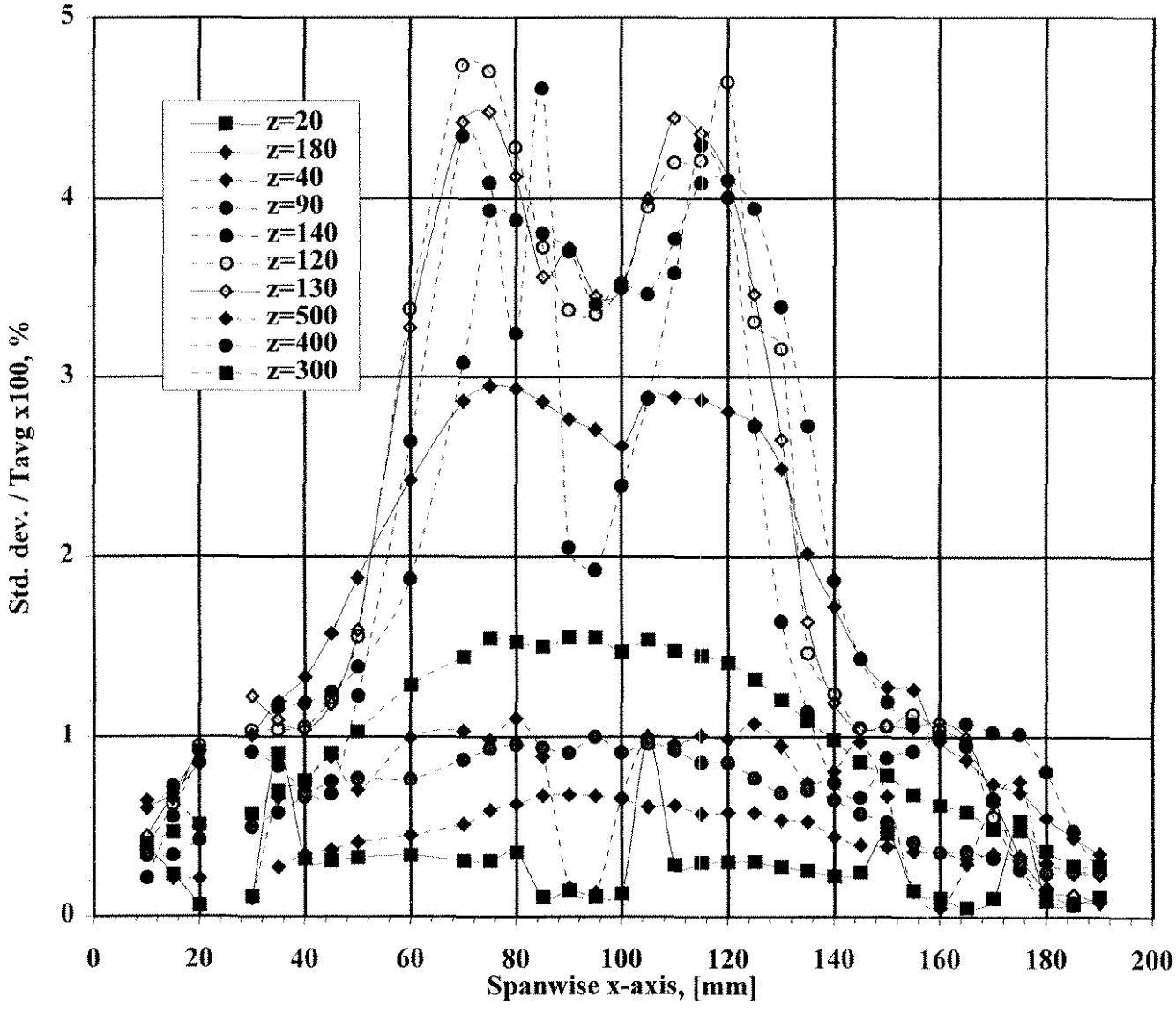

Figure 13. Spanwise standard deviation of temperature of the triple-jet at selected axial locations.

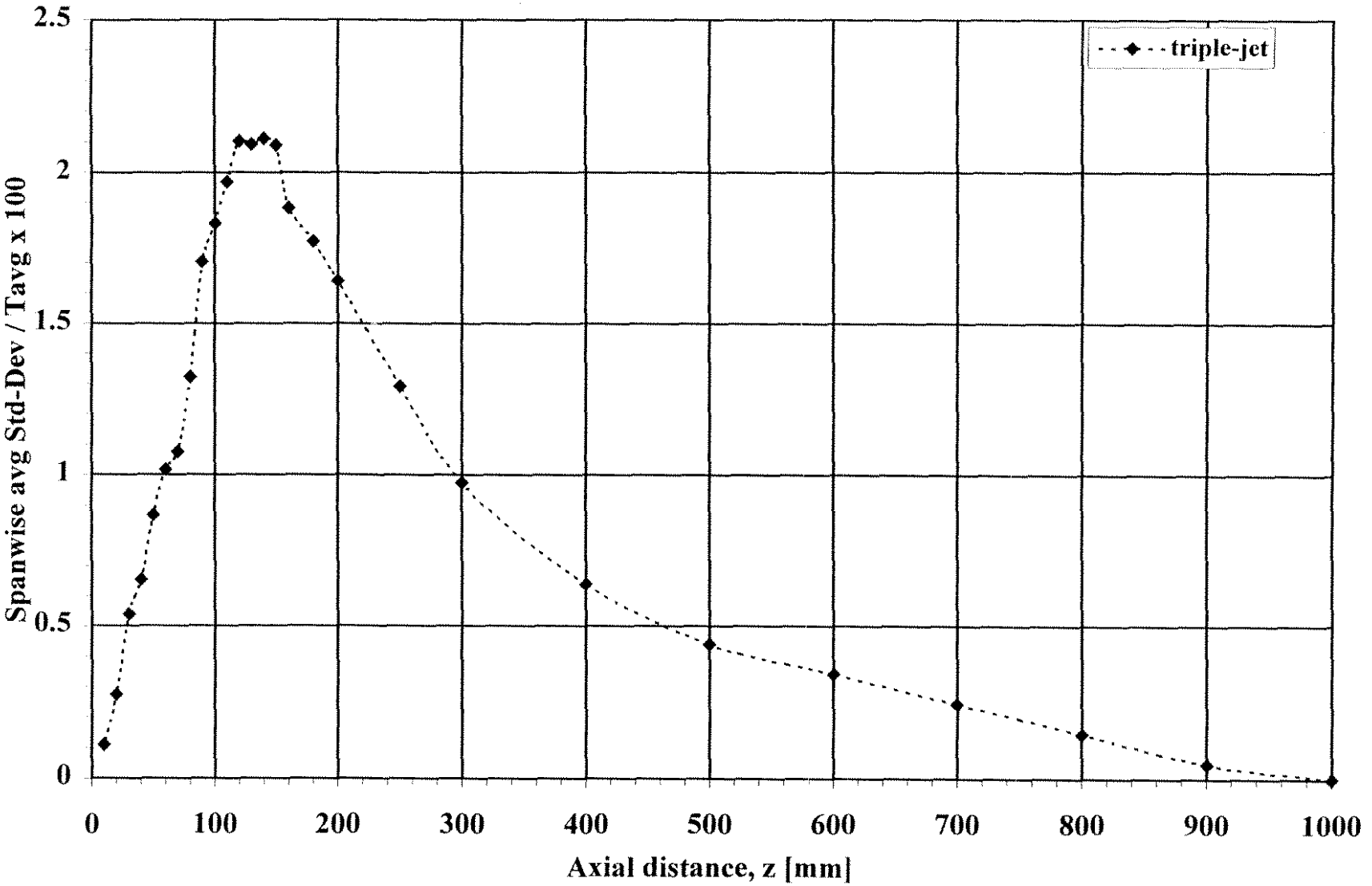

Figure 14. Average standard deviation of temperature as normalized by the average versus axial distance.

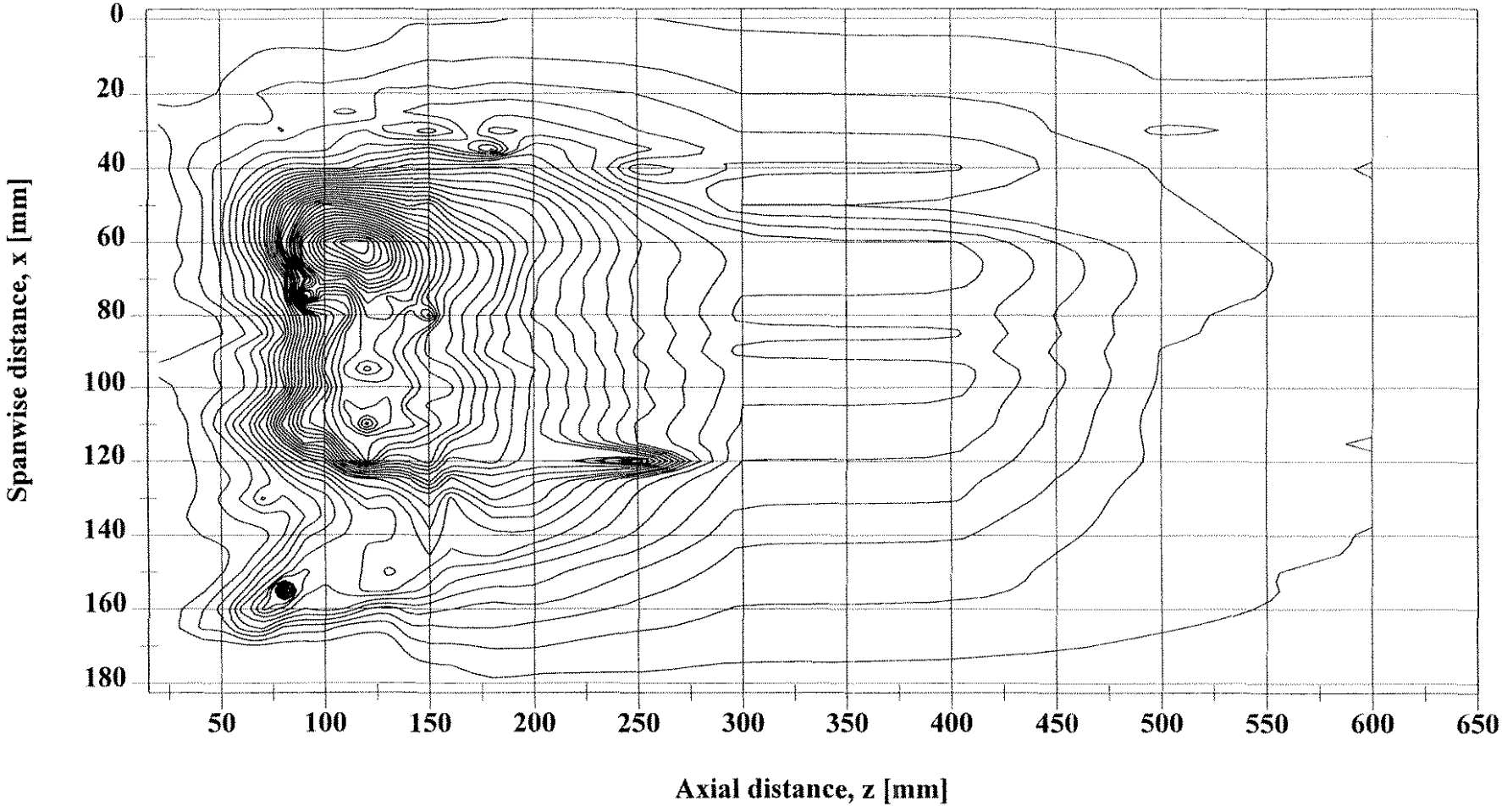

Figure 15. Estimated turbulent heat flux distribution, (scale 0-360).

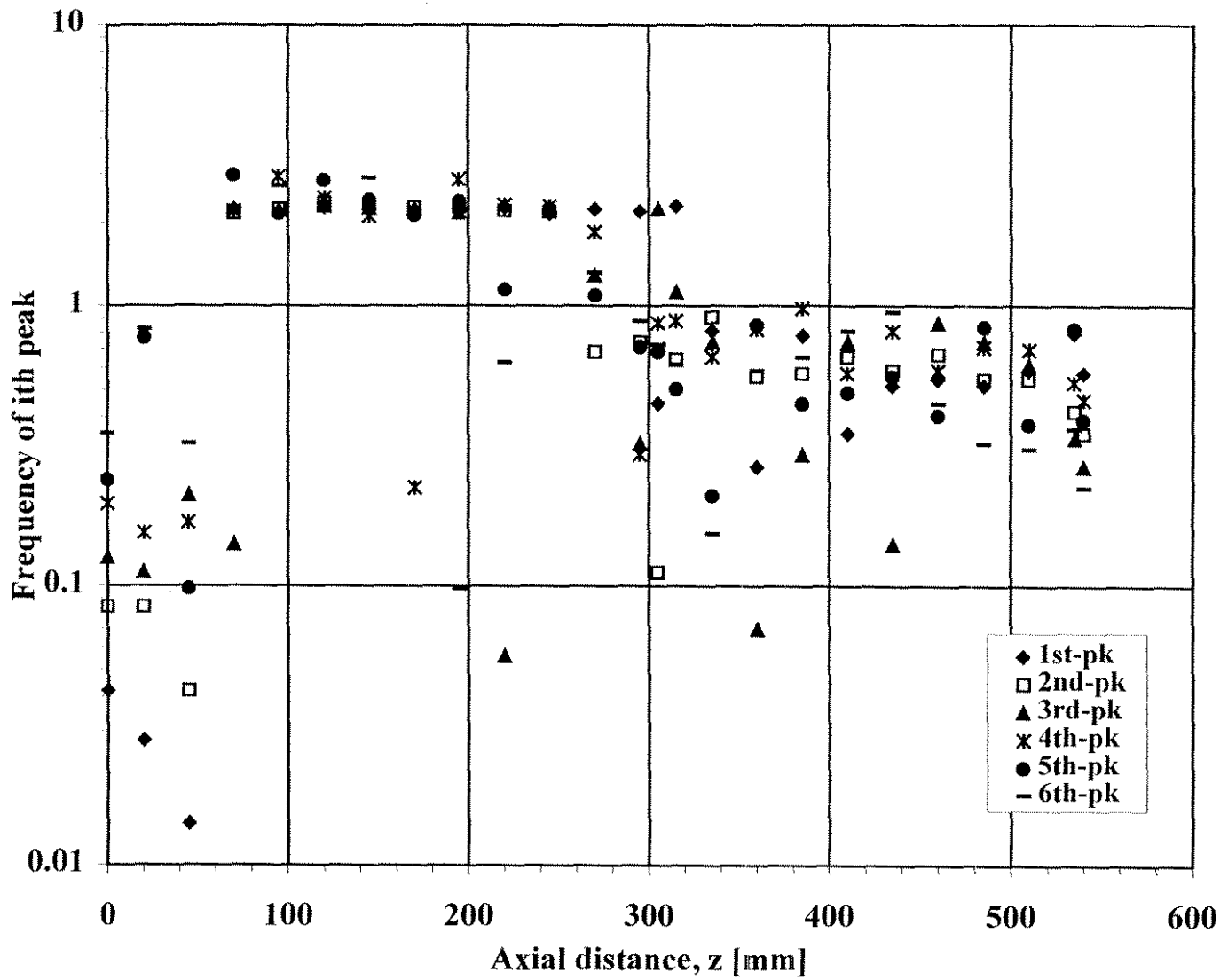

Figure 16. The frequency of the first 6 peaks based on power of the peak versus the axial distance.

Kinematic characteristics of magnetic fluid sloshing in a rectangular container subject to non-uniform magnetic fields

T. Sawada[1], H. Kikura[2] and T. Tanahashi[1]

1) Department of Mechanical Engineering, Keio University

3-14-1 Hiyoshi, Kohoku-ku, Yokohama 223, Japan

2) Paul Scherrer Institut, 5232 Villigen PSI, Switzerland

Running head: Magnetic fluid sloshing in a rectangular container

Correspondence to: T. Sawada

Department of Mechanical Engineering, Keio University

3-14-1 Hiyoshi, Kohoku-ku, Yokohama 223, Japan

E-mail: sawada@mech.keio.ac.jp

FAX: +81-45-563-5943

Abstract

Dynamic behavior of a magnetic fluid in a laterally vibrated rectangular container subject to a non-uniform vertical magnetic field has been investigated. Flow behavior was observed using the ultrasound velocity profile measuring technique. The effect of the magnetic field on the resonant frequency of the fluid-container system is discussed. Experimental results are compared with the results obtained from nonlinear theory using the perturbation method.

1. Introduction

A magnetic fluid is a stable suspension of solid magnetic particles whose diameter is 5~15nm and they are coated with a layer of surfactant which inhibits their coalescence, that is, the magnetic fluid is a stable colloidal dispersion of rather small surfactant-coated magnetic particles in a liquid carrier. When a magnetic field is applied to a magnetic fluid, magnetic particles in the fluid tend to remain rigidly aligned with the direction of the magnetic field, and several interesting characteristics have been observed (e.g. Rosensweig 1985).

Zelazo and Melcher (1969) investigated the dynamic behavior of a magnetic fluid in an oscillated container. They examined the influence of a tangential magnetic field on the resonance of surface waves, using a rectangular container partly filled with a magnetic fluid and driven by a low-frequency transducer. Also, a simulation of liquid sloshing in low-gravity were demonstrated by Dodge and Garza (1970) using a magnetic fluid. More recently, interfacial instability of a magnetic fluid in an applied magnetic field has attracted attention. Sudo et al. (1987) carried out an experimental study on the interfacial instability of magnetic fluids in a rectangular container in the presence of a magnetic field tangential to the interface and estimated the concrete configurations of

the interface in various conditions. Okubo et al. (1990) investigated the stability of the surface of a magnetic fluid layer under the influence of a vertical alternating magnetic field. Kikura et al. (1991) examined lateral sloshing of a magnetic fluid in rectangular, cylindrical and spherical containers. From these studies several characteristic properties of magnetic fluid sloshing have been clarified, for example, the effects of magnetic field on the resonant frequency and change of pressure.

Further studies have investigated the sloshing of two fluid layers (e.g. Handa and Tajima 1979). Li (1970) analyzed the stability of two liquid layers with a free surface set in motion by an oscillatory lower boundary, using two superposed fluids with different viscosities and densities. He pointed out that there are two modes of wave motion. Hashimoto and Sudo (1985) presented a linearized three-dimensional theory of the waves occurring on the free surface and liquid-liquid interface taking account of surface tension. They carried out some experiments and investigated the dynamic behavior of stratified fluids with a free surface in a rectangular container subject to vertical vibration. Sawada et al. (1993) and Matsuura et al. (1995) investigated two-layer liquid sloshing of a magnetic fluid and a silicon oil in a rectangular container, and clarified the effects of magnetic field on the resonant frequency.

The sloshing problem is not easy from a mathematical point of view. Obvious nonlinearities occur, especially in the vicinity of the resonant frequency. In order to understand and explain this complex problem, a nonlinear approach and detailed measurement of internal velocity profiles are necessary. However, optical methods like laser Doppler anemometry or the flow visualization technique have not been applicable because a magnetic fluid is opaque. Ultrasound velocity profile (UVP) measurement is a method for measuring a velocity profile on a line with respect to the velocity component along this same line. This method can be applied to an opaque fluid such as a liquid metal. Takeda

(1986) has developed UVP measuring method systematically and studied its application to the flow of mercury (Takeda 1987). The velocity profiles in a T branch were measured for several different combinations of measuring lines and flow directions, and the lengths of the flow fields were obtained. The results showed good agreement with the calculated lengths of the flow fields, implying that the velocity profile in mercury flow could be successfully measured.

The present paper examines the applicability of UVP measurement to magnetic fluid sloshing which has periodic velocity field. We attempt to obtain nonlinear sloshing responses up to the third order perturbation. The experimental and theoretical results are compared.

2. Experiments

Figure 1 shows a schematic diagram of the experimental apparatus. The rectangular container measures 80 mm×20 mm×150 mm (see Fig.2), and is made of transparent acrylic resin. An adjustable crank is mounted on the output shaft of the motor. The rotational frequency of the motor is continuously controlled by an inverter. The shaking table is oscillated sinusoidally and has a range of oscillation from 1.17 Hz to 4.33 Hz. The amplitude of the oscillation is X_0=1.5 mm for all experiments. A magnetic field is applied by a cylindrical permanent magnet whose diameter is 110 mm. The distribution of the magnetic field induction B along the normal central line of the permanent magnet is shown in Fig.3. Here h is the fluid depth, B_0 is the surface magnetic field induction at the center of the permanent magnet(z=$-h$), and h_m is the distance from the permanent magnet. The equation for B is obtained by measured results and is then used for theoretical analysis.

The magnetic fluid is a water-based 24% weight concentration of fine magnetite par-

ticles Fe_3O_4. Its kinematic viscosity, density and sound velocity are ν=4.2×10^{-6} m^2/s, ρ=1.24×10^3 kg/m^3 and c=1410 m/s at 25°C, respectively. The fluid depth is h=40 mm. Since the magnetic particles in the magnetic fluid are too small to be reflecting particles for the ultrasonic wave, we also add porous SiO_2 powder with a mean diameter of 0.9 μm (MSF-10M, Liquidgas Co., Ltd.). An ultrasonic transducer is fixed on the side wall of the container in order to measure the horizontal velocity profile V_x. The ultrasonic transducer has a nominal diameter of 5 mm and the measuring volume is a thin-disc shape, ϕ5 mm×0.71 mm. The UVP monitor is an X-1 PS manufactured by Met-Flow AG. The basic frequency is 4MHz and the pulse repetition frequency is 3906Hz.

Experiments are carried out at various motor frequencies and magnetic field intensities. The dynamic behavior of the free surface are recorded on video tape.

3. Nonlinear wave theory

Frequency responses of the free surface of a magnetic fluid have been investigated using linearized wave theory by Matsuura et al. (1995). However, the flow behavior of sloshing is essentially nonlinear. In particular, forced oscillation clearly shows nonlinear characteristics in its resonance curves. Thus, a nonlinear approach is necessary to investigate velocity fields and high frequency responses of the free surface. Here we deal with an analytical solution to sloshing subject to non-uniform magnetic field using a perturbation method (see Hayama et al. 1983). An analytical model uses the Cartesian coordinates x and z as shown in Fig.4, x is horizontal while z is vertical upward measured from the mean position of the free surface. L is the length of the container and η is the free surface elevation. X_0 and ω are the amplitude and forced angular frequency of the oscillation of the shaking table, respectively

With the assumptions of irrotational flow and an incompressible fluid, a velocity po-

tential ϕ exists which should satisfy the continuity equation:

$$\frac{\partial^2\phi}{\partial x^2}+\frac{\partial^2\phi}{\partial z^2}=0 \tag{1}$$

The unsteady Bernoulli equation is given by

$$\frac{\partial\phi}{\partial t}+\frac{1}{2}\left\{\left(\frac{\partial\phi}{\partial x}\right)^2+\left(\frac{\partial\phi}{\partial z}\right)^2\right\}+\frac{p}{\rho}+gz-\mu_0\int_0^H MdH=X_0\omega^2x\sin\omega t \tag{2}$$

where p, g, μ_0, M and H are pressure, gravitational acceleration, magnetic permeability of vacuum, magnetization and magnetic field, respectively. When the magnetization and magnetic field are assumed to be parallel, the fifth term of the left hand side of Eq.(2) is written

$$\mu_0\int_0^H M\,dH=\frac{1}{2}\mu_0\chi_m H^2 \tag{3}$$

where χ_m is susceptibility of a magnetic fluid. The magnetic field $H(z)$ is approximated by

$$H(z)=H_0e^{-\alpha(z+h)} \tag{4}$$

where H_0 is the magnetic field intensity at the bottom of the container ($z=-h$) and α is a constant which is determined by measurement of the magnetic field as shown in Fig.3. The boundary conditions on the bottom and side walls, and the kinematic and dynamic free surface conditions (e.g. Dean and Dalrymple 1984) are given by following equations:

$$\left(\frac{\partial\phi}{\partial x}\right)_{x=\pm L/2}=0 \tag{5}$$

$$\left(\frac{\partial\phi}{\partial z}\right)_{z=-h}=0 \tag{6}$$

$$\left(\frac{\partial\eta}{\partial t}+\frac{\partial\phi}{\partial x}\frac{\partial\eta}{\partial x}\right)_{z=\eta}=\left(\frac{\partial\phi}{\partial z}\right)_{z=\eta} \tag{7}$$

$$\left[\frac{\partial^2\phi}{\partial t^2}+2\left(\frac{\partial\phi}{\partial x}\frac{\partial^2\phi}{\partial x\partial t}+\frac{\partial\phi}{\partial z}\frac{\partial^2\phi}{\partial z\partial t}\right)+\left\{\left(\frac{\partial\phi}{\partial x}\right)^2\frac{\partial^2\phi}{\partial x^2}+\left(\frac{\partial\phi}{\partial z}\right)^2\frac{\partial^2\phi}{\partial z^2}\right\}\right.$$

$$+2\frac{\partial\phi}{\partial x}\frac{\partial\phi}{\partial z}\frac{\partial^2\phi}{\partial x\partial z}+g_m\frac{\partial\phi}{\partial z}-X_0\omega^3 x\cos\omega t-X_0\omega^2\frac{\partial\phi}{\partial x}\sin\omega t\Bigg]_{z=\eta}=0 \tag{8}$$

where g_m is an effective gravity due to the magnetic force and is given by

$$g_m=g+\frac{\alpha\mu_0\chi_m H_0^2 e^{-2\alpha h}}{\rho} \tag{9}$$

Since Eqs.(7) and (8) for the free surface conditions are nonlinear, they are linearized by developing ϕ, η and p into power series of small parameter $\varepsilon=(X_0/L)^{1/3}$ up to the third order perturbation. These expressions are written in the following dimensionless form:

$$\phi^*=\frac{\phi}{L^2\omega_1}=\varepsilon\phi_1+\varepsilon^2\phi_2+\varepsilon^3\phi_3+O(\varepsilon^4) \tag{10}$$

$$\eta^*=\frac{\eta}{L}=\varepsilon\eta_1+\varepsilon^2\eta_2+\varepsilon^3\eta_3+O(\varepsilon^4) \tag{11}$$

$$p^*=\frac{p}{\rho gL}=-z^*+\varepsilon p_1+\varepsilon^2 p_2+\varepsilon^3 p_3+O(\varepsilon^4) \tag{12}$$

where ω_1 is the first resonant angular frequency obtained by linearized theory and where the function O represents other perturbation orders. The first resonant angular frequency ω_1 is given by the n-th resonant angular frequency equation:

$$\omega_n=\sqrt{\frac{n\pi g_m}{L}\tanh\frac{n\pi h}{L}} \tag{13}$$

Space and time variables are also defined in dimensionless form:

$$x^*=\frac{x}{L},\qquad z^*=\frac{z}{L},\qquad t^*=\omega t \tag{14}$$

Since we are interested in the behavior at the vicinity of the resonant point, we write angular frequency ω as follows:

$$\frac{\omega}{\omega_1}=1+\varepsilon\alpha_1+\varepsilon^2\alpha_2+O(\varepsilon^2) \tag{15}$$

Using these preparations, Eqs.(7) and (8) are linearized and we obtain the following nonlinear solutions:

$$\phi_1 = \frac{a}{\pi\sigma} \sin \pi x^* C_1(z^*) \cos t^* \tag{16}$$

$$\phi_2 = -\frac{a^2}{16\sigma} \left\{ B_{02} + B_{22} \cos 2\pi x^* C_2(z^*) \right\} \sin 2t^* \tag{17}$$

$$\begin{aligned} \phi_3 = \frac{\pi a^3}{256\sigma} & \left\{ -B_{31} \sin 3\pi x^* C_3(z^*) \cos t^* + B_{13} \sin \pi x^* C_1(z^*) \cos 3t^* \right. \\ & \left. + B_{33} \sin 3\pi x^* C_3(z^*) \cos 3t^* \right\} \\ & + \frac{4}{\pi^2} \sum_{n=2}^{\infty} \frac{(-1)^{n-1} \sin(2n-1)\pi x^*}{(2n-1)^2 \left\{ \left(\omega_{2n-1}/\omega_1 \right)^2 - 1 \right\}} C_{2n-1}(z^*) \cos t^* \end{aligned} \tag{18}$$

$$\eta_1 = a \sin \pi x^* \sin t^* \tag{19}$$

$$\eta_2 = a^2 A_{22} \cos 2\pi x^* \cos 2t^* \tag{20}$$

$$\begin{aligned} \eta_3 = {} & a^3 A_{11} \sin \pi x^* \sin t^* - a^3 A_{31} \sin 3\pi x^* \sin t^* \\ & + a^3 A_{13} \sin \pi x^* \sin 3t^* + a^3 A_{33} \sin 3\pi x^* \sin 3t^* + \frac{2\sigma}{\pi} \sin \pi x^* \sin t^* \\ & + \frac{4\sigma}{\pi} \sum_{n=2}^{\infty} \frac{(-1)^{n-1} \sin(2n-1)\pi x^*}{(2n-1)^2 \left\{ 1 - \left(\omega_1/\omega_{2n-1} \right)^2 \right\}} \sin t^* \end{aligned} \tag{21}$$

where a corresponds to the free surface elevation and satisfies the following equation:

$$R\varepsilon^3 a^3 - \left(\frac{\omega}{\omega_1} - 1 \right) \varepsilon a - \frac{2\sigma X_0}{\pi L} = 0 \tag{22}$$

Finally, σ, $C_n(z^*)$, R, A_{ij} and B_{ij} are

$$\sigma = \tanh(\pi h/L)$$

$$C_n(z^*) = \frac{\cosh n\pi(z^* + h/L)}{\cosh n\pi h/L}$$

$$R = \frac{\pi^2}{64} \left(9\sigma^{-4} - 14\sigma^{-2} - 3 \right)$$

$$A_{11} = \frac{\pi^2}{64} \left(3\sigma^{-4} + 12\sigma^{-2} - 1 \right)$$

$$A_{13} = \frac{\pi^2}{256} \left(9\sigma^{-4} + 54\sigma^{-2} - 15 \right)$$

$$A_{22} = \frac{\pi}{8}\left(3\sigma^{-3} - \sigma^{-1}\right)$$

$$A_{31} = \frac{\pi^2}{256}\left(27\sigma^{-4} + 51\sigma^{-2} - 87 - 15\sigma^2\right)$$

$$A_{33} = \frac{\pi^2}{256}\left(81\sigma^{-6} - 27\sigma^{-4} + 27\sigma^{-2} - 9\right)$$

$$B_{02} = 3\sigma + \sigma^{-1}$$

$$B_{13} = 9\sigma^{-4} + 62\sigma^{-2} - 31$$

$$B_{22} = 3\left(\sigma^{-3} - \sigma\right)$$

$$B_{31} = 3\sigma^{-4} + 11\sigma^{-2} + 1 - 15\sigma^2$$

$$B_{33} = 9\sigma^{-6} + 5\sigma^{-4} - 53\sigma^{-2} + 39$$

4. Results and discussions

The frequency response of the free surface of a magnetic fluid is shown in Fig.5. Here B is the surface magnetic field induction at the center of the permanent magnet, η is the maximum free surface elevation at the side wall and ω_E is the first resonant angular frequency obtained by experiment for B=0. As the forcing frequency increases, the surface elevation also increases until the free surface is intensively shaken near the resonant frequency. After the resonant frequency, the surface disturbance is repressed. The first resonant frequency shifts to a higher frequency as the magnetic field intensity is increased. Assuming a potential flow and using a perturbation method, we have obtained nonlinear sloshing responses up to the third order perturbation $O(\varepsilon^3)$ as mentioned above. In Fig.6 experimental results are compared with the linear and nonlinear theoretical results for B=0, 40, and 80 mT. Here ω_0 is the first resonant angular frequency obtained by the linearized wave theory when there is no magnetic field. In the low frequency range, the nonlinear solution is larger than the experimental values because calculated amplitude

does not become zero with a decrease of the frequency (Hayama et al. 1983). Experimental and nonlinear theoretical results have a good agreement particularly, in the high frequency region.

UVP measurements were mainly carried out at near-resonant frequencies. Figure 7 shows maximum and minimum velocity profiles for several applied magnetic fields. There are 1024 measurement points along the measurement axis, each representing the velocity value over a 39 ms period. Here h_z is the position of the ultrasonic transducer from the bottom wall. Time dependent velocity profiles at a point, $x = -0.04$ mm, are illustrated in Fig.8. The resonant frequency obtained by experiment for B=0 is $f = 2.75$ Hz. Positive velocity means a flow direction away from the ultrasonic transducer. When the magnetic field increases, the velocity decreases because of the magnetic force. That is, the effective gravity increases as expressed in Eq.(9). The increase in effective gravity also causes the reflecting particles for the ultrasonic wave to go upward, consequently good echo signals are not received by the ultrasonic transducer. The absence of velocity data, especially for $B = 80$ mT, in Figs.7 and 8 results from this rise of reflecting particles. The spatial velocity profiles are not symmetric with respect to the central axis ($x = 0$) (as shown in Fig.7) due to the nonlinearity of the fluid motion.

From the measured velocity data, we calculated 128 power spectra by using a fast Fourier transform in the time domain. Figure 9 shows the power averaged over a central region (-9.6 mm $\leq x \leq 10.32$ mm, $h_z = 10$ mm). The most dominant peak is f_1, which corresponds to the forcing frequency. The peaks f_2 and f_3 represent two and three times the forcing frequency, respectively. The height of each peak decreases with increasing magnetic field intensity because the disturbance of the fluid is suppressed by the magnetic field.

Figure 10 illustrates time averaged spatial distributions of the power spectra for f_1,

f_2 and f_3 at a resonant state ($f = 2.93$ Hz) for $B = 40$ mT. Using the velocity potential derived from theory, the dimensionless velocity component in the x direction is given by

$$v_x^* = \frac{v_x}{L\omega_1} = \frac{\partial \phi^*}{\partial x^*} \tag{23}$$

In Fig.10, nonlinear theoretical spatial spectra for f_1, f_2 and f_3 obtained by Eq.(23) are shown by a broken line, a chain line with two dots, and a solid line, respectively. The distribution of the frequency component f_1 are in agreement with the theoretical results. However, the other power spectra deviate from the theoretical lines, especially near the side wall furthest from the ultrasonic transducer. This may be because the ultrasonic echo signal diminishes due to the clustering and chaining of the magnetic particles that occurs under an applied magnetic field (e.g. Rosensweig 1985).

5. Concluding remarks

Lateral sloshing of a magnetic fluid in a rectangular container in a vertically-applied non-uniform magnetic fields has been investigated. Assuming a potential flow and using a perturbation method, we have obtained nonlinear sloshing responses up to the third order perturbation in the vicinity of the first resonant frequency. The theoretical nonlinear solutions agree with the experimental results. However, the nonlinear solutions are a little larger than the experimental data in the lower frequency range because the amplitude of the free surface oscillation does not become zero with a decrease of the frequency. In fact, in this range, the linear solutions are in better agreement with the experimental values.

Since a magnetic fluid is opaque, it has been very difficult to obtain velocity field data using a conventional measuring technique. We have applied the UVP measurement technique to a sloshing liquid to obtain both spatial velocity profiles along horizontal lines and time dependent velocity profiles. The amplitude of the velocity decreases with a increase in magnetic field intensity because of increase of the magnetic force. Also,

the power spectra were calculated from the velocity data. The spatial distribution of the dominant peak f_1 are in good agreement with the nonlinear theoretical results, however, other power spectra deviate from the theoretical lines. In the future, we suggest the investigation of the influence of magnetic fields on ultrasound reflecting particles and the clustering mechanism of magnetic particles.

Acknowledgments

We would like to thank Prof. Y. Kurosaki (Tokyo Institute of Technology, Japan) for his assistance with UVP measurements. We wish to express our gratitude to Dr. Y. Takeda (Paul Scherrer Institut, Switzerland) for his collaboration in this work. We also acknowledge the assistance of F. Matsuura and G. Yamanaka during the experiment.

References

Dean RG; Dalrymple RA (1984) Water wave mechanics for engineers and scientists. Chap. 3, New Jersey: Prentice-Hall

Dodge FT; Garza LR (1970) Magnetic fluid simulation of liquid sloshing in low gravity. NASA Tech Rep 9: 1–29

Handa K; Tajima K (1979) Sloshing of two superposed liquid layers in a rectangular tank. Trans Jpn Soc Mech Eng 45 B: 1450–1457

Hashimoto H; Sudo S (1985) Dynamic behavior of stratified fluids in a rectangular container subject to vertical vibration. Bull JSME 28: 1910–1917

Hayama S; Aruga K; Watanabe T (1983) Nonlinear researches of sloshing in rectangular tanks (1st Report, Nonlinear responses of surface elevation). Bull JSME 26: 1641–1648

Kikura H; Sawada T; Tanahashi T (1991) Surface behavior of magnetic fluid sloshing and its frequency responses. Trans Jpn Soc Mech Eng 57 B: 1629–1634

Li CH (1970) Instability of time-periodic flows of stratified fluids. Phys Fluid 13; 1121–1134

Matsuura F; Matsubara Y; Sawada T; Tanahashi T (1995) Surface behaviors of two-layers liquid sloshing under non-uniform magnetic field. In: Advanced computational and design techniques in applied electronic systems. (ed Hahn SY), pp517–520, Amsterdam: Elsevier Science

Okubo M; Ishibashi Y; Oshima S; Katakura H; Yamane R (1990) Interfacial waves of the magnetic fluid in vertical alternating magnetic fields. J Magn Magn Mat 85: 163–166

Rosensweig RE (1985) Ferrohydrodynamics. Cambridge: Cambridge University Press

Sawada T; Kikura H; Shibata S; Tanahashi T (1993) Lateral sloshing of a magnetic fluid in a container. J Magn Magn Mat 122: 424–427

Sudo S; Hashimoto H; Katagiri K (1987) Interfacial instability of magnetic fluids in a rectangular container. JSME Int J 30: 1086–1092

Takeda Y (1986) Velocity profile measurement by ultrasound Doppler shift method. Int J Heat Fluid Flow 7: 313–318

Takeda Y (1987) Measurement of velocity profile of mercury flow by ultrasound Doppler shift method. Nuc Technol 79: 120–124

Zelazo RE; Melcher JR (1969) Dynamics and stability of ferrofluids surface interaction. J Fluid Mech 39: 1–24

1. International Symposium on Ultrasonic Doppler Method in Fluid Mechanics and Fluid Engineering,

September 9 - 11, Paul Scherrer Institut, Switzerland

List of Participants

Masaya Kumada Department of Mechanical Engineering Gifu University Yanagido 1-1 Gifu 501-11 Gifu Japan Tel. 0081 58 293 2530 Fax 0081 58 230 1892	Patrice Le Gal IRPHE Marseille 12 Avenue Général Leclerc 13003 Marseille France Tel. 0033 91505439 Fax 0033 91081637	Ulrich Lemmin Ecole Polytechnique Fédérale de Lausanne Department de Genie Civil 1015 Lausanne Switzerland Tel. 0041 21 693 2379 Fax 0041 21 693 6767
Liping Ni Paul Scherrer Institut WHGA/246 5232 Villigen PSI Switzerland Tel. 0041 56 310 4453 Fax 0041 56 310 3131	B. Ouriev Institut für Lebensmittelwissenschaft LM-Verfahrenstechnik ETH-Zentrum 8092 Zürich Switzerland Tel. Fax	P. Pinter PE Pinter Engineering Bachstrasse 30 8912 Obfelden Switzerland Tel. Fax 01-767-0982
Jean-Francis Ravoux IRPHE Marseille 12 Avenue Général Leclerc 13003 Marseille France Tel. 0033 91505439 Fax 0033 91081637	Jun Sakakibara Dept. Theoretical & Applied Mechanics University Illinois 104 S. Wright Str. 61801 Urbana IL USA Tel. 001 217 244 1101 Fax 001 217 244 5707	Tatsuo Sawada Department of Mechanical Engineering Keio University 3-14-1 Hiyoshi, Kohoku-ku 223 Yokohama Japan Tel. 0081 45 563 3119 Fax 0081 45 563 5943
Samuel Schabel Voith Sulzer Stoffaufbereitung GmbH Forschung und Entwicklung Escher-Wyss-Strasse 25 88212 Ravensburg Germany Tel. 0049 751 83 2944 Fax 0049 751 83 3030	Lionel Schouveiler IRPHE Marseille 12 Avenue Général Leclerc 13003 Marseille France Tel. 0033 91505439 Fax 0033 91081637	W. Shen Ecole Polytechnique Fédérale de Lausanne Department de Genie Civil 1015 Lausanne Switzerland Tel. 0041 21 693 2379 Fax 0041 21 693 6767
Robert Stieglitz Institute for Applied Thermo-and Fluiddynamics (IATF) Forschungszentrum Karlsruhe Postfach 3640 76021 Karlsruhe Germany Tel. 0049 7247-823462 Fax 00497247 82 4837	Yasushi Takeda Paul Scherrer Institut WMHA/B22 5232 Villigen PSI Switzerland Tel. 0041 56 310 3568 Fax 0041 56 310 3131	Peter Thomas University of Warwick Department of Engineering CV4 7AL Coventry England Tel. 0044 1203 523 523 Fax 0044 1203 52 418922
Akira Tokuhiro Power Reactor and Nuclear Fuel Development Corporation 4002 Narita, Oarai-Machi 311-13 Ibaraki-ken Japan Tel. 0081 29 267 4141 Fax 0081 29 266 3867	Katsumi Tsuda Keio University 3-14-1, Hiyoshi Kohoku-ku Yokohama, Kanagawa 223 Japan Tel. 0081 45 563 3233 Fax 0081 45 563 5943	Marcel Verduyn ETH Zürich Laboratorium fÜr Technische Chemie Universitätsstrasse 6 8092 Zürich Switzerland Tel. 0041 1 632 6183 Fax 0041 1 632 1082

1. International Symposium on Ultrasonic Doppler Method in Fluid Mechanics and Fluid Engineering,

September 9 - 11, Paul Scherrer Institut, Switzerland

List of Participants

P. Wächter LSTM Cauerstrasse 4 91058 Erlangen Germany Tel. Fax	Jean-Claude Willemetz Signal Processing SA 21, av. de la Gare 1003 Lausanne Switzerland Tel. 0041 21 312 0962 Fax 0041 21 312 0963	E. Windhab ETH-Zentrum Lebensmittelverfahrenstechnik 8029 Zürich Switzerland Tel. Fax
Shintaro Yamashita Department of Mechanical Engineering Gifu University Yanagido 1-1 Gifu 501-11 Gifu Japan Tel. 0081 58 293 2526 Fax 0081 58 230 1892	Shirong Zhou Research Laboratory for Nuclear Reactors Tokyo Institute of Technology 2-12-1 Ohokayama, Meguro-ku 152 Tokyo Japan Tel. 0081 3 5734 3063 Fax 0081 3 5734 2959	

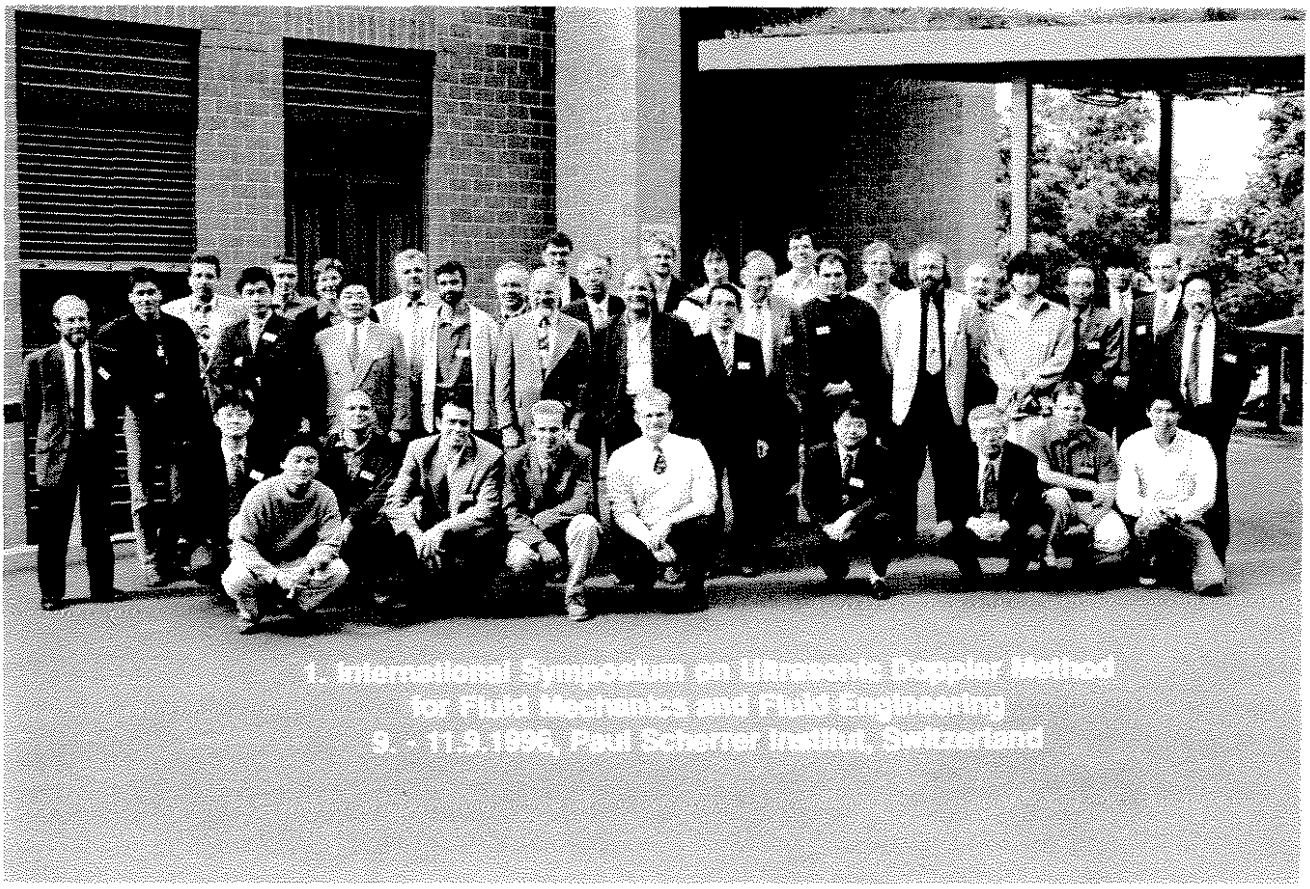

PAUL SCHERRER INSTITUT

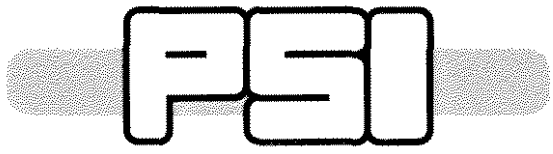

Paul Scherrer Institut
CH-5232 Villigen PSI
Internet address

Phone 056 310 21 11
Fax 056 310 21 99
http://www.psi.ch